Adsorption and reduction of actinides on iron and aluminum (oxyhydr)oxides

by

Sandra D. Taylor

A dissertation submitted in partial fulfillment
of the requirements for the degree of
Doctor of Philosophy
(Geology)
in the University of Michigan
2015

Doctoral Committee:

Professor Udo Becker, Chair
Assistant Professor Rose Cory
Professor Kim F. Hayes
Laboratory Fellow Kevin M. Rosso, Pacific Northwest National Laboratory
Assistant Professor Donald J. Siegel

DEDICATION

To my parents and Aaron

Acknowledgements

I am so grateful to everyone that has made this five year journey worthwhile. First, I would like to express my gratitude to Udo Becker for being a great advisor and mentor. Thank you for your encouragement through the years to pursue my research interests, and helping me develop as a scientist. It has been a pleasure working with you and learning from you.

I would also like to thank all of my committee members for your help throughout my graduate studies. Thanks to Kevin Rosso for teaching me Marcus Theory and for your help with all the work in this thesis. Thanks to Kim Hayes for the helpful discussions on redox reactions affecting actinide transport. Thanks to Donald Siegel for your helpful discussions on quantum mechanical modelling and modelling interfaces. Thanks to Rose Cory for giving me advice on how to communicate science clearly and effectively. I would also like to thank Greg Dick for letting me use his lab on numerous occasions. To all the rest of the EARTH faculty and staff: thank you for making this such a great environment to work in.

Special thanks to my research group members and friends, Maria, Sarah, Ben, Evan, Youngjae, Will, Ke, Cameron, and Alex. I would also like to thank all the students in the EARTH department who have made my PhD experience incredible. I've enjoyed interacting with you all on both a scientific level and a personal level. I'm lucky to have met so many great friends here.

I owe much of my success to my loving parents. Thank you for all your sacrifices and for always supporting me. A big thank you to my sister Myra as well, for being a great friend and role model.

Last, but not least, thank you to my wonderful husband Aaron for your patience, love, and support through the years. I'm so happy and grateful you took a chance five years ago to come to Michigan with me. Cheers to the many more chances in life that we'll take together! I love you!

Table of Contents

List of tables

List of figures

Abstract

Mineral-water interface geochemistry plays a critical role in the understanding the integrity of underground geologic repositories where nuclear waste will be disposed of. This dissertation seeks to provide a fundamental understanding of how sorption and/or redox processes at mineral surfaces influence the mobility of actinides, specifically plutonium (Pu) and uranium (U). Unique and novel approaches combining experiments and atomistic modeling were utilized to make detailed studies on the structure, thermodynamics, kinetics, and reaction mechanisms between actinide/metal complexes and mineral surfaces.

In Chapter 1, a series of computational simulations are used to explain the how substrates can strain the lattice of *fcc* PuO_2, in turn leading to the formation of non-*fcc* Pu nanocolloids on the surface of goethite. The remainder of the dissertation (Chapters 2-5) investigates synergistic effects between sorption and/or redox processes and mineral surfaces in controlling the mobility of U. First, the reduction $U(VI)_{aq}$ by $Fe(II)_{aq}$ is not observed in the absence of a solid substrate (at neutral pH, anoxic conditions) using batch experiments. *Ab initio* calculations coupled with Marcus Theory (MT) complement experimental observations, showing that electron transfer (ET) from $Fe(II)_{aq}$ to $U(VI)_{aq}$ is inhibited by high energetics associated with the dehydration and inner-sphere complexation of Fe and U. Heterogeneous catalysis of U(VI) reduction by Fe(II) in the presence of Fe and Al (oxyhydr)oxide minerals is also studied using batch experiments and *ab initio* models. These experiments specifically probe how a mineral's electronic properties affect the redox rate. U(VI) reduction by Fe(II) is measured to be ten times faster in the presence of semiconducting Fe(oxyhydr)oxides compared to their insulating Al isostructures using batch experiments. Models demonstrate that the enhanced catalytic abilities on semiconducting mineral surfaces are potentially heavily influenced by the proximity effect, where a semiconducting surface transports electrons between adsorbed electron donors and acceptors. MT was applied to describe the kinetics of mineral-catalyzed redox reactions in ternary, coadsorbed systems for the first time. In particular, it is found that interfacial and surficial ET reactions in hematite may

possibly be energetically limiting steps for ET through a semiconducting surface to occur via the proximity effect.

Chapter 1: Introduction

Mineral surfaces influence the chemistry of the natural environment. This is because all interactions between a mineral and its surrounding melt, aqueous fluid, or vapor phase take place at its surface [1]. Thus, mineral-water interface geochemistry plays a critical role in the quality of the world's fresh water, soil development and plant nutrient distribution, the genesis of certain types of ore and hydrocarbon deposits, and, in a global sense, the geochemical cycling of the elements [2]. This dissertation focuses on understanding mineral-water interface geochemistry in relation to the integrity of underground geologic repositories, where nuclear waste will be disposed of. Sorption and/or redox reaction mechanisms on iron and/or aluminum (oxyhydr)oxide mineral surfaces are investigated, as these reactions by themselves or coupled on mineral surfaces can significantly influence the mobility of actinides such as uranium (U) and plutonium (Pu).

1.1 Background

Soils and groundwaters across the world have been contaminated with actinides, such as U and Pu, through anthropogenic activities. In the US, there are 76 Superfund sites that are radioactively contaminated [3]. These sites include former weapons production facilities, where the degradation of storage tanks over time and subsequent leakage of radioactive waste has led to the contamination of groundwater. For instance, the Hanford site in WA produced Pu for the US's defense program for more than 40 years (1943-1987), resulting in the contamination of ~ 12 million m3 of soil with Pu waste along with U and a number of other contaminants including chromium and technetium [4]. Decommissioned mines and mine tailings have also led to the chemical weathering of uranium oxides, such as uraninite (UO2), contaminating groundwaters with U [5].

In addition to the legacy of contamination from defense and mining industries, the future disposal of spent nuclear fuel in an underground geologic repository provides another

anthropogenic source of actinides. Within the United States alone, 70,000 metric tons of radioactive waste have been generated from 104 nuclear power plants [6]. It is estimated that an additional 2,000 metric tons of radioactive waste are generated every year, suggesting that between 2040 and 2055, the amount of commercial spent fuel and radioactive waste will reach 140,000 metric tons [6].

The most viable option for disposing and isolating spent nuclear fuel is to store it in a geologic repository, although there is currently no approved site in the United States. Part of the difficulty with selecting a nuclear waste site is predicting complicated chemical reactions that influence the transport of actinides in the near- and far-field environments for the next million years, as required by the US Environmental Protection Agency [7]. In relation to the near-field environment, water that has come into contact with the waste will corrode the iron/steel canisters containing the spent fuel over time. Dissolution of the canisters and the fuel-matrix within the canisters will, for instance, yield aqueous Fe, U, and Pu species (in addition to a number of other ions) as well as solid iron (oxyhydr)oxide precipitates. Redox reactions between U and Fe ions as well as sorption and/or (co)precipitation reactions can occur concurrently. In turn, these reactions can significantly influence the mobility of U and/or other actinides (as will be discussed shortly) [8]. Thus, to better predict the migration of actinides as well as formulate strategies to prevent their exposure to the biosphere, an extensive understanding of the environment, the aqueous geochemistry of the site, and potential chemical reaction pathways and mechanisms is needed.

This dissertation seeks to provide new understanding on the interactions between actinides, metals, and minerals that will likely be present in the repository environment [5, 9], particularly focusing on how sorption and/or redox mechanisms control actinide mobility. Sorption reactions are important with respect to actinide transport because it controls whether the actinide is dissolved in water *vs.* attached to a mineral surface. Actinides that are soluble are more readily transported through the environment in groundwater. Through adsorption reaction reactions, actinides can attach to reactive functional groups on mineral surfaces. Adsorption removes the actinide(s) from solution, and thus allows them to move less freely. The mobility of mineral bound actinide is then controlled by the fate and transport of the host mineral. Within this dissertation, the influence of sorption processes at the mineral-water interface on the

transport of nanocolloids is investigated. Sorption processes are also studied to understand their role in catalyzing redox reactions.

In addition to sorption reactions, redox reactions influence the mobility of many actinides and metals, as the chemical oxidation state controls their aqueous solubility. Most actinides can exist in several oxidation states; for instance, U has a range of oxidation states including U(III), U(IV), U(V), and U(VI). The prominence of one oxidation over the other(s) is dependent on the environmental conditions present (e.g., reducing environment, pH, etc.,); for example, U(VI) is dominant in oxidizing environments while U(IV) is often found in reducing environments. U(VI) is soluble, and, thus, capable of being transported with groundwater. In contrast, U(IV) is insoluble and precipitates to $U(IV)O_{2(s)}$. Therefore, the reduction of U(VI) to U(IV) and subsequent precipitation to $UO_{2(s)}$ facilitates the removal of U from solution. Within the near-field repository environment, it is highly plausible that reduction of U(VI) will occur. Reductants such as Fe(II) will be present in repository environment through the dissolution of the waste canisters, as mentioned above. Thus, this dissertation largely focuses on the abiotic reduction of U(VI) by Fe(II) as a relevant process for retarding U transport in the subsurface.

Adsorption and redox reactions can be coupled on a variety of different mineral surfaces. More so, redox reactions are often facilitated or initiated by sorption processes on mineral surfaces; dehydration of ions upon sorption to substrate surfaces aids in catalyzing redox reactions by stripping hydration shells and enabling ions to interact with one another. Surface-mediated redox processes can be effective pathways for limiting the mobility of actinides [5, 10]. This dissertation seeks to better understand mechanisms at mineral surfaces influencing the catalysis of redox reactions. The influence of different substrates and how their respective electronic and chemical properties affect the catalysis of redox reactions is particular focus within this dissertation. For instance, Fe (oxyhydr)oxides have been shown to be very effective catalysts for the reduction of U(VI) by Fe(II) [11-15] in comparison to other minerals such as micas [16]. Of the many factors influencing the catalysis of redox reactions on mineral surfaces, the availability of different charge transfer pathways is dependent on the substrates' chemical and electronic properties. The different chemical and electronic properties of substrates provide different pathways for redox reactions to proceed by. For instance, it is hypothesized that pathways available in semiconducting minerals, where the surface participates in ET, can lead to

considerably faster and more efficient reduction rates [17, 18]. To gain a better understanding of fundamental mechanisms involved in the heterogeneous catalysis of redox reactions, research within this dissertation investigates how the substrates' electronic and chemical properties influence the redox kinetics for U(VI) reduction by Fe(II) and, as a consequence, uranium mobility.

1.2 Overview of research chapters

Research in this dissertation is part of a multi-method approach to understand synergism between sorption and/or redox processes that control the mobility of actinides (specifically Pu and U). Batch adsorption experiments, mineral characterization techniques, and molecular simulations are used to identify reaction pathways and mechanisms affecting actinide mobility in the biosphere and the function of minerals in sequestrating actinides in underground nuclear waste repositories.

The influence of the goethite (001) surface on the stability of lattice distorted PuO_2 and/or hypostoichiometric PuO_{2-x} was investigated in Chapter 1. This study was motivated by experimental observations of an unusual (rare) *bcc* Pu_4O_7 phase sorbed onto goethite (α-FeOOH, *Pnma*). This phase was postulated to have be more strongly bound to the goethite surface compared to *fcc* PuO_2, suggesting the transport of the *bcc* Pu_4O_7 phase in the environment would be controlled by the interaction with goethite as its host mineral [19, 20]. Empirical and *ab initio* methods were applied to probe the mechanisms and energetics of atomistic- and nano-scale processes at the mineral-water interface that could influence the adsorption and stability of Pu phases sorbed onto goethite. The computational models in this study are able to provide considerable insight into the molecular-scale processes and energetics of PO sorption onto goethite that support and clarify experimental observations. Combining all these observations, the computational models are able to explain that the experimentally observed non-*fcc* PO phase forms by the lattice distortion of the PO adsorbate upon formation of a heterointerface with goethite.

The remaining chapters of this dissertation (Chapters 2-5) investigate mechanisms for the removal of uranium from solution, focusing on the sorption and the chemical reduction of U(VI)

to U(V)/U(IV) by Fe(II). While the abiotic reduction of U(VI) by ferrous iron has been investigated, removal of U from solution through the reduction of U(VI) by Fe(II) in the absence of sorption to a solid surface (under anoxic conditions and near-neutral pH) has been debated [11-15]. Thus, Chapter 3 investigates mechanisms by which U(VI) is removed from an Fe(II)-containing solution, and includes an analysis of the energetic and kinetic barriers involved in the homogeneous reduction of U(VI) by Fe(II). Batch experiments helped explain contrasting observations in the literature on the precipitation of U-containing solids (without changing oxidation states) versus precipitation/reduction reactions. Ab initio, molecular models coupled with Marcus Theory are supplied the atomistic mechanisms, thermodynamics, and kinetics involved in the reduction of U(VI)aq to U(V)aq by Fe(II)aq. By combining experiments and quantum-mechanical modeling, this chapter provides an understanding of mechanisms involved in the abiotic reduction of U(VI) by Fe(II).

Building on Chapter 3 on the homogeneous reduction of U(VI) by Fe(II), Chapter 4 investigates the heterogeneous catalysis of U(IV) reduction by Fe(II), i.e., by taking into account the role of sorption onto mineral surfaces in this reduction process. The influence of minerals' electronic and chemical properties on enhancing the rate of redox reactions is also investigated. Mineral surfaces, such as those associated with iron (oxyhydr)oxides, enhance the rate that U(VI) is reduced by reductants such as Fe(II) [11-14], although these surface-mediated redox processes are not well understood [2, 21]. One idea is that iron (oxyhydr)oxides act as semiconductors, facilitating redox reactions by serving as medium for electron transport [17, 18]. To test this idea, this study compared and contrasted the rate of U(VI) reduction by Fe(II) in the presence of isostructural minerals with different electronic/chemical properties. That is, the rates of U(VI) reduction by Fe(II) in the presence of semiconducting iron (oxyhydr)oxides (i.e., hematite and goethite) were compared to those observed on the presence of their insulating Al-isostructures (i.e., corundum and diaspore, respectively). Isostructures of Al (oxyhydr)oxides are used as structural analogs for Fe (oxyhydr)oxides [10, 22]; however, their different electronic properties enable observing whether electron transfer is more prevalent in semiconducting than in insulating minerals. Similar to Chapter 3, batch sorption experiments were conducted using a range of methods (such as X-ray photoelectron spectroscopy), to characterize the redox products adsorbed at the mineral surfaces. Quantum mechanical models were applied to understand the how the different charge transfer pathways on insulating and semiconducting mineral surfaces

can affect the redox reaction. The results from this chapter demonstrate that a minerals' chemical and electronic properties can significantly influence the catalysis of redox reactions and that integration of these details into conceptual models can improve predictions of the mobility of U and other metals in the subsurface.

Mechanisms involved in the heterogeneous catalysis of U(VI) reduction by Fe(II) are further investigated using theoretical methods in Chapter 5. The objective of this study is to obtain quantitative information on energetic and kinetic barriers for ET reactions within these ternary systems where Fe and U are coadsorbed on hematite and corundum clusters. To obtain this information, MT is applied for the first time to describe the kinetics of mineral-catalyzed redox reactions in ternary, coadsorbed systems. This study builds on Chapter 4, continuing to investigate how the chemical and electronic properties of substrates can affect the rate of redox reactions. The quantum-mechanical models from Chapter 4 highlight how electronic charge transfer paths or spin transitions in semiconductors can enhance redox reaction rates, supporting previous hypotheses [17, 23-25]. In particular, the proximity effect, which describes the potential for the transfer of an electron from one coadsorbate to the other using pathways through the semiconducting surface [17, 18], is postulated to be an influential mechanism that enhances the rate U(VI) is reduced by Fe(II) when adsorbed on semiconducting mineral surfaces. While ET pathways through semiconducting surfaces have been postulated and can be identified using a combination of experimental methods and quantum-mechanical models, the lack of information on the energetics and kinetics of charge transfer pathways. For instance, while the proximity effect is thought to greatly influence ET rates on semiconducting surfaces, it is unclear whether and what energetic barriers exist for interfacial ET to occur between coadsorbed Fe(II) and U(VI) with the hematite surface. In turn, it is difficult to understand the fundamentals of heterogeneous catalysis of redox reactions and how the coadsorption of Fe and U on mineral surfaces, as described above, facilitates ET. Like Chapter 3, *ab initio*, molecular models coupled with Marcus Theory are applied in this case to describe the kinetics for the reduction of U(VI) by Fe(II) in the presence of corundum and hematite clusters. This study provides a better understanding of atomistic mechanisms involved in the reduction of U(VI) to U(V) by Fe(II) in the presence of corundum and hematite clusters; for instance, calculations show that energetic and kinetic barriers exist for ET to proceed via the proximity effect in semiconducting minerals.

This study also highlights that MT can be applied to gain a fundamental understanding of ET pathways relevant to a broad range geochemical systems.

Chapter 2:
Influence of the goethite (α-FeOOH) surface on the stability of distorted PuO_2 and PuO_{2-x} phases

S. D. Taylor[1], B. A. Powell[2], and U. Becker[1]

[1]*The University of Michigan, Department of Earth and Environmental Sciences, 2534 C. C. Little Building, 1100 North University Ave., Ann Arbor, MI 48109–1005, United States.*

[2]*Clemson University, Environmental Engineering and Earth Sciences Department, Rich Lab, 342 Computer Court, Anderson, SC 29625, United States.*

2.1 Abstract

The heteroepitaxial growth of a *bcc* Pu_4O_7 phase on goethite was deduced from *d*-spacings measured from HRTEM ED images [19], implying that Pu(IV) oxide (PO) nanocolloids are capable of being structurally and/or chemically modified when sorbed onto goethite. However, there is little information on the mechanisms leading to the sorption and formation of the non-*fcc* PO nanophase on goethite. This study aims to explain molecular-scale mechanisms leading to the formation of non-*fcc* PO phases as well as understand the influence of goethite in stabilizing this non-*fcc* PO phase. A series of computational models, utilizing both *ab initio* and empirical methods, are applied.

To begin the investigation, the formation energies for bulk lattice-distorted PuO_2 phases as well as bulk PuO_{2-x} were quantified using *ab initio* methods. The formation energies show that the *fcc* PuO_2 lattice can be distorted to match that of goethite lattice with relatively low energetic inputs (+88 kJ/mol Pu_4O_8). The distortion of the PO lattice by goethite can also be deduced from analyses of simple heterointerfaces between cubic salts using empirical models. That is, when the lattice of a 'KCl' cluster has <15% LM with that of a NaCl cluster, the sorption of the 'KCl' onto NaCl is exothermic (< –80 kJ/mol). These models suggest that the lattice of the PO

adsorbate would distort upon sorption and/or formation of a heterointerface with goethite to lower the amount of LM at the heterointerface and increase its sorption affinity.

The PO-goethite heterointerfaces modelled continue to support that the experimentally observed non-*fcc* PO adsorbate is a result of the *fcc* PuO_2 lattice being distorted to better match that of goethite. Simulated ED patterns for the PO-goethite heterointerfaces reproduce the alignment and *d*-spacings observed experimentally, showing the non-*fcc* PO nanostructures characterized experimentally result from lattice distortion *fcc* PuO_2 phase. The PO-goethite heterointerfaces also show how goethite, specifically, aids in the stabilizing the non-*fcc* PO phase. Calculation of W_{ad} shows that the PO–goethite interfaces are stable relative to the existence of separate PuO_2/ PuO_{2-x} and goethite surfaces, and that covalent- to polar-covalent bonding at the interface helps stabilize the PO-goethite interfaces.

Combining all these observations, the computational models are able to explain that the experimentally observed non-*fcc* PO phase forms by the lattice distortion of the PO adsorbate upon formation of a heterointerface with goethite. The computational models in this study are able to provide considerable insight into the molecular-scale processes and energetics of PO sorption onto goethite that support and clarify experimental observations.

2.2 Introduction

Field studies have shown that the transport of plutonium (Pu) in the subsurface is often controlled by sorption reactions at the mineral-water interface [26]. For instance, at the Nevada Test Site, Pu was introduced into the environment from the > 800 nuclear detonation tests carried out from 1956 to 1992. Field studies conducted by Kersting, *et al.* (1999) [27] found that over ~40 years Pu had been transported away from its source. More so, Pu found 1.3 km down-gradient from the source was found to be associated with the colloidal fraction of the groundwater [27]. Further support for colloid-facilitated transport has also been provided by field studies at the Mayak Site (Russia), where >70% of the Pu that was transport > 2.5 km away from its source was found to be associated amorphous iron hydroxides colloids comprised [28]. Thus, to understand the fate and transport of Pu requires an understanding of the molecular level mechanisms involved in colloid-facilitated transport.

By applying nanoscience techniques, experiments have sought to provide further insight into sorption and molecular-scale processes at the mineral-water interface that influence the mobility of actinides. Experiments characterizing the nanostructures for Pu oxides (PO) adsorbed on quartz (α-SiO_2) and on goethite (α-FeOOH, *Pnma*) have shown that the sorption processes on these minerals are considerably different, which in turn shows that Pu transport is affected by the specific host mineral that is adsorbs to [19, 20]. In these studies aqueous Pu(IV) was added incrementally to suspensions of quartz and goethite, at concentrations below and near the $PuO_{2+x\,(s,\,hyd)}$ solubility (10^{-9} M) [19, 20]. The nanostructures of PO phases adsorbed onto the minerals was then characterized using selected-area diffraction pattern (SAED) and HRTEM imaging combined with fast Fourier transform (FFT) analysis. In the presence of quartz, aggregates of *fcc* PuO_2 nanocolloids were characterized at ambient conditions [19], which agrees with thermodynamic and solubility predictions. When aqueous Pu(IV) was added incrementally to suspensions of goethite, aggregates of *fcc* PuO_2 nanocolloids were found as well as 2 – 5nm non-*fcc* PO colloids adsorbed onto goethite. These non-*fcc* PO nanocolloids were characterized to be a rare, *bcc* Pu_4O_7 phase based on *d*-spacings measured that are unique to *bcc* Pu_4O_7 ($Ia\bar{3}$) phase (Figure 2-1b) [19]. More so, it was proposed that the *bcc* Pu_4O_7 phase was heteroepitaxially grown on the goethite surface [19, 20] based on the structural orientation and alignment of the *bcc* Pu_4O_7 (110) surface with the goethite (001) surface (Figure 2-1a) [19].

Desorption experiments also showed the *bcc* Pu_4O_7 phase was more strongly associated with goethite compared to *fcc* PuO_2 [19, 20]. The difference in sorption affinities between the *fcc* and *bcc* Pu_4O_7/non-*fcc* PO phases would lead to different transport behaviors; *i.e.*, the transport of the non-*fcc* PO would be more dependent on the fate and transport of its host mineral compared to the *fcc* PuO_2 phase. The non-*fcc* PO could be immobilized by its strong sorption to goethite or, conversely, it could be transported if associated with goethite colloids [19, 20], as observed at the Mayak Site [28].

The formation of this non-*fcc* PO phase could have potentially significant implications for colloid-facilitated transport of Pu, though there is little knowledge of molecular-level mechanisms leading to the formation of non-*fcc* PO on goethite. This study seeks to investigate and determine what molecular-level mechanisms lead to the formation of the non-*fcc* PO phase and its subsequent stabilization upon formation of a heterointerface with goethite. To accomplish

this, a series of computational models are applied. First, the mechanisms involved in the formation non-*fcc* PO phases are investigated. Bulk lattice-distorted[1] (LD) PuO_2 and PuO_{2-x} phases are modelled using *ab initio* methods. Through analysis of the structure, energetics, and chemical properties of these bulk non-*fcc* PO phases, the viability of non-*fcc* PO phases forming in the absence of goethite can be determined. Empirical models using simple interfaces are also utilized to highlight mechanisms involved in heteropitaxial growth, in particularly showing the potentials effects of lattice mismatch[2] (LM) on the sorption and "growth" of the non-*fcc* PO nanophases on goethite surfaces. The remainder of the study then specifically probes the influence of goethite in the stabilization of a non-*fcc* PO. PuO_2- and PuO_{2-x} -goethite interfaces are modelled after experimental observations (Figure 2-1), and *ab initio* methods are used to analyze the structure, energetics and chemical properties of PO– goethite interfaces. The results from these computational models help explain how non-*fcc* PO nanophases form and/or are stabilized on the goethite surface. In short, the lattice of *fcc* PuO_2 is postulated to strain upon sorption to goethite, leading to the formation of a non-*fcc* PO phase. The formation of LD PO surfaces can be then stabilized upon the chemisorption and formation PuO2 or PuO_{2-x} –goethite interfaces.

2.3 Methods

2.3.1 Mechanisms leading to the formation of non-*fcc* POs

The experimental conditions under which *bcc* Pu_4O_7 is formed are poorly understood. For instance, the *bcc* Pu_4O_7 phase (PDF #41-117) has not been observed been observed prior to these experiments [19, 20]; it is a theoretical phase derived from isomorphs of lanthanides and other actinide oxide phases (Am, Cm) [29]. Thus, the structure, energetics, and chemistries of LD PuO_2 and bulk PuO_{2-x} phases are analyzed using *ab initio* methods to determine the viability for Pu_4O_7 and/or non-*fcc* PO phases to form in the absence of goethite. These analyses also provide a better indication for how influential the goethite surface is in the formation of the non-*fcc* PO phase observed experimentally.

[1] LD = lattice distorted
[2] LM = lattice mismatch

2.3.1.1 Bulk LD PuO_2 and PuO_{2-x} phases

The formation of bulk non-*fcc* PO phases is monitored in two parts, through the formation of LD PuO_2 phases and then through the formation of a number of different PuO_{2-x} phases. This study hypothesizes that the lattice of *fcc* PuO_2 is distorted upon sorption to goethite, in turn leading to the experimentally observed *d*-spacings. This hypothesis is motivated by the fact that the *bcc* Pu_4O_7 phase is deduced from *d*-spacings measured from SAED patterns (Figure 2-1) [20]. It is well-known that the *d*-spacings for cubic systems are directly proportional to the lattice parameter *a*. Thus, one way *d*-spacings for cubic crystal would change is simply by modifying *a*. By constructing and analyzing LD PuO_2 structures it can be determined whether the distortion of the *fcc* PuO_2 lattice could lead to the formation of the non-*fcc* PO phase found experimentally.

LD PO phases are constructed by distorting bulk *fcc* PuO_2 that has been geometry optimized (phase #1; *Fm3m*; PDF # 06-0360) (Table 2-1, Figure 2-2). The LD PuO_2 model (phase #3) is constructed by expanding the *fcc* PuO_2 lattice by 2.7% to match ½ *a* of *bcc* Pu_2O_3 (phase #6) (Table 2-1); *a* increases from 5.40 Å to 5.54 Å. This amount of lattice expansion would reproduce experimentally observed *d*-spacings while maintaining the *fcc* PuO_2 structure.

Given that the non-*fcc* PO phase is only found when sorbed to goethite, it is reasonable to assume that the underlying bulk goethite substrate, with a more rigid framework, would cause the lattice of the nanoparticulate Pu adsorbates to strain and distort upon sorption to the goethite surface. Thus, another LD PuO_2 structure was created where the lattice parameters of *fcc* PuO_2 were modified and distorted to those of goethite. To construct this LD PuO_2 phase, the lattice vectors of *fcc* PuO_2 had to be redefined to match those of goethite. That is, the HRTEM images from Powell, *et al.* (2011) [19] (Figure 2-1a) show the non-*fcc* PO is heteroepitaxially grown on goethite when the PO (110) surface overlies the goethite (001) surface. This alignment suggests that the lattice of the PO (110) surface are straining to match the lattice of the goethite (001) surface. Thus, the lattice vectors for *fcc* PuO_2 were redefined: $[1\bar{1}1]_{PuO2} \parallel [100]_{goe}$, $[1\bar{1}\bar{2}]_{PuO2} \parallel [010]_{goe}$, and $[110]_{PuO2} \parallel [001]_{goe}$ (Figure 2-2b). In this case (pre-LD phase #3), PuO_2 maintains its *fcc* structure but simply with lattice parameters that match those of the goethite unit cell. Redefining the lattice vectors for PuO_2 also eases the layering and alignment of PO-goethite interfaces, discussed shortly.

The *a* and *b* parameters of the lattice-redefined bulk PuO_2 were then distorted to match those of goethite (phase #3). To do this, *a* was expanded by 6.4% and *b* was compressed by 8.7%; *a* increases from 9.44 Å to 10.08 Å while *b* decreases from 6.67 Å to 6.14 Å. The *c* lattice parameter and fractional coordinates were held fixed. The lattice was also distorted such that interplanar distances within PuO_2 matched those of goethite; ***i.e.,*** the PuO_2 lattice was distorted such that Pu-Pu distances along the $[100]_{goe}$ matched Fe-Fe distances of bulk goethite. However, up to 25% distortion of the PuO_2 lattice was needed to match the interplanar distances. This large amount of lattice distortion changed the PuO_2 structure considerably, suggesting this amount of distortion would not lead to a stable PuO_2 crystal. Thus this study focuses on the LM with respect to the unit cell parameters.

Following the analyses for the LD PuO_2 phases, the formation bulk PuO_{2-x} phases was investigated. These models are motivated by experiments postulating the nanophase sorbed to goethite is *bcc* Pu_4O_7 (again, based off of measured *d*-spacings) [19, 20]. Thus, it is important to determine the viability for a *bcc* Pu_4O_7 phase to form in the absence of goethite. Because little is knowledge on the formation of PuO_{2-x} phases is available, several different bulk PuO_{2-x} structures were also constructed to determine the viability of PuO_{2-x} phases forming at ambient conditions (Table 2-1, Figure 2-2).

A simple Pu_4O_7 structure (phase #5) is first constructed by removing 1 O atom from the *fcc* PuO_2 cell, similar to the approach used by Petit, *et al.* (2003) [30]. The *bcc* Pu_4O_7 ($Ia\bar{3}$) phase referenced by Powell et al. (2011) was constructed from a *bcc* Pu_2O_3 bixbyite structure (phase #6; $Ia\bar{3}$; PDF # 109363). O atoms were added to the fractional coordinates [0.25 0.25 0.25] of the bulk Pu_2O_3 crystal to yield a stoichiometry of Pu_4O_7 while also maintaining the $Ia\bar{3}$ symmetry (phase #6).

To test if the O vacancies in other locations would yield more energetically favorable PuO_{2-x} phases, O atoms were added to two symmetric faces and interstitial spaces of the primitive *bcc* Pu_2O_3 bixbyite structure (phase #10). The $Ia\bar{3}$ symmetry could not be preserved this way, and the structure adopted a *P1,* triclinic structure.

Bulk PuO_{2-x} phases are composed of mixed-valence states; Pu_4O_7 could be of mixed valence including combinations such as 2 Pu^{4+} (spin = ± 4) and 2 Pu^{3+} (spin = ± 5). Thus,

different spin and charge configurations for the *bcc* Pu_4O_7 were also evaluated to determine which Pu valence states produce the most thermodynamically favorable phase (phases #6 - #8) and how chemically different the PuO_{2-x} phases are from PuO_2 phases.

The V_4O_7 phase (PDF # 2211) was also evaluated as an alternative structure for Pu_4O_7, where the V atoms were replaced by Pu atoms, to determine whether non-cubic phases would be energetically favorable.

The structure, energetics, and chemistry were analyzed for all the phases. Powder diffraction patterns for the simulated bulk LD PuO_2 and/or PuO_{2-x} phases were obtained to observe whether their dominant *d*-spacings correlate to those observed experimentally.

Formation energies for the LD PuO_2 and PuO_{2-x} phases were calculated to determine the amount of energy that would be needed to structurally and/or chemically transform PuO_2 into a non-*fcc* PO phase, using equation 1b:

$$Pu_4O_8 \rightarrow Pu_4O_y + N_O \cdot \tfrac{1}{2}\, O_2 \qquad \text{(Eqn. 1a)}$$

$$E_{rxn} = g_{Pu_4O_y} + N_O\mu_O - g_{Pu_4O_8} \qquad \text{(Eqn. 1b)}$$

where $g_{Pu_4O_y}$ is the computationally-derived energetics for the bulk LD PuO_2 or PuO_{2-x} phases tested in this study, $g_{Pu_4O_8}$ is the computationally-derived energetics for the bulk *fcc* PuO_2 phase, μ_O is the chemical potential of oxygen, and N_O is the number of O atoms.

The minimum and maximum μ_O limits (-540.5 kJ/mol and 0 kJ/mol, respectively) were determined (Eqn. 2 and 3):

$$\min \mu_o(T = 0, p = 0) = \frac{1}{2}(g_{PuO_2} - g_{Pu,metal}) \qquad \text{(Eqn. 2)}$$

$$\max\ \mu_O(0,0)_o = \frac{1}{2}(E_{O_2} + E_{correction} + \mu_{expt}(T = 298K, p = 1atm)) \qquad \text{(Eqn. 3)}$$

It is important to note that boundaries for the oxygen-poor and oxygen-rich conditions are theoretically well-defined limits, but represent only an estimate of the truly accessible range of the oxygen chemical potential; *i.e.,* the accessible range is temperature and pressure dependent [31]. To improve the energetics for max μ_O a couple corrections were applied. To correct for over-binding of the O_2 gas molecule that is often encountered in DFT-GGA calculations, 150.54 kJ/mol O_2 was added to max μ_O ($E_{correction}$) [32]. Additionally, to account for the gain in entropy upon formation of a PuO_{2-x} phase, the experimental entropy at 298 K ($T\Delta S$ = 61.09 kJ/mol O_2; representing the ambient conditions the experiments were performed at) was added to max μ_O.

For these calculations, *ab initio* density functional theory (DFT) was applied with the GGA-PBE functional with spin-polarization in the CASTEP module [33] (part of the MaterialsStudio6.1 software suite). Bulk PuO_{2-x} phases were geometry optimized using ultrasoft pseudopotentials to describe the H, Fe, Pu, and O atoms, a k-point set size of 8×8×8, and a planewave energy cutoff of 500 eV. For geometry optimizations of the bulk phases, structures with high symmetry and/or large structures (*e.g.,* the bixbyite stoichiometry is $Pu_{32}O_{48}$ as a conventional cell) were geometry optimized as primitive cells for efficiency. All atoms were allowed to relax and the lattice parameters were relaxed. The Bader charges and spins were compared between the different phases to observe changes in Pu oxidation states. Diffraction patterns were obtained using the wavelength of a (theoretical) Cu K-α x-ray source with the Powder Diffraction-Reflex module in the MaterialsStudio software suite.

2.3.1.2 Effect of lattice mismatch on the formation of heterointerfaces

Experimental studies attribute the formation of a bulk *bcc* Pu_4O_7 phase due to the alignment and heteroepitaxial growth of the PO on the goethite surface. Modelling the step-by-step growth of an Pu oxide phase on the goethite surface is difficult, in particular because there is a lack of data and knowledge on the alignments that favor epitaxial growth. To this extent, it is most efficient to use a simple, cubic interface between a KCl adsorbate and a NaCl substrate to gain a general understanding of processes associated with heteroepitaxial growth and/or heterointerface formation. In particular, the effect of LM (*i.e.,* differences between the lattice parameters of different substrates) [34] on the sorption and "growth" of nanocolloid adsorbates

on substrate surfaces is studied using an interface between simple cubic salts. For these models, LM is calculated as:

$$\frac{(a_{\prime KCl\prime} - a_{NaCl})}{a_{NaCl}} \times 100 = Lattice\ mismatch\ (\%) \qquad \text{(Eqn. 4)}$$

A halite (NaCl) cluster that is 12×12×1 unit cells is used as a substrate that 'KCl' clusters adsorb to. The 'KCl' clusters represent a KCl crystal whose crystalline lattice parameters were expanded from 5 to 25% to simulate the effect of LM on the stability of nanocolloids on substrate surfaces. Additionally, to simulate the growth of the 'KCl' clusters the size of the 'KCl' cluster was varied (from 1×1×1 to 12×12×1) for each LM value. 'KCl' clusters were placed on top of the NaCl substrate such that the clusters were attracted to one another; *i.e.,* Cl atoms of the 'KCl' cluster were placed on top of Na atoms of the NaCl cluster; the stacking sequence for the ions in the NaCl structure is essentially continued through the 'KCl' cluster. An example of the NaCl-'KCl' interface constructed is provided within the Supplementary information.

At each lattice distortion of the 'KCl' at cluster size, the adsorption energies were quantified for each 'KCl'-NaCl interface (Eqn. 5):

$$E_{adsorption} = E_{interface} - E_{KCl\ cluster} - E_{NaCl} \qquad \text{(Eqn. 5)}$$

An asymmetric, second-order polynomial was fit to the isotherm data to determine at what size the adsorption energy is most favorable, and thus provide an estimate as to how large the nanocolloid, as a function of percentage of LM, will grow based on thermodynamics. Thus, by quantifying the adsorption energies with respect to the growing 'KCl' clusters the influence of LM on the size of the nanocolloids sorbed to a substrate surface could be rationalized.

The simulations were conducted using empirical force-field methods in Cerius[2]. Formal charges of +1 for the K and Na atoms were assigned while a formal charge of -1 was assigned to

the Cl atoms; the Universal1.02 forcefield were used as an initial potential set but repulsive parameters were subsequently adapted to the varying lattice constants of the 'KCl' models. Single point energies of the 'KCl' and NaCl clusters by themselves as well as the energy of the interface were calculated to obtain the adsorption energies.

2.3.2 PO-goethite interfaces

The calculations conducted above provide information on the primary mechanisms involved in the formation of a non-*fcc* PO phase in the absence of goethite. To more specifically probe the influence of goethite in the stabilization of a non-*fcc* PO, the interfacial environments between PO phases and goethite are investigated. As mentioned, the goethite (001) surface was proposed to facilitate the heteroepitaxial growth of the non-*fcc* PO phase [19, 20]; HRTEM imaging and a SAED with FFT analysis showed the PO (110) surface was structurally aligned with the goethite (001) surface (Figure 2-1a) [19]. While the heteroepitaxial growth of an Pu oxide phase on the goethite surface is difficult to model due to a lack of knowledge and information on these heterointerfaces, the interfacial alignment between PO (110) surfaces and goethite (001) surfaces (provided by Figure 2-1) are modelled as a starting point to observing the structure, energetics, and chemistry within the interfacial environment.

2.2.1. PO and goethite surfaces

Prior to constructing the PO (110) – goethite (001) interfaces, the structures, energetics, and chemistries of PuO_2 (110), PuO_{2-x} (110), and goethite (001) surfaces are analyzed in order to identify changes in the slab that occur after interface formation.

A goethite (001) surface ($Fe_8O_{16}H_8$) was cleaved from a geometry optimized bulk goethite crystal (*Pnma*). While the surface terminations at the goethite (001) surface can complex and/or undergo hydration [35, 36], a charge-neutral, dipole-free termination was chosen. This termination preserves the symmetry of the bulk goethite (important in the analyses of ED patterns that will be described shortly) and better enables the PO slab to chemisorb onto the goethite surface for interface formation as reactive Fe and O atoms as well as OH ligands are exposed at the surface. The variability of surfaces and/or surface terminations and their respective heteroepitaxial growth mechanisms will be revisited in the Conclusions.

The PuO_2 (110) surfaces were cleaved from bulk *fcc* PuO_2 (pre-LD phase #3) and LD PuO_2 structures (phase #3). The structures of the surfaces show that along the [110] direction the PuO_2 crystals consist of a stacking sequence of planes, -PuO_2-PuO_2-PuO_2-, and are three formula units thick (Pu_9O_{18}). This stacking sequence results in each PuO_2 plane being "charge neutral," and so the (110) orientation is nonpolar (*i.e.*, each such PuO_2 does not have a dipole moment perpendicular to the layer) [37] [38]. The LM for the PuO_2 (110) surfaces is compared to goethite, similar to what was done using Equation 4 (Table 2-2).

Two different, hypostoichiometric PuO_{2-x} surfaces (Pu_9O_{16}) were modelled to determine the viability for PuO_{2-x} to form as a thin-film in the absence and presence of goethite. The motivation for modelling these PuO_{2-x} surfaces was due to the observance of Pu-O bond breakage for the geometry-optimized PuO_2-goethite interface (as will be discussed later). These results, which are presented later, suggested that it was possible for O to be removed from the PuO_2 slab upon formation of an interface with goethite. Thus, the O-atoms of the PuO_2 slab that become most-negative (*i.e.,* most oxidized) upon formation of the PuO_2-goethite interface were used to guide the construction of the PuO_{2-x} surfaces here (see Figure 2-8d). For the first PuO_{2-x} (110) surface ($PuO_{2-x,\ 1S}$), one O-atom was removed from both the surfaces of the PuO_2 slabs (Figure 2-8d; O atoms removed with respect to the PuO_2-goethite interface are colored pink). For the second PuO_{2-x} surface ($PuO_{2-x,\ 2S}$), two O-atoms were removed from only one surface of the PuO_2 slabs (Figure 2-8d; O atoms removed with respect to the PuO_2-goethite interface are colored purple). Thus, the PuO_{2-x} surfaces differ from one another based on the location of the O vacancies, and can provide insight into how the location of the O vacancies affects the energetics of PuO_{2-x} thin films. The lattices of these surfaces were geometry optimized (holding the angles fixed at 90º) and were also distorted to match that of goethite.

The formation energies of the LD PuO_2, $PuO_{2-x,}$ and LD PuO_{2-x} surfaces are calculated relative to the PuO_2 surface, similar to that done for the bulk PuO_2 and PuO_{2-x} phases using Equation 1b. The surface formation energies are compared to the formation energies for the bulk LD PuO_2 and PuO_{2-x} phases to observe whether distortion and/or hypostoichiometry is more easily achieved (in terms of energetics and chemical potential) in thin-films over bulk phases.

To understand the surface stabilities and reactivities relative to one another, the surface energies, σ, are calculated:

$$\sigma_{(001)\ goethite\ surface,Fe_{16}O_{32}H_{16}} = \frac{G_{slab,Fe_{16}O_{32}H_{16}} - 4\ (g_{bulk,Fe_4O_8H_4})}{2A} \qquad \text{(Eqn. 6)}$$

$$\sigma_{PO\ surface,Pu_9O_y} = \frac{G_{slab,Pu_9O_y} + \mathrm{N}_O\mu_O - 9\ (g_{bulk,\mathrm{PuO2}})}{2A} \qquad \text{(Eqn. 7)}$$

where G is the energy of the slabs, N is the number of formula units, μ_O is the chemical potential of an O atom [31], g is the energy of the bulk phases (with the same stoichiometry as the surfaces), and A is the surface area of the unit cell [39, 40].

As was done for the bulk PuO_{2-x} phases, DFT was applied with the GGA-PBE functional with spin polarization. All atoms were allowed to relax for the *ab initio* calculations using CASTEP (part of the MaterialsStudio6.1 software suite). The periodic slabs were separated by 12 Å of vacuum to avoid interaction between neighboring slabs. The surfaces were optimized using a k-point set size 2×3×1. The lattice parameters for the goethite and LD PO surfaces were held fixed during geometry optimization to maintain consistent unit cells. Bader charges and spins of the Fe and Pu cations for the goethite, PuO_2, and PuO_{2-x} surfaces were analyzed to observe whether lattice distortion influences the chemistry surfaces.

2.3.2.1 Pu-goethite interfaces

Heterointerfaces between PO and goethite were constructed using the goethite (001) surface and the LD PuO_2 or LD PuO_{2-x} surfaces mentioned above. Both PuO_2-goethite (Pu_9O_{18}-$Fe_8O_{16}H_8$) and PuO_{2-x} -goethite interfaces (Pu_9O_{16}-$Fe_8O_{16}H_8$) are investigated to observe one PO phase is more stable upon interface formation. Interfaces using LD $PuO_{2-x,1S}$ surface are analyzed in detail within the main text (as this is shown to be more thermodynamically favorable), while analysis for the interface using the LD $PuO_{2-x,2S}$ surface is provided in the Supplementary information. The LM between the goethite and PO phases requires that the PO slabs must be strained/LD to match the unit cell dimensions for the goethite (001) surface in order to construct 3D, periodic interfaces. In practice, these models are simulating regions in between dislocations.

The interfacial models can be taken to represent the sorption of a pre-formed LD PO nanocolloid on the goethite surface.

As mentioned in the construction of the LD PuO_2 phase #3, the lattice vectors have been redefined according to the experimentally observed alignment between Miller planes of the PO and goethite phases (Figure 2-8a). Thus, the lattices of the LD PO (110) surfaces are the same as that of the goethite (001) surface, and so the LD PO surfaces are essentially stacked on top of the goethite surface to build an interface. Only one interface was constructed to reduce computational effort (*i.e.,* the Pu slab was only overlain on one surface of the goethite, not on both surfaces). Additionally, both slabs are dipole-free, thus net charges or dipole moments of the individual surfaces are not an energetic contribution to be concerned with.

While experiments provide the general alignment of the Miller planes and lattice vectors, the alignment of ions at the structurally and chemically different goethite and PO the surfaces must be determined. Unlike the simple cubic interface described earlier, where Cl atoms of the 'KCl' cluster align with Na atoms of the NaCl cluster and generally preserve the *fcc* stacking sequence, it is difficult to identify the stacking sequence of the interfacial atoms between the PO and complex goethite surface (with Fe and O atoms as well as OH ligands exposed). Single-point energies calculations for the PO slab in different positions on top of the goethite slab were conducted to find the most thermodynamically favorable position for the PO slab to sit on top of the goethite slab. This position was found to be where the O atoms of the PO slab almost directly overlaid the Fe atoms at the goethite surface while the Pu atoms were located above the empty channels of the goethite structure in the [010] direction.

As done with the surfaces, the structures, energetics, and chemical nature of the interfaces were analyzed. To determine whether the structures and alignment of the interfaces matches that found experimentally, theoretical electron diffraction (ED) patterns for the goethite and LD PuO_2/ PuO_{2-x} phases were simulated. The Single-Crystal Diffraction module in Cerius[2] was used, where the energy of the (theoretical) electron beam was set to 200 keV and the zone axis was specified as needed.

The stability of the interface with respect to bulk PO phases is determined by calculating the interfacial energies (IE) of the PuO_2 – and PuO_{2-x} -goethite interfaces:

$$\gamma_{\text{goethite}-\text{PO interface}} = \frac{E_{\text{interface}} + N_O \mu_O - 9\,(g_{bulk,PuO2}) - 4\,(g_{bulk,Fe_4O_8H_4})}{A} - \sigma_{PO\ surface} - \sigma_{goethite\ surface} \quad \text{(Eqn. 8)}$$

where $E_{interface}$ is the energy between the goethite-PO system, σ are surface energies for the Pu and goethite slabs exposed in vacuum, and A is the surface area of the unit cell (u = 10.080 Å, v =6.139 Å; A= 61.879 Å^2) [41, 42].

The stability of the interface with respect to the surfaces is also calculated as the work of adhesion (W_{ad}). This is the amount of energy needed to separate an interface into two free surfaces, which can show whether the formation of the heterointerface can stabilize the LD PO phases:

$$W_{ad} = \sigma_{goethite\ surface} + \sigma_{PO\ surface} - \gamma_{goethite-PO\ interface} \quad \text{(Eqn. 9)}$$

Ab initio methods are similar to those used for calculations on the goethite and PO surface. All atoms were allowed to relax. The u and v parameters of the interface unit cell were held fixed to mimic the underlying bulk goethite structure; it also follows the logic that the underlying bulk goethite would serve as a substrate for the PO phase to sorb/grow on. Bader charges and spins of the Fe and Pu cations for the goethite, PuO_2, and PuO_{2-x} surfaces and interfaces were analyzed and compared to those observed for the separate surfaces to observe whether the formation of an interface influences the oxidation states of the cations and whether charge transfer is occurs through the formation of an interface. Visualization of the charge density difference was done using the VESTA v.3.2.1 software [43].

2.4 Results and Discussion

2.4.1 Mechanisms leading to the formation of non-*fcc* POs

2.4.1.1 Relative thermodynamic stabilities of LD PuO_2 and PuO_{2-x} phases

The structures and energetics for the bulk PuO_2 and PuO_{2-x} phases are evaluated to determine the viability for a *bcc* Pu_4O_7 phase to form in the absence of goethite. First, because the experimental observations of a *bcc* Pu_4O_7 are based off of measured *d*-spacings [19, 20], the lattice of *fcc* PuO_2 is distorted to determine the energetics associated with changing the lattice parameters and interplanar spacings, but without changing chemical properties such as the bulk stoichiometry. Uniform expansion of the *fcc* PuO_2 lattice by 2.7% (phase #2), to match $a \times ½$ of *bcc* Pu_2O_3, requires 5.84 kJ/mol Pu_4O_8 (Table 2-1). This amount of lattice distortion is capable of reproducing the dominant *d*-spacing observed experimentally (3.18 Å) though other *d*-spacings are not reproduced (2.95 Å) [19, 20] (Figure 2-5). Thus, this amount of lattice distortion does not quite match the non-*fcc* PO phase found experimentally. There is little change in the Pu-O atomic structure; e.g., the Pu-O bond distances only increase less than 0.06 Å though this does not incur bond breakage. The chemical properties of PuO_2 are also unaffected by lattice distortion. Pu(IV) cations of the monovalent PuO_2 phase observe Bader spins of 4.6 while after lattice expansion the spins of Pu cations only slightly increase to ~4.7 (Figure 2-4); the valence of the Pu atoms remains as Pu(IV) after lattice distortion.

Given that the non-*fcc* PO observed experimentally is found only when sorbed to goethite, the lattice parameters of the *fcc* PuO_2 lattice parameters were also distorted, non-uniformly, to match the goethite lattice parameters (phase #3). In this case, the *fcc* PuO_2 lattice undergoes non-uniform distortion; *a* is expanded by 6.4% and *b* is compressed by 8.7% in order to match the goethite lattice parameters (Table 2-1). This amount of lattice distortion is more endothermic than phase #2 above, requiring 88 kJ/mol Pu_4O_8. Small changes in the atomic structure of the PO phase contribute to the higher distortion energy. Some Pu-O bond lengths increase by up to 0.40 Å and are broken, in accordance with reduced electrostatic attraction between Pu and O atoms [44]. The Pu cation valences are do not change considerably with respect to *fcc* PuO_2, again showing that the chemical properties of the PO phase are not affected by distortion of the PuO_2 lattice in the absence of goethite. Based on the changes in atomic structure, such as the non-equidistant Pu-O distances, the structure of the distorted PO slab does

not reflect that of a bulk, *fcc* PuO_2 phase. More interestingly, this amount of distortion is capable of reproducing several experimentally observed *d*-spacings, including those at 2.95 Å, 2.76 Å, and 2.62 Å (Figure 2-5). Thus, with low energetic inputs the goethite substrate can induce changes to the PuO_2 structure/lattice, making the LD PuO_2 structure comparable to the structure of the non-*fcc* PO observed experimentally.

Distortion of the *fcc* PuO_2 can lead to the formation of PuO_{2-x} phases. That is, the expansion of the lattice parameters can occur from the removal O and vice versa, leading to the formation of PuO_{2-x} phases. For instance, in the simplest Pu_4O_7 model (phase #4), O removal from the *fcc* PuO_2 structure is accompanied by an increase in the lattice parameter from 5.40 Å to 5.50 Å. The lattice expansion is caused by an increased degree of *f*-electron localization, where bonding O *p*-electrons are removed and replaced with nonbonding, localized Pu *f*-electrons [30].

The removal of O and transformation of PuO_2 to PuO_{2-x} also leads to changes in the chemical properties, such as the stoichiometry and Pu valence state. An increase in the total spin density from PuO_2 to PuO_{2-x} is observed, where O^{2-} donates its electrons and chemically reduces Pu cations within the vicinity. This is confirmed through analyses of the Pu Bader spins for phase #4. The Pu(IV) cations of the monovalent PuO_2 phase observe Bader spins of 4.6 while the Pu(III) cations of the monovalent Pu_2O_3 phase observe spins of 5.1 – 5.2; the Pu cations within Pu_4O_7 (phase #6), for instance, observe absolute Bader spins of 4.9, showing the phase is some sort of intermediate with characteristics of Pu^{3+} and Pu^{4+} ions. Thus, the PuO_2 phase is both structurally and chemically modified upon formation of a PuO_{2-x} phase.

The combination of changes in the structure and chemistry in the formation of PuO_{2-x} phases lead to high energetics. At O-rich conditions, the formation of all the PuO_{2-x} phases tested in this study is endothermic with respect to *fcc* PuO_2 (Table 2-1, Figure 2-3). The triclinic *P1* Pu_4O_7 structure (phase #9) is the most energetically favorable PuO_{2-x} phase (which is likely due to the fewer constraints on the systems) though its formation would require a large energetic input of 317 kJ/mol Pu_4O_y at O-rich conditions. The formation of the experimentally postulated bulk *bcc* Pu_4O_7 phases is also highly endothermic. The most energetically favorable *bcc* Pu_4O_7 structure (Phase #7) would require 465 kJ/mol Pu_4O_y at O-rich conditions to form. The formation of bulk PuO_{2-x} phases is influenced by the O-conditions. For instance, the formation of phase #7 is exothermic with respect to *fcc* PuO_2 at O-depleted conditions (-75 kJ/mol Pu_4O_y at min μ_O),

although O-depleted conditions would not be expected to be found at the ambient conditions under which the experiments were conducted. Thus, the formation of a bulk PuO_{2-x} phase would requires higher energetic inputs at ambient/O-rich conditions.

As mentioned, the experimentally sorbed PO nanocolloid phase is identified as *bcc* Pu_4O_7 based on measured *d*-spacings from HRTEM images [19, 20]. Thus, diffraction patterns from the theoretically modelled PuO_2 and PuO_{2-x} phases were simulated to determine whether the structures generated in this study match the structure of the PO phase identified experimentally. Analyses of the diffraction patterns for the LD PuO_2 and PuO_{2-x} phases show the difficulty in confirming the identity of the PO phase through analyses of *d*-spacings alone (Figure 2-5). The experiments deduced the formation of a *bcc* Pu_4O_7 structure based on *d*-spacings , such as 2.95 Å, unique to the *bcc* structure. However, it can be seen that *d*-spacings for the *bcc* phase can be reproduced through a number of different phases, including the LD PuO_2 structures. Thus, if using *d*-spacings alone, the sorbed PO phase has the potential to be a number of LD PuO_2 or PuO_{2-x} phases, and the existence of *bcc* Pu_4O_7 cannot be confirmed.

3.1.2. Effect of lattice mismatch on the formation of heterointerfaces

The simple, cubic interfaces modelled provide considerable insight into the interconnection between LM, particle diameter, and adsorption energy, and are able to explain the stronger sorption affinities observed between the PO adsorbate and goethite surface. The maximum size of a distorted PO adsorbate is estimated through calculating the adsorption energies for a 'KCl' adsorbate on a NaCl cluster (at varying LM values). For instance, the adsorption energy for a 'KCl' adsorbate, with 10% LM to the NaCl substrate, is most exothermic when the KCl adsorbate is ~2.7 nm long (Figure 2-6a). The adsorption of particles > 2.7 nm with 10% LM would be more endothermic; e.g., adsorption of a ~3.4 nm 'KCl' adsorbate onto NaCl is ~70 kJ/mol less favorable than the sorption of a ~2.7 nm 'KCl' particle. The adsorption energy would also decrease between interfaces with increasing LM (Figure 2-6b).

The diameter of the "KCl' adsorbate is also found to decrease with increasing lattice distortion (Figure 2-6c). For instance, for a LM of 10% the adsorbate can have an estimated particle diameter of ~ 2 nm while at 25% LM the particle diameter would be estimated to be ~1 nm. The observation of smaller particle sizes with increasing LM is in agreement with

experimental results observations for Pu sorption onto goethite, as the non-*fcc* PO nanocolloids are restricted to 2 – 5 nm in size [19, 20]. These models would suggest that fairly low LM between the PO and goethite (< 15% LM if using the NaCl-KCl system as an analogy) would lead to the formation of particles within 2 – 5 nm. These lattice distortion values are in agreement with the models in this study where the Pu slabs are distorted by ≤ 10% to match the goethite lattice parameters.

These data are relevant to experimental observations for the weak sorption of aggregated PuO_2 nanocolloids on the goethite surface. Through the aggregation of the 2 – 5 nm PuO_2 nanoparticles, the *fcc* structure is preserved, as shown by experimental results [19, 20]. The sorbed aggregates of *fcc* PuO_2 postulated in this study have a high LM with the goethite (001) surface of up to 10%. The high LM of the *fcc* PuO_2 aggregates translate to a lower adsorption energy; adsorbates with 10% mismatch are 460 kJ/mol less favorable than those with 5% LM, for instance. Thus, distorting the lattice of an *fcc* PuO_2 adsorbate upon sorption to goethite would lead to more favorable adsorption energies, potentially explaining the stronger sorption affinity of the LD Pu nanocolloids onto the goethite surface.

2.4.1.2 Summary of mechanisms involved in the formation of non-fcc POs

From the study of bulk LD PuO_2 and PuO_{2-x} phases as well as the study of simple interfaces, mechanisms leading to the formation of a non-*fcc* PO phase can be proposed. The observance of non-*fcc* PO phases under experimental conditions is most likely to be due to the distortion of the *fcc* PuO_2 lattice. The distorted phases are generally capable of reproducing the experimentally measured *d*-spacings that are unique to *bcc* Pu_4O_7. More so, lattice distortion can occur at ambient conditions with low energetic inputs. For instance, if the PuO_2 lattice were to be strained and non-uniformly distorted to match that of the goethite substrate upon sorption, it would require 88 kJ/mol Pu_4O_8.

It is possible that lattice expansion can occur from or cause the removal of O, in turn leading to the formation of a hypostoichiometric PuO_{2-x} phase. However, for PuO_2 to transition to a PuO_{2-x} phase would require more O-poor conditions and/or high energetic inputs. For instance, the formation of the *bcc*, $Ia\bar{3}$ Pu_4O_7 phase would require 365 kJ/mol Pu_4O_y at O-rich conditions. It is difficult to confirm experimental deductions on the formation of the rare, theoretically postulated *bcc* Pu_4O_7 phase given the high energetics that would be associated with

its formation. It is possible that the formation of oxygen vacancies in a hypostoichiometric fluorite PuO_{2-x} phase can be related to microstrains in nanoparticles similar to those caused by epitaxy [45]. This phenomenon and the stability of PuO_{2-x} thin-films are further explored through the surface and interfacial models.

The results from the simple interfacial models, using empirical methods, further support the hypothesis that the lattice of the PO adsorbate is experiencing distortion upon sorption to the goethite substrate. The simple interfaces between cubic salts show that when the lattice of a 'KCl' cluster has <15% LM with that of a NaCl cluster, the sorption of the 'KCl' onto NaCl would be exothermic (< –80 kJ/mol) and the 'KCl' cluster would be capable of "growing" to ~2 – 5 nm on the NaCl substrate. These lattice distortion values are in agreement with the models in this study where PuO_2 is distorted by ≤ 10% to match the lattice of the goethite substrate.

The sorption affinity and growth of the Pu colloid would be affected by the amount of LM between the PO particles and goethite influences. More specifically, with increasing strain on the lattice of the PO nanocolloid the diameter of the adsorbate would decrease along with its sorption affinity to goethite. Thus LM can account for the experimental observance of the 2 – 5 nm non-*fcc* PO adsorbates found strongly sorbed to the goethite [19, 20]. The *fcc* PuO_2 particles on the other hand would have higher LM with the goethite substrate and thus a lower sorption affinity with goethite. The "growth" of *fcc* PuO_2 is not dependent on sorption onto goethite; *i.e.*, 2 – 5 nm Pu colloids form from the rapid neutralization of an acidic Pu(IV) solution and aggregate into a mass of crystalline, nano-sized Pu colloids in the absence of and presence of goethite or quartz [19]. Thus, the distortion of the PO adsorbate lattice upon sorption to goethite substrate would lead to the formation of a non-*fcc* PO phase. The growth of the non-*fcc* PO would be limited by the amount of LM between the PO and goethite phases.

2.4.2 PO-goethite interfaces

2.4.2.1 Surface and interface geometries

The structures of the separate PO and goethite surface are observed prior to interface formation to distinguish between structural changes that are caused by lattice distortion *vs.* structural changes that are induced through the formation of an interface. The geometry-

optimized *fcc* PuO_2 (110) and PuO_{2-x} (110) surfaces by themselves (*i.e.,* no lattice distortion) experience some relaxation. Similar to other studies [38], the surface Pu cations exposed to the vacuum experience some relaxation into the bulk, though the slab maintains a structure similar to that of bulk *fcc* PuO_2. Similar observations are made for the geometry optimized goethite (001) surface.

Distortion of the PuO_2 surface leads to a small amount of bond breakage; a Pu-O bond at one surface of the slab was found to increase to > 2.70 Å, potentially indicating that dislocations may be generated with the expansion of the lattice parameters. Distortion of the PuO_{2-x} surface leads to some atomic rearrangement within the vicinity of the O vacancy; the Pu atoms move away from the vacancy site and are pulled closer to O atoms that they remain bonded to. Otherwise, the structures of the surfaces do not undergo considerable structural rearrangements from lattice distortion.

Upon formation of the PuO_2- and PuO_{2-x} –goethite interfaces local structural changes within the interface occur due to bonding between atoms at the interface (Figure 2-8). The under-coordinated Fe ions at the goethite surface move slightly out of plane (*i.e.,* [001] direction) to bond with the O atoms at the surface of the PuO_2 surface. For the PuO_2-goethite interface, Pu-O bonds break as the O atoms from the Pu surface are drawn to the under-coordinated Fe atoms. The $PuO_{2-x,\ 1S}$ -goethite interface also observes structural rearrangement similar to that at the PuO_2 – goethite interface (Figure 2-8e).

Electron diffraction (ED) patterns for bulk goethite and the bulk LD PuO_2 and PuO_{2-x} phases are simulated and overlain with one another (Figure 2-8a) to observe whether the PO-goethite heterointerfaces constructed in this study are to match the PO-goethite heterointerface imaged using HRTEM (Figure 2-1b) and characterized using SAED combined with FFT analysis [19] (Figure 2-1a). The ED pattern obtained from these computational models is very similar the experimental ED pattern. Thus, these modelled heterointerfaces are accurate representations of the structures observed experimentally.

Most interestingly, the *d*-spacings measured for the LD PO and goethite phases used in this study correlate well with the *d*-spacings observed experimentally. The *d*-spacings from the simulated heterointerfacial models are within < 7% of the experimentally measured *d*-spacings.

For instance, experiments measured *d*-spacings of 2.77 Å and 3.18 Å for the non-*fcc* PO phase [19, 20] (Figure 2-8a) while the computational models reproduce *d*-spacings of 2.62 Å and 2.95 - 3.35 Å, respectively. Thus, by straining the lattice of the PO phases to match that of the goethite substrate, these models are able to reproduce the non-*fcc* PO phase that was observed experimentally within reasonable error. The computational PO-goethite heterointerfaces continue to provide strong evidence that the lattice of the sorbed PO nanocolloids is being strained by the goethite substrate.

2.4.2.2 Surface energetics

The energetics to distort and/or remove O from the PuO_2 (110) surface is calculated to determine whether a hypostoichiometric PuO_{2-x} surface could exist. To distort the PuO_2 surface lattice requires 74 kJ/mol Pu_4O_8, which is close to the amount of energy needed to distort the bulk PuO_2 structure (phase #3, 88 kJ/mol). To remove two-O atoms from the PuO_2 (110) surface requires ≥ 204 kJ/mol Pu_4O_y, which is considerably lower than the formation energies for bulk PuO_{2-x} phases (≥ 317 kJ/mol Pu_4O_y). Thus, while high energetic inputs are needed to form a bulk PuO_{2-x} phase it is possible that surfaces can exhibit hypostoichiometry given the lower energetic inputs needed. Furthermore, this suggests it is possible that a PuO_{2-x} -goethite interface exists.

Calculations of the SE for the goethite, PuO_2, and PuO_{2-x} slabs show that the surfaces exhibit similar to reactivities as one another. The SE of the (110) *fcc* PuO_2 slab is 1.11 J/m^2 , and is in agreement with other experimental [37] and computational studies [38]. The $PuO_{2-x,\ 1S}$ slabs are more reactive than the PuO_2 slab at O-rich conditions; *e.g.,* the $PuO_{2-x,\ 1S}$ slab is ~0.60 J/m^2 more reactive than the PuO_2 surface, with a SE of 1.71 J/m^2. The reactivity of the goethite (001) surface is similar to those of the PO and LD PO surfaces with a SE of 1.60 J/m^2.

It is noted that the stability of the PuO_{2-x} slabs is influenced by the location of the O vacancies and μ_O. For instance, comparison between the $PuO_{2-x,\ 1S}$ and $PuO_{2-x,\ 2S}$ surfaces shows the $PuO_{2-x,\ 2S}$ surface is more reactive (SE of 2.90 J/m^2) but less energetically favorable than the $PuO_{2-x,\ 1S}$ surface at O-rich conditions; e.g., the formation of the $PuO_{2-x,\ 2S}$ surface would requires higher energetic inputs (329 kJ/mol Pu_4O_y) than to form the $PuO_{2-x,\ 1S}$ surface (Table 2-2). This implies that other hypostoichiometric PuO_{2-x} slabs, with varying arrangements of O vacancies, at different μ_O can exist that are possibly more energetically favorable than the PuO_{2-x} structures used in this study. While the exploration of the O vacancy location is beyond the scope of this

paper, the PuO_{2-x} surfaces within this study nonetheless provide insight into how hypostoichiometric PO surfaces behave relative to PuO_2.

The reactivities of the PO slabs increase following distortion of the lattice parameters. Again, distorting the lattice of the PuO_2 slab requires 74 kJ/mol Pu_4O_8; this distortion is equivalent to an increase in SE from 1.11 J/m^2 to 1.35 J/m^2. Similarly, distorting the lattice of the $PuO_{2-x\ ,1S}$ slab requires 70 kJ/mol Pu_4O_8, resulting in an increase in SE from 1.71 J/m^2 to 1.95 J/m^2. These reactive goethite, LD PuO_2, and LD PuO_{2-x} surfaces will impact the interfacial adhesion energies for the PuO_2- and PuO_{2-x} –goethite interfaces.

2.4.2.3 Work of adhesion and interfacial energetics

Calculation of W_{ad} shows that the formation of PO–goethite interfaces is favored over the existence of separate PuO_2/ PuO_{2-x} and goethite surfaces. Regardless of the oxygen conditions, energy is needed to separate the interface into the individual PO and goethite surfaces. The W_{ad} for the PuO_2 – goethite interface is calculated to be1.43 J/m^2 while the W_{ad} for $PuO_{2-x,\ 1S}$ -goethite interface is higher at 2.02 J/m^2. The higher W_{ad} observed for the $PuO_{2-x,\ 1S}$ -goethite interface shows that the PuO_{2-x} slab is more strongly bound to the goethite surface than the PuO_2 phase. This observation is in agreement with the SE calculations, as the higher reactivity of the LD $PuO_{2-x,\ 1S}$ slab compared to the LD PuO_2 slab would lead to a higher W_{ad}. More interestingly, the higher W_{ad} for the $PuO_{2-x,\ 1S}$-goethite interface shows that the interface is strengthened from the removal of O from the PuO_2 slab.

Although the $PuO_{2-x,\ 1S}$-goethite interface has the largest W_{ad} of the PO-goethite interfaces modelled, IE calculations predict that the most thermodynamically stable PO-goethite interface at ambient conditions would be the LD PuO_2-goethite interface (Figure 2-7, Table 2-3). As shown in the analysis of the bulk PuO_{2-x} phases, the IE of the PuO_{2-x} –goethite interfaces are higher and thus less energetically favorable at O-rich conditions compared to the PuO_2–goethite interface. The IE for the LD PuO_2-goethite interface is +1.07 J/m^2 while the IE for the $PuO_{2-x,\ 1S}$ –goethite interface is +1.56 J/m^2. Similar to analyses of the bulk PuO_{2-x} phases, the PuO_{2-x} -goethite interfaces would be more stable than the PuO_2–goethite interface at more O-depleted conditions; e.g., at $\mu_O < -178.0$ kJ/mol the $PuO_{2-x,\ 1S}$ -goethite interface would be more stable

than the PuO_2-goethite interface. Thus, the PuO_2-goethite interface is predicted to be the most stable PO-goethite interface at ambient conditions, as the formation of PuO_{2-x} – goethite interfaces continues to be dependent on the energetic inputs supplied to remove O and/or the existence of O-depleted conditions.

It is possible that slightly O-poor conditions can exist at the surface of the goethite and that PuO_{2-x} -goethite interfaces can exist, which could facilitate formation of a PuO_{2-x} -goethite interface. Metallic Fe forms Fe-O bonds is at μ_O = –262.5 kJ/mol (as denoted in Figure 2-7), which is near the μ_O values were PuO_{2-x} -goethite interfaces can be stabilized relative to the PuO_2-goethite interface. Thus, at surface terminations where under-coordinated Fe atoms are exposed, it is possible that hypostoichiometric PuO_{2-x} slabs can satisfy dangling bonds at these sites on the goethite surface with $\mu_O < -178.0$ kJ/mol and lead to more stable interfaces.

2.4.2.4 Chemical properties of the interfacial environment

Information on the chemical bonding environment of the PO-goethite interfaces was obtained through analysis of Bader charges and spins as well as planar-average charge density differences. Changes in the charges and spins of the Fe cations within the goethite slab and the Pu cations within the PuO_2 and PuO_{2-x} slabs were analyzed at different stages of the interface-formation process; *i.e.,* differences between charge/spin before and after interface formation provides insight as to whether the chemical nature of the PO and/or goethite slabs changes upon formation of an interface. The plane-averaged charge density difference was also analyzed to highlight differences in the chemical bonding environment between the PuO_2– and $PuO_{2-x,\ 1S}$ – goethite interfaces, which could potentially explain the energetics observed for the interface. Analyses for the $PuO_{2-x,\ 2S}$ –goethite interface are provided in the Supplementary information.

Prior to interface formation, the spin and charges of Pu are similar to the bulk PuO_2 phase at 4.7 and ~2.1 e, respectively. The Pu cations of the PuO_{2-x} slab by itself observe higher Bader spins (up to +0.48) and lower Bader charges (up to -0.17 e) relative to those for the Pu cations of the PuO_2 slab; the PuO_{2-x} slab favors Pu that is more chemically reduced, which is in agreement with the bulk PuO_2/ PuO_{2-x} calculations. When the lattice of the PuO_2 and PuO_{2-x} surfaces are distorted to match those of the goethite surface, little change in the charge and spin of the Pu

atoms is observed (Figure 2-9b). Thus the spin and charge of the PO slab is stable in the absence of goethite, regardless of whether the lattice is undistorted or distorted.

The formation of an interface leads to changes in the chemical nature of the Pu and goethite slabs. Analysis of both Bader charges/spins and difference in plane-averaged charge density both show considerable charge and spin transfer/redistribution within the PO slabs is observed upon sorption onto the goethite (001) surface. For instance, sorption of PuO_{2-x} onto goethite leads the Bader spins of the Pu cations to decrease by up to 0.25, to values that are more comparable to Pu(IV) ions (Figure 2-9b). Charge redistribution within the goethite slab is also observed. Fe atoms in the goethite surface observe a range of spin values upon formation of the interfaces, though the spins between the PuO_2 and PuO_{2-x} –goethite interfaces are similar (Figure 2-9a). The difference in plane-averaged charge density (Figure 2-10) supports the observation of charge redistribution occurring within the goethite as well as the PO slabs upon formation of an interface. The Pu-cations in the middle of the PuO_2/ PuO_{2-x} slabs generally lose charge (or gain electrons) as the atoms in the Pu-cation layer at the interface gain charge (lose electrons).

More so, the plane-averaged charge density highlights the complex chemical bonding environment for the PO-goethite interfaces. For the PuO_2– goethite interface, there is a gain in charge on the surfaces of both goethite and PuO_2 at the interface, coincident with a comparable decrease in the interface region (Figure 2-10). The goethite slab also appears to become polarized upon interface formation, as the vacuum-exposed goethite surface is more negatively charged while the goethite surface at the interface is more positively charged. The charge density difference isosurfaces show overlap between the orbitals within the interfacial region; these observations are more indicative of covalent-like bonding occurring at the interface. PuO_2 is thus capable of chemisorbing to the goethite surface, where an increase in covalency at the interface aids in stabilizing the LD PuO_2 phase.

Differences in the chemical bonding environment between the PuO_2– and PuO_{2-x} – goethite interfaces can be observed. The $PuO_{2-x,1S}$-goethite interface appears to primarily affect the goethite surface at the interface (Figure 2-10); *i.e.,* a considerable amount of positive charge accumulates on goethite interface while the charges for the rest of the goethite slab remain constant. The charge accumulation on at the goethite surface of the interface correlates to a large charge depletion in the interfacial region. Unlike the PuO_2-goethite interface, where the PuO_2

and goethite surfaces at the interface observed comparable charge accumulation, the PuO_{2-x} surface at the PuO_{2-x} -goethite interfaces acquires only a slight positive charge. There is also less orbital overlap within the interfacial region of the $PuO_{2-x,1S}$-goethite interface. These observations potentially show that bonding at the $PuO_{2-x,1S}$–goethite interface shift towards a more polar-covalent bond character. The polar-covalent-like bonding at the interface can lead to stronger sorption affinities, and is in agreement with W_{ads} for the $PuO_{2-x,\,1S}$ -goethite interface being 0.59 J/m^2 higher than that of the PuO_2–goethite interface (Table 2-3).

2.4.2.5 Summary of PO-goethite interfacial properties

Thorough analyses of the structure, energetics, and chemistry of PuO_2 and PuO_{2-x} -goethite heterointerfaces highlight complexities that can exist at the interfacial environment, such as the distortion, alignment, and/or formation of O vacancies within a PO slab upon sorption to goethite. As shown earlier in the simple interfacial models, the sorption and/or growth of the PO adsorbate on goethite shows that the lattice of the PO adsorbate would strained to accommodate the structure of the goethite substrate. To construct the PO-goethite heterointerfaces in this study, the PO lattice is strained to match that of the goethite lattice. Simulated ED patterns for the PO-goethite heterointerfaces are capable of reproduce the alignment and *d*-spacings observed experimentally. Given the structural agreements between the computationally modelled interfaces with the experimental HRTEM images, this study provides strong evidence that the lattice of sorbed PO nanocolloids is being strained by the goethite substrate and is leading to the formation of the non-*fcc* PO phase observed experimentally.

It is postulated that either or both PuO_2- and PuO_{2-x} -goethite interfaces can be form, depending on the energetic inputs available and/or chemical potential in the experimental system. At ambient conditions, the PuO_2-goethite interface is more stable than the PuO_{2-x} -goethite interfaces. At slightly O-poor conditions (μ_O < -178.0 kJ/mol), the $PuO_{2-x,\,1S}$ - goethite interface becomes more favorable relative to the PuO_2 – goethite interface. W_{ad} calculations also show that non-*fcc* PO thin-films can be stabilized through the formation of an interface with goethite, as energy is required to separate the PO and goethite surfaces. To separate the PuO_2-geothite interface would require 1.4 J/m^2 while for the $PuO_{2-x,1S}$-goethite interface it would require 2.0 J/m^2. Furthermore, the stability of the PO-goethite interface is promoted through the chemical bonding that occurs at the interface. The PuO_2 slab is capable of chemisorbing onto

goethite via covalent bonding at the interface. The bonding at the PuO_{2-x} –goethite interface observes a more polar-covalent character; these differences in bonding between the PuO_2– and PuO_{2-x} –goethite can help explain the stronger sorption affinity of the hypostoichiometric PuO_{2-x} phase onto goethite compared to PuO_2 as the W_{ad} calculations suggest.

2.5 Conclusions and implications

Combining the results from previous experiments [19, 20] and the results from the computational models in this study, the observance of non-*fcc* PuO_2 nanostructures can be explained by molecular-level mechanisms occurring at the PO-goethite heterointerface. The formation of a non-*fcc* PO phase is determined to be due to the distortion of an initially *fcc* PuO_2 lattice upon sorption to goethite substrate. Formation energies for bulk LD and bulk PuO_{2-x} phases show that the *fcc* PuO_2 lattice can be distorted to match that of goethite lattice with relatively low energetic inputs (+88 kJ/mol Pu_4O_8).

The distortion of the PO lattice by goethite can be deduced from analyses of simple heterointerfaces between cubic salts. These models show that the lattice of the PO adsorbate would distort upon sorption and/or formation of an heterointerface with goethite to lower the amount of LM at the heterointerface and increase its sorption affinity. That is, when the lattice of a 'KCl' cluster has <15% LM with that of a NaCl cluster, the sorption of the 'KCl' onto NaCl is exothermic (< –80 kJ/mol), while at higher LM the sorption energies become more endothermic. It is also found that with <15% LM, the 'KCl' cluster is capable of "growing" to ~2 – 5 nm in size on the NaCl substrate. These observations for a simple heterointerface between cubic salts are relevant to the non-*fcc* PO phase formed. Similar to the simple 'KCl'-NaCl interfaces, the lattice of *fcc* PuO_2 can distort to reach ≤ 10% LM with that of goethite, explain why its sorption affinity to goethite is higher than that of *fcc* PuO_2. Additionally, the LM at the heterointerface limits the growth of the PO adsorbate on the goethite surface, explaining the why the size of the non-*fcc* PO adsorbates are limited to 2 – 5 nm when sorbed to goethite. Combining all these results, the computational models are able to explain that the experimentally observed non-*fcc* PO phase forms by the lattice distortion of the PO adsorbate upon formation of a heterointerface with goethite.

The PO-goethite heterointerfaces modelled continue to support that the experimentally observed non-*fcc* PO adsorbate is a result of the *fcc* PuO_2 lattice being distorted to better match that of goethite. By distorting the lattice of *fcc* PuO_2 to match that of goethite, Simulated ED patterns for the LD PO-goethite heterointerfaces reproduce the alignment and *d*-spacings observed experimentally showing that the straining the lattice of the PuO_2 phase to match that of goethite reproduces the experimentally observed non-*fcc* PO nanostructures characterized. The PO-goethite heterointerfaces also provide further information of how goethite, specifically, aids in the stabilizing the non-*fcc* PO phase. Calculation of W_{ad}, for instance, shows that the formation of PO–goethite interfaces is favored over the existence of separate PuO_2/ PuO_{2-x} and goethite surfaces. The W_{ad} for the PuO_2 – goethite interface is calculated to be1.43 J/m^2 while the W_{ad} for $PuO_{2-x,\ 1S}$ -goethite interface is higher at 2.02 J/m^2. Regardless of the oxygen conditions, energy is needed to separate the interface into the individual PO and goethite surfaces. The covalent- to polar-covalent bonding at the interface, lends to the stability of the PO-goethite interfaces. Collectively, the results from previous experiments [19, 20] and these computational models support that LD PO thin-films can be stabilized upon sorption to goethite.

The computational models in this study have been able to provide considerable insight into the molecular-scale processes and energetics of PO sorption onto goethite that support and clarify experimental observations. However, it remains uncertain whether and how the non-*fcc* PO phase is epitaxially grown on the goethite surface. That is, experiments show that the non-*fcc* PO nanoparticles are sorbed extensively onto goethite surfaces [19, 20], which suggests that, while the formation of the non-*fcc* PO nanocolloids requires the presence of goethite, the sorption of PO onto specific, preferential goethite surfaces is not required. It is possible that other heterointerfaces between different PO and goethite surfaces exist, although these have yet to be observed and studied.

The variability of surfaces and/or surface terminations present under experimental conditions will influence the formation of a heterointerface. For instance, the sorption and/or growth of PO adsorbate on a hydrated goethite (001) surface and/or goethite surfaces such as (100) and (111), which are more stable and common than the (001) surface [46, 47], (Table 1 Supplementary information ;Figure 2-7) would proceed via different mechanisms and energetic inputs. The formation of PO-goethite heterointerfaces will be affected by the structures,

chemistries, and reactivities of different PO/goethite surfaces and terminations, making it difficult to predict the most favorable bonding environment(s).

While the nature of heterointerfaces between actinide adsorbates and mineral surfaces are complex and difficult to observe, it is important to understand the reactions and processes occurring at the mineral-water interface as they influence the transport of Pu. Desorption experiments postulated that the non-*fcc* PO nanophases were more strongly associated with goethite compared to PuO_2, and can also be stable for over three months [19, 20]. The computational calculations in this study also support that non-*fcc* PO phase can sorb strongly to goethite due to the reduced LM between the substrates. The non-*fcc* PO colloids that more strongly bound to minerals like goethite can have considerably different transport properties compared to *fcc* PuO_2 aggregates weakly sorbed to minerals like quartz [19, 20]. As mentioned, the non-*fcc* PO could be immobilized by its strong sorption to goethite or, conversely, it could be transported if associated with goethite colloids [19, 20]. Thus, to account for the transport of dispersed, LD PO nanocolloids sorbed to minerals such as goethite, further information on interfacial bonding environments between actinide adsorbates and mineral surfaces is needed.

Furthermore, through understanding of molecular-scale mechanisms influencing the formation of non-*fcc* PO thin films on substrate surfaces, it is postulated that this phenomena can possibly pertain to other *fcc* actinide phases. That is, other *fcc* AnO_2 phases may also experience lattice distortion upon sorption onto minerals such as goethite. Thus, it would be interesting to extend these studies to include other *fcc* AnO_2 phases. If similar phenomena are observed, then the transport of these AnO_2 phases would also be dependent on its host minerals. This would provide even more motivation to develop models that incorporate microscopic and molecular-scale processes that more accurately represent and predict the transport of radionuclides.

2.6 Acknowledgements

This material is based upon work supported by the U.S. Department of Energy Office of Science, Office of Biological and Environmental Research, Subsurface Biogeochemical Research program under Award Number DE-SC0004883. Computational results obtained using software programs from Accelrys Software Inc. as well as Cerius^2. The *ab initio* calculations were performed using the CASTEP program, and graphical displays generated with Materials

Studio 6.1v2. The electron diffraction patterns and cluster calculations using empirical methods was done using Cerius[2]. We would also like to thank Dr. Donald Siegel at the University of Michigan, for his guidance on the construction and analysis of the interfaces, and Dr. Cameron Tracy at Stanford University, for his helpful discussions on the structures of actinide oxide phases.

2.7 Tables

Table 2-1: General structural information and formation energetics calculated for bulk LD PuO_2 and PuO_{2-x} phases investigated.

* indicates measurements with respect to PuO_2

** PuO_2 structure with *a* and *b* parameters distorted to match that of goethite

*** lattice parameter for the bixbyite unit cell

Phase #	**Structure/ stoichiometry**	**symmetry**	**Lattice parameters**	**2 × integrated spin density**	**Thermodynamic favorability * (kJ/mol Pu_4O_y)**	
					at min μ_O	**at max μ_O**
1	Fluorite/ PuO_2	*FM3M*	5.396	16	0	0
2	Fluorite/ LD PuO_2	*FM3M*	5.540	16	23.375	23.375
3	- / LD PuO_2 **	*C2/m*	*a, b, c*: 10.079, 6.139, 3.853	16	87.523	87.523
4	Fluorite/ Pu_4O_7	*P43M*	5.501	18	-167.307	372.379
5	bixbyite/Pu_2O_3	*IA3*	2×5.540***	20	-418.542	660.830
6	bixbyite/Pu_4O_7	*IA3*	2×5.511***	16	197.196	736.882
7	bixbyite/Pu_4O_7	*IA3*	2×5.518***	18	-74.869	464.817
8	bixbyite/Pu_4O_7	*IA3*	2×5.558****	20	33.550	573.236
9	- / Pu_4O_7	*P1*	9.427	18	-222.744	316.942
10	- / Pu_4O_7	*A1*	*a, b, c*: 6.814, 7.909, 13.592	18	-173.569	366.117

Table 2-2:LM and energetics for PuO_2 and PuO_{2-x} surfaces used in the construction of an interface with goethite. LD denotes the PO surfaces where the lattice was distorted to match the goethite lattice parameters.

	Surface cell (Å)		**Lattice mismatch (%) with respect to goethite**		**surface energy (J/m^2)**		**ΔE with respect to undistorted PuO_2 surface (kJ/mol Pu_4O_y)**	
	a	***b***	***a***	***b***	**min μ_O**	**max μ_O**	**min μ_O**	**max μ_O**
Goethite 001	10.079	6.139	0.000	0.000	1.602	1.602	--	--
PO surfaces								
PuO_2 (110)	9.437	6.673	6.376	-8.695	1.108	1.108	0	0
LD PuO_2 (110)	10.079	6.139	0.000	0.000	1.352	1.352	74.431	74.431
$PuO_{2-x,\ 1S}$ (110)	9.579	6.759	4.970	-10.105	0.289	1.706	-275.642	204.079
LD $PuO_{2-x,\ 1S}$ (110)	10.079	6.139	0.000	0.000	0.506	1.954	-205.941	273.779
$PuO_{2-x,\ 2S}$ (110)	9.443	6.697	6.310	-9.089	0.047	2.900	-150.468	329.253
LD $PuO_{2-x,\ 2S}$ (110)	10.079	6.139	0.000	0.000	0.054	2.892	-148.534	331.178

Table 2-3: Energetics for PuO_2 – goethite and PuO_{2-x} – goethite interfaces.

Pu-goethite interfaces	**W_{ad} (J/m^2)**	**IE (J/m^2)**		**μ_O where IE PuO_{2-x} < IE_{PuO2} (kJ/mol)**
		min μ_O	**max μ_O**	
PuO_2-goethite	1.431	1.074	1.074	--
$PuO_{2-x,\ 1S}$ –goethite	2.024	0.086	1.560	< -178.043
$PuO_{2-x,\ 2S}$ –goethite*	1.802	-0.147	2.750	< -312.274

*Further analysis of $PuO_{2-x,\ 2S}$ –goethite interfacial model is in Supplementary information

2.8 Figures

(a) 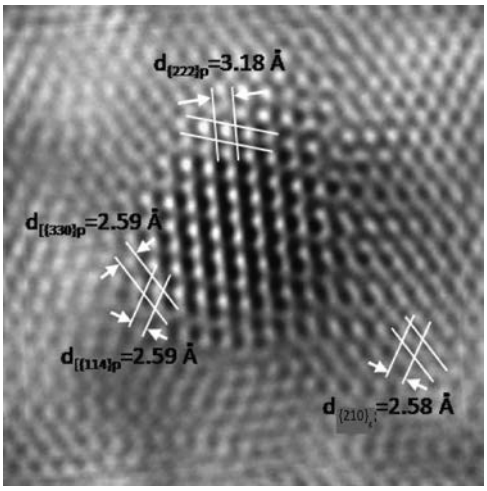

(b) 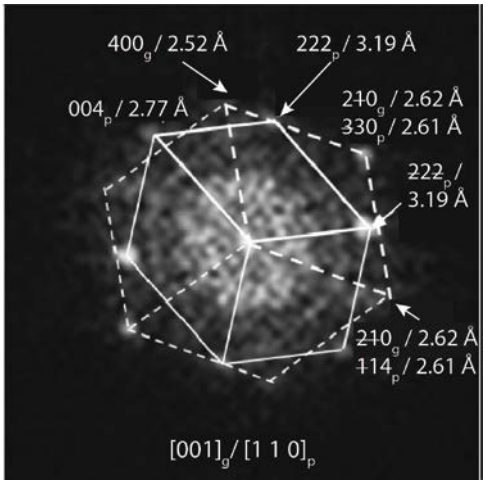

Figure 2-1: TEM images from experimental studies [19], which show the potential for a non-*fcc* PO to be heteroepitaxially grown on goethite. (a) The nanostructure of Pu(IV) adsorbed to goethite was characterized using SAED and HRTEM imaging combined with FFT analysis, showing d-spacings that are unique to *bcc* Pu_4O_7 structure. (b) HRTEM image of the non-*fcc* PO nanocolloid adsorbed on goethite. The d-spacings between goethite are shown to align with d-spacings associated with the PO nanophase. Additional d-spacings measured in experiments [19, 20] are denoted in Figure 2-5. It should be noted that the goethite Miller planes are modified from the original images to represent Miller planes associated with Pnma space group. These images are used as references this study to ultimately align and construct heterointerfaces between PO and goethite slabs (see Figure 2-8a, b).

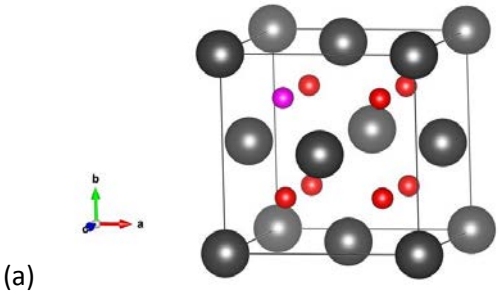

(a)

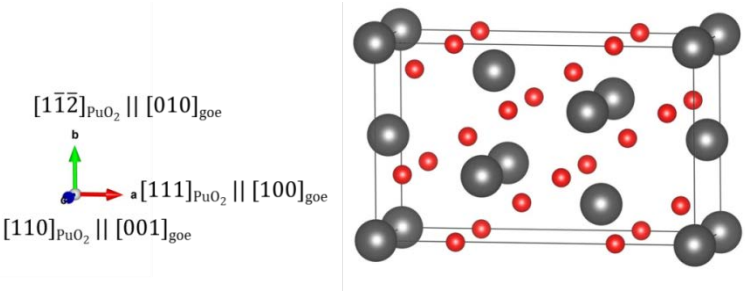

(b)

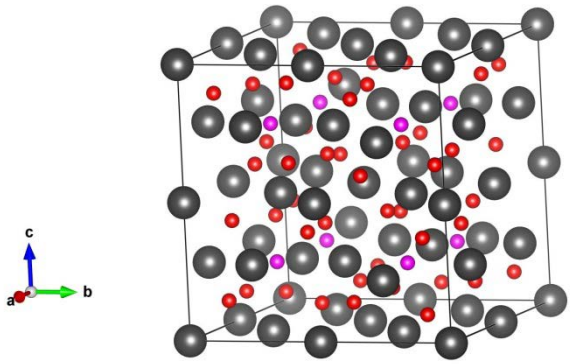

(c)

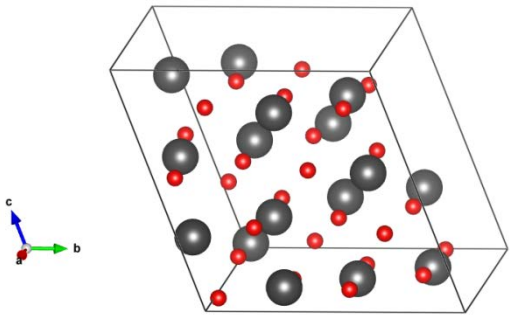

(d)

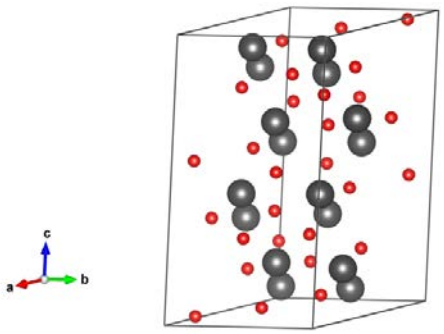

(e)

Figure 2-2: Unit cells of select bulk PuO_2 and PuO_{2-x} structures modelled, where the phase # correlates to those listed in Table 2-1. (a) phase #1 – *fcc* PuO_2, (b) phase #3 – PuO_2 distorted to goethite lattice parameters, (c) phase #6 – *bcc* Pu_2O_3 with bixbyite structure, (d) phase #9 –Pu_4O_7, and (e) phase #10 – Pu_4O_7. Pink atoms in (a) indicate O atoms that were either removed to form phase #4 – Pu_4O_7. Pink atoms in (c) indicate O atoms that were added to form phase #6 –Pu_4O_7. The correlation between lattice vectors for PuO_2 and goethite is shown for phase #3 –LD PuO_2 (b).

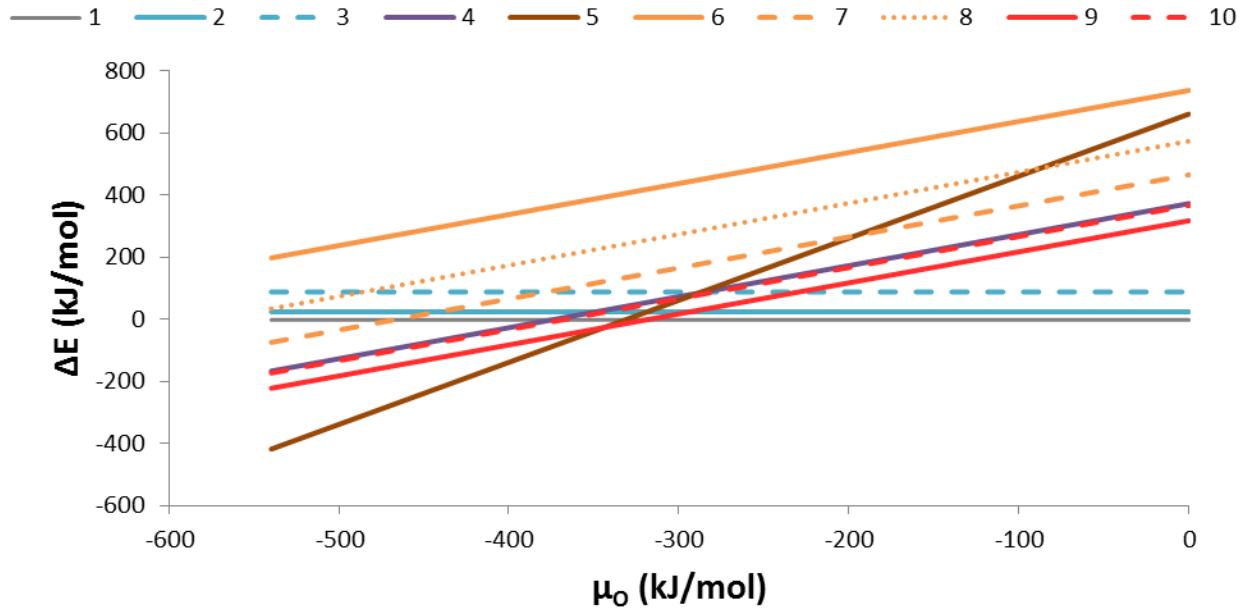

Figure 2-3: Relative thermodynamic favorability of bulk PuO_2 and PuO_{2-x} phases, with respect to bulk *fcc* PuO_2, over the range of min and max μ_O. The PO phases are labelled by their phase number as shown in Table 2-1.

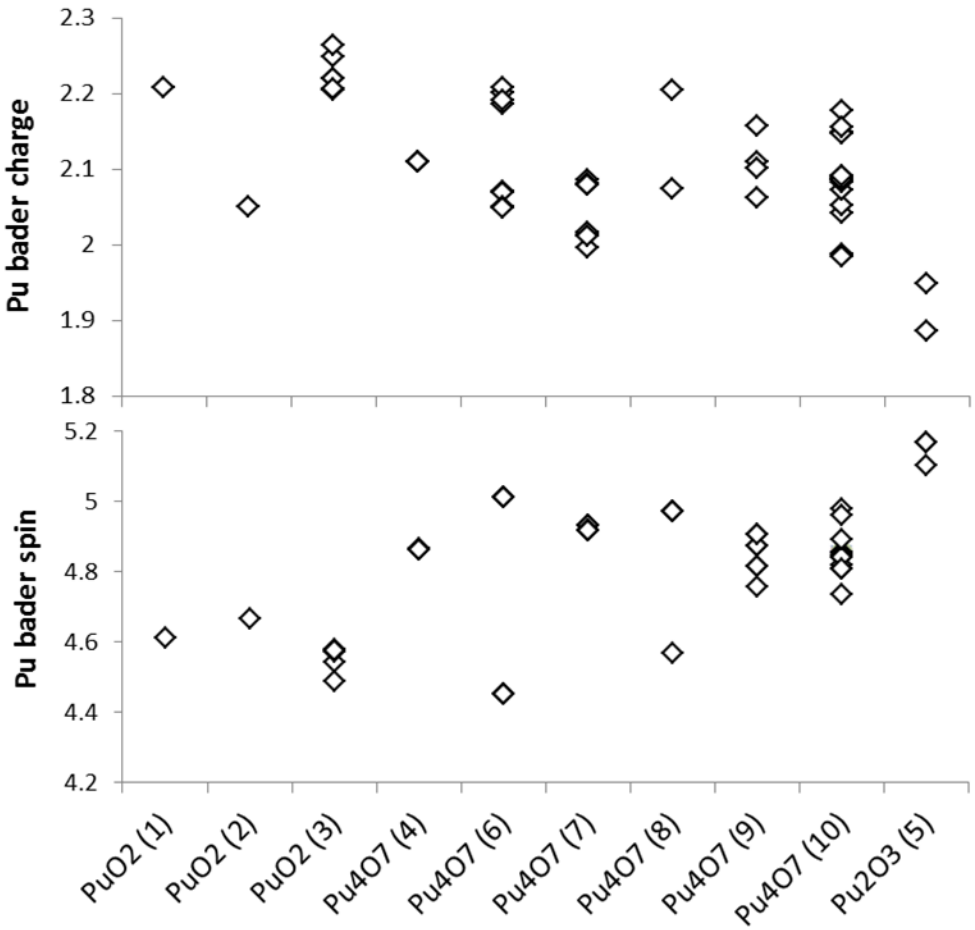

Figure 2-4: Analyses of the Bader charges and spins associated with the bulk PuO_2 and PuO_{2-x} phases to observe whether changes in chemical oxidation states accompany the divalent PO phases. The x-axis is labelled with the stoichiometry and phase number in parentheses from Table 2-1. Note that the x-axis is ordered by PO stoichiometry to show how the Pu charge/spins change from $Pu(IV)O_2$ to $Pu(III)_2O_3$ phases.

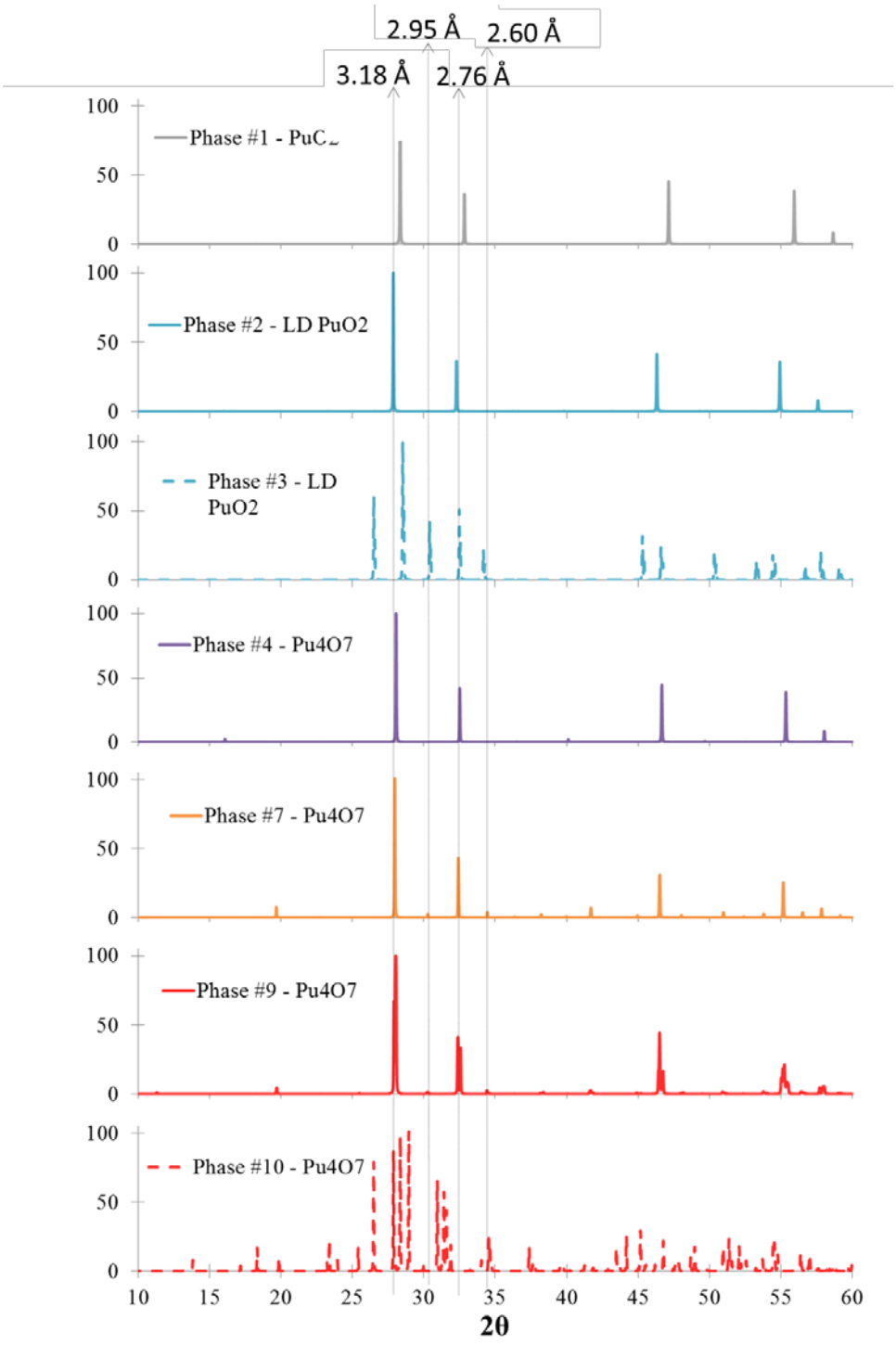

Figure 2-5: Powder diffraction patterns from computationally simulated bulk PuO_2 and PuO_{2-x} structures, showing the similarities in the dominant d-spacings observed for the different PO phases. The light gray arrow denote d-spacings for the PO nanophases measured in experiments [19, 20].

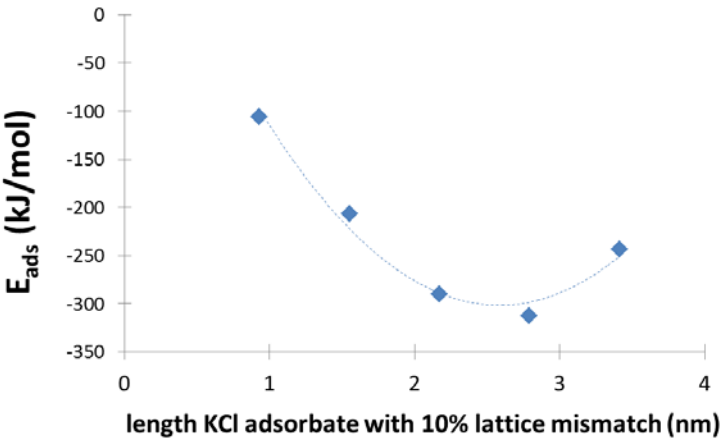

(a)

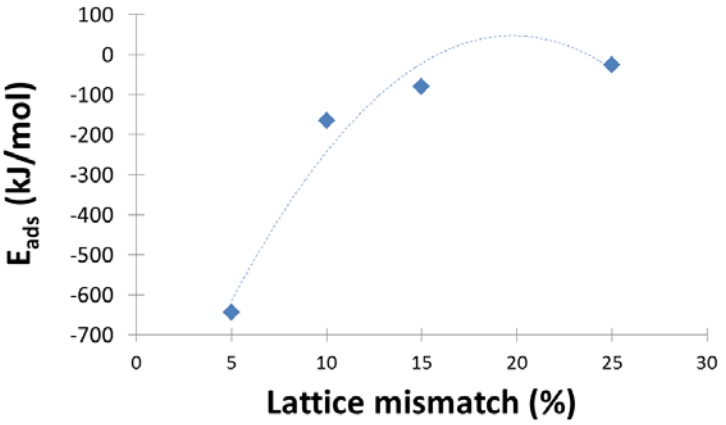

(b)

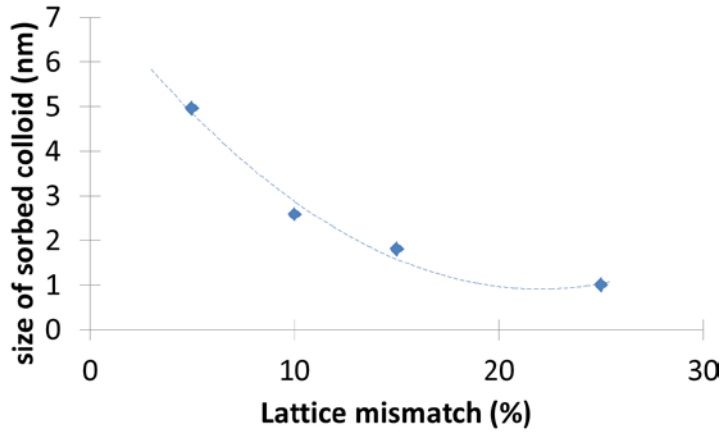

(c)

Figure 2-6: The effect of LM on the diameter of a distorted KCl adsorbate and its sorption energetics onto a NaCl slab (a), using empirical force-field models. These calculations show that the growth of a KCl adsorbate is limited by LM; in this case, the sorption of a KCl at 10%LM would be most energetically favorable when it is ~2.7 nm in length (b). With increasing LM the adsorption energy also decreases (c); the sorption energy is for the KCl adsorbate at the optimal size at the specified LM, as shown in (a).

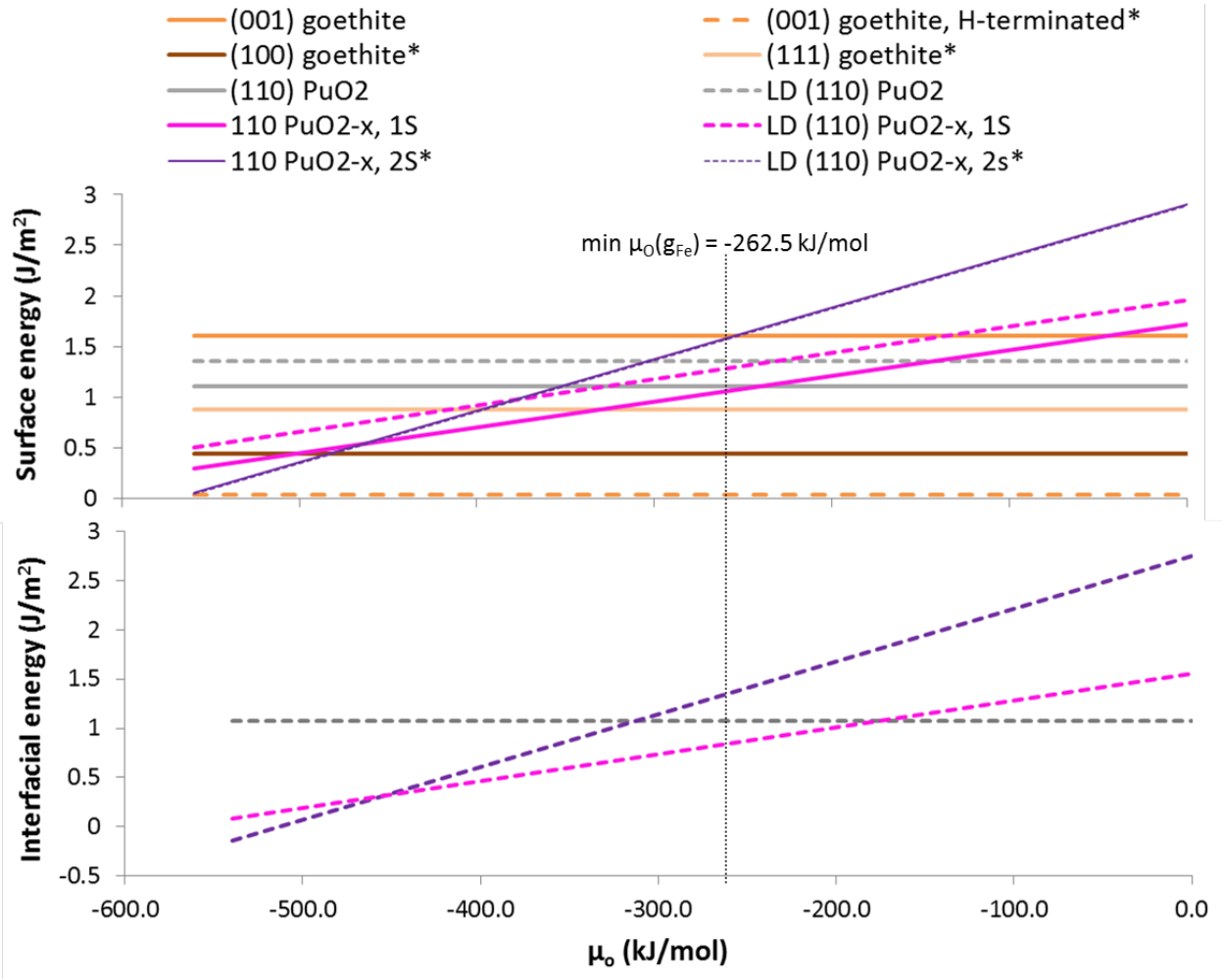

Figure 2-7: Surface and interfacial energies for goethite and PO slabs. The solid lines indicate the non-distorted PO slabs while the dashed lines indicate PO slabs that are distorted to match the goethite lattice parameters. Surface energies of additional goethite surfaces (a hydrated goethite (001) surface, (100) goethite, and (111) goethite) are also plotted to provide a relative understanding of the reactivity of goethite (001) surface compared to more common surfaces. The surfaces marked with asterisks are models that are found in the Supplementary information. The minimum chemical potential of oxygen upon the formation of Fe-O bonds (μ_O = –262.5 kJ/mol) is also shown as a vertical dashed black line for reference.

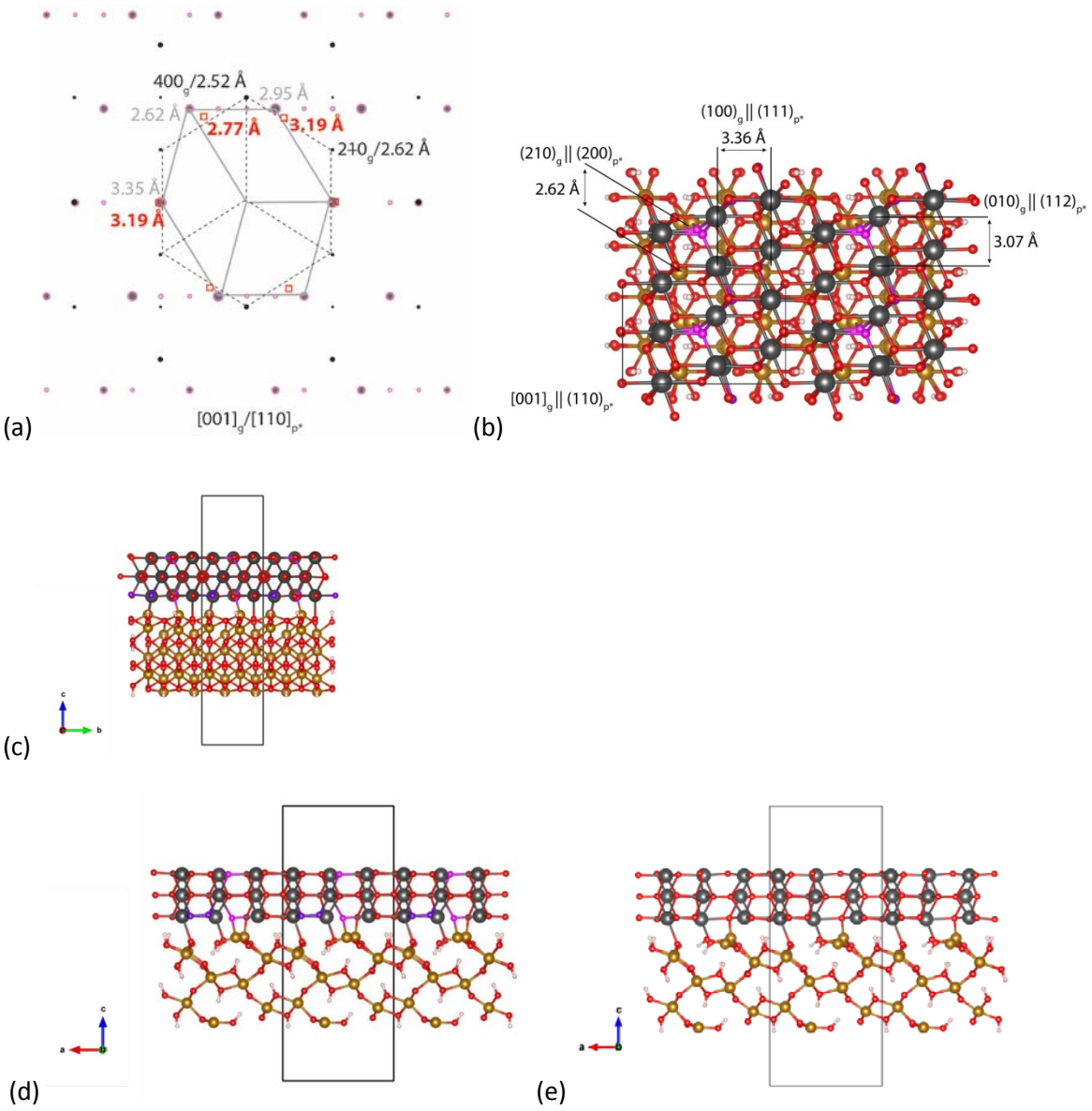

Figure 2-8: Alignment and structure of geometry optimized PuO_2-goethite interface: (a) Simulated ED pattern from computational interfaces formed between LD PuO_2 and goethite slabs. Closed, black circles represent reflections from goethite, close, gray circles represent the major reflections from the LD PuO_2 and PuO_{2-x} phases, pink open circles represent additional reflections associated with the $PuO_{2-x,\ 1S}$ phase, and red-open squares represent reflections from experiments (i.e., reflections from Figure 2-1a). *d*-spacings (color-coded) are also provided next to the major reflections. This ED pattern is comparable to the experimentally observed SAED pattern shown in Figure 2-1a. (b) The alignment of the LD PuO_2 (110) surface over the goethite (001) surface looking down $[001]_{goe}$. The alignments of the computational heterointerfaces are comparable to those found experimentally (see Figure 2-1b). Additional perspectives of the LD PuO2-goethite interface showing the alignment looking (c) down $[100]_{goe}$, and down (d) $[010]_{goe}$. Aside from the interfacial region, little structural rearrangement is observed. The light red O atoms in the PuO_2 slab indicates the O atoms removed to model the $PuO_{2-x,\ 1S}$ - goethite interface; the purple O atoms in the PuO2 slab indicate the O atoms removed to model the $PuO_{2-x,\ 2S}$ – goethite interface. (e) Geometry optimized $PuO_{2-x,\ 1S}$ – goethite interface looking down $[010]_{goe}$.

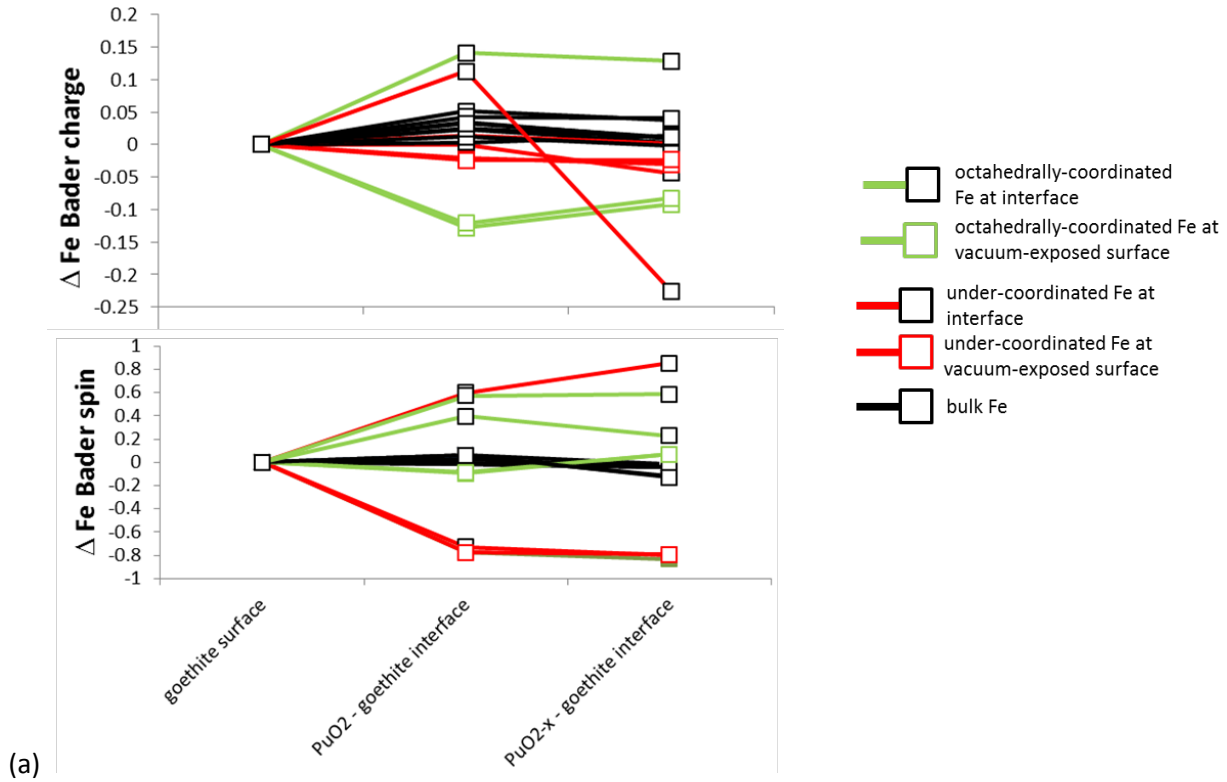

(a)

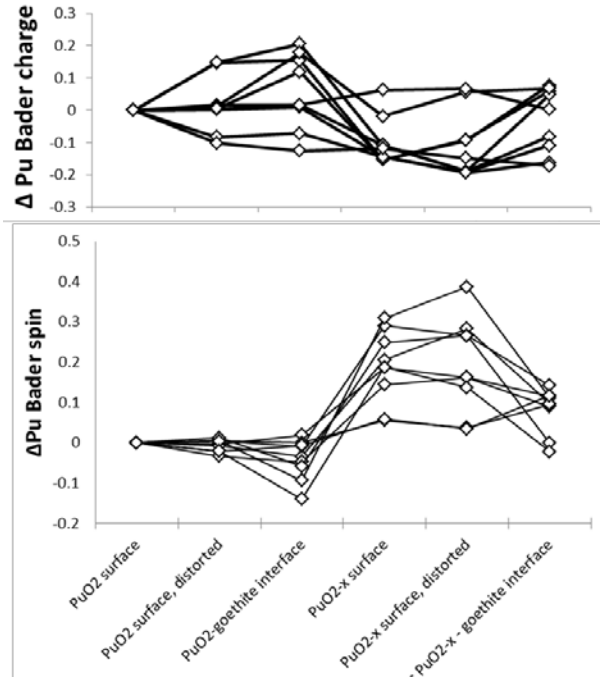

(b)

Figure 2-9: Analyses of Bader charges and spins for Fe cations in the goethite slab (a) and Pu cations in the PuO_2/ $PuO_{2-x,\ 1S}$ slabs (b) before and after distortion as well as before and after the formation of interfaces. The changes in the Bader charges and spins for the Fe atoms are all relative to the goethite surface by itself. The changes in the Bader charges and spins for the Pu atoms are all relative to that of undistorted *fcc* PuO_2.

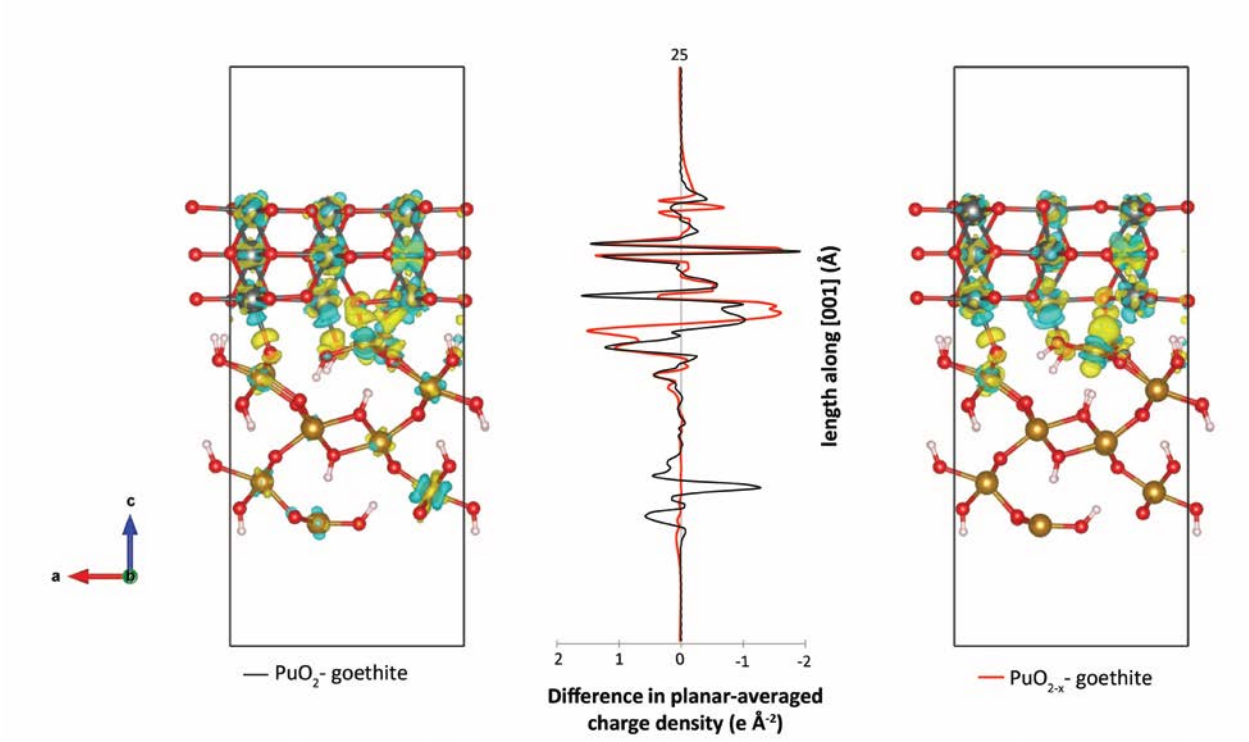

Figure 2-10: Planar averaged total charge density difference for the PuO_2-goethite interface (left-most image) and $PuO_{2-x,\ 1S}$ –goethite interface (right-most image) show the changes in charge that occur due to the formation of an interface between PO and goethite slabs. The change in charge is also measured (central plot). The yellow isosurfaces show areas of positive charge density while the blue isosurfaces shows depletions in charge density/negative charge density.

2.9 Supplementary information

Supplementary table 2-1: Calculated surface energies for various goethite surfaces showing how reactive the dipole-free goethite (001) surface is relative to more common goethite surfaces.

goethite surfaces	Surface cell (Å)		surface energy (J/m^2)
	a	b	
goethite 001	10.079	3.070	1.602
goethite 001, unrelaxed	10.079	3.070	2.449
goethite 001, hydrogenated surface	10.088	3.077	0.072
goethite 100	20.919	3.070	0.436
goethite 111	10.537	5.607	0.878

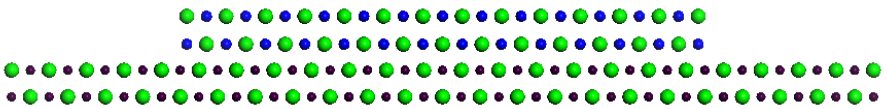

(a)

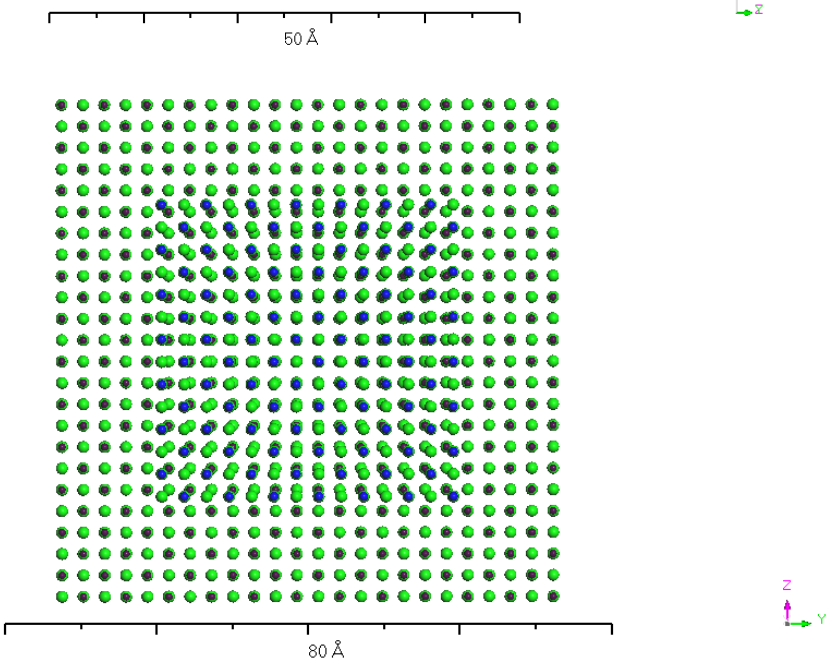

(b)

Supplementary Figure 2-1: An example of the NaCl – KCl clusters used to show the effect of lattice mismatch on particle diameter and adsorption energy, using empirical methods. The lattice of the NaCl cluster (12 unit cells long × 12 unit cells wide × 1 unit cell thick = 67.7 Å × 67.7 Å × 5.6 Å) is held fixed, while the size of the KCl cluster and lattice mismatch is varied. The KCl cluster is placed on top of the NaCl cluster to best position K atoms above the Cl atoms of the NaCl cluster and minimize repulsion between atoms. The lattice of the KCl cluster in this image is uniformly expanded by 5%, and its dimensions are 41.5 Å × 41.5 Å × 5.9 Å. The side-view (a) and view from the top (b) show how lattice mismatch propagates over of the NaCl–KCl interface. Blue atoms = K, Dark purple = Na, green = Cl.

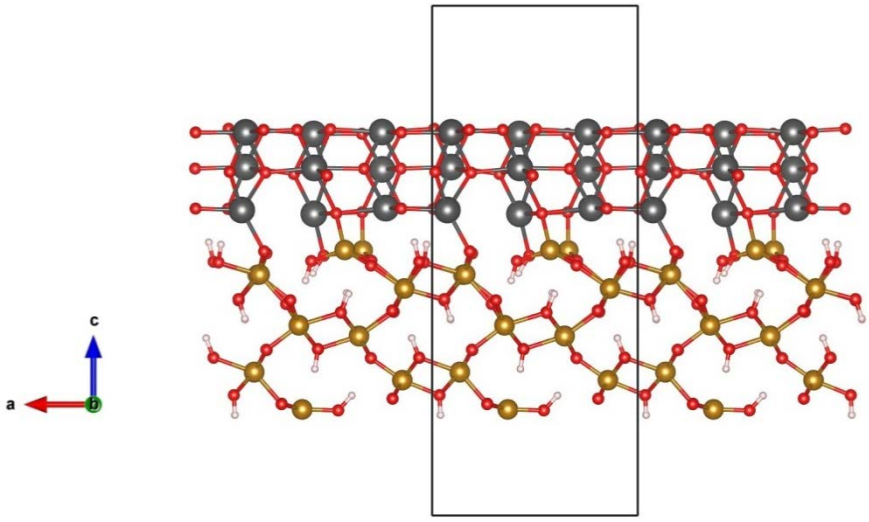

Supplementary Figure 2-2: View of the $PuO_{2-x,\ 2S}$ – goethite interface along $[010]_{goe}$, where two O atoms are removed at the interface.

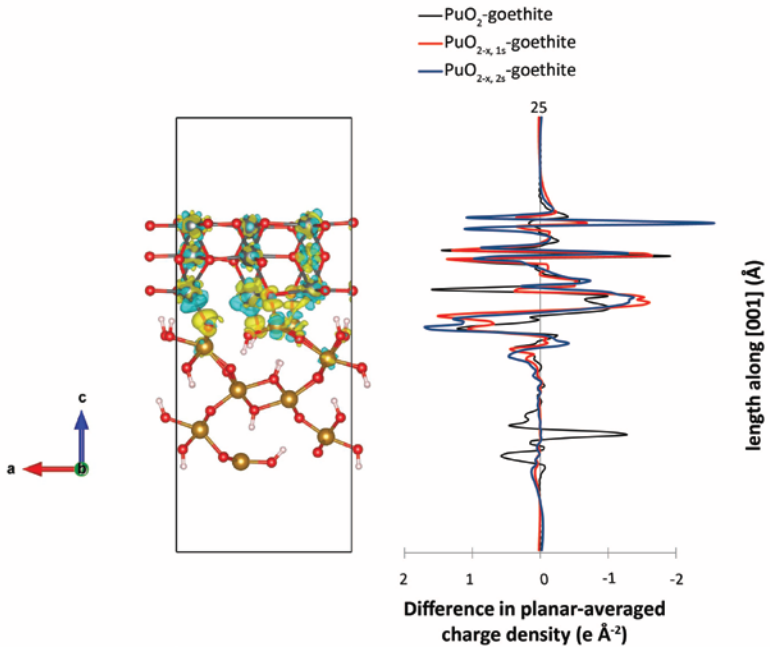

Supplementary Figure 2-3: Planar averaged total charge density difference $PuO_{2-x,\ 2S}$ –goethite interface showing the changes in charge that occur due to the formation of an interface between the Pu oxide and goethite slab. The yellow isosurfaces show areas of positive charge density while the blue isosurfaces shows areas with depletions in charge density/negative charge density. The change in charge is also measured, and is compared to the changes observed for the PuO_2 – and $PuO_{2-x,\ 2S}$ – goethite interfaces included within the main text of the manuscript.

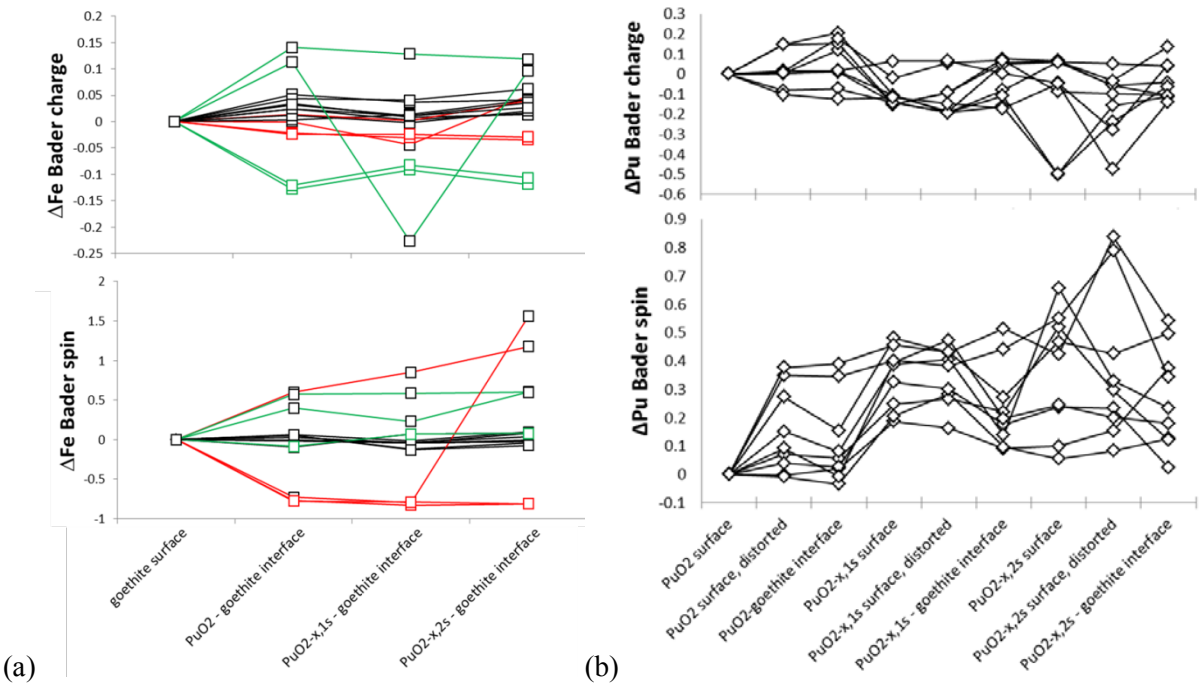

(a) (b)

Supplementary Figure 2-4: Analyses of Bader charges and spins for Fe cations in the goethite slab (a) and (b) Pu cations in the PuO_2/ $PuO_{2-x,\ 2S}$ slabs before and after distortion, as well as before and after the formation of interfaces. The changes in the Bader charges and spins for the Fe atoms are all relative to the goethite surface by itself. The changes in the Bader charges and spins for the Pu atoms are all relative to that of undistorted *fcc* PuO_2.

Chapter 3:
An experimental and *ab initio* study on the abiotic reduction of uranyl by ferrous iron

S.D. Taylor[1], M.C. Marcano[1], K.M. Rosso[2], and U. Becker[1]

[1]*The University of Michigan, Department of Earth and Environmental Sciences, 2534 C. C. Little Building, 1100 North University Ave., Ann Arbor, MI 48109–1005, United States.*

[2]*Pacific Northwest National Laboratory, Physical Sciences Division, PO Box 999, Richland, WA 99352, United States.*

3.1 Abstract

It is important to understand the mechanisms controlling the removal of uranyl from solution from an environmental standpoint, particularly whether soluble Fe(II) is capable of reducing soluble U(VI) to insoluble U(IV). Experiments were performed to shed light into discrepancies of recent studies about precipitation of U-containing solids without changing oxidation states *versus* precipitation/reduction reactions, especially with respect to the kinetics of these reactions. To understand the atomistic mechanisms, thermodynamics, and kinetics of these redox processes, *ab initio* electron transfer (ET) calculations, using Marcus theory, were applied to study the reduction of $U(VI)_{aq}$ to $U(V)_{aq}$ by $Fe(II)_{aq}$ (the first rate-limiting ET-step). Outer-sphere (OS) and inner-sphere (IS) Fe-U complexes were modeled to represent simple species within a homogeneous environment through which ET could occur.

Experiments on the chemical reduction were performed by reacting 1 mM $Fe(II)_{aq}$ at pH 7.2 with high (*i.e.,* 0.16 mM) and lower (*i.e.,* 0.02 mM) concentrations of $U(VI)_{aq}$. At higher U concentration, a rapid decrease in $U(VI)_{aq}$ was observed within the first hour of reaction. XRD

and XPS analyses of the precipitates confirmed the presence of (meta)schoepite phases, where up to ~25% of the original U was reduced to U^{4+} and/or U^{5+}-containing phases. In contrast, at 0.02 mM U, the $U(VI)_{aq}$ concentration remained fairly constant for the first 3 hours of reaction and only then began to decrease due to slower precipitation kinetics. XPS spectra confirm the partial chemical reduction U associated with the precipitate (up to ~30%). Thermodynamic calculations support that the reduction of $U(VI)_{aq}$ to $U(IV)_{aq}$ by $Fe(II)_{aq}$ is energetically unfavorable. The batch experiments in this study show U(VI) is removed from solution by precipitation and that transitioning to a heterogeneous system in turn enables the solid U phase to be partially reduced.

Ab initio ET calculations revealed that OS ET is strongly kinetically inhibited in all cases modeled. OS ET as a concerted proton-coupled ET reaction (ferrimagnetic spin configuration) is thermodynamically favorable (–35 kJ/mol), but kinetically inhibited by concurrent proton–transfer (10^{-19} s^{-1}). OS ET as a sequential proton-coupled ET reaction is thermodynamically unfavorable (+102 kJ/mol) as well as kinetically inhibited, where ET is the rate–limiting step (10^{-12} s^{-1}). In contrast, the reduction of $U(VI)_{aq}$ to $U(V)_{aq}$ by $Fe(II)_{aq}$ as an IS ET reaction is both thermodynamically favorable (–16 kJ/mol) and kinetically rapid (10^{8} s^{-1}); the IS ET rate is several orders of magnitude faster than the OS ET rate. Thus, reduction of $U(VI)_{aq}$ to $U(V)_{aq}$ by $Fe(II)_{aq}$ in a homogenous system could occur if an IS Fe-U complex can be achieved. However, the formation of IS Fe-U complexes in an homogeneous solution is predicted to be low; considerable thermodynamic and kinetic barriers exist to proceed from an OS ET reaction to an IS ET reaction, a process that needs to overcome dehydration of the first solvation shell (+96 kJ/mol) and hydrolysis of $Fe(II)_{aq}$. The computational results complement and further substantiate experimental results where the reduction of $U(VI)_{aq}$ by $Fe(II)_{aq}$ does not occur.

3.2 Introduction

The radioactive element uranium is most soluble and mobile in the hexavalent oxidation state as the uranyl ion UO_2^{2+}. Due to its solubility in oxidizing conditions, it is of interest to understand mechanisms that are capable of removing uranyl from solution. There are several mechanisms by which U can be immobilized in the subsurface. Precipitation of solid uranyl phases such as schoepite ($UO_3 \cdot 2H_2O$) can occur at higher concentrations (*e.g.,* above 10^{-6} M U(VI), log $^{*}K_{sp}$ = 5.39) at near-neutral pH [48]; schoepite can be found in contaminated sites, such as soils and groundwaters at U.S. Department of Energy sites, as well as in natural U ore

deposits. The chemical reduction of U(VI) to U(IV) is another mechanism to immobilize U, where the tetravalent oxidation state of U is sparingly soluble and precipitates as uraninite $UO_{2(s)}$. An extensive number of studies focus on this approach as it is capable of removing uranyl from solution to below the U.S. Environmental Protection Agency's maximum concentration limits (1.3×10^{-7} M, 30ppb) [49].

The abiotic reduction of soluble U(VI) by soluble Fe(II) as a homogeneous-reaction (*i.e.,* the reduction of U(VI) by Fe(II) occurs where both of the reactant species are in the aqueous phase) is a relevant process for retarding U transport in the subsurface. However, experimental results in this area remain inconclusive about the exact mechanism of precipitation or combined reduction/precipitation. One hypothesis is that the reduction of U(VI) in a homogeneous, Fe(II)–containing solution does not occur because the redox reaction is kinetically inhibited. One of the earlier studies investigating the abiotic reduction of uranyl by ferrous iron found that the chemical reduction of U(VI) does not occur in a homogeneous, Fe(II)-containing solution (at neutral pH in an anoxic system) for over three days, despite being thermodynamically favorable. However, upon addition of hematite nanoparticles (α–Fe_2O_3) to the solution, the chemical reduction of U(VI) by Fe(II) occurs rapidly, reaching equilibrium during the first hour of reaction [12]. This phenomenon has also been observed in experiments at similar conditions (*i.e.,* pH ~7.5, anoxic environment) using different U and Fe concentrations (*i.e.,* 0.1 μM to 10 μM U, reductant to oxidant ratio of about 500, growth solution supersaturated with respect to schoepite) [13]. Subsequent analyses of these results using surface-complexation models, led to the hypothesis that the reduction of U(VI) in a homogeneous, Fe(II)–containing solution is kinetically inhibited [12-14, 50]. These results imply that uranyl reduction at these experimental conditions is not a mechanism by which uranyl will be immobilized.

Conversely, the homogeneous reduction of U(VI) by S^{2-} and Fe^{2+} at higher U(VI) concentrations (at neutral pH in an anoxic system) has been reported [11, 15]. One of the hypotheses why uranyl reduction by ferrous iron occurred is that the redox reaction is governed by thermodynamics, where the reaction favorability is dependent on experimental conditions such as pH. Declining concentrations of $Fe(II)_{aq}$ correlate with the loss of $U(VI)_{aq}$. At the presumed equilibrium pH of 6.2, the ratio of consumed Fe(II) to the loss of U(VI) is ~2:1; this ratio would be consistent with a two-electron transfer (ET) to U(VI) and reduction to U(IV).

Additionally, thermodynamic calculations with different combinations of pH, [$Fe(II)_{aq}$], and [$U(VI)_{aq}$] predicted uranyl reduction to be favorable for their experimental conditions at pH > 5, as was the case for the experimental conditions of pH 7.5 used by Liger, *et al.* (1999) [12]. Thus, unlike the experiments where uranyl reduction was not observed, the reduction of uranyl by Fe(II) was found to be thermodynamically and kinetically feasible. These results in turn predict uranyl can be immobilized through reduction to U(IV) and subsequent precipitation of $UO_{2(s)}$.

The studies described above observe very different behaviors for aqueous uranyl and its chemical reduction by ferrous iron (at neutral pH values in anoxic systems), which can lead to high uncertainties in predicting the transport of U. There is a lack of knowledge in fundamental processes and mechanisms by which uranyl reduction by ferrous iron occurs; this is due to the complexity of the redox environment. The abiotic reduction of U(VI) is shown to be influenced by a number of processes in an aqueous, homogeneous system, including processes that can convert a homogeneous system to a heterogeneous system (*i.e.,* where U and/or Fe species can exist as both aqueous and solid phases) (Figure 3-1, Table 3-1). The generation of solid redox products, for instance, can enable the possibly rapid transition to a heterogeneous system where the mechanisms involved in removing uranyl from solution are more complex (Figure 3-1, Table 3-1 Processes 3–8). Understanding the mechanisms controlling uranyl removal from solution in homogeneous and heterogeneous systems, whether it be schoepite precipitation and/or the chemical reduction of U(VI) to U(IV) and subsequent precipitation of $UO_{2(s)}$, for example, is necessary to develop more effective pathways for waste isolation and environmental restoration.

Here, experimental and molecular theoretical approaches are applied to understand mechanisms removing uranyl from solution, focusing on whether the chemical reduction of aqueous U(VI) by aqueous Fe(II) in fact occurs. Experiments were designed using conditions and U concentrations that can be found in the literature and had produced conflicting results or interpretations. Analyses of the aqueous and solid fractions over time were done to accurately interpret U concentration changes and assess redox mechanisms. Finally, *ab initio* molecular modeling is applied to explain experimental and geochemical observations. Reduction of U(VI) to U(IV) occurs as a sequential two-ET process; the intermediate oxidation state of U(V) is nominally unstable in solution. It has been postulated that the rate-limiting step is the first ET, reducing U(VI) to U(V). Thus for this study, the first ET step for U(VI) reduction to U(V) by

Fe(II) was specifically investigated. By evaluating molecular mechanisms occurring in both homogeneous and heterogeneous systems, this study intends to advance our understanding of environmentally relevant actinide redox reactions.

3.3 Methods

3.3.1 Experimental

3.3.1.1 ***Batch*** experiments

All solutions were mixed using degassed water prepared by autoclaving ultrapure Milli–Q® water (typically 18.2 MΩ·cm at 25 °C) in Pyrex® Corning®C glass bottles at regular sterilizing conditions (*i.e.,* 40 minutes at 121 ºC and ~138 kPa). Out of the autoclave, purified N_2 is blown onto and bubbled into the water for about 90 minutes while it cools from ~95 ºC to ~35 ºC in a warm bath. Glass bottles are then air–tight capped and immediately transferred to a controlled atmosphere Coy® vinyl glove box. Gas in the box (5 % H in N mix) is kept dry and at O levels < 1 ppm using a desiccant and a palladium catalyst attached to a continuously running fan box. O is further removed by recirculating the glove box atmosphere through an O trap using a diaphragm pump.

Stock solutions of 0.05 M UO_2^{2+} and 0.18M Fe^{2+} were prepared from high-purity solids $UO_2(NO_3)_2 \cdot 6H_2O$ (International Bio-Analytical Industries Inc.; CAS-#: 13520-83-7) and $FeCl_2$ (Sigma-Aldrich; 99.998% trace metal basis; CAS-#: 7758-94-3) in 1% HNO_3 and HCl, respectively. Experiments were conducted at pH ~7.2, where the solution pH was buffered by 5 mM HEPES and the ionic strength was controlled at 50 mM NaCl. Intermediate 0.82 mM UO_2^{2+} and 5 mM Fe(II) stock solutions were prepared in 5 mM HEPES–50 mM NaCl (pH = 7.5) solution, further titrated with 0.1 M NaOH to pH ~7.2, and equilibrated overnight. After equilibration, solutions were filtered through 0.22 μm pore-size PVDF syringe filter membranes. The 5 mM Fe(II) solution prepared this way was used in both Experiments 1 and 2 (described below). The equilibrated 0.82 mM UO_2^{2+} solution was used only for Experiment 2, while the titration information served to make a second UO_2^{2+} intermediate stock at reaction time for Experiment 1.

Experiments were conducted at conditions similar to those where the chemical reduction of uranyl have and have not been observed; Du, *et al.* (2011) [15] observed the chemical

reduction of 0.20 mM U(VI) in a 1 mM Fe^{2+}-containing solution while Zeng and Giammar (2011) [13] did not observe uranyl reduction at 0.01 mM U(VI) in a 5 mM Fe^{2+}-containing solution. Similar concentrations were used in this study, 0.16 mM and 0.02 mM U, to further probe the mechanisms controlling removal of uranyl from solution; *i.e.*, these experiments would be able to observe if uranyl is being removed from solution by uranyl reduction occurring in a homogeneous system and the subsequent precipitation of $UO_{2(s)}$ or via other mechanisms such as precipitation of U(VI) solid phases.

For Experiment 1 (predicted to be thermodynamically-favorable and kinetically-rapid conditions for uranyl reduction by Du, *et al.* (2011) [15]), a neutral reaction solution (pH 7.2) of 1 mM Fe^{2+} and 0.16 mM UO_2^{2+} was prepared in 5 mM HEPES–50 mM NaCl solvent using the intermediate 5mM Fe^{2+} stock solution (equilibrated overnight and filtered) and 0.05 M UO_2^{2+} stock solution.

For Experiment 2 (predicted to be thermodynamically-favorable but kinetically-slow conditions for uranyl reduction by Zeng and Giammar (2011) [13]), a neutral reaction solution (pH 7.2) of 1 mM Fe^{2+} and 0.02 mM UO_2^{2+} was prepared in 5 mM HEPES–50 mM NaCl solvent, using the intermediate Fe and U stock solutions (both equilibrated and filtered). The filtered U stock solution was used to ensure uranyl in the system was present only in its aqueous state.

The solutions for both experiments were constantly agitated on a sample rotator. Aliquots of 3 ml were taken from the reactors at 0, 15, 30, 45 minutes and 1.5, 3, 5, 8, 24, 32, 48, and 72 hours from the beginning of the experiment. The aliquots were filtered through 0.22 μm pore size PVDF syringe filter membranes acidified to 1% HNO_3, and reserved for analysis by ICP-MS. The solution pH was measured at 0 and 45 minutes and 3, 8, 24, 48, and 72 hours to observe if the acidity of the solution was increasing via the generation of solid (redox) products. Solid samples were also collected on the 0.22 μm pore size PVDF syringe filter membranes at 0 and 45 minutes and 3, 8, 24, 48, and 72 hours to observe the rate of uranyl reduction occurring over time. Precipitate samples were dried on filter membranes in a dessicator under anoxic conditions in the glove box, and were set aside for XRD and/or XPS analysis.

Aqueous Fe^{2+} and UO_2^{2+} concentrations were measured from the diluted, acidified aliquots using a Perkin–Elmer ELAN DRC-e ICP–MS. The identity of Fe analyzed with the ICP was confirmed to be Fe^{2+}, as UV-Vis measurements using the ferrozine method provided similar Fe^{2+} concentrations (within 5% error). The quantitative analysis method used ten sweeps per reading, five readings per replicate, and the average of five replicates per measurement, simple linear standard calibration curve with 6 points, and Ga as internal standard. Analytical precision was better than 3% RSD for both U and Fe based on check standards, laboratory reference material, and sample replicates. Internal standard variation was never above 15%.

To determine the thermodynamics for Fe-U redox reactions, geochemical information, such as the chemical speciation of Fe^{2+} and UO_2^{2+} at the given experimental conditions, was derived using the software Visual Minteq [51]. It was of particular interest to determine the thermodynamics for redox reactions where both the Fe and U reactants and products are in the aqueous phase, similar to what was done by Felmy, *et al.* (2011) [52]. Because the solubilities of Fe^{3+} and U^{4+} are low, with respect to their corresponding oxides, redox reactions are often expressed as $UO_2^{2+}{}_{(aq)} + 2e^- \rightarrow UO_{2(s)}$, for instance, where the reactant is one phase (aqueous) and the product is a different phase (solid). However, if considering a truly homogeneous system, aqueous reactants should yield aqueous products immediately following the redox process (*e.g.*, $UO_2^{2+}{}_{(aq)} + 2e^- \rightarrow U^{4+}{}_{(aq)}$). Thus, thermodynamic calculations with products in both the aqueous and solid states were used to determine the feasibility of redox reactions occurring in homogeneous solution and the potential influence of solid phases on the reaction free energy.

Standard electrode potentials (pe^0) for UO_2^{2+}/U^{4+} ($pe^0{}_1 = 9.038$) and Fe^{2+}/Fe^{3+} ($pe^0{}_2 = 13$) were used to calculate redox potentials pe_1 and pe_2, respectively [53] (Eqn. 1):

$$pe = pe^0 - log\frac{[Reductant]}{[Oxidant]} \quad (1)$$

The experimental conditions used were: $Fe^{2+} = 6.8\times10^{-4}$ M, $Fe^{3+} = 3.2\times10^{-4}$ M, $UO_2^{2+} = 7\times10^{-7}$ M (based on experimental data in this study), $U^{4+} = 1.6\times10^{-4}$ M (assuming all uranium is reduced to U^{4+} by two-Fe^{2+}), pH=7.2. While the UO_2^{2+}/U^{4+} equilibrium is pH dependent because it involves the coupled proton transfer of 4 H^+ ions, the $UO_2^{2+}/U(OH)_4$ is not and the transition between these two equilibria can be performed using the hydrolysis of the $U(OH)_4$ complex. At these conditions, the primary electron donor from Fe^{2+}-containing species (*e.g.*, $FeCl^+$, $FeCl_2$) is

Fe^{2+} (~98% of the aqueous Fe^{2+} species) and the UO_2^{2+} electron acceptor species are $(UO_2)_3(OH)_5^+$ (~65%), $(UO_2)_4(OH)_7^+$ (~32.5%), and $UO_2(OH)_2$ (~1.5%). Redox products were chosen based on dominant aqueous and solid redox species; the aqueous redox products were $U(OH)_4$ and $Fe(OH)_2^+$ and the solid redox products used were $Fe(OH)_3$, α-FeOOH, α-Fe_2O_3, and $UO_{2(am,\ s)}$. An amorphous, solid UO_2 phase was chosen based on experimental observations of faster precipitation kinetics than crystalline UO_2 [52]. Thermodynamic data for aqueous hydrolysis species were calculated using hydrolysis constants supplied by Visual Minteq's thermodynamic database [51]. The reaction free energy, Δ*G*, for a two-ET redox reaction was calculated from the redox potentials derived from the various combinations of reactant and product species (Eqn. 2):

$$\Delta G = -n \times 2.3RT\ (pe_1 - 2 \times pe_2) \quad (2)$$

where *n* is the number of electrons transferred (two in this case), *R* is the gas constant (8.314 J mol^{-1} K^{-1}), and *T* is temperature in Kelvin (298.15 K).

3.3.1.2 Analyses of the solids

X-ray diffraction (XRD) analyses were performed on selected samples to determine the identity of the solid (redox) products formed. Again, precipitate samples had been dried on filter membranes in a dessicator under anoxic conditions. XRD spectra were acquired using a step size of 0.02˚ 2θ and a scan rate of 0.02˚/s from 5˚ to 60˚ 2θ on a Scintag X1 Powder X-Ray Diffractometer with Cu-Kα source. Background from the PVDF filters was subtracted from the XRD spectra.

A Philips XL30 FEG scanning electron microscope (SEM) was used to observe uranyl precipitation at the lower uranyl concentration (0.02 mM U). Dried filter membranes were carbon-coated and mounted using double-sided copper-tape. A thin strip of graphite paste was also painted on the filter-membranes to the sample mount to reduce the amount of charging on the nonconductive filter membranes. Images were collected using a beam current of 15 keV. Backscattered electron (BSE) imaging was used to identify solid precipitates on the filter membrane and energy-dispersive spectroscopy (EDS) spectra with an EDAX Genesis detector was used to confirm the presence of uranium in the precipitates observed.

Characterization of the chemical oxidation states of uranium was done by measuring electron binding energies (BEs) using a Kratos Axis Ultra X-ray photoelectron spectrometer (XPS) with an Al-Kα x-ray radiation source (1486.6 eV). The dried powders on the filter membranes (exposed only to the anoxic glove bag atmosphere) were transferred in a Cole-Parmer vacuum dessicator during transit to avoid exposure to atmosphere. The filters with the powders were affixed onto double-sided copper tape and loaded onto a sample bar. This is the only time where samples could have been exposed to atmosphere for up to 2 - 4 minutes. The samples were degassed in the sample-transfer chamber under a vacuum pressure of $<10^{-5}$ Torr overnight, to ensure degassing of the PVDF filters. Upon transferring the samples to the sample-analysis chamber, a vacuum pressure of $<10^{-8}$ Torr was maintained. The x-ray emission current and anode voltage used during spectra acquisition were 8 mA and 14 keV, respectively. A charge neutralizer was used during spectra acquisition due to the non-conductive behavior of the filters and powdered samples. Spectra were acquired using a hybrid lens and slot aperture (700×300 μm).

Survey scans were collected to confirm the presence of relevant elements in this study (U, C, O, Fe) in the BE range –5 to 1200 eV at 1 sweep (dwell time = 200 ms) and at a pass energy of 160 eV. Following the survey scans, narrow scans were collected under the same analyzer conditions, but at lower pass energies and with more sweeps to better resolve photopeak energies. Samples from Experiment 1 were collected using a pass energy of 20 eV while samples from the Experiment 2 used 80 eV (the lower concentrations of uranyl produced lower counts); narrow scans for U used 15 - 20 sweeps (dwell time=133 ms). The presence of U, O, C, and F (from the PVDF filters) was apparent and narrow scans could be acquired. Fe 2p photopeaks could not be found or resolved with survey or narrow scans (BE ~710 eV), despite estimated Fe cps suggesting Fe was detectable in samples for Experiment 1 (based on the ratio of Fe removed from solution to uranium removed from solution).

XPS spectra were analyzed using the Casa XPS software (v. 2.3.16). Spectra were calibrated using the adventitious carbon method [54]; the energy for the C 1s photopeak led to a shift in energy from ~282.5 to 285 eV. Narrow scans for the U 4f photopeaks were analyzed in detail to characterize uranium oxidation states. Within a simple (oxy)hydroxide system, the U 4f BE can be used to distinguish between U(VI) and more reduced U phases, where a higher BE

represents the higher U(VI) oxidation state [54]. BEs for different chemical oxidations of uranium can overlap, in which case satellite peaks (if present) are used to provide more concrete determination of the oxidation state. Quantification of the amounts of reduced uranyl on the solids collected over time were also compared to aqueous data to understand whether the aqueous data accurately reflected the amount of reduction occurring. Shirley background subtraction was applied to U 4f spectra with Gaussian-Lorentzian (GL) type curves fit to the photopeaks and satellite peaks. The FWHM for the components fit to the photopeaks were held constant and so was the FWHM for the components fit to the satellite peaks (though not necessarily the same FWHM as the photopeaks).

3.3.2 Computational

The aim of the *ab initio* calculations was to estimate the thermodynamics and kinetics of the first ET step in Fe-U complexes found in aqueous, homogeneous systems. An aquo Fe^{2+} complex ($Fe(H_2O)_6^{2+}$) and hydrated, octahedrally-coordinated $UO_2(OH)_2$ complex were constructed, consistent with their expected speciation at neutral pH (Figure 3-2a, b). The uranyl species at higher concentrations at neutral pH also exist as hydroxypolymers (*e.g.,* $(UO_2)_3(OH)_5^+$), although using these polynuclear species would significantly complicate the *ab initio* calculations (*e.g.,* reduction of the entire complex would require six-ET steps). At lower uranyl concentrations, the neutral $UO_2(OH)_2$ species is the major dissolved species and is sufficient for these calculations. An outer-sphere (OS) complex $Fe(H_2O)_6^{2+}$ -$UO_2(OH)_2(H_2O)_2$ was modeled to represent the ions in an aqueous environment being fully solvated while an inner-sphere (IS) complex $((H_2O)_4Fe(OH)_2$ - UO_2 $(H_2O)_2)^{2+}$ represents the dehydration of the OS complex and complexation of the ions through bridging-hydroxyl ligands. The IS complex is the predicted complex through which uranyl reduction can occur, and is also relevant to heterogeneous systems [12, 14, 24, 50, 55].

Ab initio calculations were applied to ET reactions to reduce UO_2^{2+} to UO_2^+ by Fe^{2+}, using the speciation as above, and in the gas-phase (*i.e.,* only the first hydration shell is explicitly treated). Marcus Theory has been used as a framework for environmental ET calculations using molecular modeling for over a decade [56-61]; detailed explanations of Marcus Theory and the calculation of ET rates are available in the literature, which the reader is referred to for more information [56, 62-64]. To model an ET reaction, the Fe^{2+} and UO_2^{2+} ion must be assigned with

the appropriate charges and spin configurations. Before ET occurs, the Fe^{2+} ion has a net charge and spin of +2 and +4, respectively, while the UO_2^{2+} ion has a net charge and spin of +2 and 0, respectively; this state is referred to as the pre-ET complex in this study. After ET, the oxidized Fe^{2+} (now Fe^{3+}) would have a net charge and spin of +3 and +5, respectively, while the reduced UO_2^{2+} (now UO_2^{+}) is +2 and ±1; this state is referred to as the post-ET complex. Ferromagnetic (same majority spin direction for Fe^{3+} and UO_2^{+}) and ferrimagnetic (opposite majority spin directions for Fe^{3+} and UO_2^{+} with a net residual moment) spin configurations for the post-ET complex were modeled to determine the most energetically favorable spin configuration as well as observe whether the spin configuration affects the thermodynamics and kinetics of ET.

The pre- and post-ET structures were geometry optimized using NWChem [65]. Basis sets used in this study were 6-31G** (O and H) [66], Ahlrichs PVDZ (Fe) [67], and the Stuttgart RLC ECP (U) [68]; the reliability of these basis sets has been demonstrated in other studies [57, 69, 70]. The structures were pre-optimized using spin-unrestricted Hartree-Fock (HF) to localize the electrons in the desired distribution, and then re-optimized using the HF-DFT hybrid B3LYP functional to improve the exchange-correlation description and produce more accurate wavefunctions and structures. Only the results of the DFT-B3LYP calculations are presented in this study, except for electronic coupling matrix elements which were calculated at the HF level.

Changes in Mulliken spin distributions for the optimized pre- and post-ET structures, as mentioned above, were analyzed to approximate ET extent. Changes in Fe and U atomic distances were monitored to confirm the appropriate oxidation state was obtained. Average bond lengths between Fe(III) and its hydroxyl or water ligands, as well as average bond lengths between U(VI) and its oxo, hydroxyl, and water ligands, are shorter than those for the Fe(II) and U(V) cations, respectively, due to the electron localization [56].

Following optimization of the pre- and post-ET structures, a potential energy (PE) profile was derived from single-point energies calculated from hybrid structures, obtained using the linear synchronous transit method (LST) [71] (Figure 3-3). Parabolic functions were fit to the reactant and product PE surfaces to derive ET parameters, namely the free energy of ET reaction, the reorganization energy, and the diabatic activation energy. The reaction free energy, ΔG^0, is the change in free energy upon ET. The reorganization energy, λ, is the energy needed to distort the configuration of the reactants into that of the products without changing the electronic

distribution. From these data the electronic coupling matrix element and adiabaticity of the reaction were also determined.

The electronic-coupling matrix element, V_{AB}, is the amount of electronic interaction between the reactant and product states at the transition state (calculated using HF wavefunctions using the ET module in NWChem). It should also be noted that the more strenuous Stuttgart RSC basis set for U [72] was used in the V_{AB} calculations to produce more reliable values. The magnitude of V_{AB} determines if the reaction proceeds adiabatically (the electronic coupling is strong; $V_{AB} > k_BT$) or nonadiabatically (weak; $V_{AB} < k_BT$) [70].

Additionally the probability for ET to occur, P_{12}, is a function of V_{AB} and λ (Eqn. 3):

$$P_{12} = 1 - \exp((-\frac{V_{ab}^2}{h\nu})\sqrt{\frac{\pi^3}{\lambda k_B T}}) \quad (3)$$

where h is Planck's constant (4.14×10^{-15} eV·s), ν is the typical frequency for nuclear motion (10^{13} s^{-1}) [57], k_B is the Boltzmann's constant (8.62×10^{-5} eV/K), and T is the temperature in Kelvin (273 K). P_{12} is another indication of whether a reaction occurs adiabatically or nonadiabatically: if the probability is high (~1), ET occurs adiabatically and vice versa.

The activation energy, ΔG^*, is the energy required to (thermally) excite the system to the transition state configuration, and can be estimated for the adiabatic case as (Eqn. 4):

$$\Delta G^* = \frac{(\lambda + \Delta G^0)^2}{4\lambda} - V_{AB} \quad (4)$$

If the electronic coupling is strong, the ET reaction occurs adiabatically and the ET rate, k_{ET}, is expressed as (Eqn. 5):

$$k_{ET} = \upsilon e^{\frac{-\Delta G*}{k_B T}} \quad (5)$$

If the electronic coupling is weak, the ET reaction occurs nonadiabatically and k_{ET} is expressed as (Eqn. 6):

$$k_{ET} = \frac{2\pi}{\hbar}|V_{AB}|^2 \frac{1}{\sqrt{4\pi\lambda k_B T}} \exp(-\frac{(\Delta G^0 + \lambda)^2}{4\pi\lambda k_B T}) \quad (6)$$

The OS-ET reaction was found to be complicated as energy minimization of the product state shows that proton transfer (PT) is coupled to the ET. Proton-coupled electron transfer (PCET) was also observed in calculations for the reduction of triscarbonato uranyl by Fe^{2+} [57]. To understand the rates of elementary steps involved, Wander, *et al.* (2006) [57] treated the OS-ET as two different models, as a concerted-PCET reaction ($PCET_{conc}$) and as a sequential-PCET ($PCET_{seq}$) reaction. The $PCET_{conc}$ reaction describes ET and PTs occurring simultaneously while the $PCET_{seq}$ reaction describes ET to occur first and was followed by PT. Separating the ET from the PT led to significantly different thermodynamics and ET rates for the reduction of triscarbonato uranyl by Fe^{2+}. More so, the comparison between the two different models enabled the authors to conclude that the ET step of the $PCET_{seq}$ was rate-limiting [57]. This approach was adopted into the present study; the two different models were applied to the OS-complex in the ferrimagnetic spin configuration. The PE surfaces for the $PCET_{seq}$ reaction showed different curvatures between the ET step and the PT step (*i.e.,* the curvature for the PT was steeper). Thus, λ values for the PT were calculated with both the shallow and steep curvatures, providing a range of values for λ, ΔG^*, V_{AB}, and k_{ET}.

The reaction energy to proceed from an OS complex to an IS complex was calculated as a dehydration reaction (Eqn. 7):

$$Fe(H_2O)_6^{2+} - UO_2(OH)_2(H_2O)_2 \leftrightarrow ((H_2O)_4Fe(OH)_2 - UO_2(H_2O)_2)^{2+} + 2H_2O \quad \Delta E_{dehydration} \quad (7)$$

The gas-phase energetics for the dehydration reaction were corrected for aqueous solution conditions by calculating the energy for the water molecule with the COnductor-like Screening MOdel (COSMO) [73, 74], as the energy of a water molecule is significantly better described by including solvation interactions. COSMO corrections for the metal species were found to cancel due to large and similar cavity sizes and identical net charge.

3.4 Results

3.4.1 Experimental Results

3.4.1.1 Experiment 1: Thermodynamically favorable and kinetically rapid conditions

At conditions where uranyl reduction had been observed (0.16 mM U(VI), 1 mM Fe(II)), the aqueous uranium concentration decreases rapidly during the first 15 minutes of reaction. Within the first hour of reaction, the concentration decreases by an order of magnitude (*i.e.,* from 0.16 mM to 0.02 mM UO_2^{2+}) (Figure 3-4a, c). After 8 hours of reaction, $U(VI)_{aq}$ reaches an equilibrium concentration of $\sim 7\times10^{-7}$ M, which remained constant until the experiment's completion. In agreement with previous studies [15], the removal of aqueous U in a Fe^{2+}-containing solution at near-neutral pH under anoxic conditions occurs rapidly.

Fe^{2+} concentrations were measured concurrently to assess whether they correlated with changes in uranyl concentrations. Such a correlation would suggest chemical reduction and eventual precipitation of $UO_{2(s)}$. $[Fe(II)_{aq}]$ show a decreasing trend similar to that of $[U(VI)_{aq}]$ (Figure 3-4b, c). However the proportion of Fe to U removed is 1.4 to 1 instead of the expected 2 to 1 ratio, considering simple mass and electron balance for reduction to U(IV) (Figure 3-4d). Thus, Fe^{2+} concentrations indicate only partial reduction of U(VI). Assuming the loss of Fe^{2+} is due exclusively to chemical reduction, an estimated maximum of ~0.02 mM U(VI) (~13%) is reduced at 45 minutes and ~0.06 mM U(VI) (~38%) by 72 hours.

The pH decreased from 7.19 to 7.09 within the first 8 hours, but remained constant at pH 7.09 from 8 hours onward to 72 hours of reaction. The pH changes also correlate to $[U(VI)_{aq}]$ changes, where the U(VI) concentration reached equilibrium after 8 hours, as mentioned above. This decrease in pH is in agreement with the generation of solid (redox) products, such as the precipitation of iron oxides and of uranium phases including schoepite and uraninite; these processes increase the acidity of the solution as discussed below.

Analyses of aqueous uranyl concentrations show uranyl is removed from solution over time, though the mechanism(s) controlling uranyl removal from solution are uncertain. Decreasing Fe(II) concentrations indicate partial U(VI) reduction occurred, though it is unclear if reduction occurred in a homogeneous environment (where aqueous U(VI) is reduced by aqueous Fe(II)) or in a heterogeneous environment (where formation of iron or uranyl-containing solids

in turn facilitate U reduction). Control experiments were conducted to show whether a homogeneous system was maintained. After equilibration, both 0.17 mM UO_2^{2+} and 1 mM Fe^{2+} stock solutions at pH 7.2 were filtered through syringe filters (25 mm–diameter PTFE membrane, 0.22 μm pore size), which were set aside for solid analyses. Equilibration of the 1 mM Fe^{2+} solution at pH 7.2 showed little to no Fe^{2+} was removed from solution after filtration, over 24 hours. The precipitation of green rust or iron redox products did not occur under these conditions. Conversely, the concentration of the 0.17 mM UO_2^{2+} solution decreased to 0.05 mM U within the first 1.5 hours (similar to the rate the in uranyl concentration decreases in the Fe-U experiment). A uniform coating of bright-yellow precipitates was observed on the filter, and the solids were characterized to be predominantly (meta)schoepite using XRD (~74% schoepite, ~16% metaschoepite, and ~10% β-$UO_2(OH)_2$) (Figure 3-5).

These control experiments show the precipitation of (meta)schoepite to be the primary mechanism controlling uranyl removal from solution. Geochemical models also indicate the system being supersaturated with respect to schoepite (Figure 3-6). The removal of uranyl could not be attributed to the chemical reduction of soluble U(VI) by soluble Fe(II) as concluded by previous experiments [15]. It is thus expected that any chemical reduction of U(VI) by Fe(II) at these conditions is a result of catalytic effects supplied by the solid substrate. This conclusion supports previous results where U(VI) reduction by Fe(II) is observed to occur only in heterogeneous systems [12, 13].

XPS analyses on the solid fractions were used to observe whether the chemical reduction of uranyl by ferrous iron had occurred. Powders covered the filters uniformly and facilitated XPS analyses. The U 4f XP spectra for the solid samples collected at 45 minutes and up to 72 hours showed clear asymmetry in the U 4f 7/2 and 5/2 peaks, indicating more than one oxidation state of uranium being present (Figure 3-7a). GL curves were fit at 381.7 ± 0.2 and 380.7 ± 0.2 eV BEs (Figure 3-7b). The component peak at 381.7 eV is attributed to U(VI). U(VI) is the predominant oxidation state of the solid, as shown by the higher intensity of the U(VI) component peak as well as the clear observance of U(VI) satellite peaks (Figure 3-7b, Table 3-2); the satellite for 7/2 peak is at 385.6 eV and the satellites for the 5/2 peaks are at 396.7 and 402.8 eV. It should also be noted that the BE for the U(VI) phase measured is lower than BEs reported for typical uranyl oxide phases such as schoepite (382.3 eV); this energy difference is

possibly due to more complex bonding environments on the surface of the solid where U(VI)–O-U(V,IV) bonds, for instance, may exist.

The lower BE component peak at 380.7 eV is associated with the reduced uranyl fraction, though it is difficult to attribute the peak to a single uranium oxidation state. U(IV) and U(V) can be difficult to distinguish because the BEs of their (pure) oxides partially overlap (379.8–380.5 eV for U(IV) oxides; 380.1 ± 1 eV for U(V) oxides) (limited information on U(V) oxides is available) [75-77]. Satellite features are often more helpful to discriminate between these oxidation states, though clear U(IV) or U(V) satellite peaks could not be observed in the spectra collected due to the small fraction of reduced uranyl present. Faint U(V) 4f 7/2 satellites (388.7 ± 0.2) were visible in some spectra (*i.e.,* 45 minutes, 24 hours, 72 hours), suggesting the chemically reduced uranyl portion may be U(V), though it was difficult to observe the 5/2 satellite due to background noise. Unfortunately, not enough information was available from the XPS analyses to determine the ratio between the concentrations of U(V) and/or U(IV) present.

The reduced uranyl portion after 45 minutes reaction time is estimated to be up to ~24% of the total uranium present (Table 2). After 72 hours, the proportion of reduced U increases slightly to ~26%. The small changes in the reduced uranyl proportions show the chemical reduction of U(VI) within the near surface of (meta)schoepite occurs rapidly and little uranyl is reduced after 45 minutes. Thus, rapid reduction of uranyl occurs at the surface of the (meta)schoepite; uranyl is rapidly precipitated from solution at the beginning of the experiment as (meta)schoepite where the formation of a solid facilitates adsorption of Fe(II) onto the surface of the bulk U phase. This result is reminiscent of heterogeneous experiments where reduction occurs at a timescale of hours [12, 13]. Additionally, the formation of a passivation layer of reduced species on the schoepite surface is believed to inhibit further reduction of uranyl within the bulk of the solid U phase [78, 79].

The estimated reduced uranyl proportions based on the decrease of Fe^{2+} concentrations in batch experiments (analyzed by ICP-MS) somewhat disagree with those derived from XPS solid analyses. As mentioned earlier, assuming the amount of Fe^{2+} removed from solution was lost entirely to the chemical reduction of uranyl, the resulting Fe to U ratios would erroneously lead to the belief that up to ~13% of uranyl was reduced to U(IV) (~0.02 mM U) after 45 minutes and ~38% of uranyl was reduced to U(IV) (or ~0.06 mM U) after 72 hours. The XPS data indicate

instead that up to ~24% of the uranyl was reduced (~0.04 mM U) within the first 45 minutes, and it is not certain whether complete reduction to U(IV) occurred. While quantification of the reduced uranyl proportion from XPS analysis is less accurate than those using aqueous methods such as ICP-MS, the XPS data imply a fraction of the Fe(II) removed from solution did not participate in uranyl reduction. It is plausible that a portion of Fe(II) removed from solution and not involved in the chemical reduction of uranyl may have precipitated with iron oxide redox products. Fe(III) generated from the oxidation of Fe(II) and reduction of mM to μM amounts of U(VI) would be well above the saturation limit of several iron oxides such as magnetite (Fe_3O_4). Characterization of the iron redox products is relevant to deciphering the mechanisms and processes that concern this study. Unfortunately, the scarcity of solids collected prevented the identification of potential iron redox products using either XPS or XRD. The relevance of characterizing these redox products will be revisited in the discussion.

3.4.1.2 Experiment 2: Thermodynamically favorable but kinetically slow conditions

For conditions where uranyl reduction had not been observed (0.02 mM U(VI), 1 mM Fe(II)) [13], $[U(VI)_{aq}]$ is constant for the first 3 hours of reaction, suggesting uranyl remains in the aqueous phase (Figure 3-4a, c). However, after 3 hours, $[U(VI)_{aq}]$ decreased by micromolar amounts (< 5 μM) and after 24 hours about 50% of the aqueous uranyl (0.01 mM) is removed from solution. At 72 hours, the uranyl concentration reaches 1.8×10^{-7} M, close to the analytical limit of detection (1.6×10^{-7} M U, 0.3 ppb) and near schoepite's solubility limit.

Fe^{2+} concentrations were measured concurrently to assess whether uranyl reduction was occurring. $[Fe(II)_{aq}]$ remain fairly constant during the 72-hour reaction period (Figure 3-4b, c), as expected. The amount of Fe(II) required to chemically reduce all the U(VI) present is within the analytical error; reduction of the 0.02 mM U(VI) would lead to a less than 4% change in the Fe^{2+} concentrations, which is within the error of the measurements (5%). Consequently, changes in Fe^{2+} concentrations could not be used as a proxy for chemical reduction. The stability of the Fe^{2+} concentrations indicates that the loss of Fe^{2+} would be due to the production of only small amounts of Fe^{3+} redox products. pH measurements also do not indicate significant generation of solid (redox) products; the pH remained constant at 7.18 ± 0.3 over the 72-hour reaction (within the error of the pH meter).

(Meta)schoepite precipitates were not visible to the naked eye at these concentrations in contrast to those observed in Experiment 1. To test whether precipitation was occurring, a control experiment for 0.02 mM U(VI) at pH 7.2 was conducted, similar to the experiment conducted for the 0.17 mM U(VI) solution. The solution was equilibrated, with solids collected on filters at 3 and 24 hours using 0.02 μm Anopore aluminum oxide membranes (Whatman Anotop syringe filters) to ensure collection of nanoparticulate uranium precipitates. SEM imaging was used to confirm precipitation of uranium solids. The filter at the 3-hour sampling time did not show uranium precipitates (Figure 3-8a). However, the filter for the 24-hour sample contained clumped aggregates of rod-shaped precipitates, generally longer than 500 nm; EDS identified the precipitates to be a uranium oxide (Figure 3-8b). This is in agreement with the aqueous data where uranyl remained in the aqueous phase for the first 3 hours and considerable precipitation occurred after 24 hours. Thus, uranyl reduction by ferrous iron at these experimental conditions is again predicted to occur via heterogeneous pathways that involve reaction on or catalysis by surfaces in contact with solution.

Solids collected on the filters were sparsely found, making it difficult to obtain high-quality XP spectra. U 4f spectra on samples from 45 minutes to 8 hours were broad, noisy, and difficult to quantify (not shown in Figure 3-7c). Distinct U 4f peaks appeared in correlation to removal of ~50% of the aqueous uranyl from solution (*i.e.,* from 24 hours onwards) (Figure 3-7c). The U 4f 7/2 and 5/2 peaks showed asymmetry, implying the presence of uranium in more than one oxidation state. GL curves were fit for the U 4f 7/2 peak with BEs of 381.5 ± 0.1 eV (U(VI) phase) and at 380.4 ± 0.1 eV (reduced uranyl phase). The predominant oxidation state of the solid was U(VI) based on the higher intensity component peak at 381.5 eV and faint U(VI) satellite peaks for the 7/2 peak at 385.0 eV and the 5/2 peak at 396.1 and 402.6 eV. The oxidation state of the reduced uranyl fraction at 380.4 eV is again less distinct; satellite peaks for U(V) and U(IV) were inseparable from the background noise. At 24 hours, an estimated 30 - 33% of the total uranium present was in the reduced phase (Table 2); the uranyl proportions remained constant at 48 and 72 hours suggesting that most of the reduction occurred within the first 24 hours. This is again consistent with uranyl reduction occurring rapidly at the onset of U(VI) precipitation.

These experimental results suggest that uranyl reduction is facilitated by the formation of a heterogeneous system. Thermodynamic calculations are compared to these observations to better understand whether uranyl is capable of being reduced by ferrous iron in a homogeneous system (Figure 3-9). Redox reaction thermodynamics (at the given experimental conditions) were calculated to be endothermic when aqueous redox products (*i.e.,* $Fe(OH)_2^+$ and $U(OH)_4$) were produced, regardless of the aqueous reactant species used (Figure 3-9) (Eqn. 8). The thermodynamic favorability of the redox reaction is heavily influenced by the formation of solid redox products, particularly the formation of specific Fe^{3+} solids. For instance, uranyl reduction to $U(OH)_{4(aq)}$ was endothermic when coupled with formation of $Fe(OH)_{3(s)}$ (Eqn. 9) but was exothermic with the formation of $Fe_2O_{3(s)}$ (Eqn. 10) (again regardless of the aqueous reactant species used).

$$2Fe^{2+} + \frac{1}{3}(UO_2)_3(OH)_5^+ + \frac{13}{3}H_2O \rightarrow 2Fe(OH)_2^+ + U(OH)_4 + \frac{7}{3}H^+ \qquad \Delta G = +161 \text{ kJ/mol} \qquad (8)$$

$$2Fe^{2+} + \frac{1}{3}(UO_2)_3(OH)_5^+ + \frac{19}{3}H_2O \rightarrow 2Fe(OH)_{3\,(s)} + U(OH)_4 + \frac{13}{3}H^+ \quad \Delta G = +19 \text{ kJ/mol} \quad (9)$$

$$2Fe^{2+} + \frac{1}{3}(UO_2)_3(OH)_5^+ + \frac{10}{3}H_2O \rightarrow Fe_2O_{3\,(s)} + U(OH)_4 + \frac{13}{3}H^+ \qquad \Delta G = -46 \text{ kJ/mol} \quad (10)$$

These thermodynamic results are in agreement with Felmy, *et al.* (2011) [52] where the free energy of the Fe^{3+} reaction product is a key factor in determining the conditions where UO_2^{2+} can be reduced by Fe^{2+}. Additionally, this study and Felmy, *et al.* (2011) [52] predict uranyl reduction by ferrous iron in a homogeneous system (where reactants and products are all in the aqueous phase) is not thermodynamically favorable at near-neutral pH values. These calculations further support experimental observations of uranyl reduction being facilitated in heterogeneous systems. They also show the importance of accounting for the aqueous redox products to form before the solid phases, as this approach leads to considerably different conditions where uranyl reduction by Fe^{2+} is thermodynamically favorable.

In summary, the removal of uranyl from solution in a homogeneous, ferrous-iron containing solution is from the precipitation of (meta)schoepite, not from the chemical reduction of uranyl by ferrous iron in aqueous phase and the subsequent precipitation of $UO_{2(s)}$. The creation of a heterogeneous system following uranium precipitation creates an environment

conducive towards the chemical reduction of uranyl by ferrous iron. This supports previous experimental results where the chemical reduction of uranyl by ferrous iron occurs in heterogeneous systems, such as in the presence of iron oxides [12, 13]. Further clarity for why uranyl reduction by ferrous iron in a homogeneous system is not observed will be provided through the thermodynamics and kinetics of molecular-scale ET reactions mechanisms modeled using *ab initio* methods.

3.4.2 Computational results

3.4.2.1 Outer-sphere ET thermodynamics and kinetics

Structures for pre- and post-ET OS-complexes were geometry optimized using a DFT-B3LYP approach (Figure 3-10a, b). Electron localization was assessed by Mulliken spin density distributions. Mulliken spin densities for the Fe^{2+} and UO_2^{2+} ions in the pre-ET model were approximately +3.85 (formal spin of +4) and 0 (0), respectively, while for the Fe^{3+} and UO_2^{+} ions in the post-ET models, they were approximately +4.26 (+5), and ±1.12 (±1), respectively (the negative sign of the U spin indicates the spin direction is opposite to the Fe spin direction). Additionally, the bond distances reflect the correct oxidation states for both the pre- and post-ET models, where shorter average bond lengths are observed for the Fe^{3+} and U^{6+} in comparison to Fe^{2+} and U^{5+}, respectively (Table 3); larger bond length changes are incurred in cations where the electron is localized.

In addition to the respective lengthening and shortening of bonds for each model, the optimized structures show the reduction of U(VI) to U(V) by Fe(II) as an OS complex proceeds as a PCET reaction. The ET from the Fe(II) to the U(VI) is accompanied by spontaneous transfer of two protons. After ET, the uranyl molecule was hydrated from $UO_2(OH)_2(H_2O)_2$ to $UO_2(H_2O)_4^{+}$; each of the hydroxyl ligands of the uranyl molecule acquired a hydrogen atom from water ligands associated with the iron complex. The aquo Fe^{2+} complex was hydrolyzed from $Fe(H_2O)_6^{2+}$ to $Fe(OH)_2(H_2O)_4^{+}$. This is in agreement with the chemical speciation and behavior of ferric iron in solution where water molecules, when bound to Fe^{3+}, are Bronsted-Lowry acids and hydrolyze to induce the formation of ferric iron hydroxide species.

From the geometry-optimized structures and their total energies for the pre- and post-ET systems, the thermodynamics and kinetics for the ET from Fe^{2+} to UO_2^{2+} were determined. The free energy of the $PCET_{conc}$ reaction was exothermic for the ferromagnetic and ferrimagnetic

cases (–19 and –35 kJ/mol, respectively). Based on just the free energy of reaction, the first ET step would be plausible for U(VI) to be reduced by Fe(II) in a homogeneous system. The thermodynamics differ between the computational and empirical calculations; thermodynamic calculations using empirical data predict uranyl reduction to be energetically unfavorable in a homogeneous system (as presented above) while these *ab initio* calculations suggest the first ET step occurs. Thermodynamic calculations using empirical calculations account for more extensive hydrolysis reactions and changes in speciation of the reduced products (*e.g.,* UO_2^{2+} + 2*e*- → $U(OH)_4$). The molecular computational models provide a quantum-level understanding of uranyl reduction and the thermodynamics reflect the energetics of atomistic redox-reaction mechanisms.

Even though the ET reaction is thermodynamically downhill, the kinetics of the reaction are predicted to be slow; the coupling of two PTs to the ET for the ferromagnetic and ferrimagnetic cases yield vanishingly small (effectively zero) rates, $\sim 10^{-21}$ and 4×10^{-19} s^{-1}, respectively (Figure 3-10c, Table 3-4). Additionally, only the ferromagnetic case proceeds adiabatically (V_{AB} = 9.9 kJ/mol), though the predicted rate remains negligible. These slow rates are due to a persistent tendency for the ET reaction to be coupled to spontaneous PTs, requiring substantial structural rearrangement through bond breaking and reforming that accompanies the redistribution of the electron density. The activated complex is thus characterized by a nuclear configuration involving two H^+ ions dissociated from water molecules in transit relatively long distances (because of the OS encounter complex treatment) to the uranium hydration sphere. High reorganization energies (+707 and +769 kJ/mol for the ferromagnetic and ferrimagnetic models, respectively) and activation energies (+192 and +176 kJ/mol, respectively) are incurred by the significant structural rearrangement of the OS complex. We consider our calculated energetics to be maximum values, as the LST method to determine the reaction coordinates does not ensure an energy minimized pathway. It is possible that second-shell waters could provide lower energy pathways for PT, particularly in the OS encounter complex, though these are not included in our treatment. Nonetheless, the coupled PTs and hydrolysis of the aquo Fe molecule lead to considerable energetic barriers affecting the ET rate for the OS $PCET_{conc}$ system.

Treatment of the OS ET as a $PCET_{seq}$ reaction was also done to observe the ET energetics without the energetic contributions from the spontaneous PTs; U(VI) was first reduced to U(V)

(an intermediate structure, using a ferrimagnetic spin configuration for this calculation) with the PTs following the ET step. To model the post-ET state without PT occurring concurrently, all OH bond distances (excluding hydrogen bonds) were fixed relative to the O atoms in the pre-ET state and the structure was energy minimized. In this treatment, the energetic barriers for ET are lowered; the activation energy decreases by ~50 kJ/mol to +117 kJ/mol and the reorganization energy decreases by ~500 kJ/mol to +210 kJ/mol (Figure 3-10d, Table 3-4). This confirms that a substantial contribution to the activation energy in the $PCET_{conc}$ treatment arises from the dissociation of OH bonds. However, the ET step for the $PCET_{seq}$ treatment is thermodynamically unfavorable (+102 kJ/mol) due to the steric constraints placed on the system. Thus, although the rate of ET from Fe(II) to U(VI) increases through a $PCET_{seq}$ reaction mechanism, the ET rate remains slow (3×10^{-12} s^{-1}).

The second step of $PCET_{seq}$, involving PTs and the structural rearrangement of the OS complex, is exothermic (-134 kJ/mol) and is characterized by lower activation energies than the ET step (+84 to +8 kJ/mol); these trends are expected given that the ET has increased the negative charge density on the uranium ion. However, the overall $PCET_{seq}$ reaction would be limited by the slower of the two component rates in the sequential mechanism – the ET step. It thus appears that the tendency for the Fe^{3+} molecule to hydrolyze during ET leads to a configurational barrier that hinders U(VI) reduction by Fe(II) as an OS encounter complex.

3.4.2.2 Inner sphere ET thermodynamics and kinetics

As was done with the OS models, the structures for the pre- and post-ET IS models were geometry optimized (Figure 3-11a, b). Correct oxidation states were also confirmed through analysis of Mulliken spin density distributions (pre-ET: $Fe^{2+} \approx +3.83$ and $UO_2^{2+} \approx -0.01$; post-ET: $Fe^{3+} \approx +4.25$ and $UO_2^{+} \approx \pm1.15$) (Table 3-3) and through assessment of calculated bond distances. Interatomic distances for the IS complex are also in good agreement with experimental results; *e.g.,* our Fe-U distance is ~ 3.5 Å, which is similar to experimentally-measured Fe-U distances observed for uranyl adsorbed on iron (oxyhydr)oxides as an IS complex (3.44 - 3.49 Å) [24, 55, 80].

Similar to the OS $PCET_{conc}$ model, the reduction of U(VI) to U(V) is found to be thermodynamically favorable for both the ferromagnetic and ferrimagnetic models (–16 kJ/mol for both reactions) (Figure 3-11c, Table 3-4). In contrast to the OS complex, the IS complex does

not exhibit spontaneous PT accompanying ET. In turn, the energetic parameters and the kinetics are not affected by large energetic contributions from the OH dissociation. The activation energies are low in comparison to those for all of the OS models (+38 and +33 kJ/mol for the ferromagnetic and ferromagnetic models, respectively). The reorganization energies for the IS models are also considerably lower than those observed in the OS $PCET_{conc}$ complex (+186 and +175 kJ/mol, respectively). The reorganization energies are close to those obtained for the ET step of the OS $PCET_{seq}$ model; this is reasonable because in both cases the absence of PTs means that internal reorganization energy arises primarily from small adjustments to bond lengths and angles in the Fe-U encounter complex. The energetic barriers for ET are thus shown to be significantly reduced upon formation of a hydroxyl-ligand bridge between the uranyl and ferrous iron ions. In turn, the resulting ET rates for the ferromagnetic and ferrimagnetic reactions are calculated to be orders of magnitude faster than the OS rates (2×10^4 and 3×10^8 s^{-1}, respectively). More so, the ferrimagnetic ET proceeds adiabatically (V_{AB} = 9.8 kJ/mol) and would represent the most likely pathway for ET to occur in the IS complex.

U(VI) reduction by Fe(II) in a homogeneous system is calculated to be thermodynamically favorable and kinetically feasible when U and Fe form an IS encounter complex via bridging-hydroxyl ligands. This suggests that ET between U(VI) and Fe(II) is highly dependent on the ease by which an IS complex may form. Our molecular computations address the thermodynamic favorability for an OS complex to transition to an IS complex (via Eqn. 7), where it is found that +96 kJ/mol of energy is required to remove two water molecules from the OS complex to become an IS complex. Thus, based on the thermodynamic unfavorability for an OS Fe-U complex to dehydrate and form an IS complex, the formation of an IS Fe-U complex within which ET may proceed is predicted to be exceptionally low in an aqueous, homogenous solution.

3.5 Discussion

The experimental results are in agreement with previous studies where the removal of uranyl at high concentrations is observed. However, the mechanisms for the removal of uranyl were not attributed to the chemical reduction of aqueous uranyl and subsequent precipitation of $UO_{2(s)}$ as in Aboud, *et al.* (2011) [81] (Figure 3-1; Table 3-1; Processes 2, 5, 6). In contrast, this study indicates the removal of uranyl due to the precipitation of (meta)schoepite and the

subsequent transitioning to a heterogeneous system further enabled uranyl reduction by ferrous iron (Figure 3-1; Table 3-1; Processes 3, 7). These results support solubility data (Figure 3-6) as well as results from previous studies concluding that the chemical reduction of U(VI) by Fe(II) proceeds rapidly in heterogeneous systems, such as uranyl and ferrous iron coadsorbed onto iron oxide minerals [12, 13]. These batch experiments show U(VI) is removed from solution by precipitation and that transitioning to a heterogeneous system enables uranyl reduction to occur, where the surface of the solid U phase is partially reduced to U(IV) and/or U(V). This study also shows redox reaction thermodynamics are endothermic in a truly homogeneous system, where aqueous redox products (*i.e.,* $Fe(OH)_2^+$ and $U(OH)_4$) are produced.

To substantiate experimental observations, *ab initio* methods and ET calculations provide further thermodynamic and kinetic data as well as an understanding of molecular-scale reaction mechanisms significantly. The progression of U(VI) reduction to U(V) as a PCET reaction leads to high energetic barriers and in turn slow ET rates. These rates and energetics are in agreement with values obtained for ET between Fe^{2+} and uranyl-carbonate complexes [57]. In contrast, achieving an IS complex through bridging hydroxyl ligands enables rapid reduction of U(VI) to U(V). This is in agreement with surface complexation models predicting U(VI) reduction by Fe(II) to proceed as an IS reaction, based on the formation of IS oxidant and reductant complexes on iron (hydr)oxide surfaces [12, 14, 50]. Furthermore, the ease with which ET proceeds in an IS complex also supports the rapid reduction rates observed in heterogeneous systems on (hydr)oxide minerals, where the reduction rates have been directly proportional to the concentration of hydroxylated Fe^{2+} surface complexes [12, 14]. However, our study suggests that formation of the IS complex necessary for facile ET in homogeneous aqueous solution is unfavorable. These models provide a fundamental understanding of why reduction for the homogeneous uranyl-ferrous iron system is rarely observed.

The *ab initio* models are in agreement with other experimental observations such as the hydrolysis of Fe^{2+} and its enhanced reactivity; the aquo Fe^{2+} ion in the OS complex undergoes hydrolysis with and/or during ET, resulting in a hydroxylated Fe^{3+} ion. It is well known that hydrolysis of Fe^{2+} increases the oxidation rate; deprotonation of the aquo Fe^{2+} ion causes an accelerated oxidation rate by a factor of 10^4 and $Fe(OH)_2$ reacts 10^5 times faster than $Fe(OH)^+$ [82]. The precipitation of (uranyl) oxide phases can also facilitate the hydrolysis of divalent

cations including Fe^{2+} compared to solution [83], in turn accelerating its oxidation rate [50, 82]. Surface complexation models also predict uranyl reduction by ferrous iron to be kinetically inhibited, where Fe^{2+} hydrolysis and formation of a redox precursor-complex such as a binary Fe-U complex, are some of the postulated barriers [12, 82, 83]. These atomistic mechanisms are observed for the OS ET models in this study and are shown to have a considerable impact on the ET reaction thermodynamics and kinetics, whereby the IS complex is the product of overcoming these energetic barriers.

Chemical speciation also significantly influences whether reduction can occur via homogeneous pathways. The IS complex is less thermodynamically favorable than the OS complex, thus the formation of IS complexes would be limited in an aqueous system. The lowered stability of the IS complex is likely due to repulsive Coulombic forces between the positively charged Fe^{2+} and UO_2^{2+} species [84]. Our results suggest that homogeneous reduction may be significantly limited due to the unfavorability of IS interactions between Fe(II) and U(VI). Similarly, it is also plausible that the homogeneous reduction of metals such as Cr(VI) and Tc(VII) by Fe(II) are facilitated through the attraction, collision, and complexation between oppositely charged ions (CrO_4^{2-} and TcO_4^- and Fe^{2+}) [58, 85]. For instance, the free energy to bring two, oppositely charged CrO_4^{-2} and Fe^{2+} ions together is approximately –23 kJ/mol [58] while this study would predict 0 to +20 kJ/mol for $UO_2(OH)_2/UO_2^{2+}$ and Fe^{2+} species. Thus, while the reduced uranyl and oxidized Fe^{2+} products may be thermodynamically favorable, the formation of an IS complex is unfavorable (in comparison to other metal systems such as Cr(VI) and Tc(VII)) based on the chemical speciation.

For future studies, it is important to address areas of analysis that can be improved upon so that more accurate observations and predictions of uranyl reduction can be made. Analysis of the aqueous U(VI) fraction can lead to inaccurate predictions of the mechanisms governing uranyl removal from solution. Studies often correlate aqueous U(VI), extracted U(VI) (via the bicarbonate method) [80, 86], and loss of aqueous Fe(II) to quantify the amount of uranyl reduced. Stoichiometric relationships between the consumption of Fe(II) and removal of U(VI) help determine whether the chemical reduction of uranyl is occurring [11, 15, 87, 88]. However, in the uranyl-ferrous iron system it is difficult to attribute reduction solely to homogeneous pathways due to the complexities introduced by the generation of solid redox products and

transition to heterogeneous redox pathways. Aqueous analyses and interpretation of the mechanisms controlling uranyl removal from solution becomes complicated, as loss of uranyl could now be due to precipitation, adsorption, chemical reduction to U(IV) and precipitation to $UO_{2(s)}$, etc.,. In addition to analyzing the rate of uranyl removed from solution, it is necessary to apply a combination of different methods to determine the removal mechanisms.

To attribute the removal of uranyl from solution by reduction, identification of the solid redox products and physical evidence of U(IV) is needed for confirmation of chemical reduction occurring [89]. In this study, correlating aqueous data to uranyl reduction leads to higher concentrations of uranyl being reduced (~38% after 72 hours) though analysis of the solids show that U(VI) is the dominant oxidation state and that ~25% of the uranyl is reduced to U(V)/U(IV) within the first hour. Partial reduction of the uranyl solid is likely reached due to the formation of a passivation layer of reduced uranyl-oxide on the surface of the (meta)schoepite, which would inhibit further chemical reduction of U(VI) within the bulk [78, 79] (Figure 3-1; Table 3-1; Processes 7c, 8c). Additionally, based on the XPS data from this study, it is possible that a portion of the reduced uranyl product is U(V); previous studies showed the existence of U(V) over U(IV) could be due to coordination environments favoring U(V) [90-92]. Thus, more detailed analyses of the solid U redox product provide insight into whether U(VI) reduction to U(IV) is proceeding to completion, which isotherms do not always show, and in turn contribute to predicting the stability and solubility of the solid U phase.

In addition to solid U redox products formed, the co-precipitation of iron redox products adds to the complexity of the system and, more importantly, impacts the energetics of uranyl reduction. Felmy, *et al.* (2011) [52] calculated the thermodynamics for the reduction of U(VI) by Fe(II) to assess the impact of different Fe(III) reaction products (using conditions from Liger, *et al.* (1999) [12]). Under these conditions, aqueous Fe(II) could only reduce aqueous U(VI) to $UO_{2(am,s)}$ at pH > 8. If stable Fe(III) reaction products form, the pH range over which U(VI) reduction can occur will increase. For instance, if hematite formed (via the overall reaction: $U(VI)_{(aq)} + 2Fe(II)_{(aq)} \leftrightarrow UO_{2(am)} + Fe_2O_{3(s)}$), it becomes thermodynamically possible to reduce U(VI) to U(IV) at pH ≥ 6. The type of Fe(III) reaction product formed (*e.g.,* $FeOH_{3(s)}$ *vs.* $Fe_2O_{3(s)}$) also has a large impact on the pH range over which the reaction occurs. Unfortunately, the Fe(III) reaction product(s) could not be determined in this study (with analysis requiring use

of a combination of Mössbauer spectroscopy, TEM, XANES, and EXAFS) [85, 93]. The free energy of the Fe(III) reaction products is a key factor in determining the range of conditions under which U(VI) can be reduced by Fe(II); future studies should emphasize characterizing the solid iron redox products to better understand its impact in redox environments.

3.6 Conclusions

A more fundamental understanding of mechanisms involved in the abiotic reduction of U(VI) by Fe(II) has been gained by combining experiments and *ab initio* modeling. Through careful monitoring and analysis of both the aqueous and solid fractions over time, experiments have clarified that U(VI) reduction by Fe(II) occurs in a heterogeneous system. *Ab initio* calculations reveal the nature of thermodynamic and kinetic barriers that must be overcome at the molecular scale in order for reduction to proceed in a homogeneous system, such as dehydration of solvated complexes and Fe^{2+} hydrolysis. In turn, reduction of U(VI) by Fe(II) in a homogeneous system is predicted to be kinetically inhibited. These atomistic details are difficult to observe using geochemical models or experiments, and have helped reinforce deductions from experiments. Our results not only show the reduction of soluble U(VI) by soluble Fe(II) to be thermodynamically and kinetically limited under the given experimental conditions, but also, and most importantly, shed light on the feasibility of uranyl reduction in a homogeneous system under different chemical conditions (*e.g.,* in the presence of naturally occurring reductants such as sulfide and hydroquinone).

This study also helps provide insight into relevant redox mechanisms in analogous systems, such as reduction on mineral surfaces. Reduction of U(VI) by Fe(II) was found to be thermodynamically favorable and kinetically feasible for an IS complex. IS complexes are often observed for uranyl adsorbed onto iron oxide surfaces [24, 55, 80]. Thus, it is possible one of the atomistic mechanisms enabling reduction of uranyl in heterogeneous systems is the ability for the mineral surface to strip solvating waters and facilitate the formation of an IS complex. More so, it is of interest to understand whether minerals (particularly semiconducting minerals like hematite) directly participate in redox processes. Semiconducting minerals are hypothesized to provide a structural template that increases the probability of forming configurations compatible with ET/PCET and/or can serve as a conduit for shuttling electron density from donor to acceptor. It is well established that semiconducting minerals possess the ability to connect redox

reactions at a distance, where an electron from a reductant at one site of the mineral surface can be transferred through the mineral and reaches an oxidant within close proximity [17, 18, 94]. The effect of the mineral surface on the thermodynamics and kinetics for ET would again be important in predicting uranyl mobility and reactivity, and is currently being investigated.

An in-depth understanding of the conditions conducive for abiotic reduction of U(VI) by Fe(II) is required to accurately predict uranyl's mobility and reactivity. These conditions are a complex function of chemical speciation and solubility, molecular-scale reaction mechanisms, and the thermodynamics, kinetics, and reduction potential of uranyl in solution or sorbed onto geologic materials. For example, it has been shown that predictions for the field-scale behavior of radionuclides at the Hanford site were significantly improved in several transport models using in-depth atomistic and molecular-scale characterization [52]. Thus, to most accurately predict the migration of radionuclides and metals for realistic systems, integration of detailed experimental and computational results into conceptual models is needed. The methodology used in this study, combining experimental and computational approaches, has broad applications and will be applied in future studies to provide insight into redox reaction pathways and mechanisms for other redox-sensitive systems.

3.7 Acknowledgements

This research was supported by the U.S. Office of Science, BES/HEC (Basic Energy Sciences, Heavy Element Chemistry) DE-FG02-06ER15783. The authors would like to thank the following scientists for their technical assistance with the instrumentation used in this study: Dr. Thomas Yavaraski (ICP-MS), Dr. Zhongrui Li (XRD), Ke Yuan (SEM; instrumentation supported primarily by DOD-G-F49620-93-1-0289, Center for Advanced Structural Metallic Materials), and Dr. Eugene Ilton, Dr. Kai Sun, and Dr. Haiping Sun (XPS; instrumentation supported by NSF grant # DMR-0420785). We would like to further thank Dr. Eugene Ilton for his help with XPS analyses and revisions of this manuscript. We would also like to thank Dr. Drew Latta and Odeta Qafoku for their help with developing experimental procedures. KMR acknowledges support from the Geosciences Program at Pacific Northwest National Laboratory (PNNL) from the U.S. Department of Energy (DOE) Office of Science, Office of Basic Energy

Sciences, Division of Chemical Sciences, Geosciences, and Biosciences. A portion of the research was performed using EMSL, a DOE Office of Science User Facility sponsored by the DOE Office of Biological and Environmental Research and located at PNNL.

3.8 Tables

Table 3-1: Description of possible behaviors for U and Fe in homogeneous systems, relevant to this study, as shown in Figure 3-1.

	Behavior	**General factors influencing proposed behavior**
1	Aqueous U(VI) and Fe(II)	Concentrations below solubility limits ($\log {}^{*}K_{sp,U(VI)\text{-}hydroxides}$=[4.9, 7.7]; $\log {}^{*}K_{sp,Fe(II)\text{-}hydroxides}$ =[12.9, 13.5]) at appropriate conditions (*e.g.,* pH) [48, 51]
2a	Complexes between aqueous Fe(II) and U(VI)	Limited experimental data
2b	Reduction of U(VI) by Fe(II) in aqueous complexation	Theoretical studies show dependence on thermodynamics, kinetics, complexing ligands, outer- vs. inner-sphere coordination, etc., [57, 95]
3	Precipitation of U(VI)	Concentrations above solubility limits at appropriate conditions (*e.g.,* pH > 4.5)
4	Precipitation of Fe(II)	Concentrations above solubility limits (*e.g.,* pH > 7.5)
5a	Oxidation of soluble Fe(II) to Fe(III)	Availability and reactivity of oxidant at appropriate conditions (*e.g.,* Eh-pH)
5b	Precipitation of Fe(III)	Above Fe(III) phase solubility products ($\log {}^{*}K_{sp,Fe(II)/(III)\text{-}(hydr)oxides}$ = [-1.4, 3.4]) [51]
6a	Reduction of soluble U(VI) to U(IV)	Availability and reactivity of reductant [15] at appropriate conditions (*e.g.,* Eh-pH)
6b	Precipitation of U(IV)	Above U(IV) phase solubility products ($\log {}^{*}K_{sp,UO2}$ = -4.7) [48, 51]
7a	Adsorption of Fe(II) on solid uranyl phase	Solids present (generated through processes such as 3 and 6b) with available surface sites, at appropriate solution conditions (*e.g.,* pH)
7b	ET between U(s) and Fe(II)	Complexation such as in process 2
7c	Formation of passivation layers on original U(s)	Surface area saturated by redox products without new surface area being exposed after reaction
8a	Adsorption of U(VI) on solid ferrous iron-containing phase(s)	Solids present (generated through processes such as 4 and 5b) with available surface sites, at appropriate solution conditions (*e.g.,* pH)
8b	ET between Fe(s) and U(VI)	Complexation such as in process 2
8c	Formation of passivation layers on original Fe(s)	Surface area saturated by redox products without new surface area being exposed after reaction

Table 3-2: Proportion of reduced U over time from XPS quantification.

Time (hour)	**Expt 1**		**Expt 2**	
	% U(VI)	**% U reduced**	**% U(VI)**	**% U reduced**
Schoepite standard	99.4	0.6	_____	_____
0.75	76.1	23.9	NA	NA
3	75.1	24.9	NA	NA
8	74.5	25.5	NA	NA
24	74.3	25.7	65.1	34.9
48	73.2	26.8	67.4	32.6
72	73.8	26.2	66.6	33.4

Table 3-3: Measured atomic distances for Fe and U cations for the outer-sphere (OS) and inner-sphere (IS) models.

Average distance (Å)	**Model**			
	Outer-sphere		**Inner-sphere**	
	Pre-ET	**Post-ET**	**Pre-ET**	**Post-ET**
U-OH_{eq}	2.219	NA	2.288	2.56
U-$OH_{2,\ eq}$	2.532	2.519	2.505	2.514
U-O_{ax}	1.769	1.803	1.752	1.795
U-Fe	4.831	4.811	3.412	3.455
Fe-OH	NA	1.875	2.105	1.896
Fe-OH_2	2.152	2.162	2.186	2.17

Table 3-4: Calculated thermodynamic and kinetic properties for the OS and IS models. *Denotes reactions that are adiabatic. **Denotes properties determined using data fit to PT values.

Model (spin-configuration)	**ΔG^0 (kJ/mol)**	**λ (kJ/mol)**	**ΔG^* (kJ/mol)**	**V_{AB} (kJ/mol)**	**P_{12}**	**k_{ET} (s^{-1})**
Outer-sphere (ferromagnetic)	-19.395	769.105	192.348	9.928	0.963	9.892×10^{-20}*
Outer-sphere (ferrimagnetic)	-35.403	707.345	176.809	1.349	0.061	3.760×10^{-19}
Outer-sphere (ferrimagnetic, ET without PT)	102.113	209.984	117.138	0.193	0.002	3.111×10^{-12}
Outer-sphere (ferrimagnetic, ET with PT)	-134.421	(524.960**, 209.984)	(83.994**, 8.399)	(0.412**, 0.167)	(0.007**, 0.002)	(1.750×10^{-3}**, 1.783×10^{9})
Inner-sphere (ferromagnetic)	-16.202	186.245	37.774	0.624	0.026	2.056×10^{4}
Inner-sphere (ferrimagnetic)	-16.376	174.558	33.493	9.8015	0.999	2.750×10^{8} *

3.9 Figures

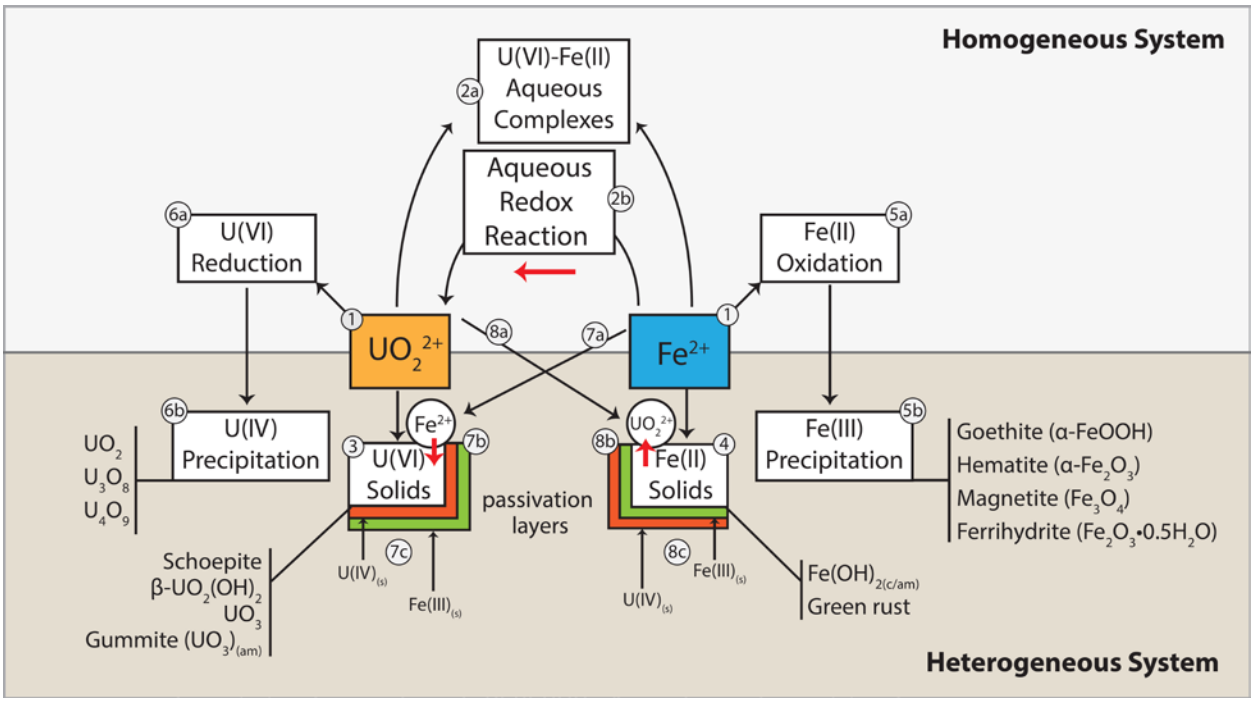

Figure 3-1: Potential processes occurring in a homogenous system between uranyl and ferrous iron, including processes leading to the transition towards a heterogeneous system. The red arrows denote processes where ET is occurring.

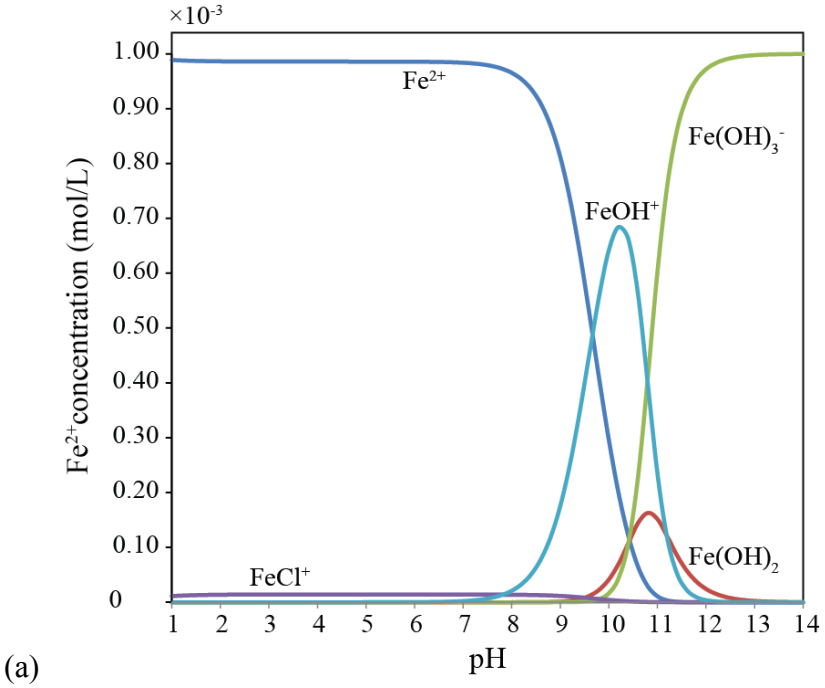

(a)

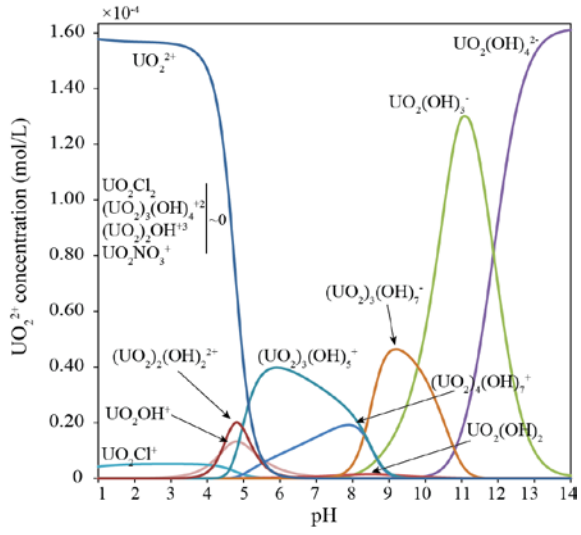

(b)

Figure 3-2: (a) Aqueous chemical speciation for 1 mM Fe(II) (in the presence of 0.16 mM U(VI)) at experimental conditions (50 mM NaCl, 5 mM HEPES, pH_2=0.05 atm, pN_2= 0.95 atm). (b) Aqueous chemical speciation for 0.16 mM U(VI) (in the presence of 1 mM Fe^{2+}) at experimental conditions.

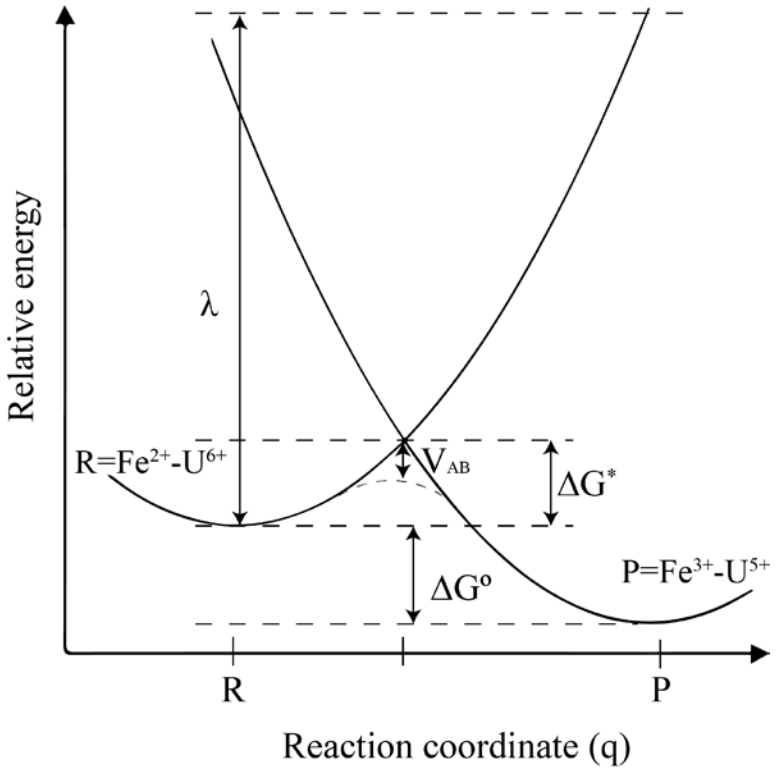

Figure 3-3: Free energy diagram of an electron transfer reaction. Modified from Kerisit *et al.*, (2006).

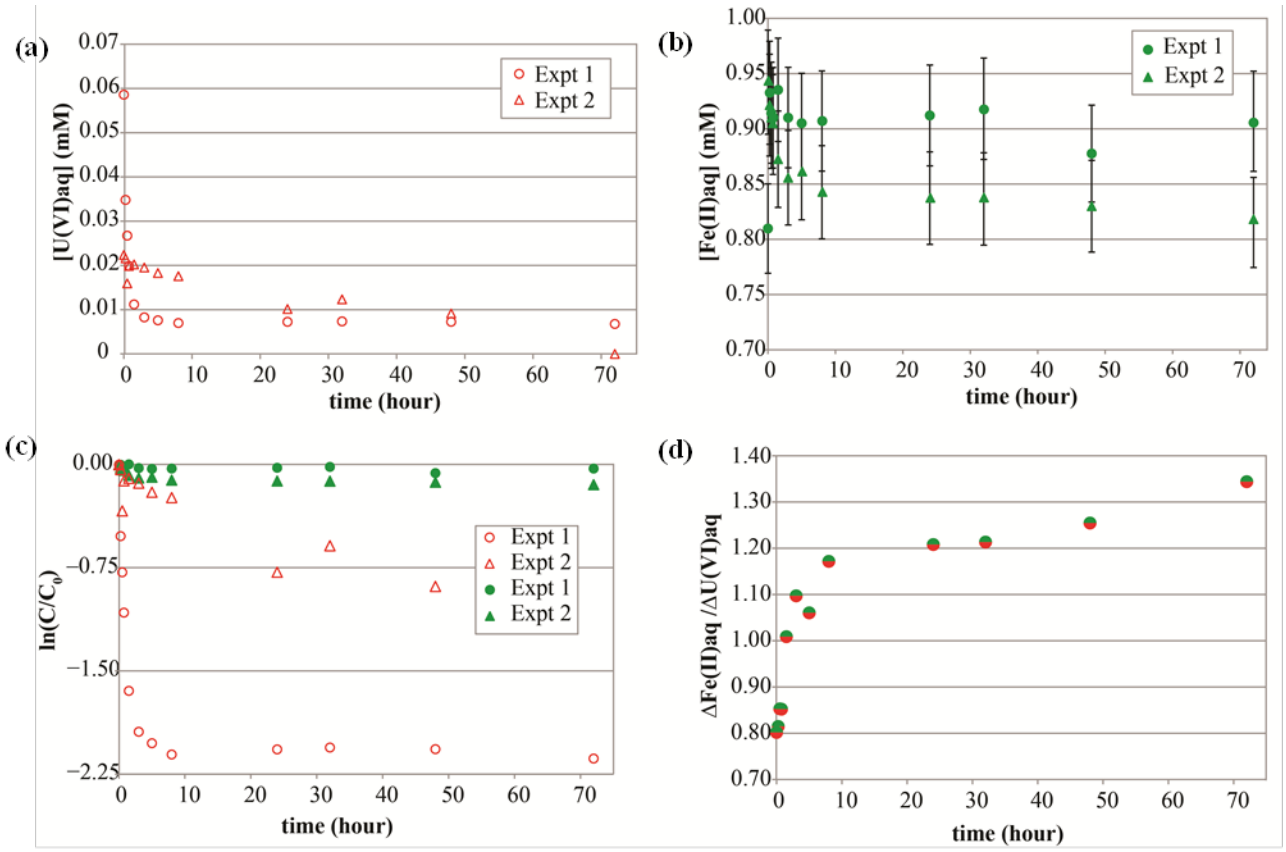

Figure 3-4: (a) Aqueous uranium concentrations over time comparing measurements from Experiments 1 (open, red circle) and 2 (open, red triangle). The initial U(VI) concentration for Experiment 1 is 0.16 mM, and is not shown on the figure in order to observe changes at lower concentrations in better detail. (b) Aqueous Fe(II) concentrations over time comparing measurements from Experiments 1 (filled, green circle) and 2 (filled, green triangle). (c) Comparison between relative uranyl and ferrous iron concentrations over time for both the Experiment 1and 2. Circle markers denote data from Experiment 1 while triangle markers denote data from Experiment 2. Open, red markers denote aqueous U concentrations for the respective experiments while filled, green markers denote aqueous Fe concentrations. (d) Correlation between U and Fe concentrations over time for Experiment 1. Markers are filled with green and red to denote the comparison between Fe and U concentrations.

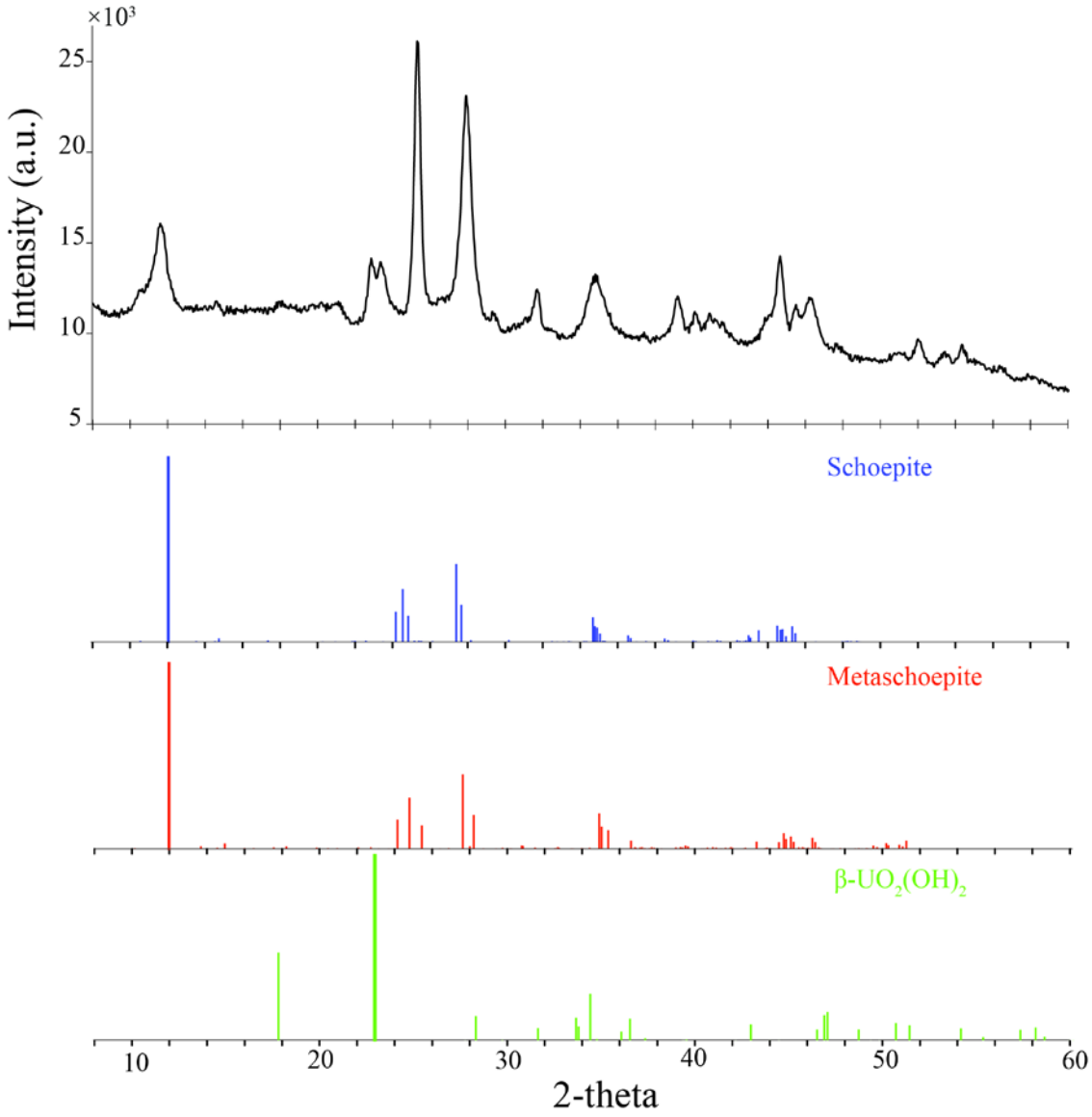

Figure 3-5: XRD pattern for the 0.17 mM U(VI) control experiment and comparison with peak lists to other uranyl solids phases; the PDF-#s for the solids are 01-086-1383 (schoepite), 01-089-7333 (metaschoepite), and 01-074-1468 (β-$UO_2(OH)_2$).

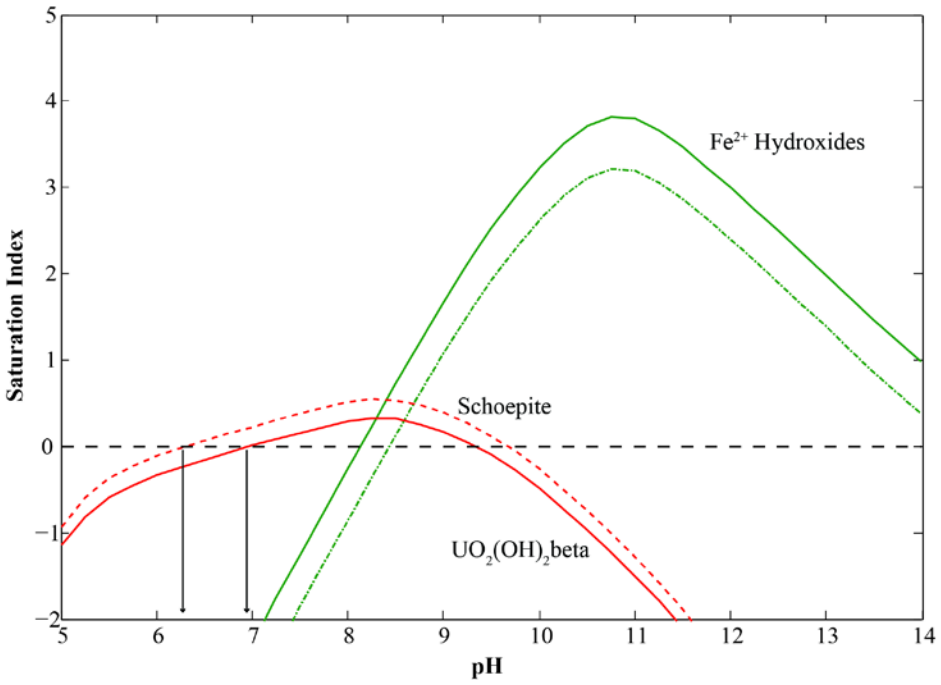

Figure 3-6: Saturation index for uranyl (red lines) and ferrous iron solids (green lines) at the experimental conditions used (0.16 mM UO_2^{2+}, 1 mM Fe^{2+}, 50mM NaCl, 5mM HEPES, pH_2=0.05 atm, pN_2= 0.95 atm).

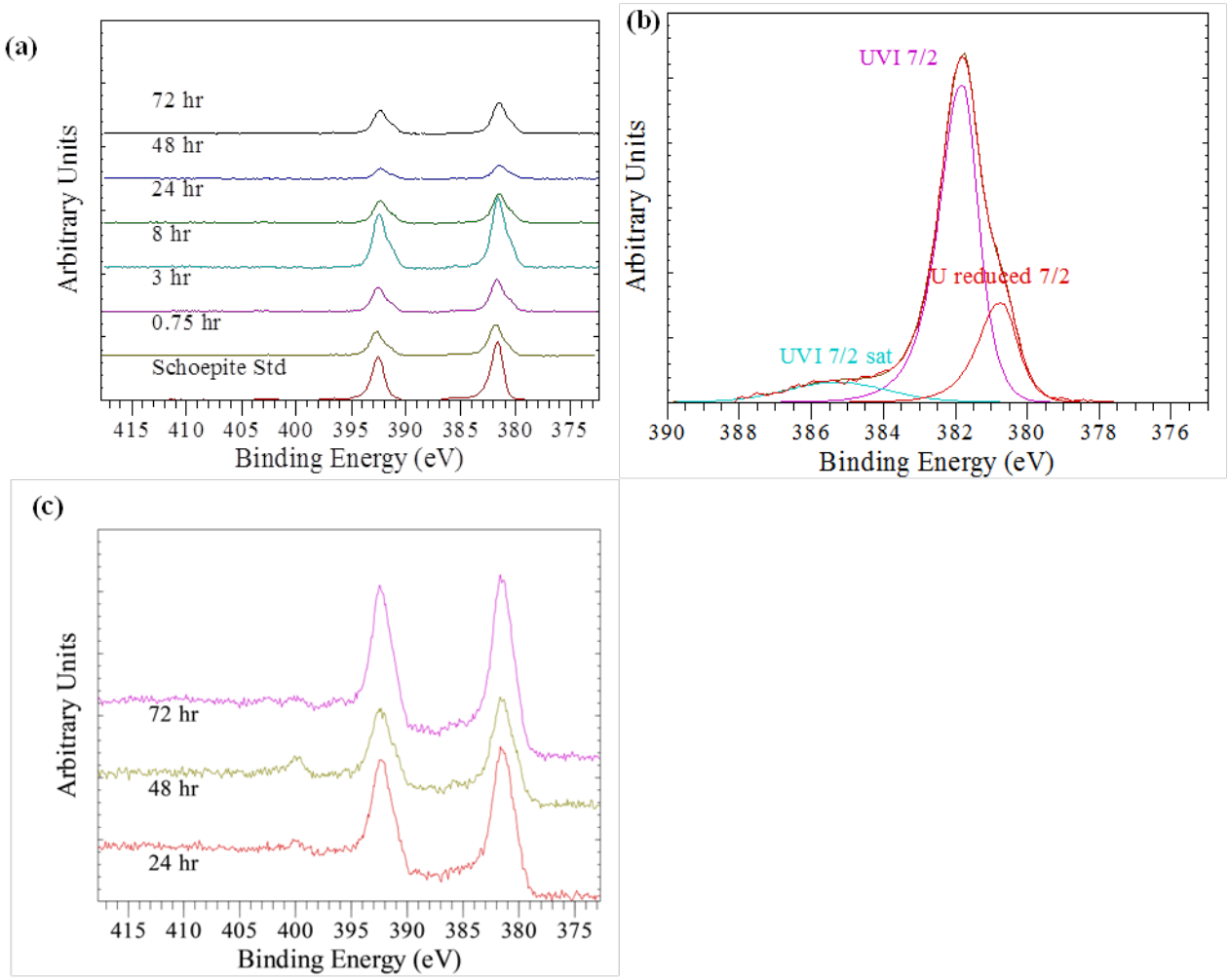

Figure 3-7: (a) U 4f XPS spectra for solids representing different times of the Experiment 1, overlain together for comparison. (b) Fitted GL curves for U4f 7/2 peak at 0.75 hours from Experiment 1, as an example of how proportions of U(VI) and reduced uranyl were quantified. (c) U 4f spectra for solids representing different times of the Experiment 2, overlain together for comparison.

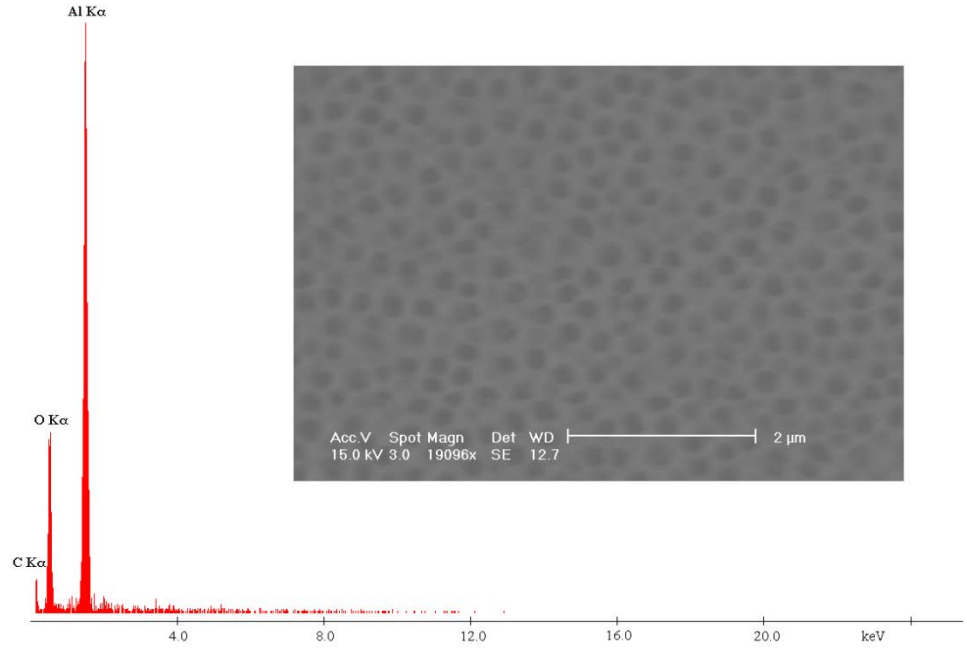

(a)

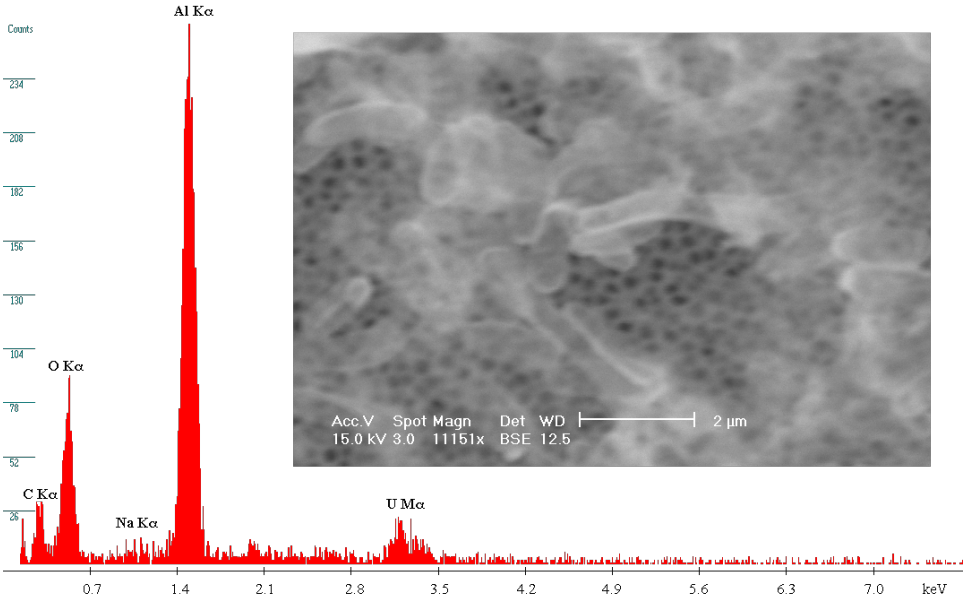

(b)

Figure 3-8: (a) BSE image and EDS spectra for filtered 0.02 mM UO_2^{2+} solution obtained at 3 hours, showing the absence of precipitates at the early stages of the experiment. (b) BSE image and EDS spectra for filtered 0.02 mM UO_2^{2+} solution obtained at 24 hours, showing the presence of uranium-oxide precipitates. The 0 – 8 keV energy region was chosen for analysis of the 24 hour sample to better resolve elemental information.

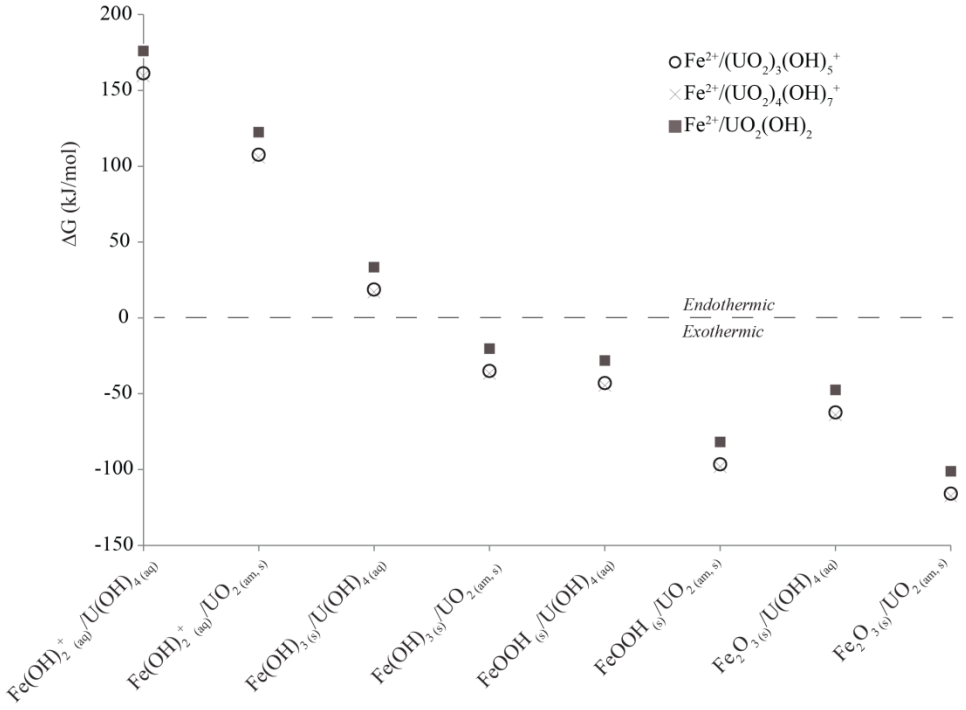

Figure 3-9: Trends in the free energies of U-Fe redox reactions as a function of aqueous and/or solid products generated. The markers indicate the aqueous reactants used in the calculation.

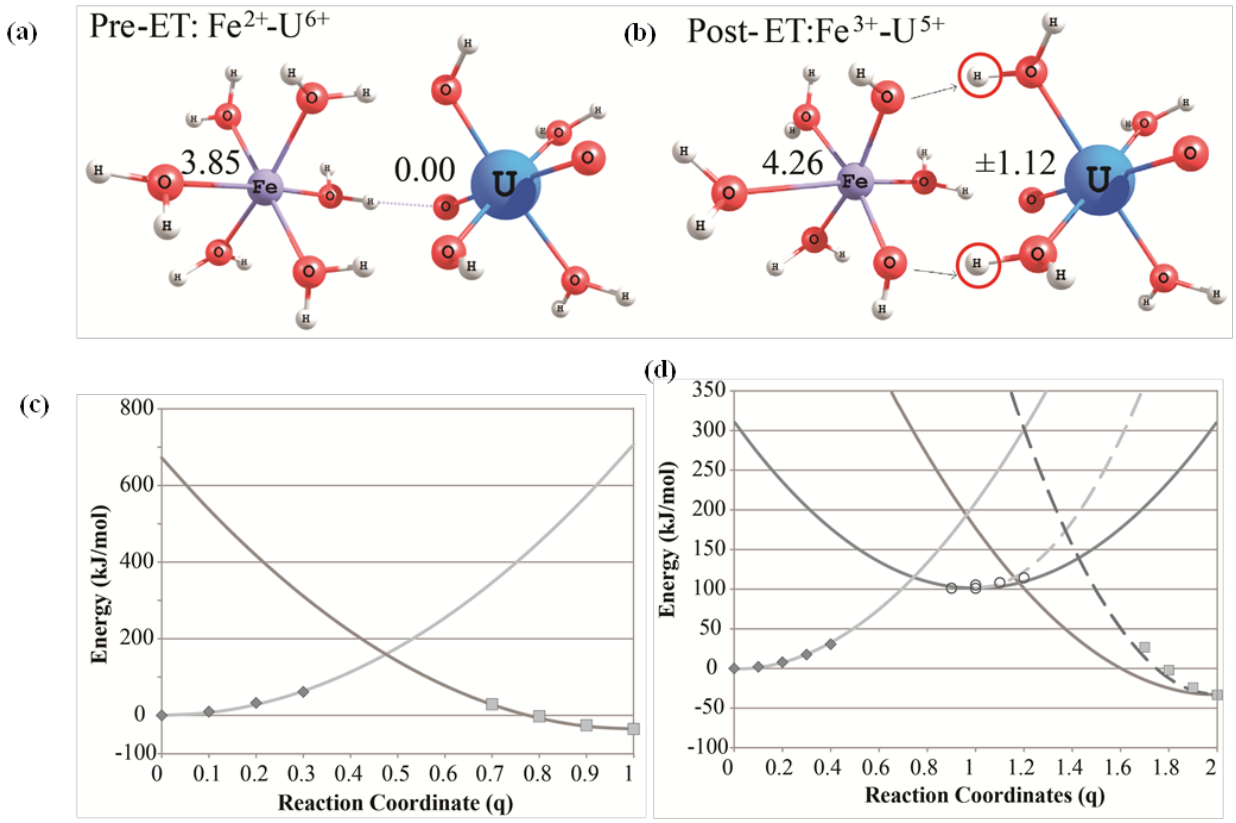

Figure 3-10: DFT geometry optimized pre–ET (a) and post–ET (b) states for the OS models, where water ligands separate Fe–U complexes. The values next to the Fe and U cations indicate the Mulliken spins for that ET state. Circled hydrogen atoms denote occurrences of PT. (c) PE surface for the ferrimagnetic, $PCET_{conc}$ reaction; solid data points are calculated values while the solid lines are the curves fitted to the properly calculated data points. Reaction coordinate 0 represents the pre-ET state and 1 represents the post-ET state. (d) PE surface for the ferrimagnetic, $PCET_{seq}$ reaction; makers are calculated values while the solid and dashed lines are the parabolas fitted to the calculated values. The solid lines are parabolas fit to the ET step (*i.e.*, the coefficient *a* is the same for each curve); the dashed curve indicates parabolas fit to the PT data values, yielding higher reorganization energies. Reaction coordinate 0 represents the pre-ET state; 1 the intermediate state; and 2 the post-ET state.

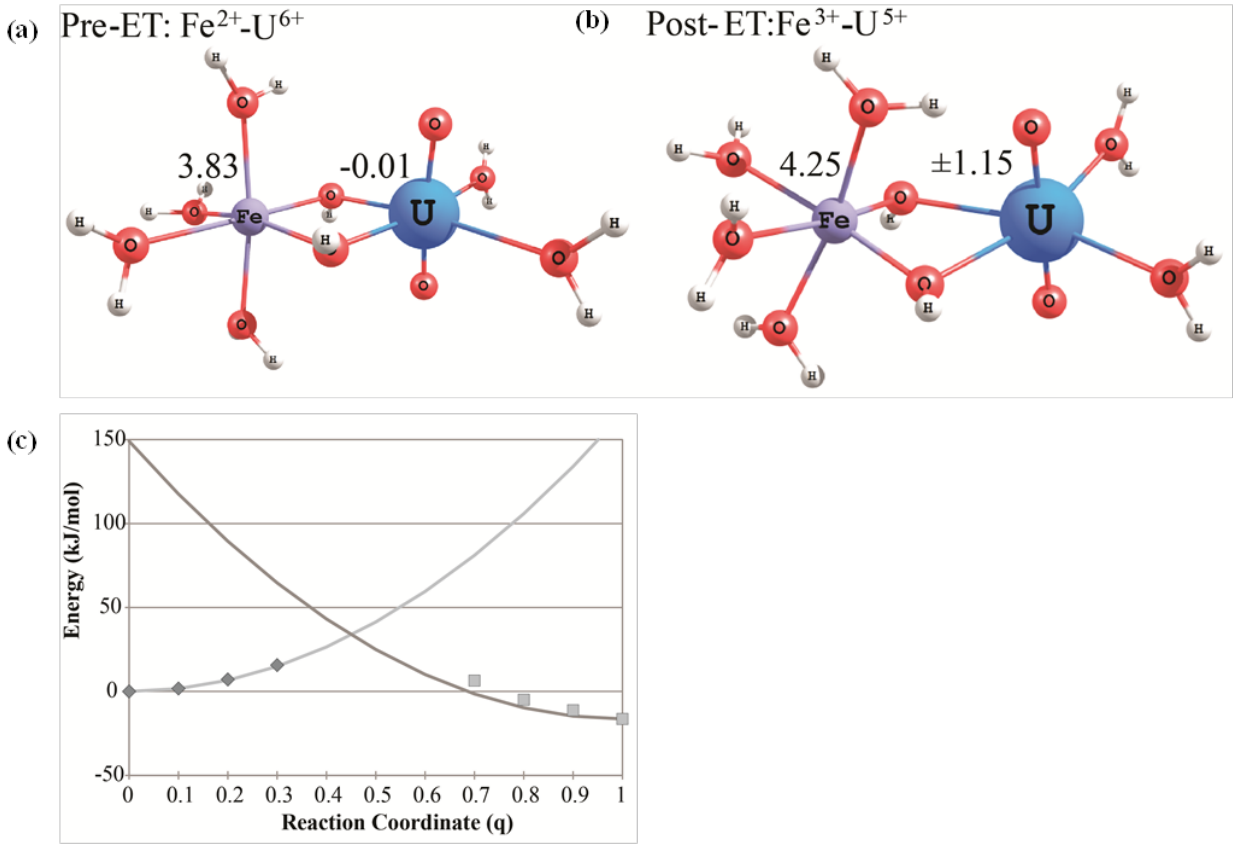

Figure 3-11: DFT geometry optimized pre–ET (a) and post–ET (b) states for the IS models, where Fe–U complexes are connected by bridging–hydroxyl ligands. The values next to the Fe and U cations indicate the Mulliken spins for that ET state. (c) PE surface for the ferrimagnetic ET reaction; solid data points are calculated values while the solid lines are the curves fitted to the properly calculated data points (the coefficient *a* is the same for each curve).

Chapter 4:
Reduction of U(VI) by Fe(II) sorbed on isostructural Fe and Al (oxyhydr)oxides: An investigation of how minerals' electronic properties influence heterogeneous catalysis of redox reactions

S. D. Taylor, M. C. Marcano, & U. Becker

The University of Michigan, Department of Earth and Environmental Sciences, 2534 C. C. Little Building, 1100 North University Ave., Ann Arbor, MI 48109–1005, United States.

4.1 Abstract

Past field studies and batch experiments have shown the reduction of U(VI) by Fe(II) is catalyzed in the presence of a broad array of minerals, although the rates of redox catalysis vary depending on the mineral; Fe (oxyhydr)oxides have been shown to be very effective catalysts for the reduction of U(VI) by Fe(II) in comparison to other minerals such as micas. Of the many factors influencing the heterogeneous catalysis of redox reactions, the availability of different charge transfer pathways is dependent on the substrates' chemical and electronic properties. To gain a better understanding of fundamental mechanisms involved in the heterogeneous catalysis of redox reactions, this study investigates how the substrates' electronic and chemical properties influence the redox kinetics for U(VI) reduction by Fe(II) and, as a consequence, uranium mobility. Batch experiments are conducted to measure the rate of uranyl reduction by Fe(II) (under anoxic conditions and near neutral pH) in the presence of semiconducting Fe(III) (oxyhydr)oxides, hematite and goethite, with respect to their insulating Al isostructures, corundum and diaspore, respectively. Measurements of the total U(VI) concentration over time and pseudo-first order reaction rates show reduction to be tens of times faster in the presence of

the Fe (oxyhydr)oxides compared to the isostructural Al (oxyhydr)oxides. XPS analyses of the oxidation states of the Fe and U adsorbed solids confirm that uranyl reduction occurs within the first 24 hours of reaction on the Fe (oxyhydr)oxides while reduced uranyl phases were not prominent until after 6 days on the corundum substrate and 19 days on the diaspore substrate.

To further understand and probe the influence of the chemical and electronic properties of insulating and semiconducting substrates on redox reaction rates, *ab initio* calculations were conducted on periodic models with molecular coadsorption. For the coadsorption of U and Fe onto a hydroxylated (001) hematite surface, analyses of the spin density and projected density of states show that the hematite slab is highly reactive and is capable of participating in sorption and redox reactions; Fe atoms within the hematite slab act as Lewis acids and can accept an electron from the Fe(II) adsorbate, which can be transported to neighboring Fe atoms and potentially reduce a nearby U(VI) adsorbate. Reduction of U(VI) by Fe(II) on an isostructural corundum surface is limited by the spatial location of the adsorbates, as the insulating nature of the slab does not facilitate ET. *Ab initio* calculations enhance our understanding of how minerals' electronic properties influence sorption/redox processes, in particular highlighting that the proximity effect can possibly be a significant mechanism contributing to the rapidity and efficiency with which semiconducting minerals catalyze redox reactions.

4.2 Introduction

An in-depth understanding of the conditions conducive for the abiotic reduction of U(VI) by Fe(II) is required to accurately predict uranyl's mobility and reactivity. These conditions are a complex function of chemical speciation and solubility, molecular-scale reaction mechanisms, and the thermodynamics, kinetics, and reduction potential of uranyl in solution or sorbed onto geologic materials. One of the conditions that tends to speed up the abiotic reduction of U(IV) by Fe(II) in an anoxic system at near-neutral pH is the presence of a solid substrate. In our previous study, the abiotic reduction of U(VI) by Fe(II) was demonstrated to be thermodynamically unfavorable and kinetically slow in a Fe(II)-containing solution unless a solid substrate was present [96]. However, the precipitation of U(VI) phases such as schoepite, ($UO_3 \cdot 2\ H_2O$, at relatively high U concentrations above the solubility limit) enabled the sorption of Fe(II) onto the schoepite surface and in turn led to the reduction of ~30% of the U(VI) at the surface of the U(VI) solid. To speed up the kinetics, the formation of inner-sphere Fe-U complexes can be

facilitated through sorption onto minerals surfaces. One process, by which this is achieved, is the dehydration of ions upon sorption to substrate surfaces, such as those of schoepite, which aids in catalyzing redox reactions through stripping hydration shells and enabling ions to interact with one another. This, in turn, speeds up the actual electron transfer (ET) process. In order to quantify the role of (de-)hydration on the electron transfer rate, ET calculations, using Marcus Theory coupled with *ab initio* methods, further supported experimental results. These calculations showed the catalysis of U(VI) reduction to U(V) by Fe(II) through the formation of inner-sphere U-Fe complexes (10^8 s^{-1}). Thus, at the given experimental conditions, the presence of a substrate considerably influences whether uranyl reduction by Fe(II) occurs.

Over the years, the catalysis of uranyl reduction in the presence of a number of different substrates has been explored. For example, systematic studies have been conducted on the reduction of U(VI) by Fe(II) sorbed on a variety of different substrates such as Fe(III) (oxyhydr)oxides including hematite (α-Fe_2O_3, *R-3c*) [12, 13], and Fe(II)-containing minerals (magnetite [97], pyrite [98], green rust [99], and micas containing structural Fe(II) [16]). Additionally, the abiotic reduction of U(VI) by Fe(II) using soils and sediments near Fe-rich oxic–anoxic boundaries in the natural environment was observed to occur in conditions favorable for the formation of structural Fe(II) [100].

While it is clear that the presence of a solid substrate affects the rate of the uranyl reduction, it is not as well understood how different substrate properties affect the catalysis of redox reactions. A substrate's catalytic efficiency is influenced by a wide variety of properties associated with a particular substrate, the different surfaces of the substrate, and the presence of specific surface sites such as steps, kinks, vacancies, and defects. For instance, the reduction of U(VI) by Fe(II) in the presence of hematite is more rapid compared with the reduction of U(VI) by Fe(II) at the surface of schoepite; partial uranyl reduction by Fe(II) occurred at the schoepite surface [96] while other studies have demonstrated that uranyl reduction by Fe(II) in the presence of hematite can reach completion within hours [12, 13]. There are a number of differences between schoepite and hematite and their surfaces that would lead to such differences in redox rates (*e.g.*, chemical composition, electronic properties, and surface structures and terminations).

Of the many factors influencing the heterogeneous catalysis of redox reactions, the influence of the chemical and electronic properties of substrates is one focus of this study. The different chemical and electronic properties of substrates provide different pathways for redox reactions to proceed by. It is hypothesized that pathways available in semiconducting minerals, where the surface participates in ET, can lead to considerably faster and more efficient reduction rates. To investigate these properties the rates for U(VI) reduction by Fe(II) when sorbed to different, isostructural Fe and Al (oxyhydr)oxides were monitored and compared. Iron (oxyhydr)oxides are good adsorbents and have been shown to facilitate ET [8, 12-14, 19, 101, 102]. As semiconductors, iron (oxyhydr)oxide surfaces are hypothesized to facilitate these reactions by acting as a medium for electrons to be transported through [17, 18, 94].

In this study, adsorption and reduction reactions between semiconducting iron (oxyhydr)oxides (*i.e.,* hematite, α-Fe_2O_3, and goethite, α-FeOOH,) and their insulating, Al-isostructures (*i.e.,* corundum and diaspore, respectively) are compared to understand the impact of chemical and electronic properties on catalyzing redox reactions. Hematite and goethite are common minerals in the environment and are predicted to be present in the near repository environment following the corrosion of the steel waste canisters [10]. Isostructures of Al-(oxyhydr)oxides are then used as analogs for Fe-(oxyhydr)oxides in terms of structure [10, 22], though their different electronic properties provide observations for how much more prevalent ET is in semiconducting than in insulating minerals. Both experiments and *ab initio* calculations are applied in this study to understand fundamental properties of mineral surfaces on redox processes. Batch sorption experiments provide empirical observations for the rate of reduction of U by Fe(II) in the presence of the isostructural but chemically and electronically different Fe and Al minerals. *Ab initio* calculations are then applied to periodic models of Fe and U (co)adsorbed onto the (001) hematite and corundum surfaces, to more specifically probe the influence of the substrates' electronic properties on sorption and/or redox processes. Analyses of properties such as the spin density provide evidence as to whether the substrates' surface chemistry and electronic properties are able to participate in sorption/redox processes [17, 23-25]. Through combining experiments and models a better understanding of microscopic and atomistic processes that influence the catalysis of redox reactions on chemically and electronic different mineral surfaces is obtained.

4.3 Methods

4.3.1 Batch experiments

To measure and compare the rates of uranyl reduction by Fe(II) in the presence of isostructural Fe and Al (oxyhydr)oxides, batch sorption experiments were conducted. The experimental conditions are similar to those used to study the reduction of 0.02 mM UO_2^{2+} and 1 mM Fe^{2+} in Taylor, *et al.* (2015) [96]. In short, all experiments were designed to study uranyl reduction in the absence of oxygen; experiments were conducted in an anoxic glove bag (5% H in N mix, O levels < 1 ppm through use of a desiccant and a palladium catalyst as well as an O trap using a diaphragm pump). All solutions were mixed using degassed water to avoid complications from O_2 and carbonate.

Stock solutions of 0.05 M UO_2^{2+} and 0.18 M Fe^{2+} were prepared in 1% HNO_3 and HCl, respectively, from high-purity solids ($UO_2(NO_3)_2 \cdot 6H_2O$ (International Bio-Analytical Industries Inc.; CAS-#: 13520-83-7) and $FeCl_2$ (Sigma-Aldrich; 99.998% trace metal basis; CAS-#: 7758-94-3)), respectively. Intermediate stock solutions of ~1 mM UO_2^{2+} and ~10 mM Fe(II) were prepared in 5 mM HEPES–50 mM NaCl solution, reaching a pH of ~7.2-7.3, equilibrated overnight, and filtered through a 0.22 μm pore-size, PVDF syringe-filter membrane (to ensure removal of Fe(III)), similar to the methods described in Taylor, *et al.* (2015) [96].

For the batch experiments, natural samples of hematite and diaspore were used, and pulverized into powders. Goethite was synthesized in the laboratory, according to Fernando, *et al.* (2012) [103], while synthetic corundum powder was purchased (Aldrich; 99.9% purity, 100 mesh, CAS-# 1344-28-1). The identity of the powders and their purity was confirmed using a Scintag X-ray diffractometer; no trace impurities were found. The grain sizes of all the powders were generally < 125 μm; the percentage of grains < 125 μm for hematite, corundum, goethite, and diaspore powders was measured to be approximately 98%, 73%, 80%, and 80%, respectively. The surface areas of the powders were measured using a Quantachrome Nova 4200e surface area analyzer by applying the five-point BET gas adsorption method with N_2.

The hematite, corundum, goethite, and diaspore powders were equilibrated in separate reactors with the 5 mM HEPES–50 mM NaCl solvent for 24 hours. The amount of powder added to each reactor was calculated in order to obtain a total surface area per reactor of about 10 m^2/L,

such that redox effects would not be a result of significantly different amounts of surface area available for sorption. The suspensions were spiked with the filtered 10 mM $FeCl_2$ intermediate stock solution, to reach an initial Fe(II) concentration of ~1 mM Fe(II), and equilibrated for another 24 hours to allow Fe(II) to adsorb to the substrate surfaces.

The concentration of Fe(II) left in solution and in turn the concentration of Fe(II) sorbed to the mineral substrates was measured using ICP-MS using aliquots of suspension that were filtered and acidified by 1% HNO_3. The sorbed Fe concentrations were also used to provide an estimate of the site saturation limit (SSL), the concentration at which a sorbate is observed to exceed monolayer coverage, according to the methods in Larese-Casanova and Scherer (2007) [104]; this limit is helpful in deducing the surface environment for Fe sorbed on the different substrates. For instance, for the Fe (oxyhydr)oxide systems, results from Larese-Casanova and Scherer (2007) [104] showed that when the sorbed Fe concentration is below the SSL, sorbed Fe(II) undergoes complete ET and is oxidized to Fe(III). If the sorbed Fe concentration surpassed the SSL a stable Fe(II) coating was capable of forming. The total Fe(II) concentration in the system was measured by equilibrating Fe(II) sorbed onto the suspension with 0.5 M HCl for 2 hours in the anoxic chamber and filtering it [93].

Following the 24 hour equilibration with Fe(II), the suspensions were spiked with 1 mM UO_2^{2+} to reach an initial concentration of ~0.02 mM U(VI); the pH throughout the experiment was ~7.2. To measure the rate of uranyl sorption onto the substrates, aqueous U(VI) concentrations (*i.e.,* the total amount of uranyl left in solution) were measured at 15, 30, and 45 minutes and 1.5, 3, 5, 8, 24, 32, 48, and 72 hours from the beginning of the experiment by filtering aliquots and acidifying them to 1% HNO_3. The total U(VI) concentrations (*i.e.,* the total concentration of U(VI) in the system – in solution and/or desorbed from the mineral surfaces) were also measured at the above times to observe the rate of uranyl reduction in the presence of ferrous iron. To measure the total U(VI) concentrations, adsorbed U(VI) is extracted from the mineral suspensions using the $NaHCO_3$ extraction method (Liger et al., 1999, Zeng and Giammar 2011), where 0.5 ml of suspension was added to 1 ml of 0.5 M $NaHCO_3$ and mixed on a sample rotator for 1.5 hours before filtering (as done with the aqueous U(VI) aliquots).

4.3.2 Analyses of solid and aqueous fractions

U(VI) and Fe(II) concentrations were measured from diluted, acidified aliquots using either a Perkin–Elmer ELAN DRC-e or an Agilent 7900 ICP–MS. The identity of Fe analyzed using the ICP-MS was confirmed to be Fe^{2+}, as UV-Vis measurements using the ferrozine method provided similar Fe^{2+} concentrations (within 5% error). Analytical precision was better than 5% RSD for both U and Fe based on check standards, laboratory reference material, and sample replicates. Pseudo-first order rate calculations, k_{ps}, were used to approximate rates for the chemical reduction of uranyl in the different U-Fe coadsorbed mineral suspensions [13].

The valence of the redox-sensitive atoms on the solid substrates was characterized using a Kratos Axis Ultra X-ray photoelectron spectrometer (XPS) with an Al-Kα x-ray radiation source (1486.6 eV). The Fe and Al (oxyhydr)oxide powders were prepared similar to the methods used in Taylor, *et al.* (2015) [96], with the powders affixed to Cu-tape. The only time the samples were exposed to atmosphere was for a maximum of 5 minutes during loading into the XPS sample transfer chamber. Survey scans were collected to determine the abundance of relevant elements in this study (U, C, O, Fe, Al) in the binding energy (BE) range -5 to 1200 eV at 1 sweep (dwell time = 200 ms) and at a pass energy of 160 eV. Following the survey scans, narrow scans were collected under the same analyzer conditions (in the order U, Fe, C, O, Al) using a pass energy of 80 eV with up to 60 sweeps (the lower concentrations of uranyl produced lower counts; these parameters allowed for better resolution and noise minimization from the background).

Fe 2p spectra and U 4f spectra from the Fe-U coadsorbed samples were analyzed to determine the oxidation state of Fe and U present in the Fe and Al (oxyhydr)oxide systems. XPS spectra were analyzed using the Casa XPS software (v. 2.3.16). Spectra were calibrated using the adventitious carbon method (calibrating C 1s to 284.6 eV) [54]. The corresponding adsorbed U samples (*i.e.,* U(VI) adsorbed to the substrate) were used as BE references for the U 4f spectra to compare peak heights, detect shifts and satellite peaks, etc. Reference BEs from literature were also used to provide an indication as to whether U(VI), U(V), and U(IV) were present in the coadsorbed samples.

Precautions were taken to avoid and/or minimize some of the issues that can arise during XPS spectra collection, such as the potential for low concentrations of redox-sensitive elements

to be reduced under ultra-high vacuum (UHV) conditions and/or exposure to the electron beam [16, 77]. Beam reduction for the Fe sorbed substrates is expected to be minimal; Fe sorbed samples exposed to the beam for ~8 hours after the first spectra acquisition did not observe measureable changes in the BEs of the Fe 2p spectra. For U(VI) adsorbed to a diaspore sample, the U(VI) BE energy shifted to a lower BE by ~0.2 eV after 8 hours (as also observed by Wersin, *et al.* (1994) [77]), though clear indications of reduced uranyl features such as satellite peaks corresponding to reduced U were not present). The differences in the proportion of reduced U between the Al and Fe minerals as revealed by the ICP-MS data provide a measure of the extent of uranyl reduction and can be used to benchmark the chemical reduction effects of UHV and beam exposure.

4.3.3 Computational methods

To determine the role of the chemical and electronic properties of insulating and semiconducting mineral surfaces on the substrates' catalytic effect on ET from a quantum-mechanical point of view, periodic models of U and Fe molecules coadsorbed on hydroxylated (001) surfaces of hematite and corundum were constructed. The (001) surfaces were modeled using three-dimensional periodic slabs consisting of four O layers and six M-cation layers (where M represents Fe and Al for the hematite and corundum slab, respectively. The O-terminated surfaces are hydrated, attaching one proton to every surface oxygen atom, to form nonpolar, charge-neutral surfaces (with stoichiometries of $M_{48}O_{96}H_{48}$) [25]. The entire slab is first geometry optimized with no symmetry imposed on the slab. For the models of U and/or Fe (co)adsorbed to the surfaces, the atoms of the middle cation bilayer are fixed to mimic the rigidity found within the bulk mineral as well as improve computational efficiency. The slab thickness does not interfere with analyses of the objectives above as the surface-region is of most interest for changes in spin and electron density and for comparative changes in adsorption thermodynamics between Al and Fe oxides.

A mononuclear uranyl ion $UO_2(H_2O)_3^{2+}$ was adsorbed each of the hydroxylated (001) surfaces, forming a bidentate complex with two oxo-ligands on the corners of two separate Al or Fe octahedra, above the cation vacancy (consistent with experimental data) [24, 70]. When U and/or Fe are (co)adsorbed to the surface, protons are removed to maintain a charge neutral model; *e.g.*, for the adsorption of $UO_2(H_2O)_3^{2+}$, two hydroxyl ligands at the hydrated (001) are

removed to accommodate the adsorbate. Fe adsorbates on mineral surfaces are more difficult to characterize, though in general they are hypothesized to observe an octahedral coordination [105] and to adopt positions where they act as a continuation of the bulk [106]. Based on this assumption, initially, a mononuclear Fe(II) ion complex, $Fe(H_2O)_3^{2+}$, was adsorbed to the (001) surfaces, forming a tridentate complex with two oxo- and one hydroxyl ligands associated with two separate edges of Al and Fe octahedra, above a cation vacancy.

U and/or Fe were (co)adsorbed onto both of sides of the hydroxylated (001) hematite or corundum surfaces. U and Fe coadsorbed onto the surfaces are at the same sites as in the adsorption models, and are within close proximity to one another (the interatomic distance between U and Fe is 6.7 Å). The appropriate formal spins and charges are assigned to all the atoms within the (co)adsorbed models prior to geometry optimization (Al spin, charge = 0, +3; O = 0, -2; H = 0, 1; hematite-Fe = ±5 (antiferromagnetic), +3; Fe adsorbate = +4, +2; U = 0, +6). It is possible that other more thermodynamically favorable phases exist that are highly dependent on micro- to nanoscale surface topography such as step and kink sites, though testing all different surface configurations is beyond the scope of this study. This study's objective is to obtain coadsorption models that are structurally similar across different mineral surfaces such that comparisons can be made between the potential ET reaction pathways at the surface of semiconducting and insulating surfaces. The coadsorbed structures were geometry optimized using plane-wave based Density Functional Theory (DFT) calculations as employed in CASTEP, using the GGA-PBE functional and accounting for spin polarization in the Materials Studio 6.1 v.2 software suite. Additional calculation parameters applied include ultrasoft pseudopotentials, an energy cutoff of 450 eV (which results in sufficient convergence when using ultrasoft potentials), an SCF tolerance of 0.002 eV/atom, and 1 k-point/2×1×1 Monkhorst-Pack grid.

The Bader spins for each adsorbed and coadsorbed model were analyzed to observe the potential for ET to occur at the corundum and hematite surfaces; differences in spin between the adsorption and coadsorption models using corundum and hematite can show whether one surface promotes ET over the other. The total spin density as well as spin density difference (*i.e.*, the difference between the (co)adsorbed model and the adsorbates and surface by themselves) show which atoms participate in charge transfer.

The projected density of states (PDOS) is used comparatively for different surfaces to determine the relative number of electron energy states available for the adsorbate interactions above and below the surface's highest occupied energy level (or Fermi level) [25, 81]. The electronic structure of solids, particular semiconductors, can be poorly approximated by DFT calculations. DFT calculations have been observed to underestimate the band gap of semiconductors and predict hematite as *d-d* Mott-Hubbard insulator rather than a charge-transfer insulator [107]. Application of DFT+U calculations are capable of describing the bulk electronic properties of semiconductors [107, 108], although there is debate of whether using DFT+U will improve the quality of the electronic structure properties for surfaces [109]. The electronic structures of the hydrated surfaces used in this study are more complex than those of the bulk; for instance, the surfaces in this study are subject to hydration and atomic relaxations that can lead to the existence of surface states at the Fermi level. Thus, for this study, the changes in the electronic structure between the bulk and hydroxylated (001) hematite surface are utilized to provide insight into local electronic rearrangements that can occur upon (coad)sorption of Fe and U, and the potential implications for charge transfer.

4.4 Results

4.4.1 U(VI) reduction by Fe(II) in the presence of Al (oxyhydr)oxides

The results for sorption Fe(II) and/or U(VI) in the corundum and diaspore suspensions are first presented to determine the rate of U(VI) reduction of Fe(II) in the presence of insulating minerals. As described in the experimental section, Fe(II) was first sorbed onto the mineral surfaces (*i.e.,* only Fe(II) sorbed to the substrate, prior to the uranyl spike) to measure the amount of Fe(II) adsorbed Al (oxyhydr)oxides that is available for ET. Measurements of the aqueous Fe(II) concentration from ICP-MS showed that ~0.07 – 0.09 mM of the ~1mM $Fe(II)_{aq}$ concentration is adsorbed to corundum and diaspore after 24 hours equilibration time (Table 4-1).

The sorbed Fe concentrations are used to estimate the Fe(II) surface coverage according to Larese-Casanova and Scherer (2007) [104]; the amount of sorbed Fe(II) exceeds the SSL, meaning that more than a monolayer of Fe(II) is sorbed onto the corundum and diaspore surfaces. It is likely that a significant portion of uranyl sorbing to the substrate surfaces comes

into contact and interacts directly with the sorbed Fe(II) at the corundum and diaspore surfaces. More so, this portion of U(VI) in contact/interacting with the sorbed Fe(II) layer has the potential to be reduced.

Fe(II) sorbed to the Al (oxyhydr)oxide surface is valence stable; ~95% and ~90% of the sorbed Fe(II) can be extracted from the corundum and diaspore suspensions, respectively. The Fe 2p XPS spectra for the Fe adsorbed on corundum and diaspore samples (*i.e.,* only Fe(II) adsorbed on the substrates) confirm the presence of Fe(II) (Figure 4-2), a satellite peak associated with Fe(II) can be observed on the shoulder of the Fe 2p 3/2 peak, ~5-6 eV away [110]. The stability of Fe(II) on the Al (oxyhydr)oxides is in accord with previous experimental results (Casanova and Scherer 2007, Williams and Scherer 2004); *i.e.,* because corundum and diaspore are insulators and the environment is anoxic and reducing, the Fe(II) would be adsorbed to corundum and diaspore only as Fe(II) without ET/oxidation occurring.

Uranyl sorption onto the Fe sorbed mineral substrates occurs rapidly (Figure 4-1); the aqueous uranyl concentration decreases to ≤ 0.2 μM within the first 15 minutes for the diaspore suspension, while the aqueous uranyl concentration for the corundum suspension is 2 μM after 15 minutes and reaches an equilibrium concentration of 0.2 μM within 1.5 hours. The rapidity of uranyl (co)adsorption onto the Al-bearing solids shows that reactions involving uranyl are occurring at the mineral surface. Precise correlation of the amount of Fe(II) removed from solution to the amount of uranyl reduced is prevented by the standard deviations of the aqueous Fe concentration measurements. However, samples comparable in reaction time of both substrates with adsorbed Fe(II) vs. coadsorbed Fe(II) and U(VI) can be used to show whether the addition of U(VI) to the suspensions affects the behavior of Fe(II). After spiking the Fe-adsorbed corundum suspension with uranyl, the aqueous Fe concentrations were fairly constant over 8 hours reaction time within the error limits. The Fe concentrations in the diaspore system decrease considerably over time in 19 days of reaction time (from 0.92 mM down to ~0.40 mM), suggesting that Fe(II) continues to sorb to the substrate after uranyl sorption/reduction occurs.

The total U(VI) concentrations over time were measured in the Fe and U coadsorbed suspensions to observe the approximate rate of uranyl reduction (Figure 4-1b). The extraction efficiencies for uranyl adsorbed to corundum and diaspore are approximately 110%, and 80%, respectively. The extraction efficiencies show that most the uranyl can be extracted; nominal

extraction efficiencies over 100% most likely indicate heterogeneities in the amount of suspension sampled. For considerable chemical reduction of U(VI) to U(V)/U(IV) by Fe(II) sorbed onto the corundum and diaspore surfaces more than 24 hours of reaction time is needed. The total uranyl concentration is fairly constant over the first 8 hours of reaction time in the corundum suspension; after 24 hours ~50% of U(VI) has been reduced, and after 6 days of reaction time the total U(VI) concentration is 0.4 μM. The diaspore system experiences the slowest redox rate of the four substrates, where reduction occurs most rapidly within the first 1.5 hours of reaction time (20% uranyl reduced). After the first day, reduction proceeds slowly for up to 12 days, and after that time, a total U(VI) equilibrium concentration is reached (60% uranyl reduced) showing incomplete uranyl reduction.

To confirm the reduction rates observed from measurements on the aqueous fraction as well as determine the nature of solid adsorbates formed, the solid fraction was collected at certain times throughout the experiments and analyzed using XPS. The U(VI) reference samples show that U(VI) BEs range from 381.3 (synthetic schoepite) to 381.7 eV (sorbed uranyl on corundum; Table 4-2). While there is uncertainty concerning determination of absolute BEs for insulating materials, such as corundum, the absolute BEs are consistent with values found in the literature for U(VI) species such as schoepite [75].

For the Fe -U coadsorbed onto the Al (oxyhydr)oxide at 24 hours, the BEs for the U 4f 7/2 peak do not change or shift considerably with respect to the uranyl sorbed reference samples. The dominant oxidation state in these systems is U(VI) which is consistent with the reference samples; distinct U(VI) satellites confirm the presence and dominance of U(VI) (Figure 4-3a, Table 4-2). Fe spectra on the Fe-U coadsorbed Al (oxyhydr)oxide samples were weak, although Fe(II) satellite features could still be observed, suggesting Fe(II) was still present in the system. Analysis of the Fe and U coadsorbed Al (oxyhydr)oxide suspensions at later times show further reduction had occurred and are in agreement with the results from the aqueous fraction. For instance, the XPS U 4f spectra for the Fe-U coadsorbed on corundum after 6 days reaction time show the reduced uranyl fraction to be most prominent; ~50% of the U present exhibits a BE of 380 eV (Table 4-2), which suggests U(IV) is the most dominant oxidation state. For the uranyl coadsorbed on diaspore (19 days reaction time), a majority of the uranyl also exists as reduced uranyl, although ~40% of the U remained as U(VI). While U(IV) and U(V) satellite features in

the U 4f spectra are difficult to clearly observe and thus attribute BEs to either U(IV)/U(IV) with high certainty, the difference in the BEs of U(VI) and U(IV) support that U(IV)/U(V) phases are present. The BE difference between monovalent U(IV) and U(VI) compounds in previous studies has been cited as 1.5 - 2.1 eV [75]. In this study, the differences between the U(IV) and U(VI) peaks (1.4 - 1.8 eV) are in general agreement with the given peak separations for U(IV) and U(VI) and support that a fraction of the reduced uranium is U(IV). The approximate ratios of reduced U(IV) to oxidized U(VI) conform to aqueous results, showing that uranyl reduction by Fe(II) in the presence of corundum and diaspore occurs on time scales of a few days to weeks.

4.4.2 U(VI) reduction by Fe(II) in the presence of Fe (oxyhydr)oxides

The results for sorption Fe(II) and/or U(VI) in the hematite and goethite suspensions are now presented to compare the rate of U(VI) reduction of Fe(II) between isostructural but chemically and electronically different minerals. For the adsorption of Fe(II) onto hematite and goethite, approximately 18% of the initial Fe(II) in solution was adsorbed to hematite and goethite (Table 4-1). The percentages of Fe(II) extracted from the sorbed Fe hematite and goethite suspensions were approximately 110% and 130%, respectively. The extraction efficiencies for the hematite and goethite suspensions exceed the initial Fe(II) concentrations, which is possibly due to the dissolution of poorly crystalline areas on the Fe substrates [111] and/or heterogeneities in the aliquots. About twice as much Fe(II) sorbs to the Fe (oxyhydr)oxides compared to the Al (oxyhydr)oxides; for instance, 0.20 mM Fe(II) is adsorbed to hematite compared to 0.09 mM Fe(II) that is adsorbed to corundum.

The sorbed Fe concentrations are estimated to exceed the SSL; more than a monolayer of Fe(II) is adsorbed on the surface though the presence of Fe(II) valence state sorbed onto the goethite and hematite is hard to verify. More so, Fe 2p XPS spectra for Fe adsorbed (and Fe and U coadsorbed) onto hematite and goethite are indistinguishable from the Fe 2p spectra for the hematite and goethite by themselves. The Fe 2p XPS spectra show the dominant oxidation state is Fe(III) (Figure 4-2); satellites associated with Fe(III) are clearly observed at ~8.5 eV away from the Fe 2p 3/2 peak and ~10 eV from the Fe 2p ½ peak (Grosvenor et al. 2004). The Fe(II) signal from any Fe(II) sorbed would be too weak to overcome the Fe(III) signal from the substrate. It is also highly possible that interfacial ET between the sorbed Fe(II) and the Fe(III)

substrate occurs (as will be discussed later), causing the relative XPS signal of ferrous (compared to ferric) iron to be even smaller/weaker.

When only uranyl is adsorbed to hematite and goethite suspensions, the aqueous uranyl concentration reached 0.2 μM and 0.3 μM over 24 hours, respectively; approximately 90% and 70% of the U(VI) is extracted from the hematite and goethite suspensions, respectively, indicating reduction does not occur without the presence of the Fe(II) reductant. When U(VI) is added to the Fe sorbed suspension, the aqueous Fe(II) concentrations are fairly constant over 8 hours reaction time (within the error limits), showing that the addition of uranyl does not considerably affect Fe in solution. More so, uranyl sorption to the Fe sorbed Fe (oxyhydr)oxide substrates occurs rapidly (Figure 4-1a). The aqueous uranyl concentrations for the Fe-U coadsorbed substrates decrease to $\leq$ 0.2 μM within the first 15 minutes for both hematite and goethite; again, it would expected that redox reactions involving uranyl would be occurring at the mineral surfaces.

The total uranyl concentrations for the hematite and goethite suspensions show that uranyl reduction occurs rapidly compared to the Al (oxyhydr)oxide suspensions. The total U(VI) concentrations decrease by an order of magnitude within the first 1.5 hours of reaction time, and the amount of total U(VI) that can be extracted from these systems reaches equilibrium within 24 hours (0.7 μM) (Figure 4-1b). The measurements for the total U(VI) concentrations show that the most uranyl reduction occurs on the hematite and goethite substrates within 1.5 hours while U(VI) is still predominant in the coadsorbed corundum and diaspore suspensions.

Pseudo-first order reduction rates, k_{ps}, for the chemical reduction of uranyl by Fe(II) on the Al- and Fe (oxyhydr)oxides substrates were calculated using the total U(VI) concentrations measured within the first 5 hours of reaction time. The datasets can deviate from linearity and were slightly to markedly curvilinear, though this is not unreasonable. If the data were to fit well to a pseudo-first order rate law, this would suggest that reduction is the most dominant reaction type occurring. However, at least two reactions occurring (sorption and reduction), simultaneously at times, within the coadsorbed system and so the isotherm is more complicated. Despite the chemical reduction of uranyl on the Fe-U coadsorbed substrates possibly being controlled by more complex kinetics, the k_{ps} values are still able to provide comparative reduction efficiencies in the Fe and Al (oxyhydr)oxide systems. Uranyl reduction by Fe(II) in the

Fe (oxyhydr)oxide suspensions are calculated to be 10×s faster than the rates calculated for the Al (oxyhydr)oxide suspensions (Figure 4-1c, Table 4-1); for instance, uranyl reduction by Fe(II) in the presence hematite occurs at a rate of 0.53 h^{-1} while reduction in the presence of corundum occurs at a rate of 0.04 h^{-1}. Given that the amount of Fe sorbed to the Fe (oxyhydr)oxides was greater than for the Al (oxyhydr)oxides, the rates are normalized to the Fe sorbed concentrations; in this case, it Is also found that the uranyl reduction rates are still an order of magnitude faster in the presence of the Fe (oxyhydr)oxides relative to the Al (oxyhydr)oxides. Thus, Fe (oxyhydr)oxides are shown to be more effective at catalyzing uranyl reduction by Fe(II) compared to their isostructural Al counterparts.

Confirmation of U(VI) reduction is obtained through XPS analyses. For the Fe-U coadsorbed Fe (oxyhydr)oxide suspensions the U BEs of the U 4f 7/2 peak shifts to a much lower BE after the 24 hour reaction time(Figure 4-3a, Table 4-2). U(VI) satellite peaks are not as distinct, suggesting that U(VI) is no longer the dominant oxidation state present. In some spectra, faint satellites of the reduced U(V) and U(IV) phases can be observed; for instance, for the Fe-U coadsorbed on hematite samples after 24 hours, the dominant U component has a BE of 379.9 eV (Figure 4-3b) and faint U(IV) 4f 7/2 satellites are also observed (6.8 eV away from the U 4f 7/2 peak), providing evidence that U(IV) is present. This BE for U(IV) is within the range of other experimentally obtained U(IV) phases [75]. For Fe-U coadsorbed on goethite, the U 4f spectra show reduced U components as well, though the U component with the lowest BE is at ~380.5 eV; some spectra show a U(V) 7/2 satellite associated with this BE (8.3 eV away), suggesting this oxidation state this BE could represent U(V). Nonetheless, after 24 hours, a considerable portion of uranyl coadsorbed to the hematite and goethite substrates has been reduced while U(VI) is dominant on the corundum and diaspore substrates after the same amount of time. These analyses complement the approximated reduction rates found through measuring the aqueous fraction, and provide further evidence of Fe (oxyhydr)oxides catalyzing the reduction of U(VI) by Fe(II) more rapidly compared to its isostructural Al counterparts.

4.4.3 Computational results

The experimental results provide evidence that the chemical and electronic properties of the Al and Fe substrates affect the efficiency and rate of catalysis, where U(VI) reduction by

Fe(II) is tens of times faster in the presence of the semiconducting Fe (oxyhydr)oxide compared to insulating Al (oxyhydr)oxides. To enhance our understanding of the mechanisms by which redox reactions can be occurring on insulating *vs.* semiconducting surfaces, computational models, where U and Fe are coadsorbed onto isostructural, hydroxylated (001) hematite and corundum surfaces $[2UO_2(H_2O)_3 - M_{48}O_{96}H_{40} - 2Fe(H_2O)_3]^0$, are analyzed in terms of the substrates' composition, geometry, and electronic properties.

In these models, U and Fe adopt similar structural configurations on the isostructural hematite and corundum surfaces (Figure 4-4). The uranyl sorbs to two bare O ligands at the surface, forming a bidentate inner-sphere complex with an interatomic distance of 3.4 – 3.5 Å between U and its nearest neighbor Fe/Al cation; one of the three water ligands becomes nonbonding (~3.2 Å) resulting in the coordination of the U atom being tetragonal instead of pentagonal. Fe^{2+} adopts an octahedral, tridentate configuration (acting as a continuation of the bulk structure) upon sorption onto the hematite and corundum surfaces, with one of the three water ligands becoming nonbonding (*i.e.,* a decrease in coordination number from 6 to 4). The structural configuration of the U adsorbate is in agreement with experimental results from X-ray absorption spectroscopy showing uranyl adsorbs to Fe (oxyhydr)oxide surfaces in a bidentate, pentagonal configuration where the interatomic distance between U and Fe is ~3.5 Å [24, 55, 80]. The structural configuration of the Fe adsorbate is also in agreement with computational observations for Fe(II) adsorption onto nontronite [106].

Partial density of states (PDOS) can provide insight into the bonding environments at the surfaces of the corundum and hematite and how these differ from one another. The orbitals of interest are those near the valence energy (near the Fermi level); this is where bonding and ET occur. The PDOS for the coadsorbed corundum model shows a low number of states for Al p-orbitals near the Fermi energy due to its insulating character (Figure 4-5a). There is little overlap between U, Fe, and Al atomic orbitals near the Fermi energy; the Al cations are limited to ionic-covalent interactions with oxygen with little interaction between the Fe and/or U adsorbates and the corundum surface. On the other hand, high concentrations of electron-acceptor sites near the Fermi level from the 3*d*-states of the Fe atoms, compared to the low number of electron acceptor sites in the 2*p*-states of the Al atoms, are observed for the Fe-U coadsorbed hematite model (Figure 4-5b). The Fe-hematite *d*-orbitals overlap with atomic orbitals from the adsorbates (U *f*-

orbitals and Fe-adsorbate *d*-orbitals), which is indicative of covalent bonding between the adsorbates and the hematite substrate.

It is clear that the number of *d*-states of the Fe atoms in hematite is high near the Fermi energy, relative to the *p*-states of the Al atoms in corundum, and contributes to a higher degree of reactivity in terms of its Lewis acid sites [81]. More so, the sorption of Fe and U shifts the empty *d*-states of the Fe atoms within the hematite towards the lower energies with respect to the empty *d*-states of the bulk hematite (Figure 4-5b), showing local electronic rearrangements occur from the sorption of Fe and U. Separate models studying sorption processes on semiconducting minerals have shown the potential for adsorbates to significantly change the local electronic structure of the surface relative to the bulk substrate. For instance, the sorption of benzene onto (0001) and (01-12) hematite surfaces was shown to shift the conduction band edge of Fe 3*d* and O 2*p* states towards the valence band, significantly reducing the band gap; in some cases, the hematite surface become metallic [108]. Thus, it is reasonable that the local electronic structure within the hematite system for our models also change upon (co)adsorption of U and/or Fe. These shifts in the empty Fe *d*-states towards lower energies can in turn facilitate and increase the favorability of ET across the band gap, as the band gap that the electron would need to overcome would be significantly reduced with respect to the bulk hematite substrate.

The covalent bonds formed between the adsorbates and the hematite surface can influence the sorption affinity, as it is observed that (coad)sorption of Fe and/or U is generally more favorable on the hematite surface compared to the corundum surface (-34.1 vs. 5.2 kJ/mol respectively, considering energies using the COSMO solvation model in DMol^3; Table 4-3). The endothermic nature of some of the (coad)sorption reactions is in line with the hypothesis of Glezakou and deJong (2011) [112] that additional proton transfer reactions occur for the stabilization of the sorbed U or Fe complexes. For instance, further hydrolysis of water ligands of the Fe and U adsorbates upon sorption to the substrates, where the protons are transferred to the oxo- and/or hydroxo-ligands at the surface, is likely needed [112]. Nonetheless, the higher stability of the Fe and U adsorbates on the hematite surface compared to the corundum surface can be partially explained by the covalent bonding with the adsorbates.

The differences in the surface reactivities of the corundum and hematite surfaces influence the mechanisms by which charge transfer occurs. PDOS analyses (Figure 4-5a) for the

coadsorbed corundum model $[2UO_2(H_2O)_3 - Fe_{48}O_{96}H_{40} - 2Fe(H_2O)_3]^0$ as well as visualization of spin density isosurfaces for the coadsorbed corundum model (Figure 4-6a) show the corundum slab, as an insulator, does not accept electrons; spin density is only associated with the Fe and U adsorbates. The spin density isosurface highlights the inability for the insulating corundum slab to accept electrons as well as the limited number of ET pathways available on insulating surfaces. Thus, while the more thermodynamically favorable electronic configuration for Fe and U is one where ET has occurred (*i.e.,* Fe^{3+}/U^{5+}), the insulating corundum surface cannot facilitate the transport of an electron from the Fe adsorbate to reach the U adsorbate ~7 Å away.

Hematite on the other hand is capable of participating in the ET reaction between the Fe(II) and U(VI) adsorbate. The hematite surface exhibits strong Lewis-acid characteristics as the Fe^{3+} cations are electron-acceptors [81]; the empty Fe *d*-states in the hematite surface located close to the Fermi level contribute to hematite surface's stronger reactivity and ability to accept electrons. Visualization of spin density isosurfaces for the coadsorbed hematite model further highlights the acidity of the hematite surface, showing the propensity for Fe atoms within the hematite slab to accommodate and/or accept electrons (Figure 4-6b). A multitude of pathways for ET to occur within the surface and bulk of hematite exist, where an electron can be transported between neighboring Fe ions in the surface. As was observed experimentally, the U(IV) and Fe(II) undergo charge transfer upon coadsorption onto the hematite and corundum surfaces. To observe the valence stability as well as potential charge/spin transfer that occur on the hematite and corundum surfaces, the Bader charges and spins are analyzed for the adsorbed and coadsorbed models. For the adsorption of U and Fe onto corundum (*i.e.,* where U and Fe are separately adsorbed to the surface; $[2UO_2(H_2O)_3 - Al_{24}O_{48}H_{20}]^0$ and $[2Fe(H_2O)_3 - Al_{24}O_{48}H_{20}]^0$, respectively), little to no charge/spin density transfer occurs between the adsorbates and the corundum slab (Figure 4-7b); for instance, the spin of the Fe atom decreases slightly (from 3.67 to 3.51) due to the dehydration of the hydration shell and covalent-bonding to O ligands at the surface that draw a fraction of the spin density. The Bader spins show the U and Fe adsorbates are valence stable (Figure 4-7c,d) and are in agreement with experimental observations made in the batch experiments.

Upon coadsorption of Fe and U onto the corundum surface [$2UO_2(H_2O)_3 - Al_{48}O_{96}H_{40} - 2Fe(H_2O)_3]^0$, charge/spin transfer between the Fe and U adsorbates occurs. The spin of the Fe adsorbates increases from 3.67 (for Fe(II) state) to 3.83 while the spin of the U adsorbate increases from 0 (for the U(VI) state) to -1.12 (Figure 4-7c,d); these changes in spin imply ET occurs, where Fe is oxidized and U is reduced (*e.g.*, comparable to the Fe^{3+}/U^{5+} redox pair). The oxo-ligands which bind the Fe and U adsorbates contribute electrons to the reduced U ion (*i.e.*, electrons are removed from the O atoms of the oxo-ligands, making the O atoms less negatively charged, and the charge/spin is transferred to the U ion). The Al cations within the corundum substrate again do not acquire spin density (Figure 4-7b), consistent with its insulating nature. Analysis of the total spin density difference for the (co)adsorbed corundum model confirms charge transfer from the Fe ion to the U ion (Figure 4-8), where the spin of the Fe atoms increases (consistent with Fe being oxidized) and the U atom acquires spin density from the Fe atom. The Fe^{3+}/U^{5+} electronic configuration is the most thermodynamically favorable structure on the corundum surface; a single-point energy calculation shows it is less energetically favorable (+40.5 kJ/mol) to maintain the Fe(II) and U(VI) oxidation states on the corundum surface. The ET reaction is postulated to be influenced by the chemical nature of the Fe and U adsorbates on the corundum surface. Fe^{2+} is dehydrated and hydrolyzed upon sorption to corundum, making it more reactive to oxidation; the presence of a strong-Lewis acid, U(VI), would further promote the oxidation of the Fe(II) ion [82, 96].

Charge transfer on the hematite surface is more complex compared to that observed for the corundum surface. The Fe(III) atoms within the hematite substrate observe absolute Bader spins of 3.84 – 3.92; a considerable amount of spin density is also distributed amongst the O atoms within hematite (*i.e.,* the O atoms can acquire an absolute spin density of up to 0.20) (Figure 4-7a,b). When Fe(II) is adsorbed onto the hematite surface [$2Fe(H_2O)_3 - Fe_{24}O_{48}H_{20}]^0$, the spin of the Fe adsorbate changes from 3.67 to 3.82 while the Fe atoms within the hematite slab generally observe spins of 3.84 - 4.00 (Figure 4-7b,c). Electron delocalization occurs, although the differences in spin are marginal; the spin density is smeared over the hematite substrate, and the spin is not indicative of distinct Fe(II) and Fe(III) oxidation states. This makes it difficult to distinguish the electronic nature of the two species computationally and even more so as experimentally (*i.e.,* this smeared-out spin density could explain the difficulty observing distinct oxidation and spin states in XPS spectra). When U(VI) is adsorbed onto the hematite

surface $[2UO_2(H_2O)_3 - Fe_{24}O_{48}H_{20}]^0$, the U atom acquires a spin density of –0.9 (Figure 4-7d); analysis of the spin density difference show that the U acquires spin density from Fe atoms within the hematite substrate, highlighting electron delocalization and the tendency for spin from Fe atoms to smear over the molecular system. Upon coadsorption of Fe and U onto the hematite surface $[2UO_2(H_2O)_3 - Fe_{48}O_{96}H_{40} - 2Fe(H_2O)_3]^0$, the Fe adsorbate exhibits a spin of +3.9, within the range of spins for the Fe atoms in the hematite surface (3.84 - 3.92), while the U atom acquires an absolute spin of 1.3. Similar to the coadsorbed corundum model, the Fe and U adsorbate the Fe^{3+}/U^{5+} electronic configuration is more thermodynamically favorable. The axial O atoms of the U molecule also acquire spin densities of approximately –0.12, which suggests protonation of the axial O atoms would better stabilize the reduced U ion [70].

The total spin density difference continues to highlight the complexity of ET within the coadsorbed hematite system as well as show potential ET pathways through the hematite slab (Figure 4-9). The hematite surface is shown to participate in the ET reaction where Fe atoms within the surface of the hematite varying degrees of oxidation/reduction, and potential ET pathways through the hematite surface can be observed (Figure 4-9b). Similar to the model for Fe adsorption onto the hematite surface, the charge density is smeared out amongst U and neighboring Fe atoms. The coadsorbed corundum model clearly shows the Fe(II) adsorbate is the electron donor and the ability for U(VI) to acquire electrons in the absence of other Lewis-acids while the coadsorbed hematite models shows both the Fe(III) atoms within the hematite substrate and U(VI) ion as Lewis-acids compete to acquire electrons. While the competition amongst U and the network of Fe(III) – electron acceptors can significantly complicate the pathway the electron can take, charge transfer through the hematite substrate can overcome spatial limitations and potentially enable an electron from the Fe(II) adsorbate to reach the U(VI) adsorbate at a ~7 Å distance. The hematite slab participating in the ET reaction via the proximity effect can have significant implications on the rapidity and efficiency that redox reactions are catalyzed.

4.5 Discussion

The experimental and computational results in this study further enhance our understanding of how the heterogeneous catalysis of U(VI) reduction by Fe(II) is influenced by substrates' chemical and electronic properties. Observations from batch experiments show that the rate and extent of U(VI) reduction by Fe(II) in the presence of isostructural Fe and Al

(oxyhydr)oxides show the rate of uranyl reduction by Fe(II) is heavily influenced by the substrate present. For instance, in the presence of the Fe (oxyhydr)oxides, the total U(VI) concentrations drop by two orders of magnitude within the first 1.5 hours of reaction time and U(VI) is reduced by Fe(II) within a short time period (< 24 hours), while in the presence of the Al (oxyhydr)oxides, four or more days are needed for pronounced uranyl reduction by Fe(II) to occur (Figure 4-3b). The rate of uranyl reduction by Fe(II) is determined to be an order of magnitude faster in the presence of Fe (oxyhydr)oxides than in the presence of Al (oxyhydr)oxides using pseudo-first order approximations, regardless of whether more Fe(II) was sorbed to the Fe (oxyhydr)oxide substrates compared to the Al (oxyhydr)oxide substrates (Table 4-1). The estimated fractions of reduced U phases obtained from XPS spectra confirm and complement the measured U(VI)/Fe(II) redox rates (Table 4-2). Analysis of the aqueous and solid fraction from the batch experiments consistently show that the reduction of uranyl by Fe(II) in the presence of the Fe (oxyhydr)oxides is significantly faster compared to when in the presence of its isostructural Al counterparts. These observations are in agreement with previous studies; for instance, the rate of Tc(VII) reduction to Tc(IV) (a three electron-transfer process) by Fe(II) was 200 times slower in the presence of Al (oxyhydr)oxides compared to Fe (oxyhydr)oxides [93].

The substrate surfaces are postulated to be covered by the Fe(II) adsorbate (assuming uniform surface coverage). Measurements of the [$Fe(II)_{sorbed}$] in this study suggest that the SSL limit is exceeded on each of the substrate surfaces, suggesting that the substrate surfaces are covered by more than a monolayer of Fe(II). However, despite a potentially significant portion of the Al substrates being covered by the Fe adsorbate, the redox rate is still significantly faster in the presence of the Fe (oxyhydr)oxide relative to the Al (oxyhydr)oxides. The redox reactions are not limited to or are not only dependent on processes occurring at the interface; the underlying substrate significantly influences the catalysis of redox reactions.

Ab initio calculations further probe and enhance our understanding of how minerals' electronic properties influence sorption/redox processes, in particular highlighting the differences in surface reactivities between insulating and semiconducting surfaces that affect charge transfer mechanisms. Insulating surfaces are capable of catalyzing U(VI) reduction by Fe(II) through the dehydration and hydrolysis of the Fe and U adsorbates upon coadsorption to the corundum

surface (as is shown through analysis of the Bader spins and charges). However, isosurfaces of the spin density and charge density difference demonstrate that, in the event that the U(VI) and Fe(II) are not directly interacting such as via an inner-sphere complex, there is not a pathway from which the electron from Fe(II) can reach the U(VI) ion on or through the corundum surface due to the corundum slab's inability to accept and transfer electrons (Figure 4-8b). The high number of empty Fe *d*-states close to the Fermi level would better enable the Fe atoms at the hematite surface, over the Al atoms at the corundum surface, to accept electrons and participate in the redox reaction (Figure 4-5b). The network of electron-accepting Fe atoms within the hematite substrate then presents a multitude of pathways from which ET through the hematite slab can occur (Figure 4-6b), where the electron from Fe(II) can be transferred to and transported between Fe atoms at the hematite surface to potentially reduce a uranyl ion sorbed on the surface, within the near vicinity (Figure 4-9b).

In accordance with conceptual models for sorption and redox mechanisms on insulating surfaces, the Al (oxyhydr)oxides facilitate uranyl reduction by Fe(II) by acting as coordinating surfaces, stripping hydration shells and enabling ions to interact with one another. Computational models from a previous study [96] demonstrated that ET occurs rapidly (10^8 s^{-1}), if U and Fe can dehydrate and form an inner-sphere complex with one another (where U and Fe could interact via bridging ligands). Thus, uranyl reduction by Fe(II) can be facilitated by dehydration of Fe(II) and U(VI) upon sorption onto insulating Al (oxyhydr)oxide surfaces and formation of Fe-U inner-sphere complexes [50, 96, 113]. However, as the computational models in this study highlight, the reduction of U(VI) by Fe(II) on an insulating surface is spatially limited, essentially showing that it is a requirement for the U and Fe to form an inner-sphere complex for the redox reaction to occur.

Semiconducting Fe(III) (oxyhydr)oxides surfaces can act as coordinating surfaces as well, though their semiconducting properties allow for uranyl reduction by Fe(II) to proceed by transporting electrons through the semiconducting surface via the conduction band, impurity bands, or localized states [113]. Thus, in addition to Fe(II) existing as dissolved and sorbed Fe(II) complexes at the substrate surfaces, Fe(II) can exist within the bulk of Fe(III) (oxyhydr)oxides through interfacial ET. In turn, the incorporation of Fe(II) and mobility of electrons through semiconducting surfaces can catalyze redox reactions via the proximity effect

and overcome spatial limitations that insulating minerals experience [17, 18]. An electron donated from an Fe(II) adsorbate to an Fe(III) cation at the surface of Fe(III) (oxyhydr)oxides can be transferred to neighboring Fe(III) cations in the near-surface of the substrate through a series of ET reactions; in turn, it is possible the electron can be transported away from the original sorption site (several Angstroms to nanometers away), as evidenced by Fe(II)-catalyzed recrystallization of ferric ox hydroxides [114]. The proximity effect can possibly be a significant mechanism that can explain the rapidity and efficiency with which semiconducting minerals catalyze redox reactions.

4.6 Conclusions

To most accurately predict the migration of radionuclides and metals in actual geochemical systems, it is necessary to integrate detailed redox reactions mechanisms of heterogeneous systems into models; observations from this study show considerably different behaviors of the redox sensitive elements Fe(II) and U(VI) in the presence of Fe and Al (oxyhydr)oxides that affect the rate of uranyl reduction by Fe(II). Batch sorption experiments show Fe(II) associated with Al and Fe (oxyhydr)oxide minerals can lead to U(VI) reduction, and imply that heterogeneous reduction of U(VI) should occur in anoxic subsurface environments. Sediments containing even small amounts of Fe(III) (oxyhydr)oxides and Fe(II) would be expected to rapidly catalyze U(VI) reduction with respect to its isostructural, insulating Al (oxyhydr)oxides.

The *ab initio* calculations within this study present the potential implications and effects of the proximity effect on the catalysis of U(VI) reduction by Fe(II) on semiconducting surfaces. While it is plausible that ET through the surface occurs, the pathway the electron chooses through a semiconducting mineral is still uncertain (Becker et al., 2001; Rosso and Becker, 2002). For instance, would an electron transported through the hematite surface always reach a U(VI) ion or would it rather be transferred to neighboring Fe cations in the hematite surface/bulk? Due to the complexities associated with these pathways through semiconducting surfaces, current metal transport models do not account for the influence and impact of redox pathways occurring through the semiconducting surface, though a wide range of specific geochemical implications hinge on better understanding and quantifying this effect.

To account for the influence of the mineral surface chemistry and electronic properties and determine the importance of these semiconducting reaction pathways, it is important to understand the thermodynamics and kinetics for these different pathways. The observation of ET and its pathways via experimental methods is difficult; only within recent years have methods been able to resolve kinetics for simple, individual ET processes [115]. One proposition is to apply an alternative method, Marcus Theory, to understand the energetics of ET processes in ternary, coadsorbed systems and elucidate energetic barriers within these computationally-modeled coadsorbed systems [69, 116]. The viability of this method is currently being tested. Continuing studies on the reaction mechanisms relevant to ternary, coadsorbed systems using both experimental and computational methods can elucidate the pathways through which redox reactions are catalyzed, and in turn contribute to predictions as to how radionuclide and metal transport in the subsurface will be influenced by the surrounding geologic media.

4.7 Acknowledgements

This research was supported by the U.S. Office of Science, BES/HEC (Basic Energy Sciences, Heavy Element Chemistry) DE-FG02-06ER15783. The authors would like to thank the following scientists for their technical assistance with the instrumentation and analyses used in this study: Dr. Ante Wong-Foy and Dr. Adam Matzger (surface area analyzer), Dr. Thomas Yavaraski (ICP-MS), Dr. Zhongrui Li (XRD), Dr. Greg Dick (UV-Vis), and Dr. Eugene Ilton, Dr. Kai Sun, and Dr. Haiping Sun (XPS; instrumentation supported by NSF grant # DMR-0420785). We would also like to thank Dr. Drew Latta and Odeta Qafoku for their help with developing experimental procedures.

4.8 Tables

Table 4-1: Experimental conditions for the coadsorption of Fe(II) and U(VI) on the Fe (oxyhydr)oxides hematite and goethite and their isostructural Al counterparts corundum and diaspore, respectively. Rates for the sorption and reduction of U(VI) by Fe(II) in the presence of the Fe and Al (oxyhydr)oxides are also included, demonstrating the influence of the substrate on catalyzing the redox reaction. In this study Fe (oxyhydr)oxides are shown to facilitate the reduction of U(VI) by Fe(II) more rapidly compared to the Al (oxyhydr)oxides.

Substrate	**Surface area**	**Mass added**	**Estimated SSL****		$[Fe]_{sorb}$	$[U(VI)]_{ads,\ 24h}$	$[U(VI)]_{total,\ 24h}$	k_{ps}	k_{ps}/Fe_{sorb}
	(m^2/g)	**(g/L)***	**(µmol/g)**	**(mM)*****	**(mM)**	**(mM)**	**(mM)**	**(h^{-1}) [R^2]**	**(h^{-1})**
Hematite	1.13	8.85	4.70	0.04(7)	0.20	1.57×10^{-4}	6.80×10^{-4}	0.53 [0.95]	2.65
Corundum	10.83	0.92	44.98	0.04(5)	0.09	7.99×10^{-4}	1.59×10^{-2}	0.04 [0.42]	0.45
Goethite	49.59	0.20	205.89	0.04(1)	0.16	2.55×10^{-4}	2.08×10^{-3}	0.45 [0.92]	2.81
Diaspore	5.56	1.80	23.08	0.04(2)	0.07	3.24×10^{-4}	1.20×10^{-2}	0.03 [0.61]	0.37

* The amount of substrate added to each reactor led to a total surface area of ~10 m^2/L; the amount of surface area is consistent between all the reactors.

** The number of sites on each of the mineral surfaces was assumed to be ~ 2.5 sites/nm2 (based off of values used in Larese-Casanova and Scherer (2007) [104] and Jeon, *et al.* (2003) [111]) to be consistent in the SSL estimations. It is probable that the number of surface sites can vary considerably by the mineral, surfaces exposed, etc., [117].

***Values for the third significant figure are included in the SSL values in mM in parentheses for additional reference.

Table 4-2: BEs for peaks fit to U 4f 7/2 and the average percentage of U components present in Fe and uranium coadsorbed samples.

U(VI) standards measured in this study

	time	FWHM	U(IV) BE (eV)	%U	U(V) BE (eV)	%U	U(VI) BE (eV)	%U	ΔBE
Schoepite	24	1.71	--	--	--	--	381.33	100	--
Hematite	24	1.99	--	--	--	--	381.65	100	--
Goethite	24	1.98	--	--	--	--	381.46	100	--
Corundum	24	2.10	--	--	--	--	381.71	100	--
Diaspore	24	2.21	--	--	--	--	381.50	100	--

Fe – U coadsorbed

Hematite	24	1.89 ± 0.1	379.89 ± 0.1	48 ± 8	380.68 ± 0.1	37 ± 4	381.65 ± 0.3	15 ± 5	1.76
Goethite	24	1.86 ± 0.1	379.82 ± 0.1	25 ± 4	380.48 ± 0.1	50 ± 1	381.39 ± 0.1	25 ± 3	1.57
Corundum	24	1.74 ± 0.1	379.80 ± 0.3	0 ± 0	380.51 ± 0.1	40 ± 1	381.60 ± 0.1	60 ± 1	1.09
Corundum	96	2.07 ± 0.1	379.95 ± 0.1	53 ± 5	380.74 ± 0.1	29 ± 4	381.61 ± 0.1	18 ± 1	1.65
Diaspore	24	2.08 ± 0.1	380.03 ± 0.1	18 ± 3	380.57 ± 0.1	29 ± 8	381.40 ± 0.1	52 ± 5	1.37
Diaspore	456	2.14 ± 0.1	380.00 ± 0.1	28 ± 1	380.66 ± 0.1	32 ± 1	381.50 ± 0.1	40 ± 1	1.50

Table 4-3: Energies for the (co)adsorption of Fe and/or U onto the hydroxylated (001) corundum and hematite surfaces quantified from the computational calculations.

(Co)adsorption model	E_{ads} in vacuum (kJ/mol)		E_{ads} with COSMO (kJ/mol)	
	Corundum	Hematite	Corundum	Hematite
$2UO_2(H_2O)_3 - M_{24}O_{48}H_{20}$	716.9	627.5	286.1	65.6
$2Fe(H_2O)_3 - M_{24}O_{48}H_{20}$	221.7	171.5	273.0	244.2
$2UO_2(H_2O)_3 - M_{48}O_{96}H_{40} - 2Fe(H_2O)_3$	68.5	118.2	5.2	-34.1

4.9 Figures

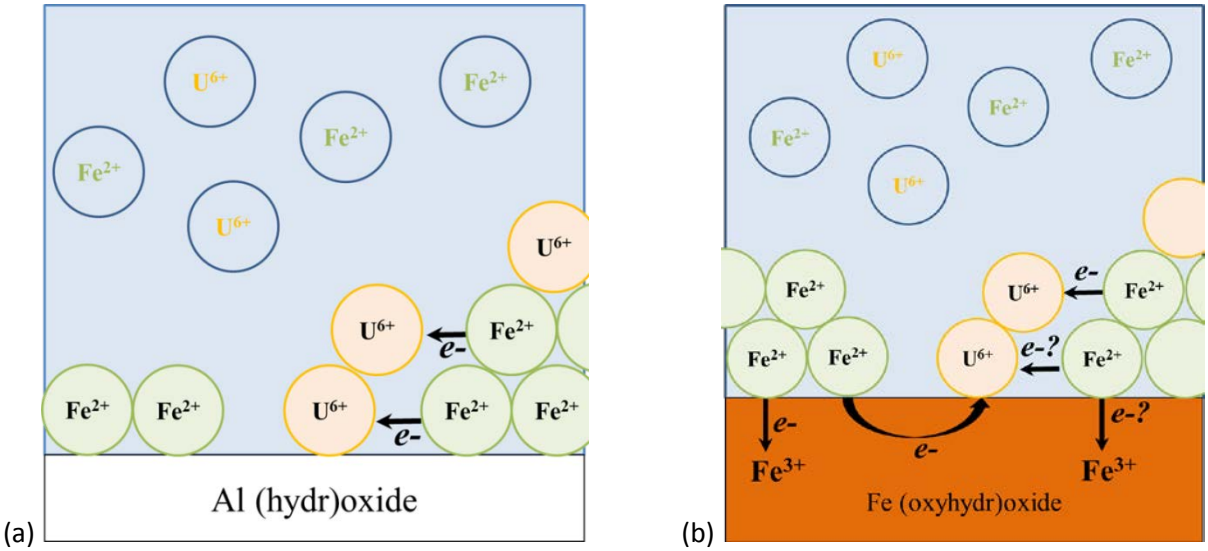

Abstract figure 4-1: Hypothesized mechanisms and pathways for electron transfer (ET) to occur by on (a) Al (oxyhydr)oxide and (b) Fe (oxyhydr)oxide surfaces. These ET pathways on the respective minerals help catalyze uranyl reduction by Fe(II); for instance, Al (oxyhydr)oxide surfaces can act as a coordinating surface, dehydrating cations and enabling them to form inner-sphere U-Fe complexes. In addition to acting as coordinating surfaces, Fe (oxyhydr)oxide surfaces can potentially participate in the redox reaction via the proximity effect; an electron can be transferred to and shuttled between Fe cations at the substrate surface, possibly reaching a nearby U(VI) ion sorbed within the vicinity.

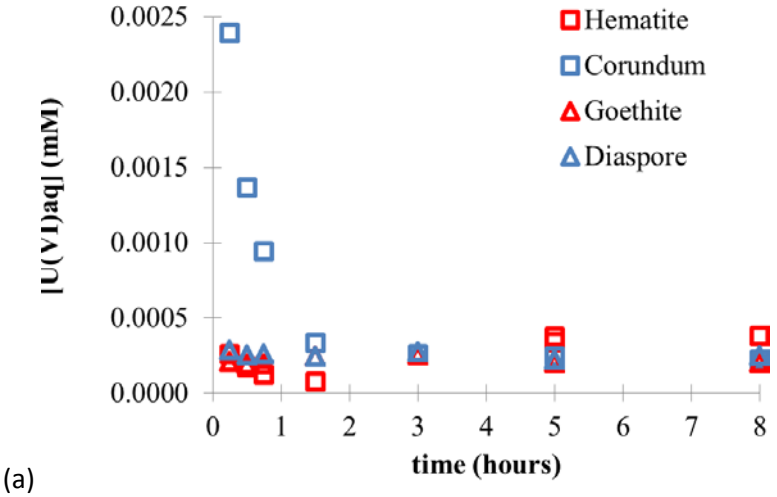

(a)

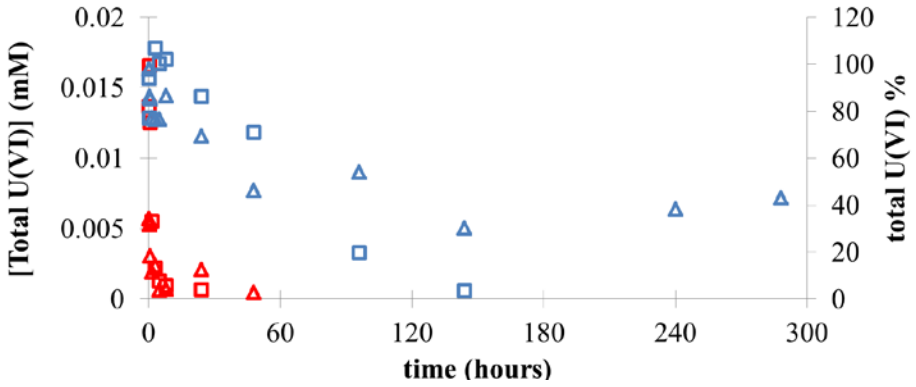

(b)

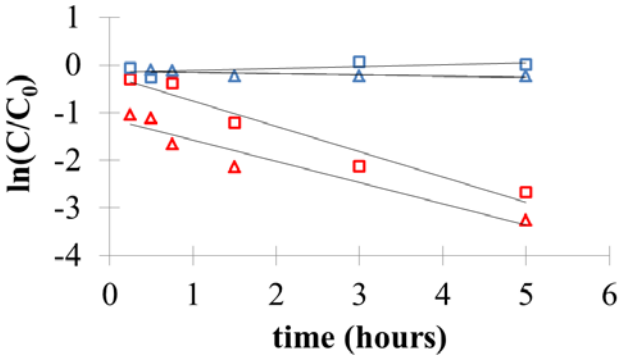

(c)

Figure 4-1: (a) Measured aqueous U(VI) concentrations over time from batch coadsorption experiments with hematite, corundum, goethite, and diaspore. (b) Calculated total concentrations of U(VI) in the coadsorbed systems, derived from the amount of U(VI) that was extractable over time. (c) The pseudo-first order reaction rate for U(VI) reduction was approximated through linearly fitting the natural logarithm of the total U(VI) concentrations measured within the first five hours relative to the initial U(VI) concentration (0.018 mM).

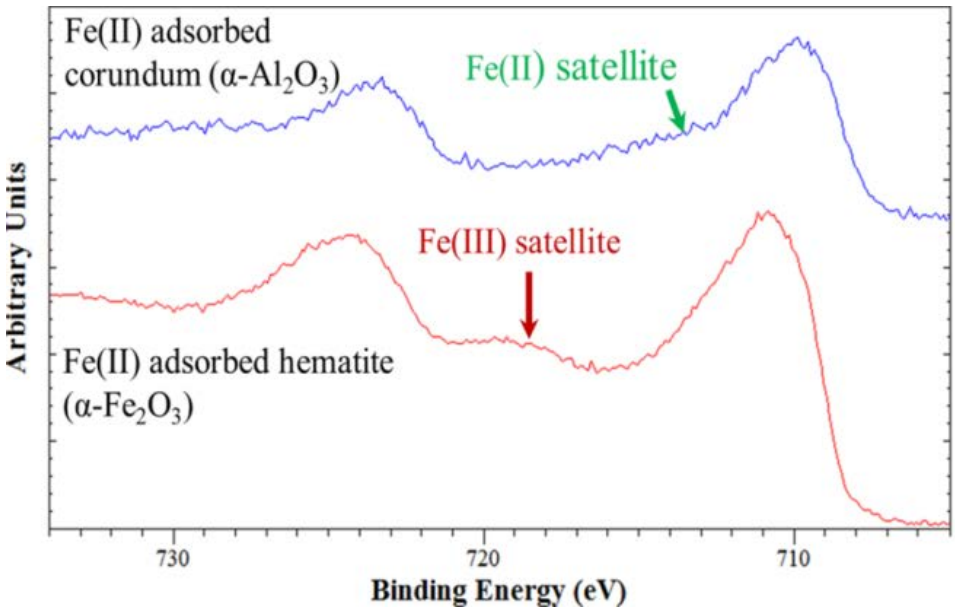

Figure 4-2: XPS spectra for Fe adsorbed onto corundum (upper spectra) and hematite (lower spectra) as representative samples for understanding the behavior of Fe(II) sorption on the Al – and Fe(oxyhydr)oxides used. Fe(II) is valence stable on the corundum surface while Fe(III) is prevalent on the hematite surface (likely due to the strong signal from the Fe(III) substrate).

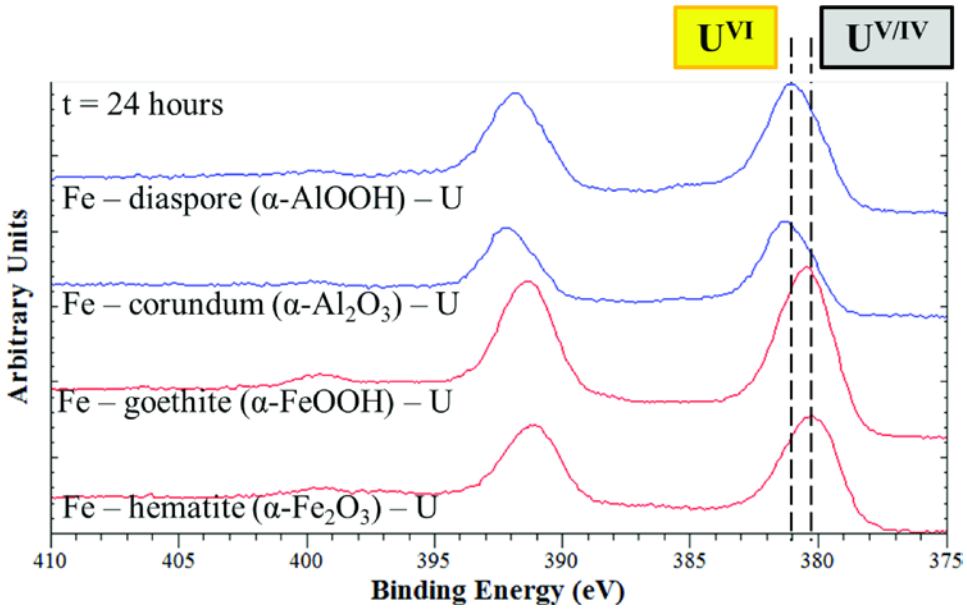

(a)

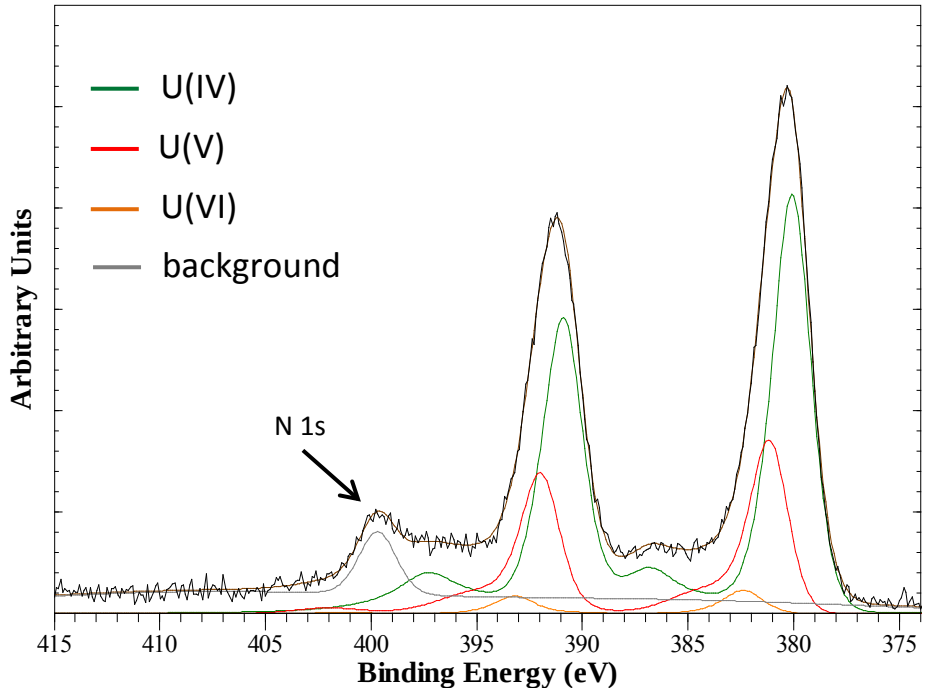

(b)

Figure 4-3: (a) XPS spectra for U 4f in the Fe-U coadsorbed Al and Fe (oxyhydr)oxide systems show the amount of U(VI) reduction that has occurred over 24 hours. (b) U4f XPS spectra for the Fe-U hematite coadsorbed system after 24 hours, showing the high proportion of U(VI) reduction to U(IV) and U(V) phases. The peak of ~399 eV is a N 1s peak that results from the experimental solutions used (e.g., uranyl nitrate is used to make the stock solution).

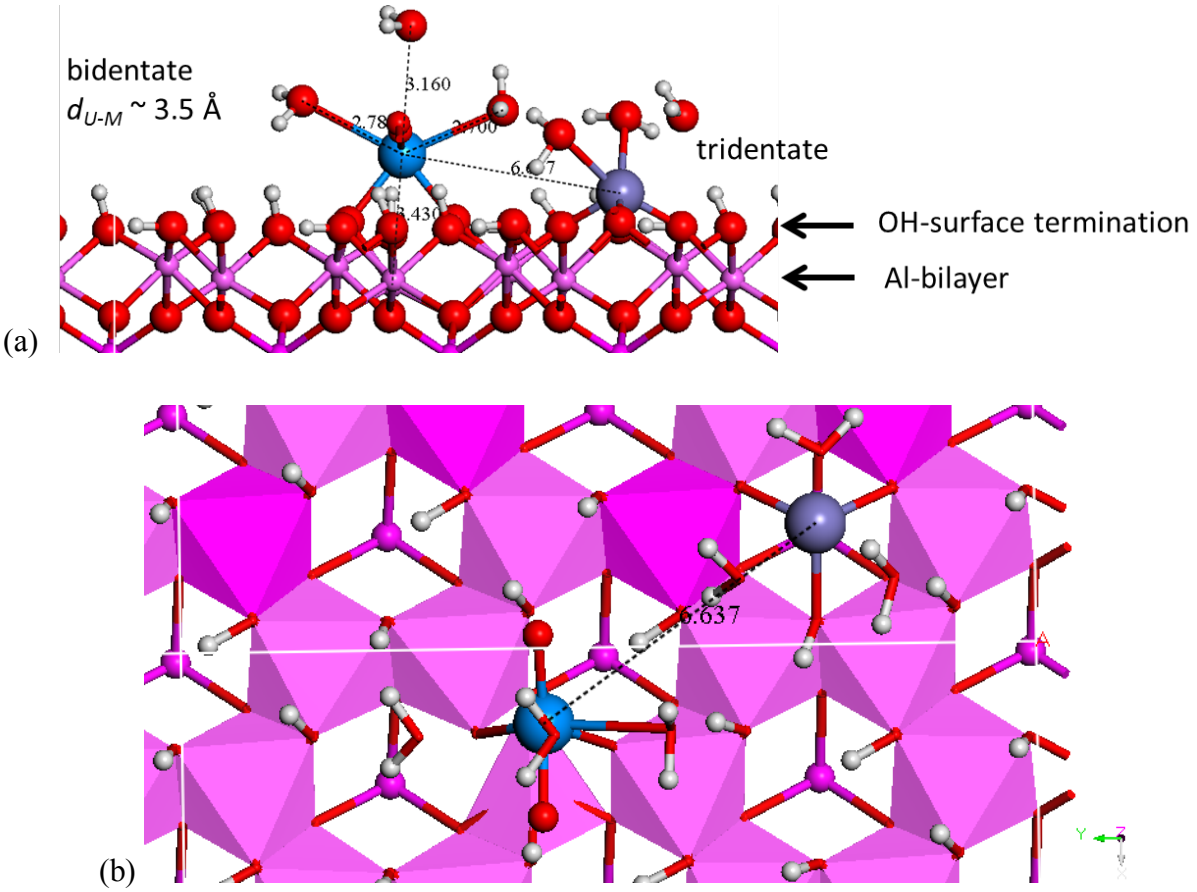

Figure 4-4: Structural configuration for U and Fe coadsorbed onto the hydroxylated (001) corundum surface, looking down [100] (a) and [001] (b). The structural configuration for the U and Fe coadsorbed onto the (001) hematite surface is essentially the same given the structural similarity between the corundum and hematite surfaces. Al = pink atoms, O = red atoms, H = white atoms, U = blue atoms, Fe = purple atoms.

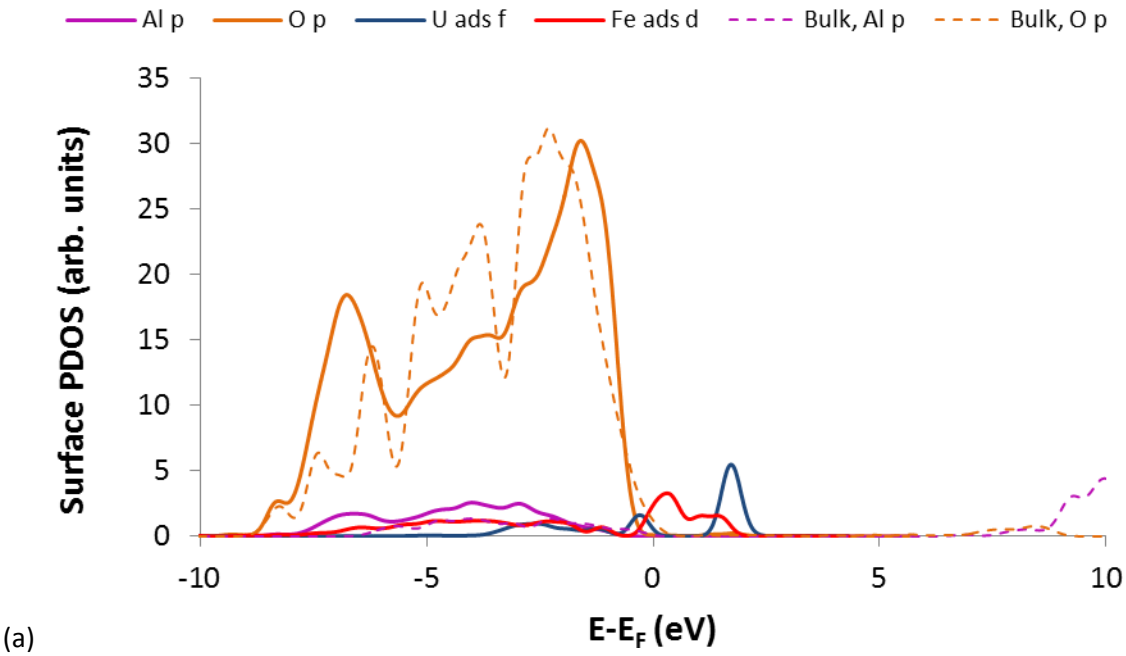

(a)

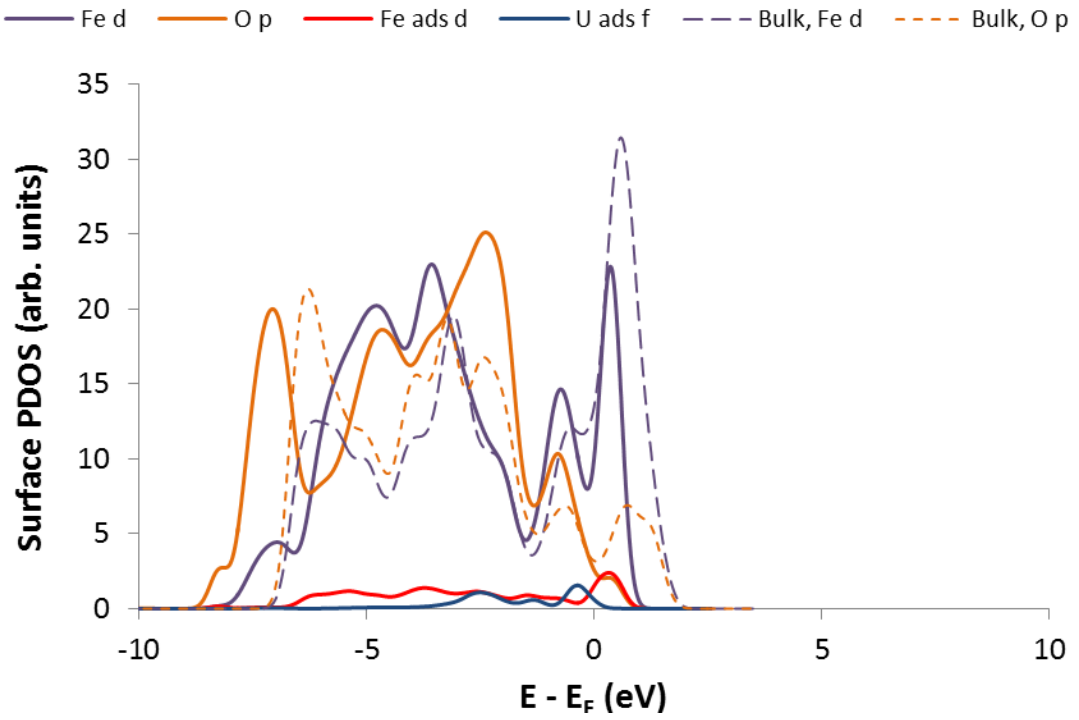

(b)

Figure 4-5: PDOS for U and Fe coadsorbed onto the hydroxylated (001) corundum (a) and hematite (b) surfaces. The PDOS for the ions from the substrate (*i.e.*, O and Al/Fe cations from corundum/hematite) are calculated from the (bi)layer at the surface, as sorption and redox processes are affecting the surface atoms most.

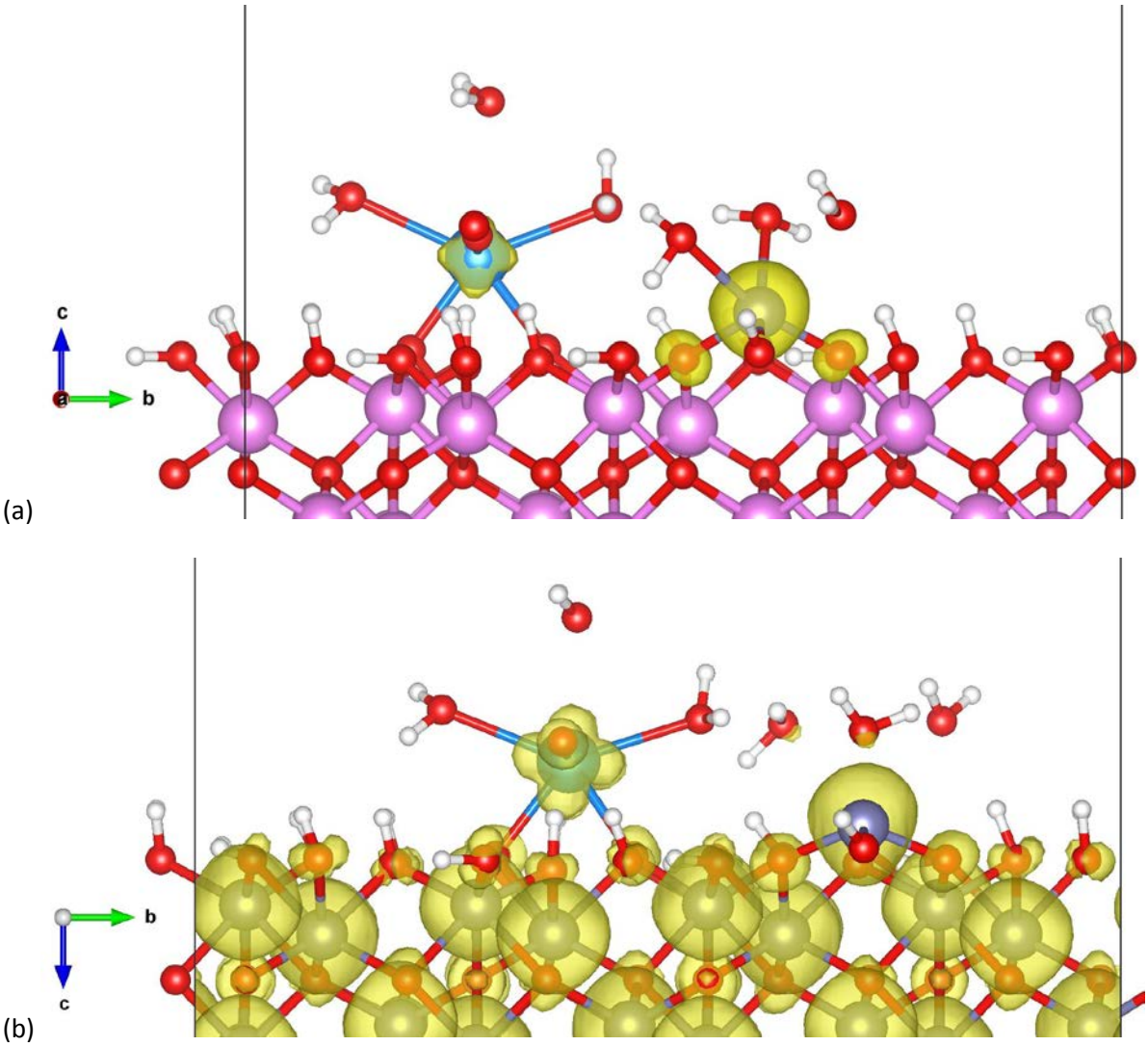

Figure 4-6: Total, absolute spin densities for U and Fe coadsorbed on the hydroxylated (001) (a) corundum and (b) hematite surfaces, showing the propensity for atoms on and within the slabs to acquire spin.

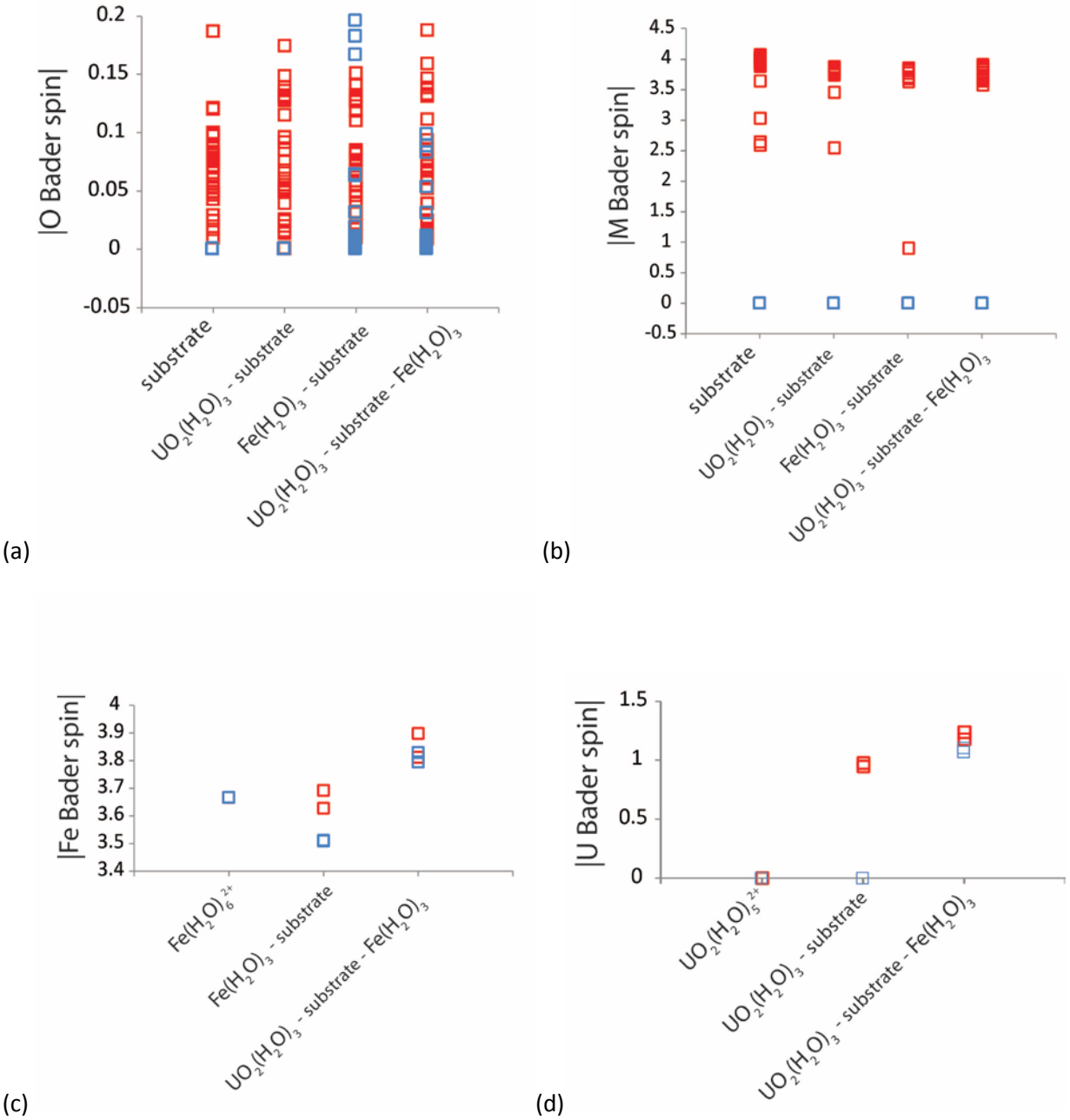

Figure 4-7: Comparison of the absolute Bader spins for the (a) O atoms within the substrates, (b) cations within the substrate (M=Al for corundum, Fe for hematite), (c) the Fe adsorbate, and (d) U adsorbate before and after (co)adsorption.

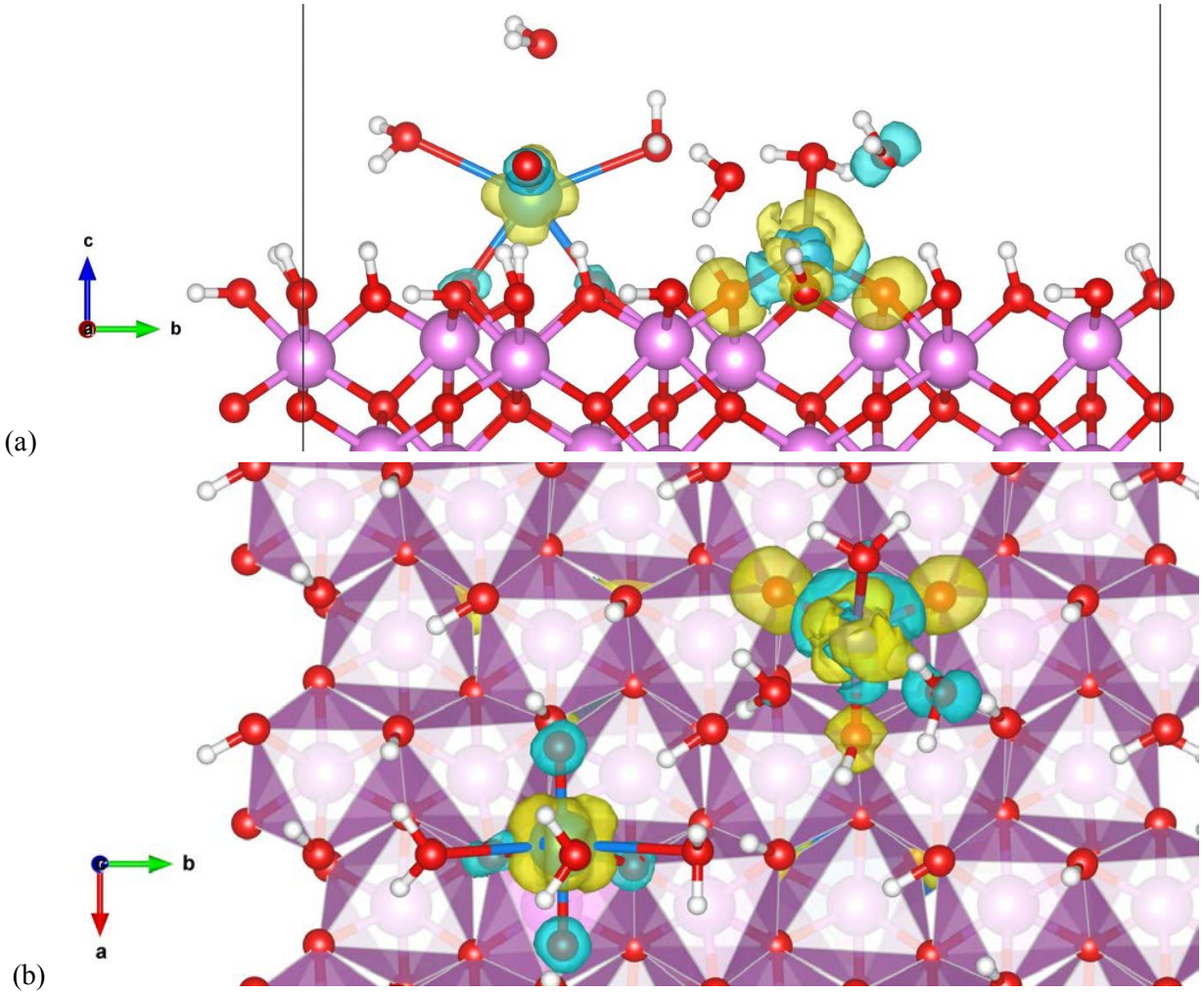

Figure 4-8: Spin density difference for U and Fe coadsorbed on the hydroxylated (001) corundum surface. Yellow isosurfaces indicate positive isovalues (e.g., the spin value of the atom increased with respect to the individual components) while blue isosurfaces indicate negative isovalues (e.g., the spin value of the atom decreased with respect to the individual components).

(a)

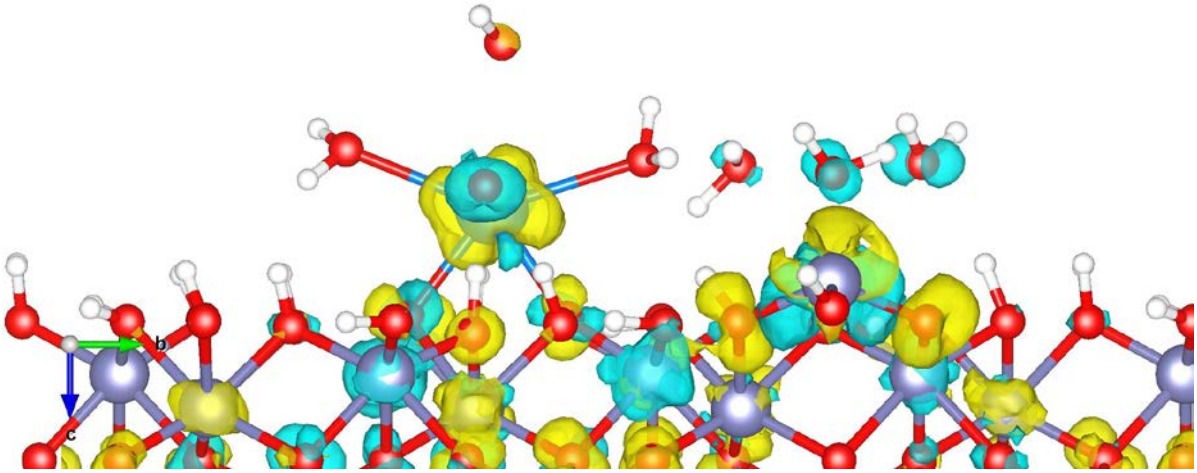

(b)

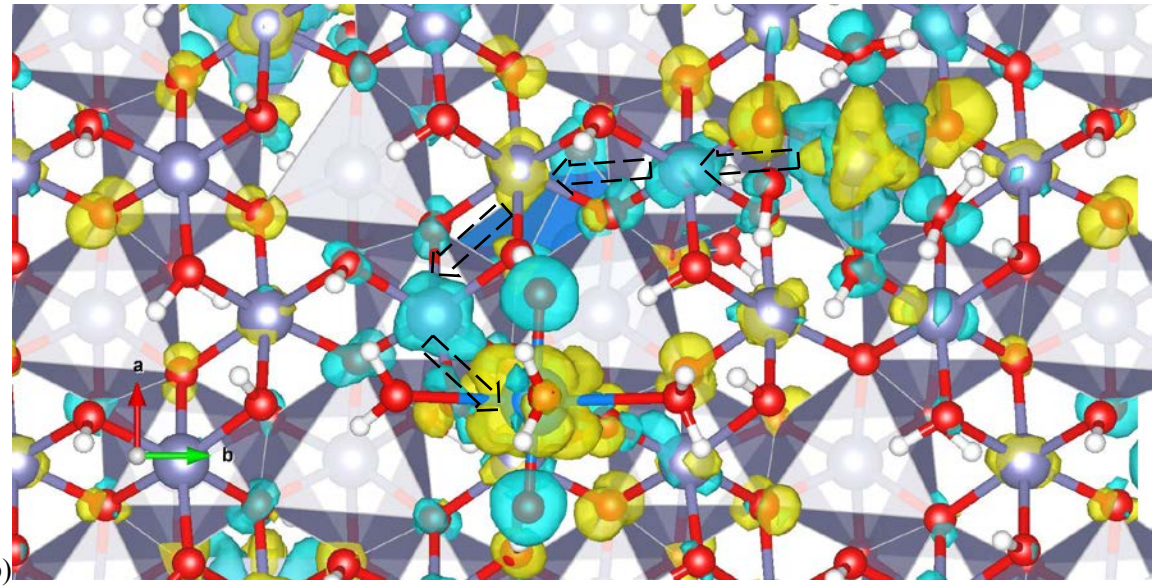

Figure 4-9: Spin density difference for U and Fe coadsorbed on the hydroxylated (001) hematite surface looking down (a) [100] and (b) [001], respectively. Yellow isosurfaces indicate positive isovalues (e.g., the spin value of the atom increased with respect to the individual components) while blue isosurfaces indicate negative isovalues (e.g., the spin value of the atom decreased with respect to the individual components). The dashed arrows indicate one of the potential charge transfer pathway where an electron from the Fe adsorbate is transferred to an underlying Fe atom within the hematite, and in turn the electron is transport through the hematite surface potentially reaching the U adsorbate.

Chapter 5:
Evaluating the energetics and kinetics for electron transfer pathways on Fe and Al oxides using Marcus Theory

S.D. Taylor[1], K.M. Rosso[2], and U. Becker[1]

[1]The University of Michigan, Department of Earth and Environmental Sciences, 2534 C. C. Little Building, 1100 North University Ave., Ann Arbor, MI 48109–1005, United States.

[2]Pacific Northwest National Laboratory, Physical Sciences Division, PO Box 999, Richland, WA 99352, United States.

5.1 Abstract

Experimental studies have demonstrated that the chemical and electronic properties of substrates can affect the rate of redox reactions. In particular, the reduction of U(VI) by Fe(II) occurs more rapidly in the presence of semiconducting Fe(oxyhydr)oxide minerals compared to their insulating Al isostructures. It is postulated that semiconducting minerals may enhance the rates of redox reaction over insulating minerals by shuttling electrons through it surface, via the proximity effect. However, there is little thermodynamic and/or kinetic data available on electron transfer pathways (ET) within these ternary, coadsorbed systems to support these conceptual models.

In this study, *ab initio* calculations coupled with Marcus Theory (MT) is used as a novel approach to understand the energetics and kinetics of redox reactions occurring in ternary, coadsorbed systems. This is the first time MT is applied to understand these mineral-catalyzed processes. Molecular simulations for the reduction of U(VI) by Fe(II) in the presence of corundum and hematite clusters are done to observe how charge transfer pathways differ between insulating and semiconducting substrates.

The reduction of U(VI) to U(V) by Fe(II) on the insulating corundum cluster is found to be enhanced through IS complexation of Fe-U ions. In this study, when U and Fe are coadsorbed on the corundum cluster ($cET_{FeAds\text{-}UAds}$) and are spatially separated by ~4.6 Å, the $cET_{FeAds\text{-}UAds}$ reaction proceeds at rate of 2×10^{2} s^{-1}. When Fe is incorporated into the corundum structure and U interacts with the Fe ion through a hydroxyl ligand ($cET_{FeInc\text{-}UAds}$), the $cET_{FeInc\text{-}Uads}$ reaction is five orders of magnitude faster (2×10^{7} s^{-1}) than that observed for $cET_{FeAds\text{-}UAds}$. Additionally, the incorporation of Fe into the corundum cluster and IS-complexation between U and Fe increases the adiabaticity of the $cET_{FeInc\text{-}UAds}$ reaction, meaning there is a higher probability of ET occurring. ET reactions on the hematite cluster generally proceed adiabatically, which is possibly one reason why ET is enhanced on semiconducting minerals.

The potential for the hematite cluster to transport electrons between Fe and U coadsorbates (*i.e.,* ET occurs via the proximity effect) is also investigated. Interfacial ET ($hET_{FeAds\text{-}FeHem1}$) is the first of the three ET reactions used to model a pathway occurring through the proximity effect. The transfer of an electron from the Fe adsorbate through the interface, to an underlying Fe-cation in the hematite cluster, is endothermic (48 kJ/mol). The $hET_{FeAds\text{-}FeHem1}$ reaction proceeds adiabatically but slowly at a rate of 10^{-3} s^{-1}. Surficial ET within the hematite cluster ($hET_{FeHem1\text{-}FeHem2}$), the second ET step, is also endothermic (76 kJ/mol), proceeds adiabatically, and slowly at a rate of 10^{-7} s^{-1}. These calculations suggest that the ET reactions between the interfacial and surficial Fe cations are the energetically and/or kinetically limiting steps for ET occurring via the proximity effect. While interfacial and surficial ET reactions between Fe cations are endothermic and proceed slowly, the reduction of U(VI) to U(V) by Fe(II) within the hematite cluster ($hET_{FeHem2\text{-}UAds}$) is highly exothermic (-270 kJ/mol). The $hET_{FeHem2\text{-}UAds}$ reactions would occur rapidly at a rate of 10^{12} s^{-1}, though ET proceeds as nonadiabatically. Thus, it postulated that the exothermicity of the $hET_{FeHem2\text{-}UAds}$ reaction could potentially drive the ET to occur via the proximity effect. To better predict the potential energetic and kinetic limitations in ET pathways, model parameters (*e.g.,* application of the DFT-B3LYP functional) are currently being applied and tested to improve the precision of the energetic and kinetic values calculated.

In general, a more fundamental understanding of ET pathways at insulating and semiconducting substrates is gained by applying MT. It is possible that, with continued

development of this approach, that MT can be used to further advance our understanding of redox-reactions for a broad range of geochemical systems, such as the geochemical cycling of As and Fe.

5.2 Introduction

Redox reactions control the mobility and the geochemical cycling of many metals in the environment. The mobility of actinides, such as uranium (U), is controlled by their redox state. U(VI) species (and other radionuclides at higher oxidations states) are soluble and are potentially mobile in the subsurface. The reduction of soluble U(VI) to U(IV) and subsequent precipitation to insoluble $U(IV)O_{2(s)}$ would decrease aqueous U concentrations to below 10^{-14} M, thereby limiting the mobility of uranium in the subsurface.

The reduction of U(VI) and other metals can be heavily influenced by heterogeneous catalysts such as mineral surfaces. For instance, the abiotic reduction of U(VI) by reductants such as Fe(II) is kinetically inhibited, but mineral surfaces, particularly those of iron (oxyhydr)oxides, can facilitate the reduction of U(VI) by Fe(II) [11-14]. Mineral surfaces are capable of overcoming energetic and/or kinetic barriers existing in redox reactions via heterogeneous pathways and mechanisms. For instance, mineral surfaces aid in stripping the hydration sphere around ions that exist as hydrated outer-sphere (OS) complexes [1, 17, 118, 119]; the dehydration of the ions and sorption onto the surface in turn promote the formation of inner-sphere (IS) complexes whereby ET occurs more readily [5, 10, 24]. The catalysis of U(VI) reduction to U(V) by Fe(II) via the OS and IS mechanisms described above is supported ET calculations using *ab initio* methods coupled with Marcus Theory (MT) [96].

While the mineral surface as a heterogeneous catalyst for redox reactions is often considered as acting as a substrate that can dehydrate ions and facilitate IS-complexation, there are potentially numerous mechanisms and pathways available on mineral surfaces that enhance the rate of redox reactions. In particular, the rate of reduction is influenced by the substrates' electronic and chemical properties. Batch experiments have been conducted (Chapters 3 and 4 within this dissertation) to observe the catalysis of U(VI) reduction by Fe(II) in the presence of different solid substrates (schoepite, hematite, goethite, corundum, and diaspore). Within Chapter 4, it was found that the reduction of U(VI) by Fe(II) in the presence of semiconducting

Fe (oxyhydr)oxide minerals (such as hematite, α-Fe_2O_3) occurs ten times faster than in the presence of insulating Al isostructures (corundum, α-Al_2O_3). Other studies have made similar observations, showing the rate of redox reactions are heavily influenced by the substrate present. For instance, the reduction of Tc(VII) by Fe(II) in the presence of Fe (oxyhydr)oxides is > 200 times faster than in the presence of Al (oxyhydr)oxides [93].

Quantum-mechanical models in Chapter 4 provide further insight into the molecular structures, thermodynamics, and potential charge transfer pathways of coadsorbed uranium species and Fe(II) reductant on periodic iron- and aluminum-oxide surfaces (*i.e.* hematite and corundum). These methods highlight how electronic charge transfer paths or spin transitions in semiconductors can enhance redox reaction rates, supporting previous hypotheses [17, 23-25]. The proximity effect describes the potential for the transfer of an electron from one coadsorbate to the other using pathways through the semiconducting surface [17, 18]. This effect may be a potentially influential mechanism that enhances the rate U(VI) is reduced by Fe(II) when adsorbed on semiconducting mineral surfaces.

While ET pathways through semiconducting surfaces have been postulated and can be identified using a combination of experimental methods and quantum-mechanical models, mechanisms for these surface-mediated redox processes and nanoscale reactions are not well understood. In particular, there is a lack of information on the energetics and kinetics of charge transfer pathways. For instance, while the proximity effect is postulated to strongly increase ET rates on semiconducting surfaces, it is unclear whether and what energetic barriers exist for interfacial ET to occur between sorbed Fe(II) and/or sorbed U(VI) with the hematite surface. In turn, it is difficult to understand the fundamentals of heterogeneous catalysis of redox reactions and how the coadsorption of Fe and U on mineral surfaces, as described above, facilitates ET.

This study provides further insight into the atomistic mechanisms that affect the thermodynamics and kinetics of different electron transfer pathways, leading to a better understanding of insulating and semiconducting substrates can catalyze redox reactions and/or facilitate ET. As was shown in Chapter 3 (for the study of U(VI) reduction by Fe(II) as OS and IS complexes) and other studies, molecular simulations coupled with MT are capable of providing information on the energetics and kinetics of ET reactions. Thus, it is postulated *ab initio* methods coupled with MT can also provide insight into the redox thermodynamics and

kinetics of coadsorbed systems. In this study MT is an alternative method that is applied for the first time to investigate the thermodynamics and kinetics of electron transfer pathways for ternary, coadsorbed systems. MT is coupled with a*b initio* methods to evaluate potential charge transfer pathways on semiconducting and insulating minerals. ET calculations on molecular models of Fe and U coadsorbed on to clusters of hematite and corundum are used to study different ET pathways; for instance, the calculations are applied to show whether semiconducting hematite serve as an electron-shuttling medium in contrast to corundum. Through combining unique and novel approaches using atomistic modeling and experiments, more detailed information on the structures, thermodynamics, kinetics, and reaction mechanisms and pathways involved in the heterogeneous catalysis of redox reactions can be gained, with applications to the geochemical cycling of other metals such as chromium and arsenic.

5.3 Methods

5.3.1 Molecular models

Molecular models of Fe(II) and U(VI) adsorbed on insulating corundum and semiconducting hematite clusters, representing the hydrated (001) surfaces, are studied to understand the energetics for different potential ET pathways on insulating and semiconducting surfaces. Previously presented geometry optimizations of Fe and/or U coadsorbed on periodic, hydrated (001) corundum and hematite slabs (conducted in Chapter 4, using CASTEP) guided the sorption configuration for the cluster models.

To represent ET reactions on the insulating corundum cluster, two different charge transfer pathways are studied. For each of these two models, one ET step is used to calculate the energetics and kinetics for the reduction of U(VI) to U(V) and oxidation of Fe(II) to Fe(III). For a one-ET step, two structures must be geometry optimized to represent the electronic configuration of the cluster before and after ET. That is, in this case, when the electron is localized on the Fe(II) adsorbate, this structure is referred to as the pre-ET structure. When the electron is transferred to U(VI) adsorbate, this structure is referred to as the post-ET structure. This will be further clarified in the explanation of MT below.

The first ET reaction ($cET_{FeAds\text{-}UAds}$) investigates ET between Fe ad U coadsorbed onto opposite ends of a small corundum cluster ($[UO_2(OH)(H_2O)_2$ - $Al_8O_{30}H_{34}$- $Fe(H_2O)_3]^{+2}$). The corundum

cluster is two cation-layers thick and is ~three octahedra wide; a small corundum cluster is applied to be consistent with the hematite models mentioned below. The Fe and U adsorbates are spatially separated by ~4.6 Å, The $cET_{FeAds\text{-}UAds}$ reactions helps to determine how spatial limitations would influence atomistic ET mechanisms.

The second ET reaction ($cET_{FeInc\text{-}UAds}$) investigates ET between U adsorbed to a corundum cluster where the Fe(II) has been structurally incorporated into the corundum cluster ($[U(OH)_2(H_2O)$ - $FeAl_7O_{30}H_{36}]^{-1}$). The structural incorporation of Fe into the corundum structure is believed to overcome energetic/kinetic barriers that exist when Fe is sorbed to the corundum surface; experimental studies have shown redox reactions were significantly catalyzed when Fe(II) was structurally incorporated into insulating surface compared to when Fe(II) was adsorbed to the insulating surface [16, 93]. The Fe cation incorporated into the corundum cluster shares an O/OH ligand with each of the Al cations in the corundum cluster, thus structural changes to the Fe upon ET/oxidation will also affect the neighboring Al atoms. The uranyl ion interacts with the Fe atom incorporated into the corundum structure through one of its two bonds to hydroxyl ligands at the corundum surface.

For the hematite system, Fe and U were coadsorbed on the basal (001) surface and opposite edges of a small hematite cluster ($[UO_2(OH)(H_2O)_2$ -$Fe_8O_{30}H_{34}$- $Fe(H_2O)_3]^{+2}$), similar to the corundum cluster mentioned above. A small hematite cluster ($Fe_8O_{30}H_{34}$) was chosen as larger spin-charged systems were computationally expensive. The substrate is also of sufficient size and thickness where we can observe if and how charge transfer occurs through the substrate, as will described below. The Fe and U adsorbates are separated by ~5.2 Å.

ET on the semiconducting hematite cluster is more complicated than that observed for the insulating cluster as there are a number of different ET pathways that can exist within the semiconducting surface. The first ET reaction on the hematite cluster ($hET_{FeAds\text{-}UAds}$) investigates ET between Fe and U coadsorbed onto opposite ends of the small hematite cluster. That is, an electron from the Fe(II) adsorbate (pre-ET structure) is transferred to the U(VI) adsorbate (post-ET structure); the hematite does not directly involve the hematite slab in the transport of the electron. The $hET_{FeAds\text{-}UAds}$ reaction is analogous to the $cET_{FeAds\text{-}UAds}$ reaction described above, such that the mineral substrate is not participating in the ET reaction. Thus, the energetics and

kinetics for the $hET_{FeAds\text{-}UAds}$ and $cET_{FeAds\text{-}UAds}$ reactions can be compared to observe how spatial limitations affect ET on semiconducting *vs.* insulating mineral substrates.

To determine whether the proximity can explain the enhanced redox rates observed on semiconducting substrates, the energetics and kinetics for ET occurring via the proximity effect is also investigated using the hematite cluster. Three ET steps are needed to represent ET through the hematite cluster via the proximity effect: (1) the electron from the Fe(II) adsorbate is transferred into ($hET_{FeAds\text{-}FeHem1}$), (2) through the hematite cluster ($hET_{FeHem1\text{-}FeHem2}$), and (3) ultimately from Fe-cation in the hematite cluster to the U(VI) adsorbate ~3.4 Å away ($hET_{FeHem2\text{-}UAds}$) (Figure 5-4a,b). In the first ET reaction ($hET_{FeAds\text{-}FeHem1}$) an electron from the Fe(II) adsorbate (pre-ET structure) is transferred to an underlying Fe(III) cation within the hematite slab (intermediate 1 structure). In the second ET reaction ($hET_{FeHem1\text{-}FeHem2}$) the electron is transferred between Fe cations in the basal plane of the hematite surface, to the Fe cation bonded with the uranyl adsorbate (intermediate 2 structure). In the third, and final ET reaction used to represent ET via the proximity effect, ($hET_{FeHem2\text{-}UAds}$) the electron is transferred from the Fe cation in the hematite substrate to the uranium cation adsorbed on the cluster surface (post-ET structure). The $hET_{FeHem2\text{-}UAds}$ reaction can also be considered to be similar to the ET reaction between U and Fe-incorporated into the corundum cluster, where the uranyl ion shares hydroxyl ligands with the Fe(II) electron donor and essentially forms an IS complex.

5.3.2 Marcus Theory

Ab initio calculations were applied to ET reactions to reduce UO_2^{2+} to UO_2^{+} by Fe^{2+} in the presence of the hematite and corundum clusters in the gas-phase (*i.e.,* only the first hydration shell is explicitly treated). MT has been used as a framework for environmental ET calculations using molecular modeling for over a decade [56-59, 61, 69]; detailed explanations of MT and the calculation of ET rates are available in the literature, which the reader is referred to for more information [56, 62-64]. Through these methods the atomistic structure, energetics, and kinetics associated with ET for molecular systems, such as Fe-dimers [56, 59] and periodic surfaces [69, 116], has been elucidated. Thus, the objective of coupling *ab initio* calculations with MT in this study is to obtain energetic and kinetic information for ET through different charge transfer pathways in ternary, (co)adsorbed systems. This information will help determine the most

effective pathways through which redox reactions are catalyzed on different mineral surfaces (*i.e.,* those where ET can occur through the surface and those where ET does not).

The means for calculating the energetic and kinetic properties of the ET reactions for these ternary, (co)adsorbed systems are similar to the methods used in Taylor*, et al.* (2015) [96], and are restated here. To model an ET reaction, the Fe^{2+} and UO_2^{2+} ions (as well as the ions within the hematite and corundum cluster) are assigned with the appropriate charges and spins. Before ET occurs between the Fe adsorbate and U adsorbate, the Fe^{2+} ion has a net charge and spin of +2 and +4, respectively, while the UO_2^{2+} ion has a net charge and spin of +2 and 0, respectively; this state is referred to as the pre-ET complex in this study. After ET between the Fe adsorbate and U adsorbate, the oxidized Fe^{2+} (now Fe^{3+}) would have a net charge and spin of +3 and +5, respectively, while the reduced UO_2^{2+} (now UO_2^{+}) is +2 and ±1; this state is referred to as the post-ET complex. Additional structures are modelled for ET on the hematite cluster (intermediate 1 and 2 structures), as mentioned above. The Fe^{3+} cations of the hematite cluster were assigned net charges and spins of +3 and +5. Al, O, and H do not have unpaired electrons (spin =0) and were assigned their ambient valence states (+3, -2, and +1, respectively). Ferromagnetic (same majority spin direction for Fe^{3+} and UO_2^{+}) spin configurations for the post-ET complex were modeled, though it is important to acknowledge that the spin configuration (*i.e.,* ferromagnetic vs. ferromagnetic vs. antiferromagnetic) can affect the thermodynamics and kinetics of ET [59, 96].

Changes in Fe and U atomic distances were also monitored between the pre-, inter1-, inter2- and post-ET states to confirm the appropriate oxidation state was obtained. Average bond lengths between Fe(III) and its hydroxyl or water ligands, as well as average bond lengths between U(VI) and its oxo, hydroxyl, and water ligands, are shorter than those for the Fe(II) and U(V) cations, respectively, due to the electron localization [56].

These clusters were geometry optimized in NWChem [65] using spin-unrestricted Hartee-Fock (UHF) to localize the electrons in the desired electronic configuration. Basis sets used for geometry optimization of the clusters were 3-21G (Al, Fe, O, and H) and Crenbl ECP (U). Both mixed HF-DFT functionals and larger basis sets have also been applied to these models to improve the structural accuracy and energetics for these models, though there are complications in obtaining stable structures and ET configurations (see Supplementary

information). For instance, UHF is known to overbind electrons and overestimate absolute energies, thus leading to higher reaction energies, reorganization energies, and activation energies compared to those obtained with DFT-B3LYP. The reaction energetics decrease with decreasing HF contributions, showing that with mixed HF-DFT functionals the ET reactions would be more favorable (*i.e.,* more negative). However, the structures of the clusters are less stable/consistent between the ET configurations when using larger basis sets and/or HF-DFT functionals; *i.e.,* despite holding the OH bond distances fixed, the structure of the pre-ET structure changes considerably, leading to considerably higher reorganization energies and in turn diminishingly small ET rates. Additionally, when using less than 0.4 HF (greater than 0.6 slater) for the exchange-contribution, the spins are no longer accurately localized on the U and Fe cations and so pre- and post-ET structures cannot be successfully optimized. Thus, although the larger basis sets and/or HF-DFT functionals lead to lower reaction energies, the structural changes within the clusters (not directly involved in ET) complicate calculation of the other energetic and kinetic values. The calculations using these mixed HF-DFT functionals and larger basis sets are an ongoing study, and so the results using the UHF theory and smaller basis sets are presented here.

For the geometry optimization of the pre-ET structures, all atoms were allowed to relax to obtain the most thermodynamically favorable (co)adsorption structures. The coadsorption energies were calculated (Eqn. 1):

$$E_{\text{Fe and U (co)adsorbed cluster}} + E_{\text{cluster}} = E_{\text{U adsorbed cluster}} + E_{\text{Fe adsorbed cluster}} \quad (1)$$

However, geometry optimization of these clusters in different electronic configurations, such as in the post-ET state, would sometimes lead to bond breakage within the clusters that were fully relaxed, though these changes were not directly related to the ET process (*e.g.,* some of the ET reactions proceed as proton-coupled ET reactions). The bond breakage and additional atomistic processes occurring that are not involved in the ET process contribute to the energetics and kinetics of the ET reaction. However, this disobeys the principle of MT where the structures should not observe considerable changes in the pre- and post-ET structures (aside from changes in bond distances associated with changes in the redox state). To mitigate the energetic contributions from non-ET processes occurring, the models used to calculate the ET energetics

and kinetics were optimized using Z-matrices, where the OH distances were held fixed (to prevent proton transfer from occurring).

Following optimization of the pre- and post-ET structures, a potential energy (PE) profile was derived from single-point energies calculated from hybrid structures, obtained using the linear synchronous transit method (LST) [71] (Figure 5-1). Parabolic functions were fit to the reactant and product PE surfaces to derive ET parameters, namely the free energy of ET reaction, the reorganization energy, and the diabatic activation energy. The reaction free energy, ΔG^0, is the change in free energy upon ET. The reorganization energy, λ, is the energy needed to distort the configuration of the reactants into that of the products without changing the electronic distribution. From these data the electronic coupling matrix element and adiabaticity of the reaction were also determined.

The electronic-coupling matrix element, V_{AB}, is the amount of electronic interaction between the reactant and product states at the transition state (calculated using HF wavefunctions using the ET module in NWChem). More strenuous basis sets was used in the V_{AB} calculations to produce more reliable values. The basis sets used for the V_{AB} calculations were 6-31G** (O and H) [66], Ahlrichs PVDZ (Fe) [67], and the Stuttgart RLC ECP (U) [68]. The magnitude of V_{AB} determines if the reaction proceeds adiabatically (the electronic coupling is strong; $V_{AB} > k_BT$) or nonadiabatically (weak; $V_{AB} < k_BT$) [70].

Additionally the probability for ET to occur, P_{12}, is a function of V_{AB} and λ (Eqn. 2):

$$P_{12} = 1 - \exp((-\frac{V_{ab}^2}{hv})\sqrt{\frac{\pi^3}{\lambda k_B T}}) \qquad (2)$$

where h is Planck's constant (4.14×10^{-15} eV·s), v is the typical frequency for nuclear motion (10^{13} s^{-1}) [57], k_B is the Boltzmann's constant (8.62×10^{-5} eV/K), and T is the temperature in Kelvin (273 K). P_{12} is another indication of whether a reaction occurs adiabatically or nonadiabatically: if the probability is high (~1 or 100%), ET occurs adiabatically and vice versa.

The activation energy, ΔG^*, is the energy required to (thermally) excite the system to the transition state configuration, and can be estimated for the adiabatic case as (Eqn. 3):

$$\Delta G^* = \frac{(\lambda + \Delta G^0)^2}{4\lambda} - V_{AB} \qquad (3)$$

If the electronic coupling is strong, the ET reaction occurs adiabatically and the ET rate, k_{ET}, is expressed as (Eqn. 4):

$$k_{ET} = \upsilon e^{\frac{-\Delta G*}{k_B T}} \quad (4)$$

If the electronic coupling is weak, the ET reaction occurs nonadiabatically and k_{ET} is expressed as (Eqn. 5):

$$k_{ET} = \frac{2\pi}{\hbar}|V_{AB}|^2 \frac{1}{\sqrt{4\pi\lambda k_B T}} \exp\left(-\frac{(\Delta G^0+\lambda)^2}{4\pi\lambda k_B T}\right) \quad (5)$$

5.4 Results

5.4.1 Energetics and kinetics for ET pathways on corundum clusters

To gain insight into atomistic mechanisms that facilitate or inhibit ET on insulating surfaces, energetics and kinetics for two different ET pathways for the reduction of U(VI) to U(V) by Fe(II) in the presence of corundum were calculated. For the first model, Fe and U are both coadsorbed onto a corundum cluster and are spatially separated by ~4.6 Å. Thus, this model represents ET between adsorbates on insulating surfaces that have spatial limitations. The uranyl adsorbs in a bidentate configuration to the edge of an Al octahedral, where $d_{\text{U-Al}}$ ~3.3 Å. The Fe(II) sorbs in a tridentate configuration to two edges of two Al octahedra (Figure 5-2a,b), where $d_{\text{Fe-Al}}$ ~3.0 Å. The interatomic distances between the U and Fe adsorbates to the Al cations are generally in agreement with experimentally measured interatomic distances [105, 120, 121]. The geometry optimized coadsorbed structure is also energetically favorable (-10 kJ/mol) (Table 5-1).

The structures for the pre- and post-ET complexes were geometry optimized using UHF. Electron localization was assessed by Mulliken spin density distributions. Mulliken spin densities for Fe^{2+} and UO_2^{2+} ion in the pre-ET model were +4.0 (formal spin of +4) and 0 (0), respectively. The spin densities for Fe^{3+} and UO_2^{+} in the post-ET model were +4.8 (+5) and 1.3 (+1), respectively. The electrons are effectively localized on the appropriate ions using UHF. Additionally, the bond distances reflect the correction oxidation states for both the pre- and post-ET states, where shorter average bond lengths are observed for Fe^{3+} and U^{6+} in comparison to

Fe^{2+} and U^{5+}, respectively (Table 5-1). Larger interatomic distances are incurred for the cations where the electron is localized as was observed in Taylor, *et al.* (2015) [96].

The reduction of U(VI) to U(V) by Fe(II) is calculated be exothermic, with a reaction energy of –40 kJ/mol (Table 5-2). The exothermicity of the $cET_{FeAds\text{-}UAds}$ reaction is postulated to be due to the chemical nature of the Fe and U (as will be discussed). The transfer of an electron from the Fe(II) to U(VI) ion ~4.6 Å does not lead to significant structural changes in the cluster (*e.g.,* proton transfer) given that the OH distances of the cluster are held fixed (Table 5-1). The overall changes in the electronic configurations and structures of the pre- to post-ET models, including the changes the bond distances of the Fe and U adsorbates as well as changes in bond distances within the corundum cluster, leads to a reorganization energy of 289 kJ/mol.

While the reduction of U(VI) to U(V) by Fe(II) is energetically favorable, the $cET_{FeAds\text{-}UAds}$ reaction is predicted to proceed nonadiabatically (V_{AB} = 2 kJ/mol). The probability for ET to occur is predicted to be ~18%. The low electronic coupling on the corundum cluster is reasonable given that the U and Fe adsorbates are spatially separated by ~4.6 Å. The amount of separation between the Fe and U adsorbate would not allow for considerable orbital overlap and coupling between the *d*- and *f*-orbitals of the Fe and U atoms, respectively. In the instances where the $cET_{FeAds\text{-}UAds}$ reaction would occur, ET would occur at a rate of 2×10^2 s^{-1}.

For the second model using the corundum cluster, U is adsorbed to a corundum cluster where the Fe ion has been incorporated into the corundum structure. Thus, ET in this model is not spatially-limited. The geometry optimized structure shows UO_2^{2+} adsorbs as a bidentate complex to one corner of an Al-octahedra ($d_{U\text{-}Al}$ = 3.9 Å) and one corner of the Fe-octahedra ($d_{U\text{-}Fe}$ = 4.0 Å) (Figure 5-3a, b). These interatomic distances are generally longer than those observed experimentally but conform with theoretical predictions for the interatomic distance of U and Fe when adsorbed onto two corners of Fe-octahedra (4.1 Å) [24]. The adsorption of U(VI) onto the Fe(II)-incorporated corundum cluster is however found to be highly endothermic +163 kJ/mol, which could be a result of the limited number of sorption sites available on the small corundum cluster. While this structure is not energetically favorable structure, the $cET_{FeInc\text{-}UAds}$ pathway for this model can still provide insight into the differences between the energetics and kinetics for ET pathways on insulating surfaces.

The electronic configurations for the pre- and post-ET complexes show the electron is correctly localized on the Fe and U cations, respectively (Table 5-1). The changes in the bond distances also confirm the correction oxidation states for ions in both the pre- and post-ET states. Upon reduction of U^{6+} to U^{5+} the U-O bonds become longer (in agreement with electron localization incurring bond lengthening). However, this bond lengthening after ET leads to an increase in the interatomic distance between U and Fe, as U moves 0.2 Å away from Fe ($d_{U\text{-}Fe}$ = 4.2 Å). The uranyl sorption configuration also changes following ET, as uranyl moves farther from the Fe ion and is sorbed to the corner of the Al-octahedra as a monodentate complex.

The reduction of U(VI) to U(V) by Fe(II) is calculated be exothermic, with a reaction energy of –90 kJ/mol (Table 5-2), again supporting that U(VI) as a Lewis-acid has a strong tendency to accept electrons. The structural and electronic changes from the pre- to post-ET structures yield a reorganization energy of 279 kJ/mol, which is similar to that calculated for the above model (289 kJ/mol). In contrast to the $cET_{FeAds\text{-}UAds}$ reaction, the $cET_{FeInc\text{-}UAds}$ reaction is predicted to occur adiabatically. The electronic coupling between the U and Fe atoms is strong (V_{AB} =19 kJ/mol), which is likely due to the initial formation of an IS-type complex between Fe and U; *i.e.,* in the pre-ET structure the uranyl and Fe were bonded by a hydroxyl ligand which enables ET to proceed more readily. The high exothermicity and adiabaticity of the $cET_{FeInc\text{-}UAds}$ reaction in turn shows ET would proceed rapidly, at a rate of 2×10^{7} s^{-1}. The $cET_{FeInc\text{-}Uads}$ reaction rate is five orders of magnitude higher than that observed for $cET_{FeAds\text{-}UAds}$. Thus, the rate of U(VI) reduction is enhanced when Fe(II) is incorporated into the corundum structure compared to when Fe and U coadsorbed model. The IS complexation between Fe and U in the $cET_{FeInc\text{-}UAds}$ models leads to ET proceeding adiabatically.

5.4.2 Energetics and kinetics for ET pathways on and through the hematite cluster

Potential ET pathways for the reduction of U(VI) by Fe(II) in the presence of hematite were calculated to gain insight into atomistic mechanisms that facilitate or inhibit ET on semiconducting surfaces. These pathways and their energetics and kinetics can be compared to those obtained for the corundum systems to observe if and how pathways through

semiconducting minerals can overcome energetic/kinetic barriers that inhibit ET on insulating substrates .

The coadsorption of Fe and U onto the hematite cluster is exothermic, with a coadsorption energy of –63 kJ/mol. The geometry optimized structure of the Fe and U coadsorbed on the hematite cluster is similar to the structure observed for Fe and U coadsorbed on the corundum cluster. Uranyl sorbs as a bidentate complex to an edge of a Fe octahedra of the hematite cluster. The interatomic distance between U and the underlying Fe ion (its nearest Fe neighbor) is ~3.4 Å, which is in agreement with experimental studies [24, 55, 80]. Fe(II) is adsorbed to the opposite end of the hematite cluster, on the same basal plane as the uranyl ion, as a tridentate complex with three water ligands. The uranyl and iron adsorbate are not connected by hydroxyl or water ligands, and are separated by ~5.2 Å (Table 5-1; Figure 5-4 a, b).

Similar to the model where Fe and U are coadsorbed onto the corundum cluster, the transfer of an electron from the Fe(II) adsorbate to the U(VI) adsorbate ($hET_{FeAds\text{-}UAds}$) is evaluated to determine whether ET occurs between the coadsorbates that are spatially separated. The hematite cluster does not directly participate in this ET. The correct electronic configurations for the pre- and post-ET complexes are confirmed by the Mulliken spin density distributions. Mulliken spin densities for Fe^{2+} and UO_2^{2+} ion in the pre-ET model were +4.0 (formal spin of +4) and 0 (0), respectively. The spin densities for Fe^{3+} and UO_2^{+} in the post-ET model were +4.8 (+5) and 1.3 (+1), respectively. Additionally, the bond distances reflect the correction oxidation states for both the pre- and post-ET states (Table 5-1).

The reduction of U(VI) to U(V) by Fe(II) is calculated be exothermic, with a reaction energy of –66 kJ/mol (Table 5-2). The transfer of an electron from the Fe(II) to U(VI) ion ~5.2 Å does not lead to significant structural changes in the overall cluster (*e.g.,* the structure of the hematite cluster appears to essentially remain the same between pre- and post-ET structures), though the distance between U_{ads} and Fe_{ads} is shortened from ~5.2 Å to ~4.9 Å (Table 5-1). The overall changes in the electronic configurations and structures from the pre- to post-ET structures lead to a reorganization energy of 259 kJ/mol (Table 5-2). The activation energy for $hET_{FeAds\text{-}UAds}$ reaction is 31 kJ/mol. The favorable energetics for the $hET_{FeAds\text{-}UAds}$ reaction in turn cause ET to occur rapidly ,at a rate of 8×10^{8} s^{-1}.

The $hET_{FeAds-UAds}$ reaction is predicted to be energetically and kinetically feasible. However, based on $cET_{FeAds-UAds}$ reaction, it was originally predicted that ET would be difficult due to the spatial separation of the Fe and U adsorbates. The electronic coupling for $cET_{FeAds-UAds}$ reaction was weak (2 kJ/mol) and the reaction proceeded nonadiabatically. This result was thought to be reasonable as the separation of between the Fe and U adsorbate would not allow for considerable orbital overlap and coupling between the *d*- and *f*-orbitals of the Fe and U atoms, respectively. In contrast to the $cET_{FeAds-UAds}$ model, the $hET_{FeAds-UAds}$ reaction is predicted to proceed adiabatically (*i.e.,* the probability for ET to occur is 100%).The strong electronic coupling between Fe_{ads} and U_{ads} (38 kJ/mol) is unexpected given that the U and Fe adsorbates are spatially separated by ~5.2 Å. It is postulated that the higher adiabaticity observed for $hET_{FeAds-UAds}$ may be due to the larger extent of orbital overlap that is present over the entire semiconducting system (this hypothesis is discussed later).

The energetics and kinetics for ET occurring via the proximity effect are also quantified to determine whether ET pathways through semiconducting minerals can enhance the rate of redox reactions. The structures, electronic configurations, energetics and kinetics for the three ET steps representing ET via the proximity effect ($hET_{FeAds-FeHem1}$, $hET_{FeHem1-FeHem2}$, and $hET_{FeHem2-UAds}$) have been quantified and compiled.

In general, the electronic configurations for all the ET complexes of this hematite system show the electron is localized on the correct Fe and U cations (Table 5-1). For instance, the Mulliken spin densities for the pre-ET state show the electron is correctly localized on the Fe adsorbate, as it observes a spin of +4.0 (formal spin of +4), while the Fe cation within the hematite cluster have spins of ~ 4.7 – 4.8 (+5) and the U adsorbate has a spin of 0 (0). Similarly, the changes in the bond distances also confirm the correction oxidation states for the correct cations in each of the ET complexes. Significant structural changes are not observed in the hematite system, again due to the fixed OH distances. Thus, much of the text in this section focuses on the energetics and kinetics measured for each of the ET steps.

For ET from the Fe adsorbate to an Fe cation in the underlying hematite slab ($hET_{FeAds-FeHem1}$) the ET reaction energy of 48 kJ/mol, showing the reaction is endothermic. The $hET_{FeAds-FeHem1}$ reaction invokes changes in the positions of the other Fe atoms and shared O/OH ligands and the uranyl sorption complex; the uranyl adsorbate is drawn closer to the Fe_{Hem2} where the

electron is localized (Table 5-1). The structural change in the uranyl adsorbate and rearrangements within the hematite cluster lead to a reorganization energy 270 kJ/mol (Table 5-2), which is within the range of energies found for the corundum models. The $hET_{FeAds\text{-}FeHem1}$ reaction energy and reorganization energy in turns lead to a high activation energy of 71 kJ/mol. While the energetics for the $heET_{FeAds\text{-}FeHem1}$ reaction are unfavorable, the electronic coupling is strong (V_{AB} =19 kJ/mol) and the $hET_{FeAds\text{-}FeHem1}$ reaction would proceed adiabatically. The high activation energy associated with injecting an electron into the hematite slab in turn leads to a slow ET rate of 2×10^{-3} s^{-1}. The $hET_{FeAds\text{-}FeHem1}$ reaction energetics suggests that interfacial ET is an energetic barrier for ET occurring via the proximity effect, and would lead to slow ET rates.

Surficial ET is also shown to be an energetic barrier for ET occurring via the proximity effect. As observed for the $hET_{FeAds\text{-}FeHem1}$ reaction, ET from the Fe_{Hem1} to Fe_{Hem2} ($hET_{FeHem1\text{-}FeHem2}$; where the Fe cation are in the same basal place of the hematite cluster) is also endothermic (76 kJ/mol) (Table 5-2). ET within the basal plane leads the changes in the position of the uranyl adsorbate, where uranyl is again drawn towards the Fe cation where the electron is localized, Fe_{Hem2}. The reorganization energy is similar to that measured for the $hET_{FeAds\text{-}FeHem1}$ reaction (269 kJ/mol). The high endothermicity of the $hET_{FeHem1\text{-}FeHem2}$ reaction leads to a high activation energy of 108 kJ/mol. The electronic coupling between the Fe cations in the basal plane is considerably weaker than that observed for $hET_{FeAds\text{-}FeHem1}$ (V_{AB} = 3 kJ/mol) , although the $hET_{FeHem1\text{-}FeHem2}$ reactions still proceeds adiabatically. The unfavorable energetics for $hET_{FeHem1\text{-}FeHem2}$ reaction predict ET would occur very slowly, at a rate of 4×10^{-7} s^{-1}. The rate for the $hET_{FeHem1\text{-}FeHem2}$ reaction is the slowest of the ET rates measured on the hematite and corundum clusters in this study. The energetics and kinetics $hET_{FeHem1\text{-}FeHem2}$ contrast with results from previous studies [59, 69], which predict ET to occur most easily and rapidly through the basal plane. These results are revisited and further examined in the Discussion section.

In the final ET step within this series, representing a pathway via the proximity effect, ET from Fe_{Hem2} to U_{ads} ($hET_{FeHem2\text{-}UAds}$) is highly exothermic, with a reaction energy of –230 kJ/mol (Table 5-2). Structural changes between the reduced U adsorbate and underlying Fe cation in the hematite cluster lead to a reorganization energy of 264 kJ/mol. Although the reorganization energy is similar to those measured for $hET_{FeHem1\text{-}FeHem2}$ and $hET_{FeHem1\text{-}FeHem2}$, the high exothermicity of the reaction leads to a low activation energy (1 kJ/mol). While the energetics

for $hET_{FeHem2\text{-}UAds}$ reaction are considerably more favorable than those measured for the $hET_{FeHem1\text{-}FeHem2}$ and $hET_{FeHem1\text{-}FeHem2}$ reactions, the electronic coupling between the Fe and U cations is weak (V_{AB} = 0.5 kJ/mol).The $hET_{FeHem2\text{-}UAds}$ reaction with a 2% probability of ET occurring. In the instances where $hET_{FeHem2\text{-}UAds}$ reaction occurs, ET would occur rapidly, at a rate of 6×10^{12} s^{-1}, due to the favorable reaction energetics.

The non-adiabatic behavior for the $hET_{FeHem2\text{-}UAds}$ reaction is unexpected; as the proximity between the Fe and U as well as the IS complexation of the ions are expected to lead to strong electronic coupling; *e.g.,* the electronic coupling for the $cET_{FeInc\text{-}UAds}$ reaction was postulated to be strong (V_{AB} = 39 kJ/mol) primarily due to the IS-type complexation between the Fe and U. This result will be further examined in the Discussion section. Through combining observations for the energetics and kinetics for $hET_{FeAds\text{-}FeHem1}$, $hET_{FeHem1\text{-}FeHem2}$, and $hET_{FeHem2\text{-}UAds}$ reactions, it is postulated that the reduction of U(VI) by Fe(II) by ET via the proximity effect would have to overcome energetic barriers, primarily from interfacial and surficial ET between Fe cations, although the reduction of U(VI) to U(V) would be highly endothermic and kinetically feasible.

5.5 Discussion

MT coupled with *ab initio* calculations are used to study ET pathways relevant to ternary, coadsorbed systems involving insulating and semiconducting substrates for the first time. Through this approach has allowed, atomistic mechanisms involved in the reduction of U(VI) to U(V) by Fe(II) in the presence of corundum and hematite can be observed. A better understanding of energetic and kinetic parameters affecting the rate of redox reactions on mineral surfaces is also gained.

Throughout this study, the reduction of U(VI) to U(V) by Fe(II) is consistently shown to be energetically favorable; *i.e.,* the $cET_{FeAds\text{-}UAds}$, $cET_{FeInc\text{-}UAds}$, $hET_{FeHem2\text{-}UAds}$, and $hET_{FeAds\text{-}UAds}$ reactions (where U is being reduced by either the Fe(II) adsorbate or Fe(II) within the mineral cluster) are calculated to be exothermic. It is postulated that the chemical nature of Fe and U promotes the ET reactions involving Fe(II) and U(VI) to occur exothermically. As shown through the models in Chapter 4, where Fe and U coadsorbed on the periodic, hydroxylated corundum (001) surface, Fe^{2+} is dehydrated and hydrolyzed, making it more reactive to

oxidation, and the presence of a strong-Lewis acid U(VI) would promote further oxidation of the Fe(II) ion [82, 96]. Thus, the energetics driving the reduction of U(VI) by Fe(II) are strong, and the reduction of U(VI) to U(VI) by Fe(II) would be predicted to occur via certain ET pathways.

Conceptual models for catalysis of redox reaction on insulating surfaces imply that the ability for U(VI) to be reduced by Fe(II) sorbed on the corundum cluster would be governed by U(VI) and Fe(II) interacting with one another via an IS-complex. The catalysis of U(VI) reduction by Fe(II) through the formation of an Fe-U IS complex has been studied in detail (in the absence of a mineral substrate and using stricter calculation parameters such as DFT-B3LYP and larger basis sets) [96]. *Ab initio* ET calculations revealed that OS ET is strongly kinetically inhibited in all cases modeled. OS ET as a sequential proton-coupled ET reaction is found to be thermodynamically unfavorable (+102 kJ/mol) as well as kinetically inhibited (10^{-12} s^{-1}). In contrast, the reduction of $U(VI)_{aq}$ to $U(V)_{aq}$ by $Fe(II)_{aq}$ as an IS ET reaction is both thermodynamically favorable (–16 kJ/mol) and kinetically rapid (10^{8} s^{-1} for a ferrimagnetic electronic configuration) [96]. Thus, it is clear that the reduction of U(VI) to U(V) by Fe(II) can be catalyzed through IS complexation of the Fe-U ions.

Comparing the energetics and kinetics for two different ET pathways on the insulating corundum clusters also highlights that the U(VI) reduction by Fe(II) is more effectively catalyzed via IS-complexation. In this study, when U and Fe are coadsorbed on the corundum cluster and are spatially separated by ~4.6 Å (U and Fe are not interacting with one another via IS- complexes), the $cET_{FeAds\text{-}UAds}$ reaction proceeds at rate of 2×10^{2} s^{-1}. In comparison, incorporating Fe into the corundum cluster and bonding the U to one of the hydroxyl ligand of the Fe ion, leads the $cET_{FeInc\text{-}UAds}$ reaction to occur more rapidly, at a rate of 2×10^{7} s^{-1}. One of the differences in energetics for these models is the higher electronic coupling observed for the $cET_{FeInc\text{-}UAds}$ reaction compared to that calculated for the $cET_{FeAds\text{-}UAds}$ reaction. Through these ET models, the electronic coupling is postulated to be an influential parameter determining whether ET occurs on insulating system, in particular.

The electronic coupling describes the mixing between the wavefunctions of the reactants and product states at the transition point and influences the ET probability [56], and determine the adiabaticity of an ET reaction. The adiabaticity of an ET reaction is postulated to be a particularly influential property in determining whether ET proceeds on insulating surfaces. As

mentioned, when Fe and U are coadsorbed onto corundum and are spatially separated, the reaction proceeds nonadiabatically. The low electronic coupling means that the electronic interaction is weak, and that the system will evolve on the reactant surface for the most part upon excitation to the transition state and only tunnel to the product surface at times [56] (Figure 5-1). This observation conforms to results from computational models in Chapter 4; overlap between *d*- and *f*-orbitals of U and Fe, respectively, spatially separated is not observed and so ET is physically limited.

In contrast to the model where U and Fe are coadsorbed onto corundum and are spatially separated, ET between U and the Fe-incorporated corundum cluster proceeds adiabatically. The larger electronic coupling obtained when U is adsorbed onto a Fe-incorporated corundum cluster means that the electronic interaction is strong; the system evolves on the lower surface and, barring multiple crossings of the transition state, is capable of leading to the formation of the ET products [56]. Thus, the incorporation of Fe into the corundum cluster and existence of a hydroxyl bridge between the U and Fe ions, leads to a larger electronic coupling and transition to an adiabatic reaction.

The adiabaticity of the ET reactions is also shown to be influenced by the clusters electronic character. Comparison between ET reactions between corundum and hematite , particularly for the coadsorbed Fe and U models, show ET reactions involving hematite are generally found to proceed adiabatic (except for $ET_{FeHem2\text{-}UAds}$) compared to ET reaction involving corundum. Adiabatic ET reactions involving corundum are influenced by the ability for U-Fe IS complexation to occur, which better enables orbital overlap and coupling between the *d*- and *f*-orbitals of the Fe and U atoms. The generally higher adiabaticity of ET reactions involving hematite seems reasonable because Fe and/or U *d*- and/or *f*-orbitals can be more easily coupled in semiconducting systems. This observation is in agreement with computational models in Chapter 4 which show orbital overlap between Fe and U *d*- and *f*-orbitals can enable ET between the two ions.

However, there are uncertainties pertaining to the adiabaticity of some of the ET reactions involving hematite. For instance, it was unexpected for the $hET_{FeAds\text{-}UAds}$ reaction to proceed adiabatically, given that Fe and U are spatially separated by ~5.2 Å. The analogous $cET_{FeAds\text{-}UAds}$ reaction involving the corundum cluster was found to proceed nonadiabatically;

this result is reasonable given the spatial limitations within the system. It is postulated that the higher adiabaticity observed for $hET_{FeAds\text{-}UAds}$ may be due to the larger extent of orbital overlap that is present over the entire semiconducting system. In Chapter 4, ET from the Fe(II) adsorbate to a U(VI) adsorbate on the hydroxylated (001) hematite surface was not represented by a single ET event. That is, a single electron from the Fe(II) adsorbate was not directly transferred to the U(VI) adsorbate; the spin density difference showed the spins for a number of the Fe cations within the hematite slab observed changes that correlated to the ET event. Thus, it is possible that in a semiconducting system electronic coupling is stronger due to spin being smeared across the network of electron accepting Fe atoms. However, this does not explain why the $hET_{FeHem1\text{-}UAds}$ reaction is predicted to proceed nonadiabatically. In this case, ET occurs via IS complexation, where U_{Ads} is reduced by an underlying Fe_{Hem2} cation; thus, it was expected that $hET_{FeHem1\text{-}UAds}$ reaction would proceed adiabatically, as was observed for the $cET_{FeInc\text{-}UAds}$ reaction.

A few different factors can affect the electronic coupling values. The basis sets used for the calculations affect the calculated values for V_{AB}. Modelling these systems using more strenuous basis sets (*e.g.,* Ahlrichs PVDZ for Fe) [67] can improve the precision of the V_{AB}. It is also interesting to point out that the electronic coupling for these models is computed over the entire cluster. That is, asymmetry of these cluster models (*e.g.,* U and Fe are coadsorbed on opposite ends of the basal hematite plane of the cluster) may affect the electronic coupling of the system. In contrast, other studies have applied constant electronic couplings (dependent on the direction of ET, basal vs. c-direction), obtained using symmetric Fe-dimers to the surface and bulk hematite [69]. Thus, with continued ET over a certain surface topology and distance the adiabaticity of the ET reaction would change. The influence of basis set and the structure of the cluster on the calculated V_{AB} values are currently being investigated.

The proximity effect is proposed as a mechanism that enhances redox rate in semiconducting systems. To determine whether the proximity can explain the enhanced redox rates observed on semiconducting substrates, the energetics and kinetics for a series of ET reactions using the hematite cluster are calculated. The first ET step, within the series of ET reactions used to model a pathway via the proximity effect, the interfacial $hET_{FeAds\text{-}FeHem1}$ reaction would require +48 kJ/mol. The $hET_{FeAds\text{-}FeHem1}$ reaction proceeds adiabatically but

slowly at a rate of 10^{-3} s^{-1}. Surficial ET within the hematite cluster $hET_{FeHem1\text{-}FeHem2}$ reaction is more endothermic than interfacial ET, requiring an energy input of 76 kJ/mol. The $hET_{FeHem1\text{-}FeHem2}$ reaction proceeds adiabatically but slowly at a rate of 10^{-7} s^{-1}. The calculations show the ET reactions between the interfacial and surficial Fe cations is energetically unfavorable ($hET_{FeAds\text{-}FeHem1}$ and $hET_{FeHem1\text{-}FeHem2}$ reactions, respectively), suggesting that interfacial and surficial ET are energetically and/or kinetically limiting steps for ET to occur via the proximity effect. The $hET_{FeHem1\text{-}FeHem2}$ reaction appears to be the most energetically and kinetically-limiting step of the ET reactions used to model the proximity effect. While interfacial and surficial ET reactions are endothermic and proceed slowly, the reduction of U(VI) to U(V) by Fe(II) for $hET_{FeHem2\text{-}UAds}$ is highly exothermic (-270 kJ/mol), and could provide enough energy to overcome and facilitate $hET_{FeAds\text{-}FeHem1}$ and $hET_{FeHem1\text{-}FeHem2}$ reactions, driving ET occurring via the proximity effect. The $hET_{FeHem2\text{-}UAds}$ reaction however proceeds nonadiabatically but rapidly at a rate of 10^{12} s^{-1}.

From the several ET pathways modelled in this study, the reduction of U(VI) to U(V) by Fe(II) is consistently predicted to be an exothermic reaction and rapid, while ET reactions between Fe-cations are predicted to be endothermic and considerably slower than ET between Fe and U. The reaction endothermicity and the slow ET rates measured for ET between Fe cations potentially conflict with experimental observations. For instance, it is well-known that interfacial ET between Fe adsorbates and iron (oxyhydr)oxide minerals occurs; for instance, results from Mossbauer spectroscopy show interfacial electron transfer occurs from Fe(II) to Fe (oxyhydr)oxides, where the degree of electron transfer is determined to some extent by sorbed Fe concentrations with respect to the SSL. For the Fe (oxyhydr)oxide systems [104]. However, little is known about the ET mechanisms, energetics, and kinetics involved in these experimental systems, and so it is difficult to determine whether the calculated energetics and kinetics truly agree or disagree with experimental observations. Recent experiments using time-resolved x-ray absorption spectroscopy show electron-hopping rates through hematite to be ~10^{8} s^{-1} [115], though the pathway the electron takes through hematite is unknown. Empirical models calculating the energetics and kinetics for ET between Fe cation within a thicker hydrated (001) hematite slab predict the ET rates to be orders of magnitude higher, with rates within the range of 10^{6} s^{-1} to 10^{10} s^{-1} [69] (Table 5-2). As mentioned in the discussion on factors influencing electronic coupling, it is possible that asymmetry within this hematite cluster may lead to

considerably different ET energetics and rates that what is observed experimentally or in periodic models.

While the reactions are calculated reaction energies and rates for the $hET_{FeAds\text{-}FeHem1}$ and $hET_{FeHem1\text{-}FeHem2}$ reactions may be imprecise, it is plausible that interfacial and surficial ET reactions are energetically and kinetically inhibited. That is, it is possible that ET within and at the topmost layers of a mineral surface can be less energetically favorable with respect to ET through the bulk. For instance, empirical models calculating ET energetics and kinetics of a thicker hydrated (001) hematite slab, show the energetics and kinetics for ET within the couple topmost layers differ from ET within the bulk [69]. The ET reaction energies, reorganization energies, and, in turn, the activation energies are generally higher at the surface compared to the bulk; for instance, ET is slightly endothermic at the topmost layers (8 kJ/mol for ET in the topmost basal plane) while ET in the bulk it is slightly exothermic (-3 kJ/mol). The higher energetics in surficial ET reaction contribute to lower electron transfer rates; e.g., the basal ET rate decreases by up to three orders of magnitude compared to the bulk ($\sim 10^{7}$ s^{-1} *vs.* $\sim 10^{10}$ s^{-1}, respectively). Thus, while improvements to the models in this study can be made (*e.g.*, use of DFT-B3LYP) to obtain more precise ET energetics, it is plausible that the interfacial and surficial ET reactions within hematite energetic present energetic/kinetic barriers for ET occurring via the proximity effect.

5.6 Conclusions

Overall, this study has shown that MT coupled with *ab initio* calculations is capable of elucidating atomistic mechanisms involved in the reduction of U(VI) to U(V) by Fe(II) in the presence of corundum and hematite clusters. There are uncertainties with some of the calculated energetic properties (e.g., a low electronic coupling for the $hET_{FeHem2\text{-}UAds}$ reaction), though the ET calculations provide insight into potential energetic and kinetic limitations that are encountered with different ET pathways. In particular, this study shows the adiabaticity of reactions on insulating substrates can affect the reduction of U(VI) by Fe(II). ET on semiconducting substrates is more complex, as numerous ET pathways via the proximity effect can exist in a semiconducting substrate. For Fe and U coadsorbed on a small hematite cluster (spatially separated by ~5.2 Å), the ET calculations suggest there are potentially considerable energetic and kinetic barriers that must be overcome. In particular, ET between interfacial and

surficial Fe cations of the hematite cluster are found to be energetically and/or kinetically limiting steps for ET via the proximity effect; interfacial and surficial ET reactions between Fe cations are endothermic and proceed slowly. However, it is postulated that the reduction of U(VI) to U(V) by Fe(II) within the hematite cluster may be able to drive the ET to occur via the proximity effect.

While MT has provided a further understanding of fundamental ET processes that can occur on insulating and semiconducting surfaces, improvements can be made to these models to obtain more precise energetic/kinetics. For instance, the results and prediction for ET through the basal plane of the hematite cluster ($hET_{FeHem1\text{-}FeHem2}$) in this study suggests that ET would proceed slowly (10^{-7} s^{-1}) due to the high endothermicity of the ET reaction (76 kJ/mol); this is in contrast to previous measured ET rates shows that transport through the basal plane is rapid (10^{7} s^{-1}) and can potentially occur over long lateral distances [59, 69]. The ET parameters can be improved through the application of stricter, more rigorous computational parameters, such as through the application of a more DFT-B3LYP-like functional as well as a larger basis set. As mentioned briefly in the methods, the used of mixed HF-DFT functionals, where the UHF contributions were lowered, lead to lower overall reaction energies (*i.e.,* more energetically favorable ET reactions) although these also led more considerable structural rearrangement (leading to non-parabolic and complex PES). The effect of these different factors on ET energetics and kinetics is currently being applied.

Through continued testing and improvement of the computational parameters, a thorough understanding of energetic and kinetic parameters influencing the heterogeneous catalysis of U(VI) reduction by Fe(II) can been obtained. Furthermore, it is possible that this approach can be extended towards understanding a broad range of redox-sensitive systems; increasing our understanding of fundamental mechanisms involved in heterogeneous catalysis can provide considerable insight into the transport of metals such as arsenic to the geochemical cycling of Fe in the environment.

5.7 Acknowledgements

This research was supported by the U.S. Office of Science, BES/HEC (Basic Energy Sciences, Heavy Element Chemistry) DE-FG02-06ER15783. KMR acknowledges support from the Geosciences Program at Pacific Northwest National Laboratory (PNNL) from the U.S. Department of Energy (DOE) Office of Science, Office of Basic Energy Sciences, Division of Chemical Sciences, Geosciences, and Biosciences. A portion of the research was performed using EMSL, a DOE Office of Science User Facility sponsored by the DOE Office of Biological and Environmental Research and located at PNNL.

5.8 Tables

Table 5-1: Compilation of changes in Mulliken spins as well as interatomic distances before and after ET reactions on the corundum and hematite clusters. The stoichiometries and (co)adsorption energies for the models calculated are also provided. For the Fe and U coadsorbed on the hematite cluster, the following notations mean: O_{ax} = axial O, Fe_{ads} = Fe adsorbate, Fe_{hem1} = Fe cation that accepts electron from the Fe adsorbate (reduced Fe in intermediate 1 structure), and Fe_{hem2} = Fe cation that accepts electron from the Fe within the hematite basal surface (reduced Fe in the intermediate 2 structure).

Model	***Fe and U coadsorbed on corundum cluster***		***U adsorbed Fe-incorporated corundum cluster***			***Fe and U coadsorbed on hematite cluster***				
Stoichiometry	$[UO_2(OH)(H_2O)_2 - Al_8O_{30}H_{34}-Fe(H_2O)_3]^{+2}$		$[U(OH)_2(H_2O) - FeAl_7O_{30}H_{36}]^{-1}$			$[UO_2(OH)(H_2O)_2 - Fe_8O_{30}H_{34}- Fe(H_2O)_3]^{+2}$				
(Co)adsorption energy (kJ/mol)	-10.071		162.581			-62.723				
Mulliken spins	**Pre-ET**	**Post-ET**	**Mulliken spins**	**Pre-ET**	**Post-ET**	**Mulliken spins**	**Pre-ET**	**Inter1**	**Inter2**	**Post-ET**
U	0	1.29	**U**	0	1.24	**U**	0	0	0	1.29
Fe	3.97	4.78	**Fe**	3.87	4.42	**Fe_{ads}**	3.97	4.8	4.79	4.8
						Fe_{hem1}	4.66	3.85	4.65	4.65
						Fe_{hem2}	4.78	4.78	3.97	4.78
Averaged interatomic distances (Å)										
U-Fe_{ads}	4.576	4.648	**U-Fe_{ads}**	4.036	4.283	**U-Fe_{hem2}**	3.419	3.369	3.268	3.440
U-Al	3.287	3.343	**U-Al**	3.881	3.847	**U-O_{ax}**	1.763	1.766	1.775	1.883
Fe-Al	2.957	2.936	**Fe-Al**	2.680	2.601	**U-O**	2.420	2.552	2.307	2.466
U-O_{ax}	1.772	1.907	**U-O_{ax}**	1.775	1.910	**U-OH**	2.432	2.508	2.346	2.608
U-O	-	-	**U-O**	-	-	**U-OH_2**	2.404	2.427	2.464	2.454
U-OH	2.357	2.429	**U-OH**	2.305	2.413	**Fe_{ads}-O**	-	-	-	-
U-OH_2	2.549	2.535	**U-OH_2**	2.550	2.542	**Fe_{ads} -OH**	2.157	1.964	1.977	1.997
Fe-O	-	-	**Fe-O**	2.107	2.053	**Fe_{ads} – OH_2**	2.109	2.038	2.030	2.018
Fe-OH	2.121	2.039	**Fe-OH**	2.038	1.925	**Fe_{hem1}-O**	1.999	2.110	1.962	1.975
Fe-OH_2	2.124	2.026	**Fe-OH_2**	2.115	2.100	**Fe_{hem1}-OH**	1.972	2.037	2.040	2.007
						Fe_{hem1}-OH_2	-	-	-	-
						Fe_{hem2}-O	2.049	2.046	2.165	2.059
						Fe_{hem2}-OH	1.984	1.984	2.113	1.979
						Fe_{hem2}-OH_2	1.963	1.959	2.060	1.954

Table 5-2: Calculated thermodynamic and kinetic properties for the various ET pathways modelled on the corundum and hematite clusters. * denotes reactions that occur adiabatically. [1]Reference thermodynamic and kinetic properties from Kerisit and Rosso (2006) [69] for ET at the (001) hydroxyl-terminated hematite surface in vacuum; used as comparison to ET values calculated in this study

Model	**ΔG^o (kJ/mol)**	**λ (kJ/mol)**	**V_{AB} (kJ/mol)**	**ΔG^* (kJ/mol)**	**P_{12}**	**k_{et} (s^{-1})**
U and Fe coadsorbed on corundum, $cET_{FeAds\text{-}UAds}$	-39.758	289.404	1.930	51.917	0.181	1.978×10^{2}
U adsorbed onto Fe-incorporated corundum, $cET_{FeInc\text{-}UAds}$	-89.842	279.368	13.317	21.230	1.000	2.340×10^{7} *
U and Fe coadsorbed on hematite, $hET_{FeAds\text{-}UAds}$	-65.639	258.910	38.537	30.567	1.000	7.865×10^{8} *
U and Fe coadsorbed on hematite, $hET_{FeAds\text{-}FeHem1}$	47.839	256.443	18.813	71.448	1.000	1.543×10^{-3} *
U and Fe coadsorbed on hematite, $hET_{FeHem1\text{-}FeHem2}$	75.932	269.254	2.859	107.774	0.540	4.167×10^{-7} *
U and Fe coadsorbed on hematite, $hET_{FeHem2\text{-}UAds}$	-229.770	264.228	0.418	0.706	0.020	6.356×10^{12}
FeII-Fe(III), basal (001) hematite surface, topmost layer (Layer 1)[1]	7.720	188.175	17.756	51.145	96.500	9.264×10^{9} *
FeII-Fe(III), c-direction [001], two topmost layers (Layers 1-2)[1]	0.965	214.230	2.702	51.145	20.265	2.123×10^{6} *

5.9 Figures

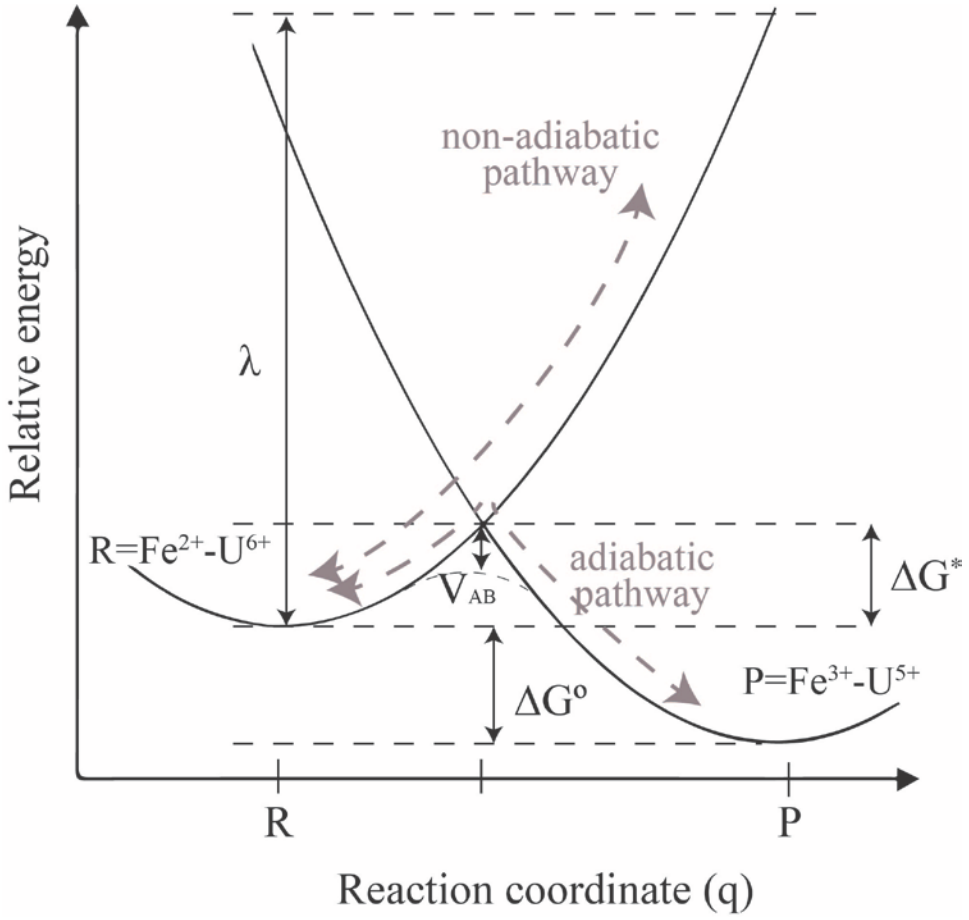

Figure 5-1: Potential energy surface of an ET reaction. Modified from Taylor, *et al.* (2015) [96].

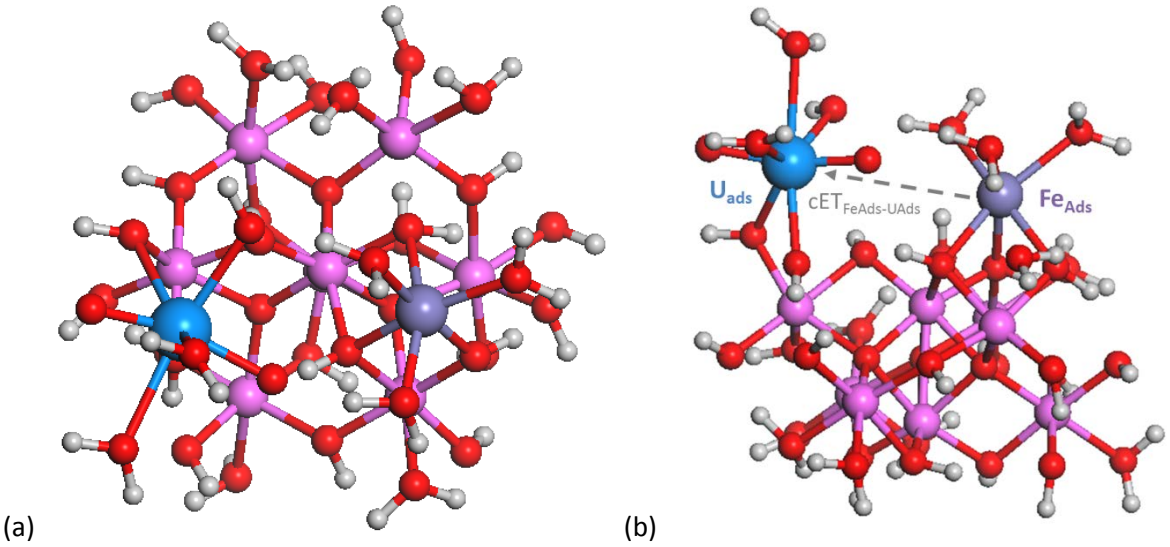

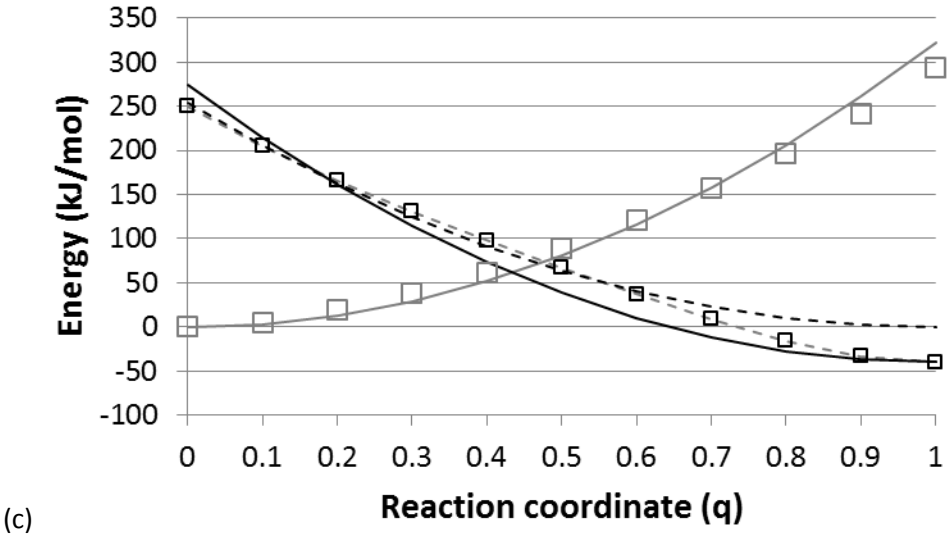

Figure 5-2: Geometry optimized pre-ET structure for Fe and U coadsorbed on the corundum cluster, looking (a) down [001] and (b) the basal plane. The colors of the atoms denote the elements: blue =U, purple = Fe, pink = Al, gray = H and red =O. This coloring scheme for the atoms is applied for all models. The U and Fe ions participating in the $cET_{FeAds-UAds}$ reaction are labelled. The dashed gray arrow represents the ET pathway for $cET_{FeAds-UAds}$ reaction. (c) PES for the $cET_{FeAds-UAds}$ reaction; q=0 represents the pre-ET structure while q=1 represents the post-ET structure. The open, gray square markers are energies calculated for structures with the Fe(II)/U(VI) electronic configuration while -open, black square markers are for structure with the Fe(III)/U(V) electronic configuration. The solid lines show symmetric parabolas fit to the calculated data. The dashed lines denote there is slight asymmetry between the parabolas fit to the pre- and post-ET structure, although the solid lines show that the energetics would not be significantly affected.

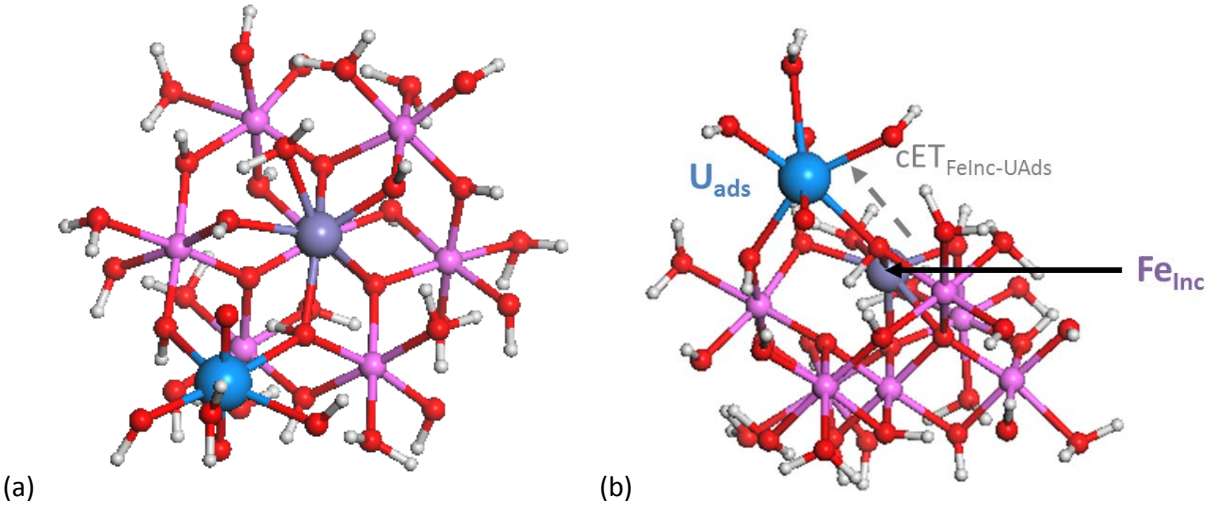

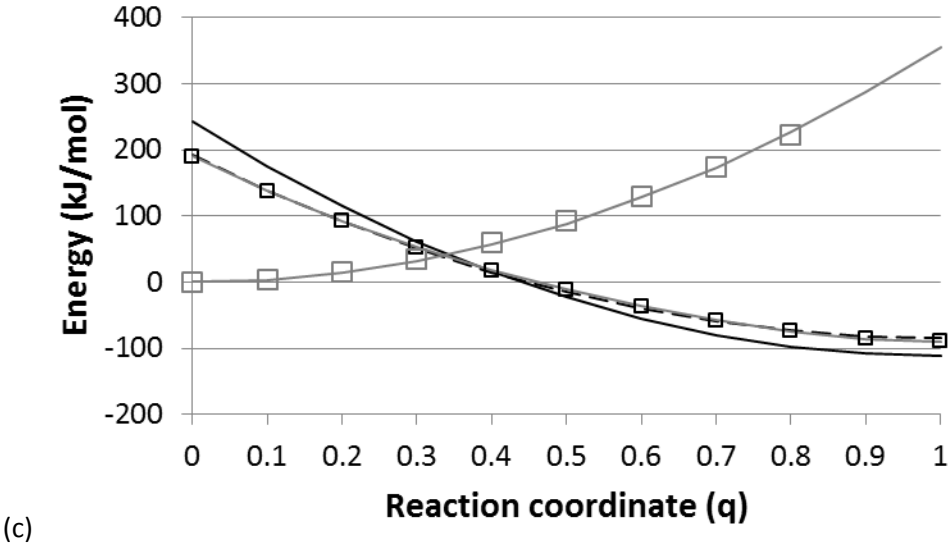

(c)

Figure 5-3: Geometry optimized pre-ET structure for U adsorbed onto the Fe-incorporated corundum cluster, looking (a) down [001] and (b) the basal plane. The U and Fe ions participating in the $cET_{FeInc-UAds}$ reaction are labelled. The dashed gray arrow represent the ET pathway for $cET_{FeInc-UAds}$ reaction. (c) PES for $cET_{FeInc-UAds}$.

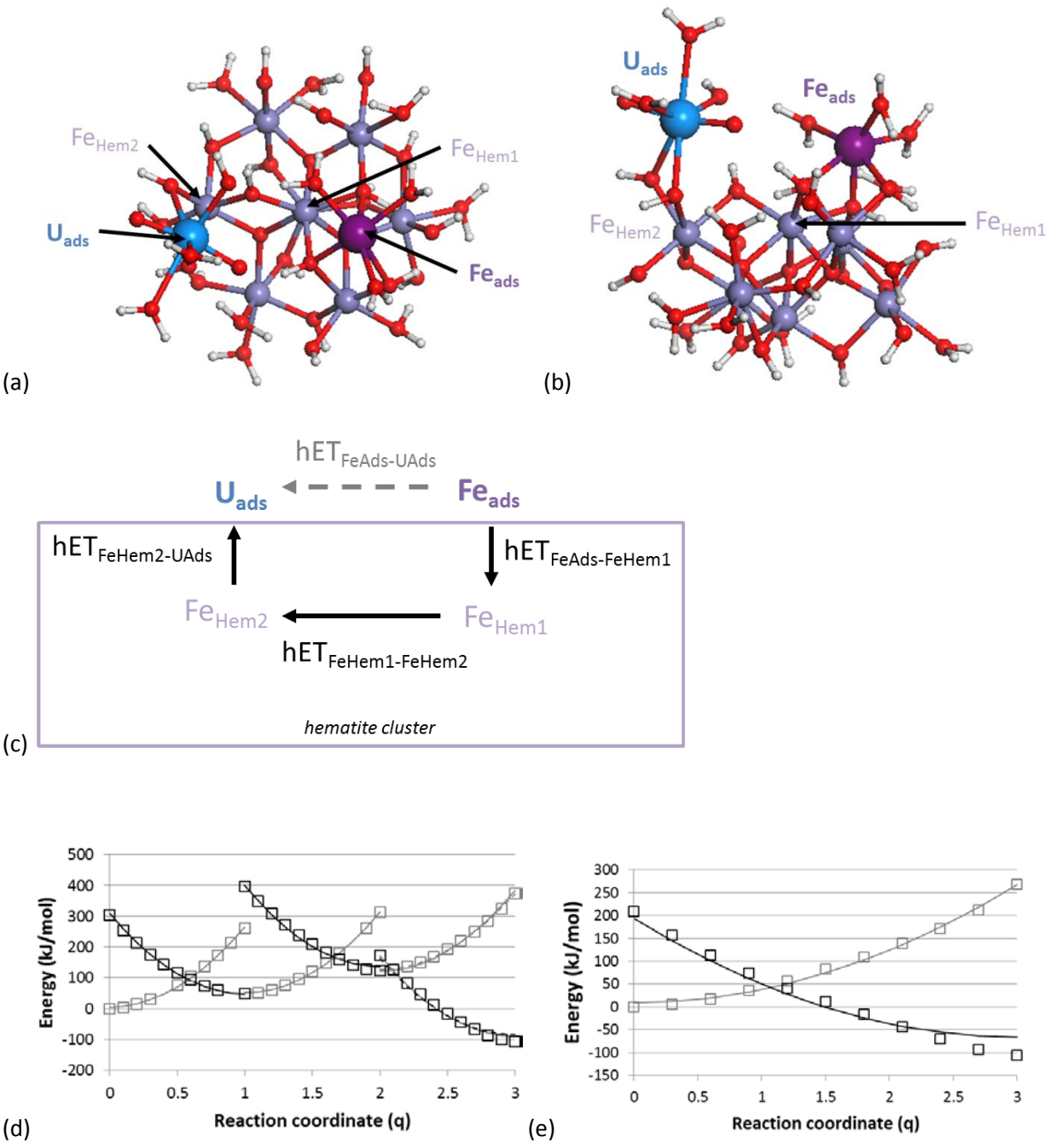

Figure 5-4: Geometry optimized pre-ET structure for Fe and U coadsorbed on the hematite cluster, looking (a) down [001] and (b) the basal plane. Fe_{ads} is colored dark purple in this figure to distinguish it from the underlying Fe-cations, which are light purple. Black arrows point to the cations that participate in ET. (c) Simplified schematic of ET reactions modelled with hematite cluster. Solid, black arrows and black text denotes ET reactions used to model ET occurring via the proximity effect. The dashed, gray arrow and gray text denote a ET pathway where hematite does not directly participate in ET; this pathway is similar to $cET_{FeAds\text{-}UAds}$. (d) PES for ET reactions used to model ET occurring via the proximity effect ($hET_{FeAds\text{-}FeHem1}$, $hET_{FeHem1\text{-}FeHem2}$,and $hET_{FeHem2\text{-}UAds}$); q=0 denotes the pre-ET structure, q=1 denotes the intermediate 1 structure, q=2 denotes the intermediate 2 structure, and q=3 denotes the post-ET structure. Thus, the energetics for the $hET_{FeAds\text{-}FeHem1}$ are plotted from q=0 to q=1, etc., (e) PES for $hET_{FeAds\text{-}UAds}$.

5.10 Supplementary information

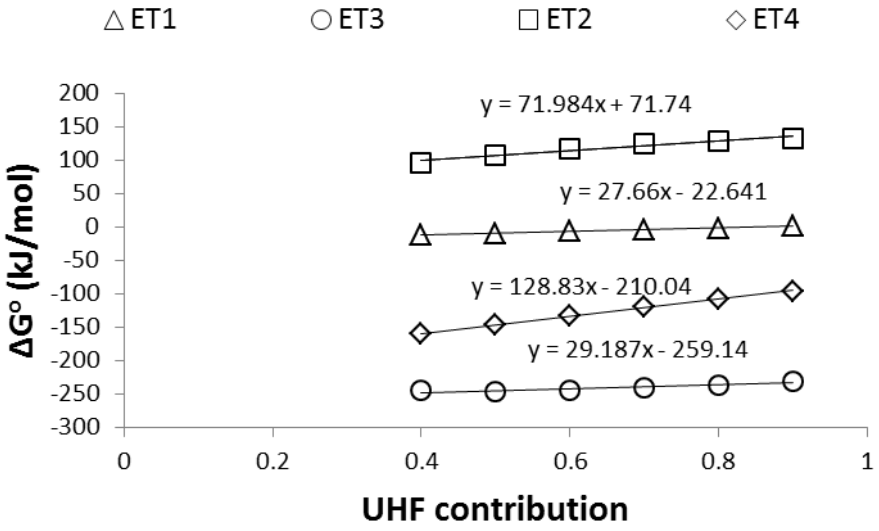

(a)

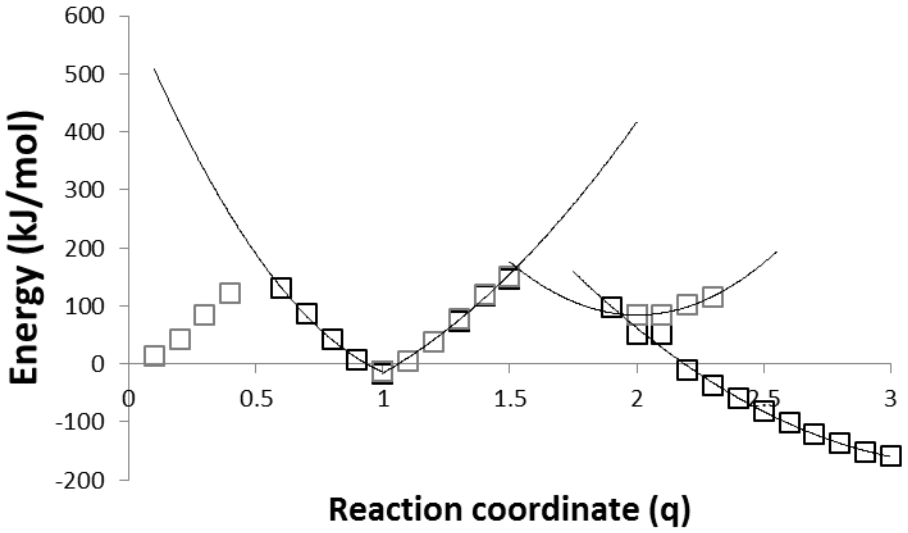

(b)

Supplementary figure 5-1: (a) For the Fe and U coadsorbed onto hematite, the clusters were geometry optimized (using the z-matrices, OH distances fixed) using functionals with decreasing contributions from UHF (*e.g.*, a geometry optimized structure with 0.2 UHF would be equivalent to optimization using the DFT-B3LYP functional). It is shown that with decreasing UHF contributions that the reaction energies, ΔG^{o}, for all the hET reactions all decrease; the ET reaction becomes more energetically favorable with decreasing UHF contributions. (b) PES for $hET_{FeAds\text{-}FeHem1}$, $hET_{FeHem1\text{-}FeHem2}$,and $hET_{FeHem2\text{-}UAds}$ for the Fe and U coadsorbed on the hematite cluster using 0.4 UHF. While the reaction energy decreases, there are considerable structural changes (though no bond breakage) that lead to steep, somewhat parabolic PES profiles. The higher reorganization energy obtained from these calculations would still complicate the calculation of the ET rates for these systems.

Chapter 6: Conclusions

The research presented in this dissertation is part of a multi-method approach that is employed to understand synergistic effects between sorption and/or redox processes and mineral surfaces in controlling redox reaction rate kinetics, by way of mineral catalysis, and therefore actinide mobility, with applications to the geochemical cycling of other metals such as Cr and As. Unique and novel approaches combining experiments as well as atomistic modeling are utilized to make detailed studies on the structure, thermodynamics, kinetics, and reaction mechanisms of actinide complexes and their interactions with minerals. Through combining experiments and calculations a more thorough and fundamental understanding of reactions occurring at the mineral-water interface from the microscopic to molecular level is obtained.

The results from Chapter 2 show complexities can exist at the Pu oxide–goethite interface, such as the distortion, alignment, and formation of O vacancies within a Pu oxide slab upon sorption to goethite. Through the results from this study, the observance of non-*fcc* PuO_{2-x} structures sorbed to goethite surfaces in previous experimental studies [19, 20] is proposed to be due to the distortion of the *fcc* PuO_2 lattice due to combined effects from the Pu oxide's sorption onto goethite and nanoparticulate properties. The lattice mismatch between the goethite and Pu oxide prevents the growth and aggregation of the PuO_2 nanocolloids, so the Pu oxide adsorbates remain as 2 – 5 nm particles. Upon sorption to goethite, the Pu oxide phase can be more stabilized, and distortion of the PuO_2 lattice and structure is necessary to better accommodate the goethite substrate structure. Thus, these models show the potential for non-*fcc*, nanoparticulate Pu oxides to form through distortion of the lattice upon sorption onto goethite. In turn, it is important to understand the reactions and processes occurring at the mineral-water interface as they influence the transport of Pu

The results from Chapter 3 elucidate the mechanisms involved in the removal and abiotic reduction of U(VI) in an Fe(II)-containing solution at neutral pH and anoxic conditions. The removal of uranyl from solution at high concentrations occurs through the precipitation of

(meta)schoepite, where the subsequent transitioning to a heterogeneous system enables uranyl reduction by ferrous iron. The surface of the solid U phase is then capable of being partially reduced to U(IV)/U(V) through the sorption of Fe(II) onto the substrate surface. The thermodynamics for redox reactions show that U(VI) reduction is unfavorable in a homogeneous aqueous system, *i.e.,* in the presence of aqueous species such as $Fe(OH)_2^+$ and $U(OH)_4$ but without the presence of a solid surface. Thus, the experimental results from this study demonstrate that the homogeneous reduction of U(VI) by Fe(II) would not be a viable means of removing uranium from solution. *Ab initio* methods and electron transfer (ET) calculations further substantiate experimental observations, providing thermodynamic and kinetic data as well as an understanding of molecular-scale reaction mechanisms. The progression of U(VI) reduction to U(V) as a proton-coupled ET reaction leads to high energetic barriers and in turn slow ET rates. Through formation of an inner-sphere (IS) complex where Fe and U share bridging hydroxyl ligands, reduction of U(VI) to U(V) can proceed rapidly. However, the formation of the IS complex necessary for facile ET in homogeneous aqueous solution is thermodynamically unfavorable. These models provide a fundamental understanding of why reduction for the homogeneous uranyl-ferrous iron system is rarely observed.

Observations from previous experiments and Chapter 3 show the chemical reduction of U(VI) by Fe(II) proceeds rapidly in heterogeneous systems, such as when uranyl and ferrous iron coadsorbed onto iron oxide minerals [12, 13]. Chapter 4 investigates the influence of a mineral substrate's chemical and electronic properties on the heterogeneous catalysis of U(VI) reduction by Fe(II) on isostructural Fe- and Al (oxyhydr)oxides. Batch experiments show that U(VI) reduction by Fe(II) is tens of times faster in the presence of Fe (oxyhydr)oxides than when in the presence of isostructural Al (oxyhydr)oxides. *Ab initio* calculations for Fe and U coadsorbed on periodic slabs support conceptual models, further highlighting differences between the semiconducting hematite and insulating corundum (001) slabs, such as their surface reactivities and ET pathways, and the implications these would have on catalyzing redox reactions. ET pathways on insulating surfaces are spatially limited while spatial limitations for ET on semiconducting surface can be overcome via the proximity effect, where an electron can be shuttled and/or redistributed within the network of electron-accepting Fe atoms at the semiconducting surface to potentially reach a U(VI) ion sorbed on the substrate and within the vicinity of the reductant. Accounting for the influence of mineral properties, such as their

chemical and electronic character, on the heterogeneous catalysis on of redox reactions would provide more accurate predictions on the viability and effectiveness for U(VI) reduction by Fe(II) to occur on different substrate surfaces.

To further substantiate the postulated ET pathways found in Chapter 4 and their impacts on the catalysis of redox reactions, molecular simulations coupled with Marcus theory were applied to describe the energetics and kinetics of mineral-catalyzed redox reactions in ternary, coadsorbed systems for the first time. Key Results from Chapter 5 show the electronic coupling parameter to influence the catalysis of redox reactions on insulating corundum clusters. When U and Fe are coadsorbed onto corundum cluster and are spatially separated by ~4.6 Å, the electronic coupling between the U and Fe adsorbates is weak, which lowers the probability for ET to occur. In contrast, when ET occurs between a U(VI) adsorbed to an Fe(II)-incorporated corundum cluster, the electronic coupling increases, meaning ET has a high probability of occurring and the reaction proceeds adiabatically. The potential for ET to occur via the proximity effect in the hematite cluster is also investigated. While potentially numerous ET pathways through the hematite cluster can exist, as shown in Chapter 4, interfacial ET and transport of the electron through the hematite surface via the proximity effect can be energetically inhibited due to potentially high reaction and activation energies that must be overcome. Through coupling *ab initio* calculations with MT considerable insight into the catalysis of redox reactions in ternary, coadsorbed systems has been gained. Through continued developments in this approach, it is possible that MT can be applied to understand a broad range of redox cycles, such as the geochemical cycling of Fe and Mn.

Through utilizing experimental and computational approaches, a more thorough understanding of metal mobility and chemical behavior is obtained. Such a multi-method approach can contribute to the development of conceptual models to more accurately predict the redox kinetics and the resulting migration velocities of radionuclides and metals for realistic environmental systems. Batch sorption experiments, mineral characterization techniques, and atomistic modeling are utilized to help identify reaction pathways and mechanisms affecting uranium mobility. Molecular simulations are utilized to measure the energetics and kinetics of the sorption and redox processes as well as gain insight into the atomistic mechanisms influencing actinide mobility at mineral surfaces. In a broader context, this dissertation also

demonstrates the significance of fundamental materials' properties in contaminant transport and heavy metal cycling; this knowledge being applicable towards in situ remediation processes including permeable reactive barriers, chemical stabilization, and biotransformation.

References

[1] Putnis, A., Becker, U., Bosbach, D., Mineral surface science: Principles, applications and case studies, Nato. Adv. Sci. I. C-Mat1999, pp. 595-628.

[2] Hochella, M.F., White, A.F., Mineral-Water Interface Geochemistry - An Overview, Rev. Min.1990, pp. 1-16.

[3] EPA, Cleaning up radioactive sites, 2012.

[4] Powell, B.A., Environmental Chemistry of Uranium and Plutonium, Radiochemistry Webinars. Actinide Chemistry Series, 2012.

[5] Brown, G.E., Calas, G., Mineral-Aqueous Solution Interfaces and Their Impact on the Environment, *Geochem. Persp.*, **1** (2012) 483-742.

[6] Johnson, J., Talk, No action on nuclear waste plan, *Chem. Eng. News*, **90** (2012) 44-46.

[7] EPA, Public health and environmental radiation protection standards for Yucca Mountain, Nevada, 2008.

[8] Kim, J.I., Grambow, B., Geochemical assessment of actinide isolation in a German salt repository environment, *Eng. Geol.*, **52** (1999) 221-230.

[9] Roberts, K.E., Wolery, T.J., Atkins-Duffin, C.E., Prussin, T.G., Allen, P.G., Bucher, J.J., Shuh, D.K., Finch, R.J., Prussin, S.G., Precipitation of crystalline neptunium dioxide from near-neutral aqueous solution, Radiochimica Acta/International journal for chemical aspects of nuclear science and technology, 2003, pp. 87.

[10] Geckeis, H., Lutzenkirchen, J., Polly, R., Rabung, T., Schmidt, M., Mineral-Water Interface Reactions of Actinides, *Chem. Rev.*, **113** (2013) 1016-1062.

[11] Hua, B., Xu, H.F., Terry, J., Deng, B.L., Kinetics of uranium(VI) reduction by hydrogen sulfide in anoxic aqueous systems, *Environ. Sci. Technol.*, **40** (2006) 4666-4671.

[12] Liger, E., Charlet, L., Van Cappellen, P., Surface catalysis of uranium(VI) reduction by iron(II), *Geochim. Cosmochim. Acta*, **63** (1999) 2939-2955.

[13] Zeng, H., Giammar, D.E., U(VI) reduction by Fe(II) on hematite nanoparticles, *J. Nanopart. Res.*, **13** (2011) 3741-3754.

[14] Charlet, L., Silvester, E., Liger, E., N-compound reduction and actinide immobilisation in surficial fluids by Fe(II): The surface≡ $Fe^{III}OFe^{II}OH^{o}$ species, as major reductant, *Chem. Geol.*, **151** (1998) 85-93.

[15] Du, X., Boonchayaanant, B., Wu, W.-M., Fendorf, S., Bargar, J., Criddle, C.S., Reduction of uranium(VI) by soluble iron(II) conforms with thermodynamic predictions, *Environ. Sci. Technol.*, **45** (2011) 4718-4725.

[16] Ilton, E.S., Haiduc, A., Moses, C.O., Heald, S.M., Elbert, D.C., Veblen, D.R., Heterogeneous reduction of uranyl by micas: Crystal chemical and solution controls, *Geochim. Cosmochim. Acta*, **68** (2004) 2417-2435.

[17] Becker, U., Rosso, K.M., Hochella, M.F., The proximity effect on semiconducting mineral surfaces: A new aspect of mineral surface reactivity and surface complexation theory?, *Geochim. Cosmochim. Acta*, **65** (2001) 2641-2649.

[18] Rosso, K.M., Becker, U., Proximity effects on semiconducting mineral surfaces II: Distance dependence of indirect interactions, *Geochim. Cosmochim. Acta*, **67** (2003) 941-953.

[19] Powell, B.A., Dai, Z.R., Zavarin, M., Zhao, P.H., Kersting, A.B., Stabilization of plutonium nano-colloids by epitaxial distortion on mineral Surfaces, *Environ. Sci. Technol.*, **45** (2011) 2698-2703.

[20] Zavarin, M., Zhao, P.H., Dai, Z.R., Kersting, A.B., Plutonium sorption and precipitation in the presence of goethite at 25 and 80 degrees C, *Radiochim. Acta*, **102** (2014) 983-997.

[21] Brady, P.V., Physics and Chemistry of Mineral Surfaces, CRC Press, Boca Raton, 1996.

[22] Catalano, J.G., Park, C., Fenter, P., Zhang, Z., Simultaneous inner- and outer-sphere arsenate adsorption on corundum and hematite, *Geochim. Cosmochim. Acta*, **72** (2008) 1986-2004.

[23] Steele, H.M., Wright, K., Hillier, I.H., Modelling the adsorption of uranyl on the surface of goethite, *Geochim. Cosmochim. Acta*, **66** (2002) 1305-1310.

[24] Sherman, D.M., Peacock, C.L., Hubbard, C.G., Surface complexation of U(VI) on goethite (α-FeOOH), *Geochim. Cosmochim. Acta*, **72** (2008) 298-310.

[25] Mason, S.E., Iceman, C.R., Tanwar, K.S., Trainor, T.P., Chaka, A.M., Pb(II) adsorption on isostructural hydrated alumina and hematite (0001) surfaces: A DFT study, *J. Phys. Chem. C*, **113** (2009) 2159-2170.

[26] Kersting, A.B., Plutonium transport in the environment, *Inorg. Chem.*, **52** (2013) 3533-3546.

[27] Kersting, A.B., Efurd, D.W., Finnegan, D.L., Rokop, D.J., Smith, D.K., Thompson, J.L., Migration of plutonium in ground water at the Nevada Test Site, *Nature*, **397** (1999) 56-59.

[28] Novikov, A.P., Kalmykov, S.N., Utsunomiya, S., Ewing, R.C., Horreard, F., Merkulov, A., Clark, S.B., Tkachev, V.V., Myasoedov, B.F., Colloid transport of plutonium in the far-field of the Mayak Production Association, Russia, *Science*, **314** (2006) 638-641.

[29] Coffinberry, A.S., Miner, W.N., The Metal Plutonium, University of Chicago Press, Chicago, 1961.

[30] Petit, L., Svane, A., Szotek, Z., Temmerman, W.M., First-principles calculations of $PuO2_{+/-x}$, *Science*, **301** (2003) 498-501.

[31] Reuter, K., Scheffler, M., Composition, structure, and stability of RuO_2 (110) as a function of oxygen pressure, *Phys. Rev. B*, **65** (2002).

[32] Sun, B., Liu, H.F., Song, H.F., Zhang, G.C., Zheng, H., Zhao, X.G., Zhang, P., The environmental dependence of redox energetics of PuO_2 and α-Pu_2O_3: A quantitative solution from DFT+U, *Phys. Lett. A*, **376** (2012) 2672-2676.

[33] Clark, S.J., Segall, M.D., Pickard, C.J., Hasnip, P.J., Probert, M.J., Refson, K., Payne, M.C., First principles methods using CASTEP, *Z. Kristallogr.*, **220** (2005) 567-570.

[34] Schnitker, J., Srolovitz, D.J., Misfit effects in adhesion calculations, *Model Simul Mater Sc*, **6** (1998) 153-164.

[35] Kubicki, J.D., Paul, K.W., Sparks, D.L., Periodic density functional theory calculations of bulk and the (010) surface of goethite, *Geochem. Trans.*, **9** (2008).

[36] Rakovan, J., Becker, U., Hochella, M.F., Aspects of goethite surface microtopography, structure, chemistry, and reactivity, *Am. Min.*, **84** (1999) 884-894.

[37] Jomard, G., Bottin, F., Thermodynamic stability of PuO_2 surfaces: Influence of electronic correlations, *Phys. Rev. B*, **84** (2011).

[38] Rak, Z., Ewing, R.C., Becker, U., Hydroxylation-induced surface stability of AnO_2 (An = U, Np, Pu) from first-principles, *Surf. Sci.*, **608** (2013) 180-187.

[39] Siegel, D.J., Hector, L.G., Adams, J.B., Adhesion, stability, and bonding at metal/metal-carbide interfaces: Al/WC, *Surf. Sci.*, **498** (2002) 321-336.

[40] Siegel, D.J., Hector, L.G., Adams, J.B., Adhesion, atomic structure, and bonding at the Al (111)/α-Al_2O_3 (0001) interface: A first principles study, *Phys. Rev. B*, **65** (2002).

[41] Batirev, I.G., Alavi, A., Finnis, M.W., Deutsch, T., First-principles calculations of the ideal cleavage energy of bulk niobium (111)/α-alumina (0001) interfaces, *Phys. Rev. Lett.*, **82** (1999) 1510-1513.

[42] Wang, Z.C., Saito, M., Tsukimoto, S., Ikuhara, Y., Heterointerfaces: Atomic structures, electronic states, and related properties, *J. Ceram. Soc. Jpn.*, **119** (2011) 783-793.

[43] Momma, K., Izumi, F., VESTA 3 for three-dimensional visualization of crystal, volumetric and morphology data, *J. Appl. Cryst.*, **44** (2011) 1272-1276.

[44] Hailstone, R.K., DiFrancesco, A.G., Leong, J.G., Allston, T.D., Reed, K.J., A study of lattice expansion in CeO_2 nanoparticles by transmission electron microscopy, *J. Phys. Chem. C*, **113** (2009) 15155-15159.

[45] Wu, L.J., Wiesmann, H.J., Moodenbaugh, A.R., Klie, R.F., Zhu, Y.M., Welch, D.O., Suenaga, M., Oxidation state and lattice expansion of CeO_{2-x} nanoparticles as a function of particle size, *Phys. Rev. B*, **69** (2004).

[46] Barron, V., Torrent, J., Surface hydroxyl configuration of various crystal faces of hematite and goethite, *J. Coll. Interf. Sci.*, **177** (1996) 407-410.

[47] Cornell, R.M., Schwertmann, U., The Iron Oxides : Structure, Properties, Reactions, Occurrences, and Uses, 2nd, completely rev. and extended ed., Wiley-VCH, Weinheim, 2003.

[48] Jang, J.-H., Dempsey, B.A., Burgos, W.D., Solubility of schoepite: Comparison and selection of complexation constants for U(VI), *Water Res.*, **40** (2006) 2738-2746.

[49] EPA, National primary drinking water regulations; radio-nuclides; final rule, in: F. Register (Ed.) 236, 2000.

[50] Charlet, L., Bosbach, D., Peretyashko, T., Natural attenuation of TCE, As, Hg linked to the heterogenenous oxidation of Fe(II): An AFM study, *Chem. Geol.*, **190** (2002) 303-319.

[51] Gustafsson, J.P., Visual Minteq v. 3.0, 2010.

[52] Felmy, A.R., Ilton, E.S., Rosso, K.M., Zachara, J.M., Interfacial reactivity of radionuclides: Emerging paradigms from molecular-level observations, *Min. Mag.*, **75** (2011) 2379-2391.

[53] Morel, F.M.M., Hering, J.G., Principles and applications of aquatic chemistry, John Wiley & Sons, Inc., New York, NY, 1993.

[54] Hochella, M.F., Auger-electron and X-ray photoelectron spectroscopies, Rev. Min.1988, pp. 573-637.

[55] Singh, A., Catalano, J.G., Ulrich, K.U., Giammar, D.E., Molecular-scale structure of uranium(VI) immobilized with goethite and phosphate, *Environ. Sci. Technol.*, **46** (2012) 6594-6603.

[56] Rosso, K.M., Smith, D.M.A., Dupuis, M., An *ab initio* model of electron transport in hematite (α-Fe_2O_3) basal planes, *J. Chem. Phys.*, **118** (2003) 6455-6466.

[57] Wander, M.C.F., Kerisit, S., Rosso, K.M., Schoonen, M.A.A., Kinetics of triscarbonato uranyl reduction by aqueous ferrous iron: A theoretical study, *J. Phys. Chem. A*, **110** (2006) 9691-9701.

[58] Wander, M.C.F., Schoonen, M.A.A., Green rust reduction of chromium part 2: Comparison of heterogeneous and homogeneous chromate reduction, *J. Phys. Chem. C*, **114** (2010) 16408-16415.

[59] Iordanova, N., Dupuis, M., Rosso, K.M., Charge transport in metal oxides: A theoretical study of hematite α-Fe_2O_3, *J. Chem. Phys.*, **122** (2005).

[60] Rosso, K.M., Dupuis, M., Electron transfer in environmental systems: A frontier for theoretical chemistry, *Theor. Chem. Acc.*, **116** (2006) 124-136.

[61] Rosso, K.M., Smith, D.M.A., Dupuis, M., Aspects of aqueous iron and manganese (II/III) self-exchange electron transfer reactions, *J. Phys. Chem. A*, **108** (2004) 5242-5248.

[62] Marcus, R.A., Sutin, N., Electron transfers in chemistry and biology, *Biochim. Biophys. Acta*, **811** (1985) 265-322.

[63] Farazdel, A., Dupuis, M., Clementi, E., Aviram, A., Electric-field induced intramolecular electron-transfer in spiro pi-electron systems and their suitability as molecular electronic devices - A theoretical study, *J. Am. Chem. Soc.*, **112** (1990) 4206-4214.

[64] Marcus, R.A., Electron transfer reactions in chemistry: Theory and experiment (Nobel lecture), *Angewandte Chemie International Edition in English*, **32** (1993) 1111-1222.

[65] Valiev, M., Bylaska, E.J., Govind, N., Kowalski, K., Straatsma, T.P., Van Dam, H.J.J., Wang, D., Nieplocha, J., Apra, E., Windus, T.L., de Jong, W., NWChem: A comprehensive and scalable open-source solution for large scale molecular simulations, *Comput. Phys. Commun.*, **181** (2010) 1477-1489.

[66] Harihara.Pc, Pople, J.A., Influence of polarization functions on molecular-orbital hydrogenation energies, *Theor. Chim. Acta*, **28** (1973) 213-222.

[67] Schafer, A., Horn, H., Ahlrichs, R., Fully optimized contracted gaussian-basis sets for atoms Li to Kr, *J. Chem. Phys.*, **97** (1992) 2571-2577.

[68] Küchle, W., Dolg, M., Stoll, H., Preuss, H., *Ab initio* pseudopotentials for Hg through Rn. I. Parameter sets and atomic calculations, *Mol. Phys.*, **74** (1991) 1245-1263.

[69] Kerisit, S., Rosso, K.M., Computer simulation of electron transfer at hematite surfaces, *Geochim. Cosmochim. Acta*, **70** (2006) 1888-1903.

[70] Skomurski, F.N., Ilton, E.S., Engelhard, M.H., Arey, B.W., Rosso, K.M., Heterogeneous reduction of U^{6+} by structural Fe^{2+} from theory and experiment, *Geochim. Cosmochim. Acta*, **75** (2011) 7277-7290.

[71] Halgren, T.A., Lipscomb, W.N., Synchronous-transit method for determining reaction pathways and locating molecular transition-states, *Chem. Phys. Lett.*, **49** (1977) 225-232.

[72] Dolg, M., Stoll, H., Preuss, H., Pitzer, R.M., Relativistic and correlation-effects for element 105 (Hahnium, Ha) - A comparative study of M and Mo (M = Nb, Ta, Ha) using energy-adjusted *ab initio* pseudopotentials, *J. Phys. Chem.*, **97** (1993) 5852-5859.

[73] Klamt, A., Schuurmann, G., COSMO - A new approach to dielectric screening in solvents with explicit expressions for the screening energy and its gradient, *J. Chem. Soc.-Perk. Trans. 2*, DOI Doi 10.1039/P29930000799(1993) 799-805.

[74] Delley, B., The COnductor-like Screening MOdel for polymers and surfaces, *Mol. Sim.*, **32** (2006) 117-123.

[75] Ilton, E.S., Bagus, P.S., XPS determination of uranium oxidation states, *Surf. Int. Analy.*, **43** (2011) 1549-1560.

[76] Allen, G.C., Crofts, J.A., Curtis, M.T., Tucker, P.M., Chadwick, D., Hampson, P.J., X-ray photoelectron spectroscopy of some uranium oxide phases, *J. Chem. Soc. Dalt. Trans.*, DOI Doi 10.1039/Dt9740001296(1974) 1296-1301.

[77] Wersin, P., Hochella, M.F., Persson, P., Redden, G., Leckie, J.O., Harris, D.W., Interaction between aqueous uranium(VI) and sulfide minerals - Spectroscopic evidence for sorption and reduction, *Geochim. Cosmochim. Acta*, **58** (1994) 2829-2843.

[78] Fredrickson, J.K., Zachara, J.M., Kennedy, D.W., Duff, M.C., Gorby, Y.A., Li, S.-M.W., Krupka, K.M., Reduction of U(VI) in goethite (α-FeOOH) suspensions by a dissimilatory metal-reducing bacterium, *Geochim. Cosmochim. Acta*, **64** (2000) 3085-3098.

[79] Duff, M.C., Coughlin, J.U., Hunter, D.B., Uranium co-precipitation with iron oxide minerals, *Geochim. Cosmochim. Acta*, **66** (2002) 3533-3547.

[80] Waite, T.D., Davis, J.A., Payne, T.E., Waychunas, G.A., Xu, N., Uranium(VI) adsorption to ferrihydrite - Application of a surface complexation model, *Geochim. Cosmochim. Acta*, **58** (1994) 5465-5478.

[81] Aboud, S., Wilcox, J., Brown, G.E., Density Functional Theory investigation of the interaction of water with α-Al2O3 and α-Fe2O3 (1-102) surfaces: Implications for surface reactivity, *Phys. Rev. B*, **83** (2011).

[82] Wehrli, B., Sulzberger, B., Stumm, W., Redox processes catalyzed by hydrous oxide surfaces, *Chem. Geol.*, **78** (1989) 167-179.

[83] Schindler, P.W., A solution chemists view of surface-chemistry, *Pure Appl. Chem.*, **63** (1991) 1697-1704.

[84] Rosso, K.M., Morgan, J.J., Outer-sphere electron transfer kinetics of metal ion oxidation by molecular oxygen, *Geochim. Cosmochim. Acta*, **66** (2002) 4223-4233.

[85] Zachara, J.M., Heald, S.M., Jeon, B.H., Kukkadapu, R.K., Liu, C.X., McKinley, J.P., Dohnalkova, A.C., Moore, D.A., Reduction of pertechnetate [Tc(VII)] by aqueous Fe(II) and the nature of solid phase redox products, *Geochim. Cosmochim. Acta*, **71** (2007) 2137-2157.

[86] Gabriel, U., Gaudet, J.P., Spadini, L., Charlet, L., Reactive transport of uranyl in a goethite column: An experimental and modelling study, *Chem. Geol.*, **151** (1998) 107-128.

[87] Hua, B., Deng, B.L., Reductive immobilization of uranium(VI) by amorphous iron sulfide, *Environ. Sci. Technol.*, **42** (2008) 8703-8708.

[88] Eary, L.E., Rai, D., Chromate removal from aqueous wastes by reduction with ferrous iron, *Environ. Sci. Technol.*, **22** (1988) 972-977.

[89] Noubactep, C., Comment on "Reductive immobilization of uranium(VI) by amorphous iron sulfide", *Environ. Sci. Technol.*, **43** (2009) 1236-1236.

[90] Ilton, E.S., Heald, S.M., Smith, S.C., Elbert, D., Liu, C.X., Reduction of uranyl in the interlayer region of low iron micas under anoxic and aerobic conditions, *Environ. Sci. Technol.*, **40** (2006) 5003-5009.

[91] Ilton, E.S., Boily, J.F., Buck, E.C., Skomurski, F.N., Rosso, K.M., Cahill, C.L., Bargar, J.R., Felmy, A.R., Influence of dynamical conditions on the reduction of U(VI) at the magnetite-solution interface, *Environ. Sci. Technol.*, **44** (2010) 170-176.

[92] Ilton, E.S., Pacheco, J.S.L., Bargar, J.R., Shi, Z., Liu, J., Kovarik, L., Engelhard, M.H., Felmy, A.R., Reduction of U(VI) incorporated in the structure of hematite, *Environ. Sci. Technol.*, **46** (2012) 9428-9436.

[93] Peretyazhko, T., Zachara, J.M., Heald, S.M., Kukkadapu, R.K., Liu, C., Plymale, A.E., Resch, C.T., Reduction of Tc(VII) by Fe(II) sorbed on Al (hydr)oxides, *Environ. Sci. Technol.*, **42** (2008) 5499-5506.

[94] Renock, D., Becker, U., A first principles study of the oxidation energetics and kinetics of realgar, *Geochim. Cosmochim. Acta*, **74** (2010) 4266-4284.

[95] Privalov, T., Schimmelpfennig, B., Wahlgren, U., Grenthe, I., Reduction of uranyl(VI) by iron(II) in solutions: An *ab initio* study, *J. Phys. Chem. A*, **107** (2003) 587-592.

[96] Taylor, S.D., Marcano, M.C., Rosso, K.M., Becker, U., An experimental and *ab initio* study on the abiotic reduction of uranyl by ferrous iron, *Geochim. Cosmochim. Acta*, **156** (2015) 154-172.

[97] Scott, T.B., Allen, G.C., Heard, P.J., Randell, M.G., Reduction of U(VI) to U(IV) on the surface of magnetite, *Geochim. Cosmochim. Acta*, **69** (2005) 5639-5646.

[98] Renock, D., Mueller, M., Yuan, K., Ewing, R.C., Becker, U., The energetics and kinetics of uranyl reduction on pyrite, hematite, and magnetite surfaces: A powder microelectrode study, *Geochim. Cosmochim. Acta*, **118** (2013) 56-71.

[99] O'Loughlin, E.J., Kelly, S.D., Cook, R.E., Csencsits, R., Kemner, K.M., Reduction of uranium(VI) by mixed iron(II/iron(III) hydroxide (green rust): Formation of UO_2 nanoparticles, *Environ. Sci. Technol.*, **37** (2003) 721-727.

[100] Latta, D.E., Boyanov, M.I., Kemner, K.M., O'Loughlin, E.J., Scherer, M.M., Abiotic reduction of uranium by Fe(II) in soil, *Appl. Geochem.*, **27** (2012) 1512-1524.

[101] Powell, B.A., Fjeld, R.A., Kaplan, D.I., Coates, J.T., Serkiz, S.M., $Pu(V)O_2^+$ adsorption and reduction by synthetic hematite and goethite, *Environ. Sci. Technol.*, **39** (2005) 2107-2114.

[102] Zhang, H.Z., Bayne, M., Fernando, S., Legg, B., Zhu, M.Q., Penn, R.L., Banfield, J.F., Size-dependent bandgap of nanogoethite, *J. Phys. Chem. C*, **115** (2011) 17704-17710.

[103] Fernando, S., Baynes, M., Chen, B., Banfield, J.F., Zhang, H.Z., Compressibility and structural stability of nanoparticulate goethite, *RSC Adv.*, **2** (2012) 6768-6772.

[104] Larese-Casanova, P., Scherer, M.M., Fe(II) sorption on hematite: New insights based on spectroscopic measurements, *Environ. Sci. Technol.*, **41** (2007) 471-477.

[105] Elzinga, E.J., Formation of layered Fe(II)-Al(III)-hydroxides during reaction of Fe(II) with aluminum oxide, *Environ. Sci. Technol.*, **46** (2012) 4894-4901.

[106] Alexandrov, V., Neumann, A., Scherer, M.M., Rosso, K.M., Electron exchange and conduction in nontronite from first-principles, *J. Phys. Chem. C*, **117** (2013) 2032-2040.

[107] Rohrbach, A., Hafner, J., Kresse, G., *Ab initio* study of the (0001) surfaces of hematite and chromia: Influence of strong electronic correlations, *Phys. Rev. B*, **70** (2004).

[108] Dzade, N.Y., Roldan, A., de Leeuw, N.H., A density functional theory study of the adsorption of benzene on hematite (α-Fe_2O_3) surfaces, *Minerals-Basel*, **4** (2014) 89-115.

[109] Pacchioni, G., Modeling doped and defective oxides in catalysis with Density Functional Theory methods: Room for improvements, *J. Chem. Phys.*, **128** (2008) 182505.

[110] Yamashita, T., Hayes, P., Analysis of XPS spectra of Fe^{2+} and Fe^{3+} ions in oxide materials, *Appl. Surf. Sci.*, **254** (2008) 2441-2449.

[111] Jeon, B.H., Dempsey, B.A., Burgos, W.D., Kinetics and mechanisms for reactions of Fe(II) with iron(III) oxides, *Environ. Sci. Technol.*, **37** (2003) 3309-3315.

[112] Glezakou, V.A., deJong, W.A., Cluster-models for uranyl(VI) adsorption on α-alumina, *J. Phys. Chem. A*, **115** (2011) 1257-1263.

[113] Scherer, M.M., Balko, B.A., Tratnyek, P.G., The Role of Oxides in Reduction Reactions at the Metal-Water Interface, Mineral-Water Interfacial Reactions, American Chemical Society1999, pp. 301-322.

[114] Handler, R.M., Frierdich, A.J., Johnson, C.M., Rosso, K.M., Beard, B.L., Wang, C.M., Latta, D.E., Neumann, A., Pasakarnis, T., Premaratne, W.A.P.J., Scherer, M.M., Fe(II)-catalyzed recrystallization of goethite revisited, *Environ. Sci. Technol.*, **48** (2014) 11302-11311.

[115] Katz, J.E., Zhang, X.Y., Attenkofer, K., Chapman, K.W., Frandsen, C., Zarzycki, P., Rosso, K.M., Falcone, R.W., Waychunas, G.A., Gilbert, B., Electron small polarons and their Mobility in iron (oxyhydr)oxide nanoparticles, *Science*, **337** (2012) 1200-1203.

[116] Skomurski, F.N., Kerisit, S., Rosso, K.M., Structure, charge distribution, and electron hopping dynamics in magnetite (Fe_3O_4) (100) surfaces from first principles, *Geochim. Cosmochim. Acta*, **74** (2010) 4234-4248.

[117] Koretsky, C.M., Sverjensky, D.A., Sahai, N., A model of surface site types on oxide and silicate minerals based on crystal chemistry: Implications for site types and densities, multi-site adsorption, surface infrared spectroscopy, and dissolution kinetics, *Am. J. Sci.*, **298** (1998) 349-438.

[118] Estes, S.L., Arai, Y., Becker, U., Fernando, S., Yuan, K., Ewing, R.C., Zhang, J.M., Shibata, T., Powell, B.A., A self-consistent model describing the thermodynamics of Eu(III) adsorption onto hematite, *Geochim. Cosmochim. Acta*, **122** (2013) 430-447.

[119] Skomurski, F.N., Shuller, L.C., Ewing, R.C., Becker, U., Corrosion of UO_2 and ThO_2: A quantum-mechanical investigation, *J. Nucl. Mater.*, **375** (2008) 290-310.

[120] Moskaleva, L.V., Nasluzov, V.A., Rosch, N., Modeling adsorption of the uranyl dication on the hydroxylated α-Al_2O_3 (0001) surface in an aqueous medium: A Density Functional Study, *Langmuir*, **22** (2006) 2141-2145.

[121] Hennig, C., Reich, T., Dahn, R., Scheidegger, A.M., Structure of uranium sorption complexes at montmorillonite edge sites, *Radiochim. Acta*, **90** (2002) 653-657.